The alignment of galaxies across all scales

Georgiou, C.

The Alignment of Galaxies Across All Scales

Proefschrift

ter verkrijging van
de graad van Doctor aan de Universiteit Leiden,
op gezag van Rector Magnificus prof. mr. C.J.J.M. Stolker,
volgens besluit van het College voor Promoties
te verdedigen op donderdag 12 december 2019
klokke 12:30 uur

door

Christos Georgiou
geboren te Ioannina, Greece
in 1992

Promotiecommissie

Promotores:	Prof. dr. K.H. Kuijken	
	Prof. dr. H. Hoekstra	
Overige leden:	Dr. N.E. Chisari	(Universiteit Utrecht)
	Prof. dr. H. Hildebrandt	(Ruhr-Universität Bochum)
	Prof. dr. M. Franx	
	Prof. dr. H.J.A. Röttgering	

ISBN: 978-94-028-1827-7
Cover: Rescaled colour image of the largest galaxy group in the Galaxy And Mass Assembly (GAMA) survey's public galaxy group catalogue, composed using the g, r and i-band imaging data from the Kilo Degree Survey, flipped and rotated accordingly. Over-plotted is the average ellipticity field of intrinsically red satellite galaxies of all GAMA groups, centred on the group's centre. The size of the image is ~ 3.6 arcmin.

To the pursuit of knowledge,
and the happiness that comes with it.

Contents

Chapter 1

Introduction

The topic of cosmology has been in the interest of humans for thousands of years. It is easy to understand why this is the case, since cosmology tries to tackle the largest and most mysterious questions we can impose: how is the Universe and everything in it created and what makes it evolve and appear as it is today. It is only reasonable to expect the curious nature of humans will lead to the study of the Universe, initially from a philosophical perspective, but later, especially during the last century, from a scientific point of view. In particular, during the last few decades, we have been able to construct a broad view of the different ingredients and physical processes taking place during the history of our Universe, and settled on a standard cosmological model which encompasses our understanding. We have been able to parametrise the Universe into a few cosmological parameters and, with improving technological and statistical techniques, measured them with great accuracy using many independent observations.

The success of the standard cosmological model in describing astronomical observations is perhaps overshadowed by the two main questions it raises: what is the nature of dark matter and dark energy. These two are components of the Universe that make up approximately 95% of the energy density of the present day Universe, and their existence is evidenced by many independent observations. In general, dark matter has the effect of increasing structure formation while dark energy halts it. However, there is very little we currently understand about the fundamental physics that describe these components, and observations sensitive to them are crucial in increasing our understanding.

Several observational techniques can provide insight into dark matter and dark energy, but of particular interest in this thesis is weak gravitational lensing. This is the coherent distortion of light sources from the intervening matter as light traverses through the spacetime. The distortion can be extracted by statistically analysing shapes of a large ensemble of galaxies, and is related to the matter content as well as the geometry and expansion history of the Universe. This makes weak gravitational lensing sensitive to dark matter and dark energy, and with current and future astronomical surveys designed specifically to exploit this phenomenon, it has become a competitive cosmological probe with great statistical power in measuring cosmological parameters.

The statistical power and promise of future weak gravitational lensing surveys can only be realised if systematic contamination to the measured signal is controlled to very high accuracy. The most important astrophysical contaminant is intrinsic alignments, the correlation of galaxy shapes with the tidal gravitational field. Since lensing relies on measuring correlations of galaxy shapes, intrinsic alignments will cause shape correlations that are not due to gravitational lensing, and can bias the cosmological parameters extracted from lensing, if unaccounted for (see e.g. Kirk et al. 2015). The main focus of this thesis is the exploration of the galaxy intrinsic alignment signal, as measured from state of the art astronomical data, and the dependence of the signal on several galaxy properties, such as colour and galaxy scale.

1.1 Introduction to cosmology

Cosmology is a subject of astronomy that tries to answer two key questions. The first question is with regards to the Universe's origins, and understanding the physical laws and processes that took place at the beginning of the Universe with the goal of explaining its existence. The common approach to this question is the development and formulation of a quantum gravity theory, and the difficulty stems from the complexity of the problem as well as the lack of an observational testing ground for such models. The second question is about understanding the processes involved in evolving the Universe, from a small age and given initial conditions, to the way the Universe is observed today. This question is often approached with statistical studies of the Universe's properties and observational data.

It is now widely theorised that the Universe was created at the Big Bang, a single point in time which marks the generation of spacetime and our Universe. This idea was mainly motivated by the observation of the expansion of our Universe and the postulate that, some finite time ago, the observable Universe had to be confined in a very small (if not infinitely small) space with extremely high energy density and temperatures. Particles at these conditions are strongly interacting with each other and, at later times, as the Universe expands and cools, atomic nuclei and atoms are formed, according to the Big Bang Nucleosynthesis.

With the Big Bang hypothesis, two important predictions can be made. The first is the existence of a radiation observed at every point in the sky, leftover from the epoch of recombination, when the Universe's energy density allows electrons to be captured by atoms and photons to traverse freely. This radiation, called the Cosmic Microwave Background (CMB), was predicted to have a temperature of $\sim$ 3 - 5 Kelvin, and was first directly observed by Penzias and Wilson in 1964. The small inhomogeneities in the CMB, illustrated in Fig. 1.1, now serve as a highly important observable of the content and initial conditions of our Universe (e.g. Hinshaw et al. 2013; Planck Collaboration et al. 2018). The second prediction concerns the primordial creation of atoms in the Universe, and their relative abundances. Big Bang nucleosynthesis suggest that about 75% of the primordial baryonic matter in the Universe is hydrogen, 25% is helium and there is a very small amount of Deuterium, Helium-3 and Lithium. Observations of the CMB and abundance of elements have established the Big Bang hypothesis in the standard cosmological paradigm.

Another important era of the Universe's history is inflation, a short period of time right after the Big Bang and before the nucleosynthesis, during which the Universe is believed to grow exponentially in size. Inflation manages to provide explanation for key questions raised by the standard model of cosmology. These are the homogeneity and Gaussianity of the CMB temperature map, the lack of magnetic monopoles as well as the observation of a geometrically Euclidian universe, which would otherwise require a very precise fine tuning of the Universe's initial conditions.

1.1.1 The flat ΛCDM cosmology

In order to predict the evolution of the Universe given its initial conditions, a mathematical framework is provided by general relativity. However, the complexity of Einstein's field equations necessitate the use of several hypotheses. General relativity already assumes the universality of the physical laws, regardless of the point in spacetime. In addition, motivated by the homogeneity of the

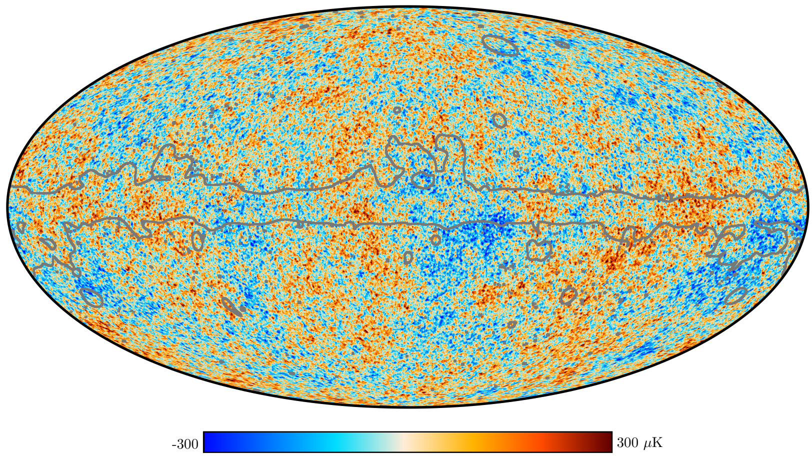

Figure 1.1: Temperature anisotropies from the Cosmic Microwave Background radiation, emitted at the early Universe at the time of recombination. The grey regions show masked areas due to our galaxy's and light from other bright objects. *Credit: ESA/NASA*.

CMB, it is assumed that the Universe is homogeneous and isotropic, leading us to spherically symmetry (also referred to as the *cosmological principle*). This assumption is also supported by the belief that the Universe as a whole should not appear different to two observers in different locations.

These assumptions result in what is called the Friedmann Universe, and allow the calculation of the evolution of the different components in the Universe. According to this model, the Universe started from a radiation dominated era, when radiation dominates the expansion history at the high energy densities of the Big Bang, and later went through a matter dominated era. This transition happens closely before the emission of the CMB, after which the Universe can be considered to be matter dominated.

Considering the amplitude of the anisotropies in the CMB, a universe dominated by baryonic matter does not have enough time to evolve and create structures such as galaxies and galaxy clusters, that we observe today. One way to solve this problem is to introduce another, non-baryonic matter component in the Universe, which is collisionless and interacts only gravitationally. Such a component will be unaffected during the radiation dominated era, and will be able to cluster and form gravitational wells in which baryonic matter will fall

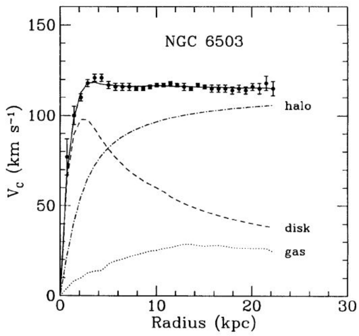

Figure 1.2: *Left:* Rotational curves as a function of distance from the galaxy's centre for NGC6503, with the curve profile due to stars, gas and dark matter overplotted. *Right:* Colour image of the bullet cluster (merging of two clusters), with the x-ray gas emission in pink (which represents most of the luminous matter in the clusters) and the total mass obtained with gravitational lensing in blue (see Sec. 1.2). The displacement in mass suggests that the luminous matter does not correspond to the total observed matter in the clusters, providing evidence for the existence of dark matter. *Credit:* Freese (2017)

into and speed up structure formation. This component is called dark matter.

Evidence for the existence of dark matter has been found in many different, independent observations (Figure 1.2). For example, rotational velocity curves measured in spiral galaxies cannot be explained by the visible baryonic matter of the galaxies alone, but are understood if the galaxies are assumed to reside embedded in a large and smooth halo of dark matter particles. Moreover, observations of collisions between galaxy clusters show that the total mass of the clusters does not coincide with the visible mass (Clowe et al. 2004). Analysis of the power spectrum from the CMB anisotropies is also fit best by a Universe whose matter content is both baryonic and non-baryonic (Planck Collaboration et al. 2018). Dark matter is, therefore, accepted within the standard model of cosmology, with many observations hinting its existence.

Another important component observed in the Universe is dark energy, an unknown form of energy density which causes the expansion of the Universe to accelerate at late times, ending the matter dominated era. This acceleration was evidenced in distance measurements of type Ia supernovae via their luminosity curves (Riess et al. 1998), and many observations, such as the CMB power spectrum, are consistent with the existence of dark energy. The impact of dark energy in the evolution of the Universe is encoded in the cosmological constant, Λ, which is considered to be constant in the standard model of cosmology.

The various components of the Universe are commonly parametrised with the energy density ratios, which are measurable quantities in many independent astronomical observations. The latest constraints of the density ratios at present day show a universe dominated by dark energy, with $\Omega_\Lambda \sim 69\%$. The ratio for dark matter is $\Omega_\mathrm{c} \sim 26\%$, for baryonic matter and radiation is $\Omega_\mathrm{b} \sim 5\%$ and $\Omega_\mathrm{r} \sim 10^{-5}$, respectively, while the curvature of the Universe is measured to be consistent with zero.

1.1.2 Basics of galaxy formation and evolution

Given the standard cosmological model, solving for the evolution of the Universe beyond the linear regime is a very complicated problem. Moreover, as baryon density rises, interactions between baryons add an additional large complexity to this problem. For this reason, the most accurate qualitative and quantitative predictions come from numerical methods for solving the dynamics and interactions of matter contents in the Universe, also called cosmological simulations.

The first attempts at cosmological simulations involved numerically solving for a N-body system of dark matter "particles" (in a numerical sense, which doesn't correspond to the actual fundamental dark matter particle but to a numerical quantity that describes a region of certain dark matter mass). The generally small gravitational forces involved during these calculations allow for the approximation of gravitational interactions with Newtonian dynamics, as well as using the Poisson equation. These simulations revealed that dark matter particles collapse into smooth, triaxial halos with a universal radial density profile, known as the Navarro-Frenk-White profile.

Baryonic gas generally follows the structure of dark matter, through gravitational interactions. However, gas is able to cool through baryonic interactions. The most important of these is bremsstrahlung radiation and photon emission from atomic and molecular excited states. This has the effect of allowing the gas to contract and increase its density even more, eventually being able to form stars and galaxies which are believed to be embedded in a halo of dark matter.

Galaxies and their host halos do not evolve in isolation but interact with other galaxies, and one way of interacting is called merging. During merging, the less massive galaxy will be stretched and stripped from its gas, and can end up orbiting the massive one. In this way, satellites and central galaxies are formed, in knots of high matter density, and a large number of gravitationally bound galaxies will form galaxy groups and galaxy clusters. Merging can also result in a new more massive galaxy, formed from the coalition of the merged galaxies. In this way, more and more massive galaxies can form, in a "bottom-up" scenario, i.e. smaller galaxies merge to produce more massive ones. An elliptical galaxy is often the result of the merging of two approximately equal mass galaxies, with disk structures forming if angular momentum and cooling are high. For further information on galaxy evolution we refer the reader to Mo et al. (2010) and references therein.

In order to observe the matter content of the Universe, luminous tracers are often used, most commonly galaxies. However, given their formation and evolution mechanisms, galaxies are biased tracers of the matter density, with the bias depending on the galaxy properties. Moreover, since dark matter makes up for the majority of the matter content and interacts only gravitationally, observational techniques sensitive to gravity are optimal to study not only the matter content of the Universe, but the physics and behaviour of dark matter and its interplay with galaxies. A successful technique is gravitational lensing, which we introduce below.

1.2 Weak gravitational lensing

General relativity predicts that spacetime is curved due to the presence of mass. Moreover, light particles follow null geodesic curves, which minimize the distance between two points in space. If the space is curved, the geodesics will follow this curvature. Consequently, when light bundles travel near a massive object, their path is curved and the original shape and position of the source of these light bundles is distorted, a phenomenon called gravitational lensing (for an extensive review see Bartelmann & Schneider 2001).

The displacement due to gravitational lensing was first observed by Eddington in 1920 for stars deflected by the Sun, and was an important step towards establishing general relativity as the standard theory of gravity. For more massive and distant objects, there can be more than one null geodesic connecting the source and observer, passing near the lensing mass, which will result in the observer seeing multiple images of the source object. This was first discovered by Walsh et al. (1979). Moreover, light from extended sources can be distorted enough that the source appears as a ring, first observed by Hewitt et al. (1988).

The phenomena described above manifest only when the light source is very close to the lens object in the sky plane. However, massive objects can distort the shape of background sources (commonly galaxies) across the whole

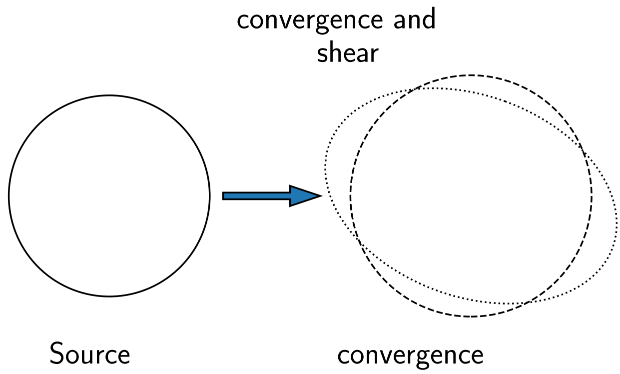

Figure 1.3: The effect of gravitational lensing on the shape of a circular source. The convergence alone has the effect of magnifying the radius of the circle (dashed line), while adding a non-zero shear will generally stretch the source and result in an apparent elliptical shape (dotted line).

sky plane, although weakly enough that they cannot be disentangled from the source galaxy's intrinsic elliptical shape. The distortion pattern is coherent and tangential to the lens position, and can be extracted by statistically analysing a large number of background sources (in the case of massive galaxy clusters) or by stacking multiple lenses and their sources. This regime is referred to as weak gravitational lensing, and it follows three main assumptions; the validity of general relativity, the gravitational potential of the lens is weak and can be described in Newtonian fashion, i.e. $\Phi \ll c^2$, and the peculiar velocities of the lens object are small compared to the speed of light, which holds true for all astrophysical lenses except compact objects (which we do not analyse here).

1.2.1 Lensing by galaxies

Often the distance among the lensing object, the observer and the light source is much larger than the size of the lens, such as in the case of galaxies or galaxy clusters. This allows us to use the "gravitational lens theory", where the lens is considered to be in a plane perpendicular to the line of sight.

The strength of the distortion caused by the lens is quantified by the convergence, κ, which is related to the lens 2-dimensional surface mass density. When

$\kappa \geq 1$ the observer will see multiple images of the source, which, however, is not a necessary condition. In the case of weak gravitational lensing, the convergence is typically very small, i.e. $\kappa \ll 1$. Another useful quantity is the gravitational shear, which describes specifically the shape distortion of a background source due to gravitational lensing. In the case of a circular source, the gravitational shear will stretch the observed image and make it appear elliptical (see Fig. 1.3). In addition to this, because the surface brightness of lensed background sources does not change (since photons are neither emitted nor absorbed due to gravitational lensing) the observed brightness of sources will be changed. This is quantified by the magnification μ, which depends on both shear and convergence. The magnification on weak lensing applications is generally small and biases arising from it can be neglected for state of the art measurements.

By measuring the shear of source galaxies, we can infer the surface mass of the lensing objects, which encodes valuable information on their baryonic and dark matter density. For massive galaxy clusters, a mass map can be directly reconstructed if deep observations are available, with high enough number density of background source galaxies. For less massive clusters or galaxy groups, or even individual galaxies, a stacking technique can be applied, where all lens-source pairs are considered and an average surface mass for the whole lens sample can be computed.

1.2.2 Lensing by the large scale structure

When light traverses through space to reach the observer, it encounters overdensities and underdensities along its path, which will distort its path through gravitational lensing. The thin-lens approximation that was discussed in the previous section is not applicable in this case, however, light can be considered to be propagating in a homogeneous and isotropic Friedmann Universe with local density perturbations described by the Newtonian potential $\Phi << c^2$. In this way an effective convergence of the light bundle, $\kappa_{\rm eff}$, can be computed.

We are mainly interested in statistically analyzing a large ensemble of galaxies, and the quantity of interest is the power spectrum of the convergence, P_κ. Several estimators have been developed to connect the convergence power spectrum to observations. Some examples are Pseudo-Cl's (Hivon et al. 2002), 3D cosmic shear which analyzes weak lensing in three dimensions (e.g. Kitching et al. 2014) and the quadratic estimator (Hu & White 2001). A more common approach is to use two point correlation functions (Bartelmann & Schneider 2001).

The two point correlation functions can be estimated by measuring the ellipticity of galaxies and computing the functions in tomographic bins, which allows the measurement of lensing from the large scale structure (also called cosmic shear) in different redshift ranges. This allows us to map out the history of structure formation in the Universe, and provides competitive measurements on a combination of matter density and the amplitude of density perturbations, $S_8 = \sigma_8 \Omega_m^{0.5}$ (e.g. Abbott et al. 2018; Hikage et al. 2019; Hildebrandt et al. 2018).

Regardless of the choice of estimator, cosmic shear measurements face several important systematic errors. A large effort has been made in the last few decades in controlling and modelling these effects, increasing the precision with which cosmological parameters can be measured from cosmic shear. Upcoming surveys plan to increase the statistical power of cosmic shear measurements significantly, that these systematic errors need to be controlled to a precision of $\sim 0.1\%$ (e.g. Massey et al. 2013). Therefore, understanding and modelling weak lensing systematics is of crucial importance. The most important systematics include errors in the photometric redshift distributions, shear measurement bias and galaxy intrinsic alignments, the last of which we discuss below.

1.3 Galaxy intrinsic alignments

Under the assumptions that galaxies are randomly oriented in the sky, the average ellipticity of an ensemble of background source galaxies directly estimates the gravitational shear. However, galaxies are affected by the tidal gravitational field since their formation, and interact with it through their evolution. This causes them to be aligned with the tidal gravitational field, and consequently with the matter distribution and with each other (for extensive reviews, see Joachimi et al. 2015; Kirk et al. 2015; Kiessling et al. 2015).

Galaxy intrinsic alignments are believed to be generated according to the tidal alignment mechanism. For rotationally supported galaxies, alignments are imprinted at the time of formation, with their angular momentum correlated with the tidal gravitational field. The strength of this alignment is decreasing with redshift, with interactions and merging washing it out. Currently, observations have not conclusively detected this alignment, and tight constraints have been put on its amplitude.

For pressure supported galaxies, the most commonly used model is the linear alignment model (Hirata & Seljak 2004), which relates the intrinsic ellipticity linearly to the matter density contrast. The linear alignment model is successful in describing the intrinsic alignments of red central galaxies on large scales $\gtrsim 10$

Mpc/h, and has been tested in observations, where a significant alignment signal has been observed for massive, intrinsically red galaxies. An empirical model called the non-linear linear alignment model (NLA, Bridle & King 2007) is successful in describing intrinsic alignments in smaller scales down to a few Mpc/h, and relies on substituting the linear power spectrum with its non-linear counterpart.

On smaller scales, the non-linear evolution of galaxies becomes important and a general consensus for a model describing the intrinsic alignments has not yet been reached. A promising empirical approach is the halo model for intrinsic alignments, which describes how satellite and central galaxies populate dark matter halos, as well as how they are aligned, and is motivated by predictions from cosmological simulations. These simulations suggest satellite galaxies are radially aligned with their host halo, and the strength of the alignment drops at large radial separations.

Recent observations of intra-halo alignments have yielded conflicting results, with several studies suggesting a non-detection while others measured radial satellite alignment. Understanding and modelling the intrinsic alignment signal on small scales is important if we hope to exploit the weak lensing signal on small scales, where a lot of cosmological information is available.

1.4 This thesis

It is clear that weak gravitational lensing is a powerful tool with which cosmology and the nature of dark matter and its interplay with galaxies can be studied. In order to push the field further, with the next generation surveys, systematic contaminants to weak lensing measurements need to be further controlled, and the most important astrophysical contamination is intrinsic alignments. In this thesis, the galaxy intrinsic alignments are measured in state-of-the-art data which allow for studying the dependence of the alignment signal on various properties related to the way observations and measurements are made as well as the galaxy samples. With this, more informative priors can be used to mitigate the effect of intrinsic alignment on weak lensing measurements, as well as provide insight into more accurately modelling the phenomenon.

Chapter 2 studies the intrinsic alignment signal and its dependence on wavelength. To do this, the fact that outer regions of galaxies are more susceptible to the tidal interactions is considered. The resulting alignment signal may therefore depend on the passband if the colours of galaxies vary spatially. To quantify this, shapes of galaxies with spectroscopic redshifts from the Galaxy

And Mass Assembly (GAMA, Driver et al. 2011) survey are measured, using deep *gri* imaging data from the KiloDegree Survey (KiDS, de Jong et al. 2015). Shapes are obtained using the moment-based shape measurement algorithm DEIMOS (Melchior et al. 2011), and its performance is assessed using dedicated image simulations, which shows that the ellipticities can be determined with an accuracy better than 1% in all bands. Additional tests for potential systematic errors did not reveal any issues. A significant difference of the alignment signal between the g, r and i-band observations is measured. This difference exceeds the amplitude of the linear alignment model on scales below 2 Mpc/h. Separating the sample into central/satellite and red/blue galaxies, it is found that the difference is dominated by red satellite galaxies.

In **Chapter 3** the NLA model of intrinsic galaxy alignments is directly constrained, analysing the most representative and complete flux-limited sample of spectroscopic galaxies available for cosmic shear surveys. The projected galaxy position-intrinsic shear correlations and the projected galaxy clustering signal is measured using high-resolution imaging from the KiDS overlap with the GAMA spectroscopic survey, and data from the Sloan Digital Sky Survey (York et al. 2000). Separating samples by colour, no significant detection of blue galaxy alignments is made, constraining the blue galaxy NLA amplitude $A_{\rm IA}^{\rm B} = 0.21^{+0.37}_{-0.36}$ to be consistent with zero. Robust detections ($\sim 9\sigma$) for red galaxies are made, with $A_{\rm IA}^{\rm R} = 3.18^{+0.47}_{-0.46}$, corresponding to a net radial alignment with the galaxy density field, and no evidence for any scaling of alignments with galaxy luminosity is found. My contribution to this work, in particular, was the development of the highly accurate shape measurement catalogue, and its calibration. In addition, my input concerned the calculation of the data covariance, the understanding of the signal around random points as well as the interpretation of the results and the data splitting. As a result form this analysis, informative priors for current and future weak lensing surveys are provided, an improvement over de facto wide priors that allow for unrealistic levels of intrinsic alignment contamination. For a colour-split cosmic shear analysis of the final KiDS survey area, it is forecasted that these priors will improve the constraining power on S_8 and the dark energy equation of state w_0, by up to 62% and 51%, respectively. The results indicate, however, that the modelling of red/blue-split galaxy alignments may be insufficient to describe samples with variable central/satellite galaxy fractions.

Following these results, **Chapter 4** looks into the alignment of shapes of satellite galaxies, in galaxy groups, with respect to the brightest group galaxy (BGG), as well as alignments of the BGG shape with the satellite positions, using the GAMA and KiDS surveys. Systematic errors are controlled with dedicated image simulations and shapes obtained with the DEIMOS shape measurement method are used. A significant satellite radial alignment signal is detected, which vanishes at large separations from the BGG. No strong trends of the signal with galaxy absolute magnitude or group mass is found. The alignment signal is dominated by red satellites. In addition, it is found that the outer regions of galaxies are aligned more strongly than their inner regions, probed by varying the radial weight employed during the shape measurement process. This behaviour is evident for both red and blue satellites. BGGs are also found to be aligned with satellite positions, with this alignment being stronger when considering the innermost satellites, using red BGGs and the shape of the outer region of the BGG. Lastly, measurements of the global intrinsic alignment signal are made for two different radial weight functions and no significant difference is found.

Finally, in **Chapter 5**, the alignment between galaxies and their dark matter halos is studied. Cosmological simulations predict dark matter halos that are triaxial, in the standard cosmological paradigm, which makes the ellipticity of dark matter halos a useful quantity to test cosmology and structure formation. To study this, the ratio of halo-to-galaxy ellipticity, f_h, is measured, using weak gravitational lensing. Since satellite galaxies complicate the interpretation of the measurement, their contamination is minimised by developing an algorithm to construct a highly pure ($\sim 93.5\%$) sample of central galaxies from photometric data (KiDS) to be used as lenses, based on selecting the brightest galaxy in a galaxy-dense space. The purity of the sample is demonstrated using group catalogues from spectroscopic data (GAMA) as well as from numerical simulations (MICE, Crocce et al. 2015). A non-zero $f_{\rm h}$ is measured, with 1-σ and 2-σ statistical significance for the full and intrinsically red galaxy samples, respectively. The results are in agreement with previous studies, and indicate that lower mass halos are rounder and/or less aligned with their host galaxy than samples of more massive galaxies, studied in galaxy groups and clusters.

Chapter 2

The dependence of intrinsic alignment of galaxies on wavelength using KiDS and GAMA

Based on
C. Georgiou, H. Johnston, H. Hoekstra, M. Viola,
K. Kuijken, B. Joachimi, N.E. Chisari, D.J. Farrow,
H. Hildebrandt, B.W. Holwerda, A. Kannawadi
A&A 622, A90 (2019)

2.1 Introduction

In the last few decades advances in studying the cosmos have led to a regime of "precision cosmology". New probes and techniques have significantly increased the sensitivity with which we can measure cosmological parameters that describe our Universe (see e.g. Planck Collaboration et al. 2016; Alam et al. 2017; Scolnic et al. 2017). This has set the foundations for the establishment of the ΛCDM model as the concordance cosmological model. However, this standard model of cosmology is surrounded by a big mystery: we are not at all certain as to what dark matter and dark energy consist of, components that make up approximately 95% of the Universe's energy density at the present epoch. The standard ΛCDM model assumes general relativity with Λ, a cosmological constant, to explain the Universe's accelerated expansion, but this Λ is extremely small compared to the vacuum energy expected from quantum field theory. In addition, the interpretation of this cosmological constant is a missing piece of the standard model. To address this problem one can introduce a new dark energy fluid (see e.g. Kunz 2012), whose nature remains an open question, or modify the equations of General Relativity to explain the late time accelerated expansion of the Universe (for a review see Koyama 2016).

Studying the "dark sector" of the Universe is critical in solving this mystery, but is also very challenging. Dark energy models and modified gravity theories are very hard to distinguish among themselves, and dark matter is "invisible" since it interacts only gravitationally with baryonic matter. The first problem can be tackled with the acquisition of more, higher quality data. As for the second problem, weak gravitational lensing has proven to be a powerful tool (for a review see Bartelmann & Schneider 2001). Coherent distortion of light rays is caused by the matter between the source and the observer, and it can be used to study dark matter directly (e.g. Clowe et al. 2004; Massey et al. 2010). In addition, weak gravitational lensing is also sensitive to the geometry of the Universe making it a powerful tool for constraining cosmology and gravity (e.g. Hoekstra & Jain 2008; Kilbinger 2015).

Weak lensing changes the observed ellipticity of galaxies at the per cent level which is much smaller than variations in intrinsic ellipticities between galaxies, and as a result, the lensing distortion patterns can only be observed statistically, by correlating shapes of a large ensemble of galaxies. Many ongoing surveys such as the Kilo Degree Survey[1], the Dark Energy Survey[2] and the Hyper

[1] http://kids.strw.leidenuniv.nl/
[2] https://www.darkenergysurvey.org/

Suprime Cam survey[3], as well as upcoming surveys such as *Euclid*[4] and the Large Synoptic Survey Telescope[5], aim to exploit the phenomenon and measure cosmological parameters to very high precision (e.g. Hildebrandt et al. 2017; Troxel et al. 2017). The statistical power of future surveys is high enough that the systematic uncertainty in measured shapes needs to be ultimately controlled to permille precision (e.g. Massey et al. 2013 for *Euclid*).

If galaxies are intrinsically randomly oriented in the sky, any shape correlation observed could be attributed solely to gravitational lensing. However, shape correlations can also be induced during structure formation, since large-scale tidal gravitational fields affect the orientation of galaxies with respect to the matter density field, a phenomenon called intrinsic alignment. Physically associated galaxies form and evolve in similar gravitational fields, hence they are coherently aligned to some extent (e.g. Joachimi et al. 2015; Troxel & Ishak 2015). Consequently, intrinsic alignments are a major astrophysical contaminant of weak lensing and modelling the effect is of crucial importance for high precision weak lensing measurements.

Intrinsic alignments have been studied through cosmological numerical simulations. These have revealed that dark matter haloes tend to align with each other and the matter density field and that red galaxies tend to align with red centrals (for a review see Kiessling et al. 2015). This picture has been broadly confirmed by observations (e.g. Mandelbaum et al. 2006b; Hirata et al. 2007; Okumura et al. 2009; Joachimi et al. 2011; Li et al. 2013; Singh et al. 2015). Interestingly, alignments between blue galaxies have not yet been firmly detected (Mandelbaum et al. 2011; Heymans et al. 2013) while luminous red galaxies give a significant alignment signal.

Another important characteristic of the intrinsic alignment signal is its dependence on the galaxy's radial scale. By their nature, tidal interactions have a stronger impact on the outer parts of a galaxy than the inner ones (Kormendy 1982). Since intrinsic alignments are attributed to tidal gravitational fields, one can expect that measuring shapes of galaxies at larger radii would give a stronger alignment signal. This dependence has been established using several cosmological hydrodynamical simulations where the alignment signal was measured using two different shape estimators: the signal was weaker for estimators that up-weighted the inner regions of a galaxy and down-weight the outer ones (Chisari et al. 2015; Velliscig et al. 2015b; Hilbert et al. 2017).

Evidence for such a dependence in the alignment of galaxies is also provided

[3]http://hsc.mtk.nao.ac.jp/ssp/
[4]https://www.euclid-ec.org/
[5]https://www.lsst.org/

by observations. Singh & Mandelbaum (2016) used a galaxy sample with shapes from three different estimators to measure intrinsic alignments. The amplitude of the signal was lower for shape measurements that give more weight to the inner parts of galaxies. Similar results were seen for the alignment of central galaxies with the group satellites (Huang et al. 2016) as well as for the radial alignment of satellites with respect to their BCG (Huang et al. 2018). However, these results were based on shapes from different shape estimators, which are sensitive to systematic uncertainties in different ways, so drawing a firm conclusion is difficult. Ideally, one would want to measure the alignment signal using a consistent shape measurement method that can be adjusted to measure shapes from different galaxy scales, without introducing further systematic errors.

A complication in the interpretation is that in general, both spiral and elliptical galaxies appear to have outer regions that are bluer than the inner ones (de Jong 1996; Franx et al. 1989; Peletier et al. 1990), a result mainly attributed to radial gradients in the stellar populations (e.g. Tortora et al. 2010). Since the outer regions of galaxies are more luminous in blue filters, we expect the sizes of these galaxies to be larger in these filters as well (MacArthur et al. 2003). Thus, observing in blue filters gives more weight to the outer regions of galaxies, while red filter observations are mostly revealing their inner regions. This can potentially lead to a difference in the intrinsic alignment signal as measured from different broad band images, with blue filters exhibiting a stronger signal than red ones, for a given galaxy.

In this work we measure differences in the intrinsic alignment signal obtained from different broad band filter observations by combining data from the Galaxy And Mass Assembly survey[6] (GAMA; Driver et al. 2009, 2011; Liske et al. 2015) and the Kilo Degree Survey (KiDS; de Jong et al. 2015, 2017). The latter is a deep imaging survey designed primarily for weak gravitational lensing science, providing imaging data of exquisite quality. We measure galaxy ellipticities in *gri* broad band imaging data using the same shape measurement estimator, DEIMOS (Melchior et al. 2011), a moment-based method that is described in Sect. 2.2. This shape measurement method includes an exact treatment of the point-spread function (PSF) and a correction for the weighting scheme introduced in measuring galaxy brightness. Moreover, this work is an extension to the shape catalogues already produced by the KiDS team, which do not include galaxies with magnitude $r < 20$. The data used are described in Sect. 2.3, and in Sect. 2.4 we present the PSF modelling. To calibrate our shape measurements, we use dedicated image simulations, outlined in Sect. 2.5, trying

[6]http://www.gama-survey.org

to accurately replicate our galaxy sample's properties. Our results are presented in Sect. 2.6, followed by summary and discussion in Sect. 2.7. Throughout this work, we assume a flat ΛCDM cosmology with $h = 0.7$ and $\Omega_m = 0.25$, to be consistent with Johnston et al. (in prep.), as well as previous works on galaxy intrinsic alignments.

2.2 The DEIMOS shape measurement method

Measuring accurate shapes of galaxies from optical astronomical images is a non-trivial task. Among other things, one needs to account for the presence of noise in the data and the distortion caused by the point-spread function (PSF), and these are treated differently by different shape measuring methods. The method that we chose to use is DEIMOS (Melchior et al. 2011), which stands for DEconvolution In MOment Space. This is a moment-based method, meaning that surface brightness moments are calculated from image data to extract shape information of galaxies. It is an improvement over some similar approaches, such as the KSB method (Kaiser et al. 1995), because the moments of the galaxies are corrected exactly for the effect of the PSF. In addition, the effect of the weighting function employed when measuring galaxy moments (which is required to suppress the noise) is compensated using measurements of higher order moments of the galaxies. Since DEIMOS is moment-based, no assumption is made for a galaxy's model and morphology, it is much faster than model-fitting shape measurement methods and also allows flexibility in varying the weighting function, consequently enabling us to measure shapes at different galactic scales. In future work, we aim to use this flexibility to probe directly the dependence of the intrinsic alignment signal on the galaxy scales probed. Melchior et al. (2011) demonstrated the high accuracy of the method, using image simulations of the GREAT08 challenge (Bridle et al. 2010).

The (unweighted) moments of the surface brightness distribution $G(\mathbf{x})$ of a galaxy are expressed by the integral

$$Q_{ij} \equiv \{G\}_{i,j} = \int G(\mathbf{x})\, x_1^i\, x_2^j \,\mathrm{d}\mathbf{x}\,, \tag{2.1}$$

where $\mathbf{x} = \{x_1, x_2\}$ are the Cartesian coordinates with the galaxy's centroid at the origin. The second order moments can be combined to estimate the ellipticity of the object:

$$\epsilon \equiv \epsilon_1 + \mathrm{i}\epsilon_2 = \frac{Q_{20} - Q_{02} + \mathrm{i}2Q_{11}}{Q_{20} + Q_{02} + 2\sqrt{Q_{20}Q_{02} - Q_{11}^2}}\,, \tag{2.2}$$

where $|\epsilon|$ is related to the semi-minor to semi-major axis ratio q of by $|\epsilon| = (1-q)/(1+q)$.

2.2.1 Distortion due to the PSF

Images obtained with an optical telescope undergo a series of transformations that alter the observed brightness profile of objects and complicate the measurement of the galaxy shapes. One inevitable example is the effect of the PSF on the image, which is caused by the atmospheric blurring (for ground-based observations) and the optics of the telescope.The object's surface brightness $G(\mathbf{x})$ is not directly accessible in image data because it is convolved with the PSF kernel $P(\mathbf{x})$ and in practice what we observe is the PSF-convolved image,

$$G^*(\mathbf{x}) = \int G(\mathbf{x}')\, P(\mathbf{x}-\mathbf{x}')\, \mathrm{d}\mathbf{x}' \,. \tag{2.3}$$

This convolution smears and distorts the true object and needs to be accounted for in order to accurately retrieve shape information. Melchior et al. (2011) showed that the moments of the *true* surface brightness of the galaxy G are related to those of the observed G^* and the PSF kernel P, through

$$\{G^*\}_{i,j} = \sum_k^i \sum_l^j \binom{i}{k}\binom{j}{l} \{G\}_{k,l}\{P\}_{i-k,j-k} \,. \tag{2.4}$$

In order to calculate the unweighted moments of G up to 2nd order all we need to know are the moments of the image G^* as well as the moments of P up to the same order. This does not impose any prior assumption on the profile of the PSF, contrary to some other moment-based methods such as the KSB (Kaiser et al. 1995) and re-Gaussianization (Hirata & Seljak 2003) methods. The moments of the PSF can be calculated by modelling the PSF, and we describe our modelling in Sect. 2.4.

2.2.2 Effect of noise and weighting

Another very important feature of real images is the presence of noise, which is mainly caused by the shot noise of counting photons, the read-out process of the detector and the sky background noise. When sky-background limited, noise in astronomical images is typically Gaussian and uncorrelated between pixels. With $N(\mathbf{x})$ expressing the noise, the flux we measure in imaging data is

$$I(\mathbf{x}) = G^*(\mathbf{x}) + N(\mathbf{x}) \,. \tag{2.5}$$

The second order moments of the image have a quadratic radial weighting that enhances the sensitivity of regions far from the galaxy's centre and, in the presence of noise, leads to infinite variance. In practice, we need to choose a large enough image section, or "postage stamp"[7] on which we calculate the integral of equation (2.1), but the second order moments will be completely dominated by noise in regions far from the galaxy's centre. This is dealt with by applying a weight function $W(\mathbf{x})$, centred on the galaxy, in order to suppress the noise at large separations. The measured flux then becomes

$$I_w(\mathbf{x}) = W(\mathbf{x})\, I(\mathbf{x})\,. \tag{2.6}$$

Typically a Gaussian weight function centred on the galaxy's centroid is employed in the measurements (e.g. Kaiser et al. 1995). Ideally, we want the weight function to match the shape of the galaxy, so that galaxy light is suppressed as little as possible, and its Signal-to-Noise ratio (SNR) is maximised. Since galaxy shapes are usually elliptical, it makes sense to employ an *elliptical* Gaussian weight function whose centroid, size and ellipticity are matched to that of the galaxy. This is done according to the algorithm described in Bernstein & Jarvis (2002), Sect. 3.1.2, and the weight function employed in this work is

$$W(\mathbf{x}) = \exp\left[-(\mathbf{x}-\mathbf{x}_c)^{\mathrm{T}} \begin{pmatrix} 1-\epsilon_1 & -\epsilon_2 \\ -\epsilon_2 & 1+\epsilon_1 \end{pmatrix} \frac{(\mathbf{x}-\mathbf{x}_c)}{2r_{\mathrm{wf}}^2}\right], \tag{2.7}$$

where ϵ_i are the ellipticity components of the weight function, $\mathbf{x}_c$ is the centroid of the galaxy and r_{wf} is the scale of the weight function.

The value for r_{wf} is usually optimized such that the weight function matches the galaxy's surface brightness profile, thus maximizing the SNR of the measurement. However, its value also describes the physical scale for which the galaxy's shape is measured: a small r_{wf} will make the shape measurement sensitive to the galaxy's bulge, while a larger r_{wf} will make the shape measurement more sensitive to the outskirts of the galaxy.

The weight function is iteratively matched to each galaxy through the following procedure:

1. First, the centroid of the galaxy is calculated by requiring the first order moments to vanish. These moments are weighted with a circular Gaussian function of size r_{wf}.

[7] The dimension of the postage stamp should be set by the desired accuracy. A small postage stamp can end up truncating the moments and lead to biased results (truncation bias). See Sect. 2.5 for more information on the choice of a postage stamp.

2. Once the centroid is determined, the second order moments (weighted with a circular Gaussian function of size $r_{\rm wf}$) are used to measure the ellipticity through Eq. (2.2).

3. Then, the measured ellipticity is used to define the new, elliptical weight function with which the galaxy's shape is measured again.

4. This procedure is repeated until the SNR[8] of the measurement converges.

The weight function's ellipticity components and centroid are determined for every galaxy individually. We also choose to preserve the area of the weight function between each matching iteration. This means that starting from a circular shape, the weight function will become more stretched along the semi-major axis of the galaxy with each iteration, and squeezed in the direction of the semi-minor axis, eventually matching the size of the galaxy. Our choice of $r_{\rm wf}$ is described in Sect. 2.5.1.

This results in estimates of the weighted moments $\{I_w\}_{i,j}$; to obtain the correct shape information we need the unweighted moments of equation (2.1). Employing a weight function biases the shape measurement, and to minimise this a de-weighting procedure is required. This is done by inverting equation (2.6) for $I = I_w/W$ and expanding $1/W$ in a Taylor series around $\mathbf{x}_c$ (see Melchior et al. 2011 for details). The maximum order of the Taylor expansion is a free parameter, denoted by n_w. The de-weighting procedure relies on calculating higher order weighted moments and the inevitable truncation of the Taylor series expansion introduces a bias to the measured shapes, dubbed de-weighting bias. The overall bias of the shape measurement (which includes bias due to noise and de-weighting) is characterized in Sect 2.5.1.

2.2.3 Error and flags

The error calculation on the measured de-weighted moments is described in Melchior et al. (2011). It takes advantage of the nearly linear response of the measured ellipticity dispersion to the correction order n_w. The covariance matrix of the weighted moments is used for the calculation of the error on the de-weighted moments. However, this matrix is sensitive to the weighting function. We observe that, for a small weight function the error on the measured ellipticity is small but the shape measurement is strongly biased as a result of using a small weight function. To avoid this discrepancy, when calculating correlation functions to measure the intrinsic alignment signal, we do not use the

[8]The SNR is calculated according to Eq. 3.14 of Bernstein & Jarvis (2002).

errors on the ellipticities. This is not expected to affect our results, because our galaxy sample is bright, with a high SNR, and the ellipticity errors are generally much smaller than the ellipticity rms.

Furthermore, there are four different flags for keeping track of problematic shape measurements. The first one is raised when the centroid determination gives a final centroid shifted by more than 5 pixels from the input one. Two flags are related to measurements of non-sensical moments or ellipticity (i.e. $Q_{00}, Q_{20}, Q_{02} < 0$, $Q_{11}^2 > Q_{20}Q_{02}$ or $\epsilon > 1$). One of the flags is raised when the measurement is done prior to deconvolution and the other is raised for measurements after deconvolution. The fourth flag indicates that the ellipticity matching has failed. This means that during the iterative process of matching a weight function to the galaxy (described in the previous section) the SNR of the shape measurement for the different weight functions did not converge. In our analysis, we only consider shapes of galaxies that do not raise any of these flags.

2.3 Data

Intrinsic alignments between galaxies are believed to be caused by tidal gravitational forces and their measurement require physically associated galaxies, which can be identified as long as precise distance information is provided, usually made available with spectroscopy. Since the phenomenon is a correlation of galaxy shapes, high quality images are also needed from which shapes of galaxies can be accurately measured. The galaxy sample used in this work is obtained from the GAMA survey, which provides spectroscopic redshift information, and shapes were measured from KiDS deep imaging data.

2.3.1 GAMA

Galaxy And Mass Assembly (GAMA, Driver et al. 2009, 2011; Liske et al. 2015) is a spectroscopic survey of $\sim 300,000$ galaxies with a magnitude limit of Petrosian $r_{\rm AB} < 19.8$ mag covering ~ 286 deg^2 of the sky in five patches. In this work we will use the three 12×5 deg^2 equatorial fields, centred at approximately 9^h, 12^h and 15^h RA, named G09, G12 and G15, respectively, which contain $\sim 180,000$ galaxies. One advantage of the GAMA survey is its high completeness: in the three equatorial regions the redshift completeness exceeds 98%. This results in a clean galaxy sample and measurement, without the complications of selection effects.

2.3.2 KiDS

Kilo Degree Survey (KiDS, de Jong et al. 2015, 2017) is an ongoing deep imaging survey carried out with the OmegaCAM CCD mosaic camera mounted on the VLT Survey Telescope (VST). The survey aims to cover 1350 deg^2 area on the sky in four SDSS-like bands (u, g, r and i) down to a limiting magnitude of 24.3, 25.1, 24.9 and 23.8 (5σ in a 2 arcsec aperture), respectively. As the primary science goal of the survey is cosmology with weak lensing, tight constrains are set on the observing conditions and the camera performance which guarantee a well-behaved, small and nearly round PSF.

The images used in this work are from the KiDS-450 dataset (Hildebrandt et al. 2017) and they completely cover the three GAMA equatorial patches. Sub-exposures from the four bands are reduced and calibrated using the Astro-WISE system (Valentijn et al. 2007; Begeman et al. 2013). This procedure involves de-trending of the raw images which takes care of cross-talk correction between CCDs, artefacts such as cosmic rays and flat-fielding as well as background subtraction. Next, the sub-exposures are photometrically and astrometrically calibrated and the images are co-added to produce the final image product.

We use these co-added images in g, r and i-band filters to measure the shapes of GAMA galaxies. We choose to not process the u-band image data because the image quality and depth are significantly lower than the other bands and the measured shapes will be harder to interpret. A main difference from the shear catalogues used in Hildebrandt et al. (2017) is the fact that our measurements are done on the Astro-WISE reduced images, instead of the Theli reduced ones (see Kuijken et al. 2015 and references therein), because only the r and i-band images are reduced with the Theli pipeline.

Since the co-added images consist of multiple dithers, the corners of adjacent image tiles will share a common section of the sky. This results in objects being imaged in 2,3 or 4 different image tiles and leaves us with multiple shape measurements of the same galaxy. To deal with this, we make use of the corresponding weight maps: cutting a postage stamp (50×50 pixels) of the weight map around the galaxy's position for each image, we calculate the mean value of this postage stamp and keep the shape measurement for which the mean value of the weight map is the largest. This ensures that, for all the multiply imaged galaxies, we use the shape measurement from the "cleanest", highest SNR co-added image.

2.4 Modelling the spatial variation of the PSF

All astronomical observations in optical wavelengths are carried out using optical systems that alter the observed image. In addition, ground-based observations suffer from time-depended atmospheric distortions that are caused by turbulence in the atmosphere. All these effects are quantified by the PSF and shape measurement techniques need to account for this blurring in order to retrieve shapes accurately.

To correct for the distortion caused by the PSF, in the framework of DEIMOS, we require the calculation of up to 2nd order unweighted moments of the PSF. The PSF can be measured using stars (point sources) detected in the image. However, we are interested in the PSF at the positions of the galaxies, so interpolation of a PSF model is required. The accuracy of the interpolation depends on the star number density and distribution across the image (e.g. Hoekstra 2004).

A big advantage of using KiDS imaging data for shape measurements is the well behaved PSF of the images. In Kuijken et al. (2015) the smoothness of the PSF across the whole focal plane is demonstrated, which can also be seen from PSF ellipticity and size distributions in de Jong et al. (2017). The r-band PSF has a median full-width at half maximum (FWHM) of 0.68 arcsec while the values in the g and i-band are 0.85 and 0.79 arcsec, respectively. The mean ellipticity is $\sim$0.05 in all three filters.

In this work, stars used for the PSF modelling are selected using SExtractor: unsaturated, high-SNR objects are detected and the `FLUX_AUTO` vs. `FLUX_RADIUS` plot is used to identify the stellar locus in an automated way, as described below:

1. Firstly, the median `FLUX_RADIUS` is calculated for the brightest objects ($f_{\rm max}/30 <$ `FLUX_AUTO` $< f_{\rm max}$) with sizes larger than 0.5 image pixels. Here, $f_{\rm max}$ is the flux of the 20th brightest object in the image (the first 20 are excluded as saturated sources).

2. Secondly, a new median size $r_{\rm med}$ is obtained using objects smaller than 1.5 times the previous median size and with flux larger than $f_{\rm max}/100$.

3. As a final step, the selected stars are objects with sizes between $r_{\rm med}/2$ and $r_{\rm med} + 0.2$" and fluxes larger than $f_{\rm max}/100$.

This procedure manages to isolate the area of very compact and bright objects in the flux versus size plot and the resulting star density is a few thousand stars per 1x1 deg^2 image tile.

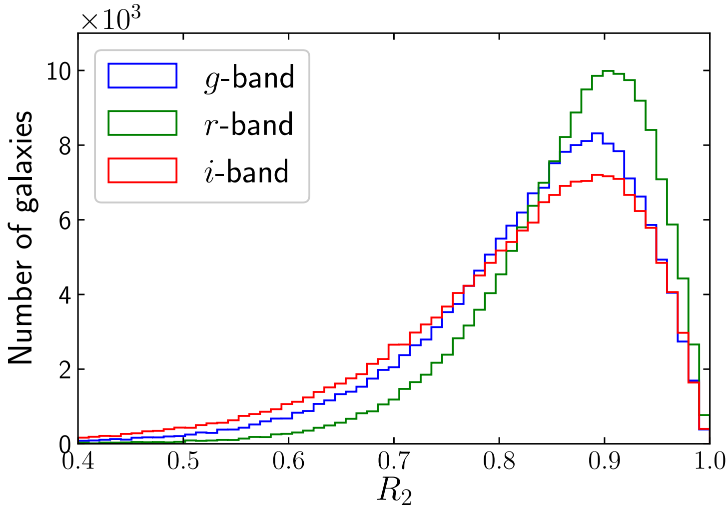

Figure 2.1: Galaxy resolution distribution of GAMA galaxies for the different broad band filters as measured from KiDS image data. If the galaxy is much larger than the PSF, R_2 is close to 1.

The selected stars are then used to model the shape of the PSF at their position using the shapelets expansion (Refregier 2003) and the procedure is described in Appendix A1 of Kuijken et al. (2015)[9]. Shapelets refer to a set of basis functions for images, constructed by the product of Gaussians and Hermite polynomials in 2-dimensions. Any 2-dimensional image can be described by a linear combination of shapelets but the accuracy depends on the maximum Hermite polynomial order. We model the shape of the PSF using Hermite polynomials of up to 10th order (set by the pixel scale of the images, following Kuijken et al. 2015). The spatial variation of the PSF across the image is then modelled with a 4th order polynomial and the PSF moments at the position of galaxies can be analytically computed. We chose this polynomial order to be consistent with previous analysis of KiDS data, where it has been shown that this PSF model does not produce large correlations in residuals between stars and the PSF model (Kuijken et al. 2015, Fig. 5). We refer the read to Kuijken

[9]The difference being that in Kuijken et al. (2015) the different sub-exposures are used while, in this work, the modelling is done on the co-added images.

et al. (2015) for a mathematical description of the PSF model.

In Fig. 2.1 we show the histograms of the galaxy resolution R_2 for our GAMA galaxy sample, as measured from KiDS imaging data. R_2 is defined as

$$R_2 = 1 - \frac{T^{\mathrm{PSF}}}{T^{\mathrm{gal}}} , \tag{2.8}$$

where $T^{\mathrm{PSF}} = Q_{20}^{\mathrm{PSF}} + Q_{02}^{\mathrm{PSF}}$ is the trace of the matrix of the unweighted second order moments of the PSF while T^{gal} makes use of the de-weighted moments of the *convolved* galaxy (which are approximately its unweighted moments). R_2 is effectively comparing the size of the galaxy to the size of the PSF (Mandelbaum et al. 2012). A value close to 1 means the PSF is much smaller than the galaxy's size and R_2 close to zero means the PSF and galaxy have similar sizes. Figure 2.1 demonstrates that GAMA galaxies are generally well resolved, being much larger than the PSF, and also shows the difference of R_2 in the three broad band filters: in the r-band galaxies are best resolved, followed by g and then i-band.

2.5 Image simulations

Measurements of galaxy ellipticities require some non-linear manipulation of the image pixel data. Because of this, PSF convolution and noise in these image data will bias the measurement (e.g. Massey et al. 2013; Viola et al. 2014). If this bias is not accounted for, it can lead to incorrect determination of the intrinsic alignment signal (Singh & Mandelbaum 2016, Sect. 3.3.5). Fortunately, the bias can be characterized using images of simulated galaxies for which the input parameters are known. Ultimately, the precision in the bias measurement needs to be better than the statistical error on the alignment signal. Note that lowering the amplitude of the bias is not the most crucial task, but rather showing its robustness, i.e. how sensitive the bias is to changes of galaxy properties (Hoekstra et al. 2017).

The performance of shape measurement methods depends on the input parameters of the image simulations. The bias is a function of size, ellipticity and SNR of the galaxies in the sample (but also depends on other properties of the simulated images, as discussed in Hoekstra et al. 2017). Consequently, the image simulations need to be as realistic as possible, representing closely the real data and galaxy properties. This requirement is not very strict in our case because the GAMA galaxies are very large, bright, with high SNR (Fig. 2.2), the PSF size is generally much smaller than the galaxies (see Fig. 2.1) and noise is not expected to give rise to very large biases for a reasonable weight

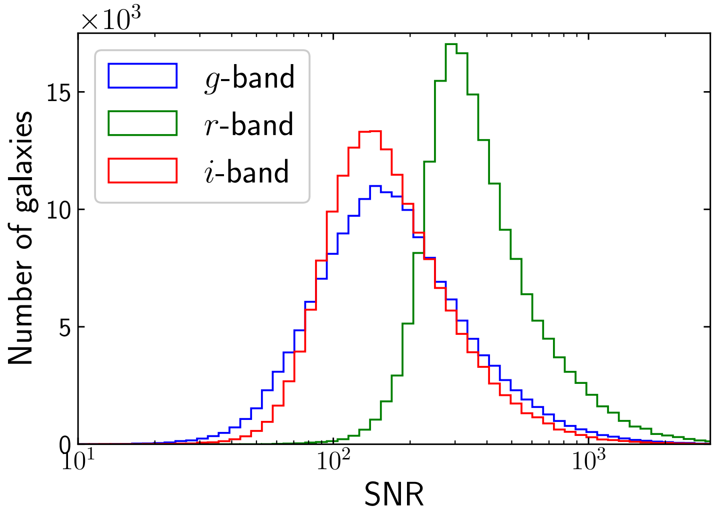

Figure 2.2: Signal-to-Noise ratio distributions for GAMA galaxies in the KiDS g, r and i-band images shown in green, red and blue, respectively. The SNR has been calculated using the weight function as in Eq. (2.7).

function. With this in mind, the PSF used in the simulations is a Gaussian with FWHM equal to the mean FWHM of the KiDS images for the respective broad band filter. In Sect. 2.5.2 we explore the effect of shearing this PSF with an ellipticity equal to the PSF in the KiDS images.

We mimic our galaxy sample by using the Sérsic photometry catalogue described in Kelvin et al. (2012) and the SNR measured from KiDS image data (Fig. 2.2). The catalogue is a single-Sérsic fit produced with Sigma, a wrapper around several astronomical codes such as SExtractor (Bertin & Arnouts 1996) and GalFit (Peng et al. 2002). The fit is done for 167600 galaxies in the GAMA equatorial fields for each of the bands ugrizYJHK, using images from SDSS DR7 (Abazajian et al. 2009) and UKIDSS-LAS (Lawrence et al. 2007), with morphological properties extracted for every galaxy, such as Sérsic index and half-light radius. The morphological parameters of the r-band images are used to produce image simulations representative of our galaxy sample (see Kelvin et al. 2012, Fig. 15). We require the Sérsic fits for these galaxies to pass certain quality controls using the flags present in the catalogue. Specifically we only consider galaxies that have `GAL_QFLAG`, `GAL_GHFLAG` and `GAL_CHFLAG` equal to 0 in all *gri* bands, which means that the final fit, global fitting history and component fitting history were not problematic. We also remove stars present in the catalogue by applying a redshift cut at $z > 0.002$. Finally, we only keep galaxies for which a SNR measurement was possible in the KiDS imaging data for all three bands. This leads to a sample of 101209 galaxies from this catalogue.

We use GalSim (Rowe et al. 2015), a widely used Python package developed for the GREAT3 challenge (Mandelbaum et al. 2015), to generate image simulations. The galaxy model we adopt is a Sérsic profile, motivated by the Sérsic photometry catalogue, and the surface brightness of the profile is given by

$$I(r) \propto \exp\left[-\beta_{n_\mathrm{s}}\left(\left(\frac{r}{r_\mathrm{e}}\right)^{1/n_\mathrm{s}} - 1\right)\right] , \tag{2.9}$$

where n_s is the Sérsic index, r_e is the half-light radius and $\beta_{n_\mathrm{s}} \approx 2n_\mathrm{s} - 0.324$ (Capaccioli 1989). The galaxy profile is truncated at a radius of $4.5 \cdot r_\mathrm{e}$. The galaxy is then sheared (in order to give each galaxy an intrinsic ellipticity) based on the ellipticity and position angle from the Sérsic photometry catalogue, from which n_s and r_e are also obtained. These parameters are obtained from the $r-$band columns of the Sérsic photometry catalogue and the same ones are used in the g and i-band simulations.

The morphological parameters on g and i-band images can be systematically different from the ones in r-band. We choose to fix them between simulations in order to quantify the bias in the shape measurement solely due to different image depth and quality. Moreover, we have checked that the measured bias does not depend strongly on these morphological parameters, so a slight systematic change in them will not affect our quoted biases significantly.

We only use galaxies with a Sérsic index $0.3 < n_\mathrm{s} < 6.2$ (which holds for 96% of the galaxies in the catalogue) as GalSim suffers from severe numerical problems for $n_\mathrm{s} < 0.3$ (1% of the galaxies) and for $n_\mathrm{s} > 6.2$ (3% of the galaxies) the shearing is not accurate (Rowe et al. 2015). The bias of the shape measurement depends on the galaxy's Sérsic index and, in the case of DEIMOS, it increases (in absolute value) with increasing n_s. However, we observed that this increase is not very rapid, and since only 3% of our galaxy sample has $n_\mathrm{s} > 6.2$ we do not expect this cut to affect our bias calibration significantly. For every galaxy we simulate two images that are rotated by 90 degrees, in order to eliminate intrinsic shape noise (e.g. Fenech Conti et al. 2017).

We model the ellipticity bias similarly to Heymans et al. (2006), with a multiplicative and additive term, given by

$$\epsilon_i^{\mathrm{obs}} = (1 + m_i)\epsilon_i^{\mathrm{true}} + c_i \, , \tag{2.10}$$

where $i = \{1, 2\}$, m_i is the multiplicative bias and c_i is the additive bias. Note that, unlike the definition in Heymans et al. (2006), the bias here concerns the *ellipticity* and not the shear. Generally, we do not expect the bias in the ellipticity measurement to be linear since the ellipticity is a bounded quantity between 0 and 1, which is typically not small enough to ignore higher order biases (e.g. Miller et al. 2013; Pujol et al. 2017). This is the main reason the ellipticity bias is not used when calibrating shear measurements. However, given the high SNR of our galaxy sample and the de-weighting procedure of DEIMOS, we show in Sect. 2.5.1 that this is very close to true for our shape measurements.

In the end, we need to define a postage stamp which will be used to measure the moments of each galaxy. The integrals involved in moments calculation theoretically extend from $-\infty$ to $+\infty$, and the postage stamp should be large enough to approximate this integral with enough accuracy. To determine how large the postage stamps should be, we calculate the integrand of the 6th order moment for a sheared Sérsic profile (which as we will see in Sect. 2.5.1 is the highest order required for the shape measurement). We set the Sérsic index to 6 as a worst-case scenario, where the galaxy's profile extends far from the centroid. The postage stamp is then chosen by equating the 6th moment integrand with the noise level in the image, meaning that extending the postage stamp beyond this point will include noise dominated parts of the image and is therefore not expected to contribute to the moments calculation. To avoid extreme cases we set a minimum and maximum size of 50×50 and 300×300 pixels, respectively, for the postage stamp. We find that increasing the maximum postage stamp size does not improve the accuracy of the measured shapes. This procedure results in optimizing the postage stamp size for each galaxy individually, using its flux, half-light radius and rough ellipticity (i.e. the `Elongation` output of `SExtractor`), thus reducing the runtime of the shape measurements significantly, compared to using a fixed postage stamp for each galaxy.

2.5.1 Choosing the weight function

The weight function described in Sect. 2.2 is defined for every galaxy by the size r_{wf} in equation (2.7). This expresses the standard deviation of the initial circular Gaussian weight function employed in the first iteration of the matching procedure, and is generally different for every galaxy, depending on its surface brightness profile. In order for our shape measurement to be consistent between the three broad band filters, we determine $r_{\rm wf}$ in the r-band images, and use this value for the shape measurement in the other two filters. To choose an optimal value for this we investigated a range of possible choices for which we calculated the bias. This range is based on the radius of the circularised isophote of each galaxy, $r_{\rm iso}$, which is related to the area of the galaxy's isophote $A_{\rm iso}$ through

$$r_{\rm iso} = \sqrt{A_{\rm iso}/\pi}\,. \tag{2.11}$$

$A_{\rm iso}$ is calculated using the `ISOAREA_IMAGE` parameter from SExtractor[10].

Another choice we need to make before measuring galaxy shapes is the maximum Taylor expansion order used for de-weighting n_w. The larger this number, the higher the order of moments used to correct for the weight function. Note that this number is even, since we have picked a symmetric weight function. To explore this, we picked $r_{\rm wf} = r_{\rm iso}$ and calculated the bias as a function of the input ellipticity for different values of n_w. We used equation (2.10) and performed a simple linear regression analysis for variables m_i and c_i.

The results are presented in Fig. 2.3, where we show the mean multiplicative bias[11] as a function of the input ellipticity of the galaxies in our simulation for four values of n_w. These results are for simulations of GAMA galaxies observed in the KiDS r-band filter. When no correction is applied ($n_w = 0$ in Fig. 2.3) the bias increases up to 5% as the input ellipticity becomes large. Applying the simplest correction ($n_w = 2$) already improves the shape measurement significantly. We can see that for small ellipticities the bias is around -2% rising up to 1.5% as we move to large input ellipticities. Further correction reduces this rising trend significantly, as seen in Fig. 2.3 for $n_w = 4$. Including even higher order corrections to improve the de-weighting comes with a price. Besides increased computational time, the dispersion in the measured shapes becomes larger (i.e. the estimated ellipticities become more noisy) as shown in Fig. 2 of Melchior et al. (2011). This is also seen in Fig. 2.3, where the errors and the noise bias become larger as n_w increases. We adopt $n_w = 4$, given the fairly constant response of the bias to input ellipticity (compared to $n_w = 2$) and the relatively low effect of noise (compared to $n_w = 6$).

Having determined the maximum Taylor expansion order to use, we need to find the optimal value for $r_{\rm wf}$, the size of the initial circular weight function. We

[10] The isophote is measured at 3σ above the background noise RMS.

[11] Additive bias arises mostly from imperfect PSF modelling (or more generally from spurious ellipticity correlations) and is consistent with zero at the 3-sigma level for all our measurements, unless stated otherwise.

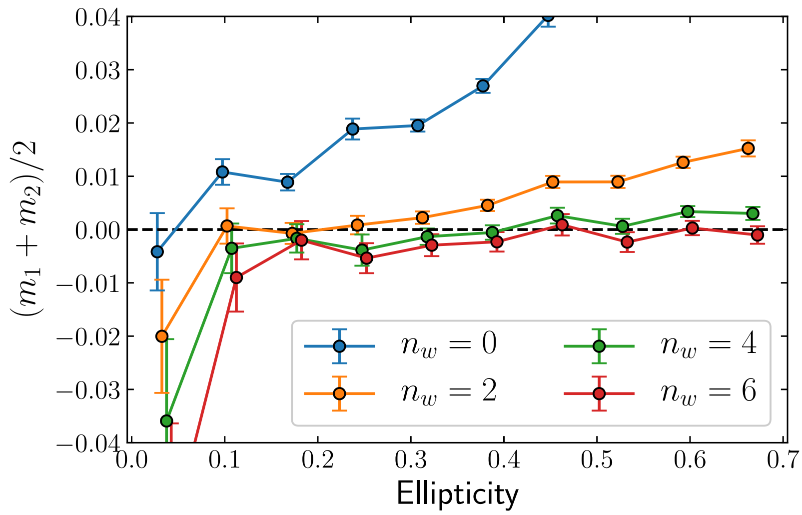

Figure 2.3: Mean multiplicative bias as a function of ellipticity for different values of the maximum Taylor expansion order n_w. Points are horizontally displaced for clarity.

do so by calculating the multiplicative bias as a function of $r_{\rm wf}/r_{\rm iso}$. The results are shown in Fig. 2.4. The bias seems to be fairly constant for an initial weight function between 0.75 and 1.5 times the circularized isophote of each galaxy. A larger weight function results in an increase in bias as well as a decrease in the accuracy with which the bias can be measured. This is caused partly due to the shape measurements being more noisy but also due to loss of statistical power, as more and more shape measurements are flagged as problematic (since larger weight function results in including more noise in the measurements). For a very small weight function the bias is positive, and we see a point where the bias must be zero. However, this does not mean that the bias is better calibrated because the noise bias has been traded off with model bias. In the end, we choose to use an initial weight function of size $r_{\rm wf} = r_{\rm iso}$, around which the bias remains fairly constant.

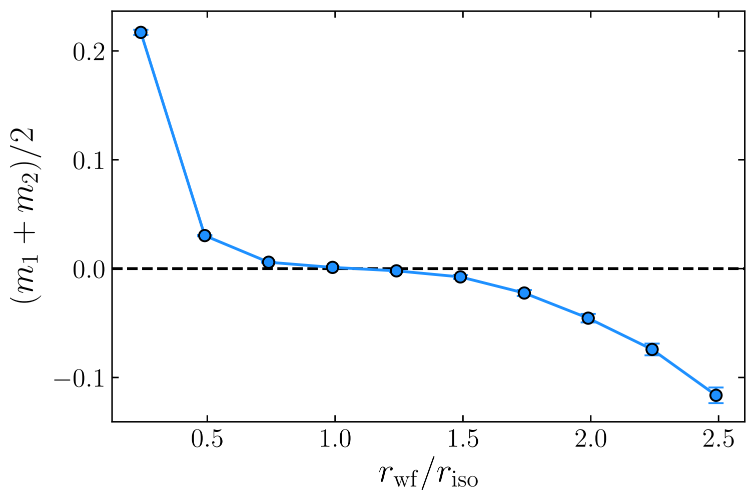

Figure 2.4: Mean multiplicative bias as a function of the size of the initial weight function used in our simulations.

2.5.2 Masking and PSF anisotropies

Galaxies observed in imaging data are generally not isolated but have neighbouring galaxies. These neighbours need to be masked in order to measure the shape of the galaxy robustly. The masking is done using the segmentation map produced by SExtractor, which identifies the pixels associated with every source in the image. The pixels *not* associated with the galaxy, whose shape is measured, are replaced with random Gaussian noise with variance equal to the background noise RMS.

However, this masking affects the integration required to calculate the galaxy's moments, since essentially there are certain values of the x, y Cartesian coordinates over which the galaxy's flux is replaced by the expected noise level. Consequently, the masking of neighbouring galaxies will introduce an extra source of bias in the shape measurements. Here we aim to quantify this bias using our image simulations. For every galaxy simulated, we also create a cut-out of the segmentation map obtained from the KiDS imaging data for this particular galaxy, and measure the galaxy's shape using this segmentation map. We

Table 2.1: Multiplicative and additive bias obtained from our image simulations in the three *gri* broad-band filters.

Simulation	$m_1 \times 10^{-2}$	$m_2 \times 10^{-2}$	$c_1 \times 10^{-5}$	$c_2 \times 10^{-5}$
g-band	-0.73 ± 0.16	-0.45 ± 0.17	(24.9 ± 34.0)	(-8.3 ± 35.2)
r-band	-0.40 ± 0.08	-0.35 ± 0.08	(-4.3 ± 18.2)	(-11.0 ± 18.1)
i-band	-0.84 ± 0.17	-0.83 ± 0.16	(-0.5 ± 35.2)	(-10.2 ± 34.6)

observe a general shift of the bias towards lower values, similar to the effect of noise bias. For example, the mean ellipticity m-bias in the r-band simulation shifts from a value of 0.12 % to -0.37 %.

In addition to masking, anisotropies in the PSF are also expected to impact shape measurements to some degree. With DEIMOS, however, this is not expected to be important since the PSF convolution is treated in an exact analytical way. In addition, the galaxies in our sample are much larger than the PSF (Fig. 2.1) and their shape determination is not expected to be significantly affected by this. We test these with our simulations by considering elliptical Gaussian PSF, arbitrarily oriented, with its ellipticity equal to the mean PSF ellipticity of KiDS images, which is approximately $\epsilon_{\rm PSF} = 0.05$ in all three gri filters (de Jong et al. 2017). A small shift in the recovered m-bias of the order of 0.01% was observed, which is negligible compared to the statistical uncertainty with which the bias is determined (i.e. the statistical error in the linear regression analysis).

2.5.3 Bias of the ellipticity

We now quantify the shape measurement bias on the ellipticity of our galaxy sample. Choosing $r_{\rm wf} = r_{\rm iso}$ and $n_w = 4$, we measure ellipticities $\epsilon_i^{\rm obs}$ and calculate the bias for simulated GAMA galaxies in gri images, using the SNR measured from KiDS g, r and i-bands. The initial weight function $r_{\rm wf} = r_{\rm iso}^r$ is determined from simulated r-band images (the superscript defines the band used to determine $r_{\rm iso}$) and is then also used for the g and i-band images. We choose to use the r-band measured isophote since $r-$band images are of higher quality and we wanted to measure the shape of the same parts of the galaxies by using the same weight function on all three bands. The actual $r_{\rm iso}^g$ and $r_{\rm iso}^i$ values are not very different than $r_{\rm iso}^r$, and as we can see from Fig. 2.4 the bias is fairly constant around $r_{\rm wf} = r_{\rm iso}$, therefore this choice will not result in significantly larger biases in the g and i-band. However, galaxies imaged in the g and i-band filters have lower SNR compared to the r-band images and therefore we expect a larger noise bias on the g and then i-band shapes.

In Table 2.1 we present the bias of measured shapes on simulated galaxies for the three broad band filters. As a sanity check, we note that $m_1 = m_2$, within the error bars, for each set of simulated galaxies. In addition, additive biases are consistent with zero. The lowest bias is obtained for r-band image simulations, as expected, followed by i and g-bands.

2.6 Results

Having calibrated the shape measurement method against realistic image simulations, we present our results in this section. Shapes of galaxies in g, r and i-band images were measured and the final sample consists of galaxies for which the shape was successfully measured in all three filters, which is the case for 89.7% of the initial galaxy sample. We have checked that the galaxies that were rejected follow the same redshift distribution as the whole galaxy sample. We first examine the distributions of ellipticity and size for our galaxy sample in the three filters. Then, we investigate differences in the intrinsic alignment signal measured in the three filters, and try to understand the source of the observed difference, by splitting the galaxy sample into further sub-samples based on colour, redshift and central/satellite galaxies.

2.6.1 Ellipticity and size distributions

The ellipticity distributions (after applying the bias correction) for all the galaxies in our sample, as measured from the three filters, are shown in Fig. 2.5. The shapes from the g and i-band images have similar ellipticity distributions while the ellipticity measured in the r-band follows a distribution that peaks at lower ϵ and drops more quickly as ϵ increases. This behaviour is expected solely due to the non-linear nature of the ellipticity (i.e. a ratio of surface brightness moments). As shown in Melchior & Viola (2012), noise causes the ellipticity distribution to be generally asymmetric and skewed, pushing its peak to higher values. As noise increases, this peak is pushed further away from its true value and we see this behaviour in our image simulations as well. Keeping all morphological parameters the same, the measured ellipticity distribution of our g and i-band image simulations is pushed to slightly higher values than the higher-SNR r-band image simulations.

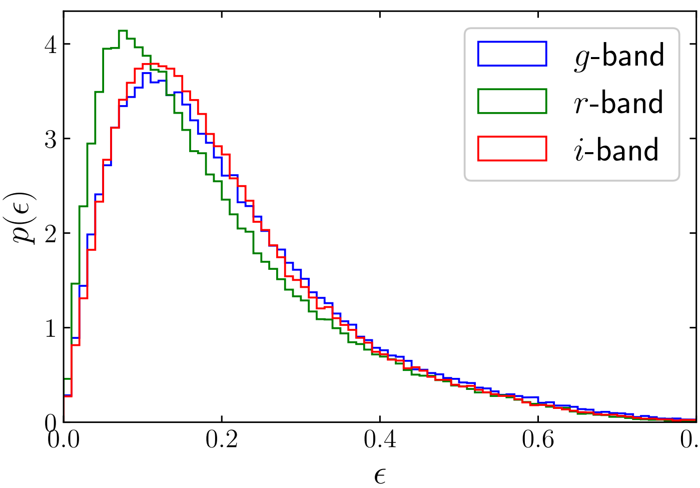

Figure 2.5: Distribution of ellipticity of GAMA galaxies as measured from the three broad band gri KiDS images. The qualitative difference observed between the r-band and the ellipticities in the other filters is found to be caused due to higher noise in the g and i-band ellipticities.

However, the ellipticity distributions in Fig. 2.5 are much more significantly different compared to what we see in our image simulations. We visually inspected galaxies with largely different ellipticities between r-band and g or i, and discover that most of them where due to relatively bright concentrated circular bulges present in the r-band images. Therefore, these differences, while partly caused due to noise, are also attributed to morphological differences in the galaxy g, r and i-band images. We also note that the ellipticity distributions where observed to be more discrepant in high redshift galaxies ($z > 0.26$) compared to low redshift. This suggest that, at least partly, these differences could be caused by the fact that different parts of a galaxy's spectral energy distribution is observed in a given filter for galaxies at varying redshift. In Sect. 2.6.1 we discuss the possible contamination to the intrinsic alignment measurement from these different ellipticity distributions.

As mentioned in Sect. 2.1, galaxy colour gradients tend to make galaxies appear larger in blue than in red filters. Having measured quadrupole moments

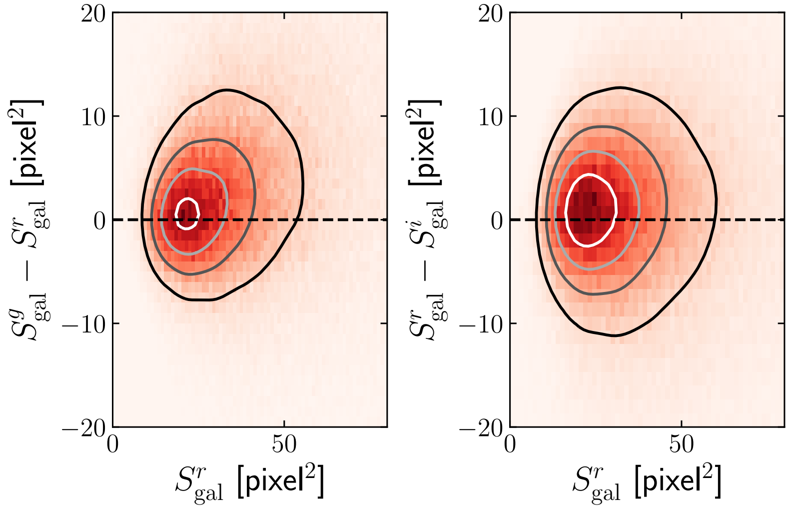

Figure 2.6: Comparison of galaxy sizes, given from Eq. (2.12), between g and r-band sizes (left) and r and i-band (right). The density map is shown, with denser regions appearing redder. Equally spaced contours are overlaid for clarity.

for galaxies in the three gri broad bands, we are in a position to test this hypothesis. We quantify the size of a galaxy as

$$S_{\rm gal} = \sqrt{Q_{20}Q_{02} - Q_{11}^2} \Big/ Q_{00}\,, \tag{2.12}$$

where we use the deconvolved, de-weighted moments Q_{ij}. The comparison is presented in Fig. 2.6, where the density map is shown for the sizes measured in the three filters. We can see that sizes measured in the g-band are generally larger than those measured in the r-band, in agreement with our expectations. The r and i-band sizes seem to be very similar, hinting, however, towards slightly larger sizes for galaxies in the r-band. Note that the weight function used for the shape measurements have been defined in the r-band images, and the differences could potentially be larger than what is seen in Fig. 2.6.

2.6.2 Intrinsic alignment measurement methodology

Intrinsic alignments are commonly quantified by the projected correlation function between galaxy ellipticity and galaxy density,

$$w_{g+}(\mathbf{r}_p) = \int_{-\Pi_{\max}}^{+\Pi_{\max}} \xi_{g+}(\mathbf{r}_p, \Pi)\mathrm{d}\Pi \,, \tag{2.13}$$

where ξ_{g+} is the three-dimensional correlation function. The line-of-sight distance between the galaxy pairs is Π and $\mathbf{r}_p$ is the transverse separation of these galaxies. We measure ξ_{g+} using the modified Landy-Szalay estimator[12] (Landy & Szalay 1993; van Uitert & Joachimi 2017), given by

$$\xi_{g+}(\mathbf{r}_p, \Pi) = \frac{S_+D}{D_\mathrm{S}D} - \frac{S_+R}{D_\mathrm{S}R} \,, \tag{2.14}$$

In the above equation capital letters define a particular galaxy sample, with S_+ for a sample of galaxy shapes, D for for galaxy density and R containing random points in the survey area. D_S is the density field traced by the sample of galaxy shapes. D_SD and D_SR are the (normalised) number of pairs in the respective catalogues (see Eq. 16 in Kirk et al. 2015, for a detailed description). The alignment is essentially quantified by

$$S_+D = \sum_{i \neq j} \epsilon_+(i|j) \,, \tag{2.15}$$

where galaxy i is taken from the shape sample and j from the density sample (or the random sample, for S_+R). The tangential ellipticity component $\epsilon_+(i|j)$, defined between galaxies i and j, projects the ellipticity along the vector connecting the two galaxies, and is defined by

$$\epsilon_+ = \epsilon_1 \cos 2\theta_p + \epsilon_2 \sin 2\theta_p \,, \tag{2.16}$$

where θ_p is the angle between the x-axis of the coordinate system and the line connecting the galaxy pair. The ellipticity components ϵ_1, ϵ_2 are defined for galaxy i with respect to the x-axis of the coordinate system. A positive/negative value of ϵ_+ implies radial/tangential alignment. Rotating by 45 degrees, we can define the cross ellipticity component as

$$\epsilon_\times = \epsilon_1 \sin 2\theta_p - \epsilon_2 \cos 2\theta_p \,. \tag{2.17}$$

[12]For a discussion on the choice of the estimator used see Johnston et al. (in prep.).

The ellipticities are corrected for multiplicative bias according to Table 2.1. We note here that the intrinsic alignment signal is measured using ellipticities and not shear, with the latter usually preferred when quantifying the contamination of IA to weak lensing measurements. For the random sample R we use random catalogues specifically designed for GAMA (Farrow et al. 2015), downsampled to contain roughly 100 times more galaxies than the number of galaxies in the shape sample, which we confirmed to be sufficiently large to produce consistent random signals. In an analogous way, $w_{g\times}$ can be measured, which is expected to be zero and can serve as a test for systematic errors.

The correlation function in equation (2.13) can be connected to analytical predictions for intrinsic alignments. For details on modelling the intrinsic alignment signal, as well as a discussion on the contamination of this signal to future cosmic shear surveys, we refer the reader to Johnston et al. (in prep.). In this work we will focus only on potential differences in the measured intrinsic alignment signal between the different broad band filters. To measure projected correlation functions, we integrate over $-60 \leq \Pi \leq 60$ Mpc/h (in bins of $\Delta\Pi = 4$ Mpc/h) and then consider 11 bins of transverse separation r_p, logarithmically spaced between 0.1 and 60 Mpc/h.

Since we are interested in the *difference* of the signal between broad band filters (using the same galaxies in all three filters to compute this), we expect no sample variance, justifying our approach where we only account for shape measurement noise. We do so by creating 100 realisations of the shape catalogues, adding a random position angle to each galaxy (making sure the same angle is added to the same galaxies in all three filters for each realisation).

2.6.3 Intrinsic alignment differences in the gri filters

We now quantify the difference in the intrinsic alignment signal measured among the three gri broad bands. This is expected to be zero if the correlation of galaxy shapes and positions is not systematically different between the three bands. Therefore, measuring a non-zero difference in the correlation functions would suggest that the intrinsic alignment signal is different for observations at different wavelengths. We note that, for each galaxy, the same weight function has been applied to all three broad band images, and only galaxies with reliable shapes in all three images are used for the shape sample. This ensures that the exact same galaxies are used to calculate the intrinsic alignment signal in each filter, and the weight function is fixed on the same physical size for each galaxy. Several tests for systematics were performed, which did not reveal any problems with the analysis (see Appendix 2.A)

We calculate $\Delta w_{g+} = w_{g+}^{\mathrm{band1}} - w_{g+}^{\mathrm{band2}}$, among the three bands ($g - r$ and $r - i$)[13] as a function of the transverse separation of the galaxy pairs, r_p. We use all galaxies with reliable shapes in unmasked regions for the shape population and all the galaxies for the density population. We perform a redshift cut $0.01 < z < 0.5$ which matches the redshift range over which the random catalogue was generated (Farrow et al. 2015). The results are shown in Fig. 2.7. The difference in the correlation functions is non-zero for small galaxy separations, $r_p \lesssim 2$ Mpc/h, whereas, on the largest scales the difference in the signals is consistent with zero. By examining the individual IA signal for the $w_{g+}^{\mathrm{g,r,i}}$ we see that they are all positive (indicative of radial alignments, where the semi-major axis of galaxies points towards each other). Conclusively, the signal is lower in the r band, compared to g and i.

As a reference, we show the intrinsic alignment signal measured in the r-band for scales up to ~ 30 Mpc/h. The error bars are estimated using a jackknife technique to obtain the covariance matrix, cutting the survey area in 3D cubes to achieve large enough number of jackknife samples. The GAMA survey geometry limits us to using scales only up to ~ 30 Mpc/h, since covariance on larger scales cannot be captured by the jackknife configuration. For a detailed analysis on the jackknife error estimation, as well as the r-band signal itself, we refer the reader to Johnston et al. in prep.

We see that, at large scales, the difference is generally smaller than the r-band signal. At smaller scales, below 2 Mpc/h, the difference is larger, even though the r-band signal is generally noisy at these scales[14]. Interestingly, the Δw_{g+} values for these scales are comparable to the value of w_{g+} of the r-band measurement on large scales. Through this comparison, we conclude that the difference observed in alignment with wavelength is large enough that it cannot be neglected.

Since the data points are correlated, we use the full shape-noise covariance matrix and a χ^2 analysis to assess the significance of the signals. We test the 11 data points against a null-signal hypothesis and quote the p-values for 95% confidence level. The difference in alignment signal is significantly non-zero, both in $g - r$ and $r - i$ measurements, with p-values of 0.02015 and 0.00048, respectively. We also restrict the analysis to the largest scales, beyond $r_p > 6$

[13] We check that the Δw_{g+} for the $g - i$ filter combination is roughly the sum of the other two combinations and is therefore omitted.

[14] We note here that the error bars on Δw_{g+} are significantly smaller than the ones in the individual signals. We are able to calculate such small error bars because we use exactly the same galaxies to calculate Δw_{g+} and are only left with the errors due to shape measurement noise, which are generally very small.

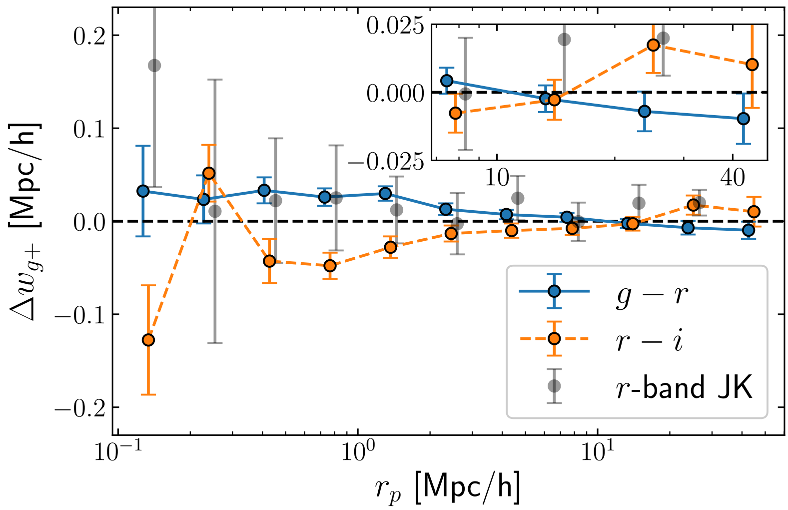

Figure 2.7: Difference in projected density-shape correlation function between the $g-r$ and $r-i$ filters (blue and orange points respectively). The x-axis shows the transverse separation of galaxy pairs. For reference, the signal measured in r-band is shown with grey points, with errors obtained from 3D jackknife resampling. The in-line figure is a zoom-in on the last four data points, in the highest separations. Points are horizontally displaced for clarity.

Mpc/h, which includes the last four data points shown zoomed in, in the in-line figure of Fig. 2.7. For these large scales the difference in signals is consistent with zero, with p-values equal to 0.56 and 0.16 for the $g-r$ and $r-i$ difference, respectively.

2.6.4 Tracing the origin of the difference

In order to investigate the source of the wavelength dependence of the intrinsic alignment signal, evident in Fig. 2.7, we calculate the IA signal splitting the galaxy sample into sub-samples. Using the stellar masses catalogue `StellarMassesLambdarv20` from the GAMA DMU (Taylor et al. 2011) we acquire colour information for our galaxy sample and split in intrinsically red and blue galaxy population (using the rest-frame $g-i$ colours of the stars in the galaxy, `gminusi_stars`> 0.75 and < 0.75, respectively). We observe that Δw_{g+}, measured for these two populations, is non-zero in both cases but larger in amplitude for red galaxies. They are also seen at different scales: on smaller scales for the blue galaxy sub-sample and on larger scales for the red sub-sample (see Appendix 2.B). This behaviour is expected according to the tidal alignment model and tidal torque model (for pressure and rotationally supported galaxies, respectively, see Kiessling et al. 2015), according to which alignments between blue galaxies manifest generally on small scales, while alignments in red galaxies can be observed further out, and generally reach higher amplitudes. For blue galaxies, any difference in the signal would be observed on smaller scales as well.

Moreover, we split the whole galaxy sample into low and high redshift sub-samples ($z < 0.26$ and $z > 0.26$, respectively). We observe a null Δw_{g+} for high redshift galaxies, while the Δw_{g+} for the low redshift sample looks very similar to what is seen in Fig. 2.7 (see appendix 2.B). While this would suggest an evolution of the intrinsic alignment difference with time, we find that the alignment signal does not vary greatly with redshift (see e.g. Johnston et al. in prep.). On the other hand, since our galaxy sample is flux limited, less luminous galaxies are observed in the lower redshift sample compared to the higher one. More interestingly, due to this fact, at lower redshift we observe more satellite galaxies than at high redshift.

To investigate whether satellite galaxies can affect the difference in intrinsic alignment signal between bands, we use the Group catalogue of the GAMA DMU Robotham et al. (2011). We find that the lower redshift sample contains more than twice as many satellite galaxies than the high redshift one. Furthermore, we split our sample of galaxies into satellite (column `RankBCG`> 1 in the Group catalogue) and central galaxies, where we take all the “field” galaxies (i.e. those not associated with a group) and all the brightest central galaxies (BCG) of groups as the central galaxies sample (`RankBCG`≤ 1). The reason for including the field galaxies is that we expect most of these to be the BCG of a galaxy group whose satellites are too faint to be observed.

We correlate the shapes of central galaxies against the density of central galaxies and plot the difference in the obtained projected correlation function Δw_{g+} in Fig. 2.8. We find that the difference in alignment is consistent with zero between the three broad band filters for this sample of galaxies. The same conclusion is reached when correlating shapes of satellite galaxies against the density of central galaxies. Note that we do not restrict the correlation measurement to satellites and their corresponding group BCG, but rather correlate all identified satellites against all other galaxies in the sample. When the alignment signal is measured using shapes of central galaxies correlated with the density of

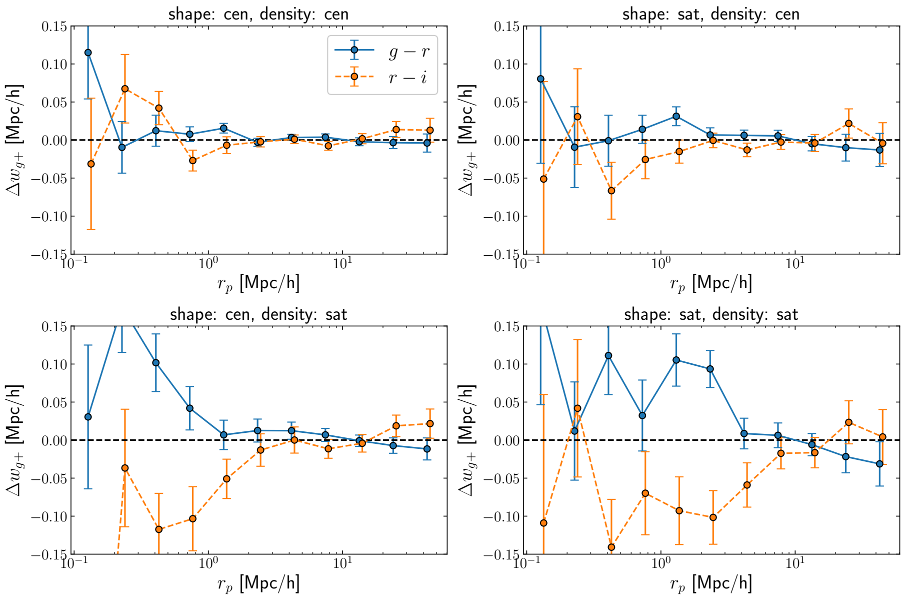

Figure 2.8: Difference in projected density-shape correlation function between the $g-r$ and $r-i$ filters (blue and orange points, respectively). The correlations were measured using the following shape/density samples: centrals vs centrals (top left), satellites vs centrals (top right), centrals vs satellites (bottom left) and satellites vs satellites (bottom right). The x-axis shows the transverse separation of galaxy pairs. Points are horizontally displaced for clarity.

satellite galaxies, the difference Δw_{g+} between the three bands is significantly non-zero at scales below 1 Mpc/h, reaching values roughly twice as much as the ones seen in Fig. 2.7. As in Sect. 2.6.2, the IA signal $w_{g+}^{\mathrm{g,r,i}}$ is positive in each band, and hence the alignment signal in the r-band is the weakest. The same behaviour is observed when correlating shapes of satellite galaxies against position of satellites. In this case, the difference in the alignment signal extends further, up to around 3 Mpc/h.

To further pinpoint the galaxy population responsible for the observed IA difference, we split the satellite galaxies into intrinsically red and blue, in the same way as for the whole population, described above. When blue satellites are considered, the intrinsic alignment difference has a very small amplitude and

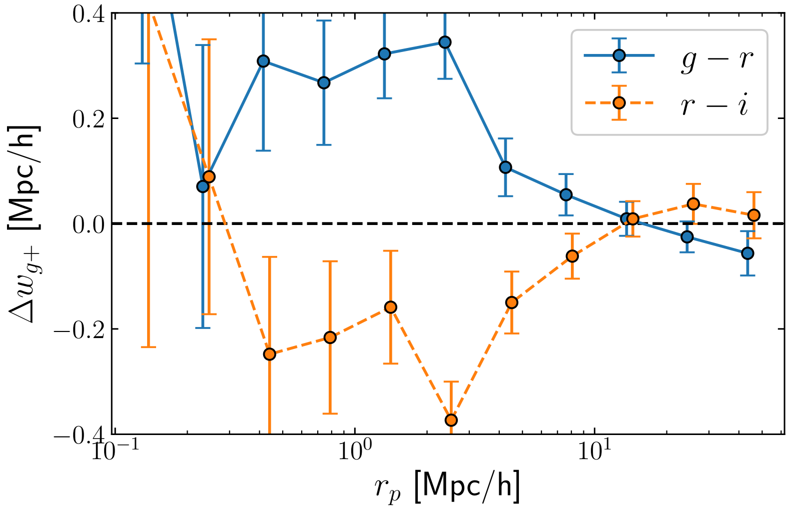

Figure 2.9: Difference in projected density-shape correlation function between the $g-r$ and $r-i$ filters (blue and orange points, respectively) measured using red satellites as shape and density samples. The x-axis shows the transverse separation of galaxy pairs. Points are horizontally displaced for clarity.

becomes noisy. When we correlate shapes and positions of red satellite galaxies, however, the IA difference is larger, up to twice the amplitude seen in Fig. 2.8. This result can be seen in Fig. 2.9.

2.6.5 Investigating ellipticity distribution differences

As seen in Fig. 2.5, the distributions in ellipticity for the g, r and i band shape measurements are not identical. Here, we investigate whether our results are a manifestation of this ellipticity difference. The first thing we looked at was the distribution of ellipticity for satellite and central galaxies. In their respective bands, these ellipticities were shown to be very similar. If the ellipticity distribution differences were to play a major role in our results, the Δw_{g+} of central galaxies should be similar to that of satellite galaxies, which is clearly not the case, as seen in Fig. 2.8.

The w_{g+} estimator described in (2.13)-(2.16) is essentially weighted by the

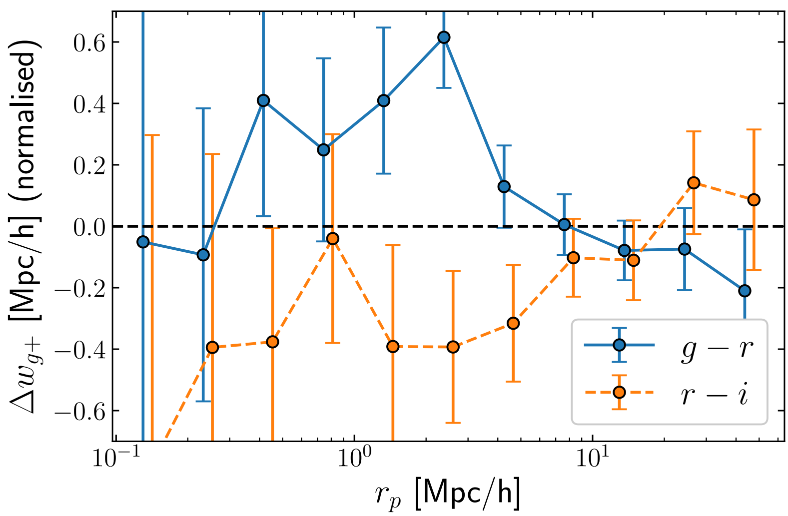

Figure 2.10: Difference in projected density-shape correlation function between the $g-r$ and $r-i$ filters (blue and orange points, respectively) but using the normalised ellipticities of galaxies, measured using satellites as shape and density samples. The x-axis shows the transverse separation of galaxy pairs. Points are horizontally displaced for clarity.

absolute value of the galaxy's ellipticity $|\epsilon|$. To nullify the effect of the ellipticity distribution to the calculation of correlations, we calculate w_{g+} using *normalised* ellipticities for each galaxy, i.e. $\epsilon_i \mapsto \epsilon_i/|\epsilon|$. This ensures that the alignment is not weighted by the ellipticity of each galaxy. The results obtained using this "pure" alignment estimator are shown in Fig. 2.10. We see that the IA difference is still non-zero, the amplitude is now larger and the measurement has become more noisy. This is expected because more elliptical galaxies will show their alignment more clearly when weighted by their ellipticity, hence the noisier measurement of the normalized Δw_{g+}. On the other hand, nearly round galaxies will have a boosted signal when the estimator is divided by $|\epsilon|$, hence the larger amplitude. We conclude that the measured IA difference is not caused by the difference in ellipticity distributions of galaxies measured in the three broad band filters.

Another complication can arise from the fact that the PSF is generally larger in the g and i-band images than in the r-band. Since we are using the same, fixed weight function size on all three bands, we cannot probe exactly the same physical scales of each galaxy in the three bands. However, that would imply that in g and i-band images we are probing smaller galaxy scales, where the alignment signal is expected to be smaller, than in the r-band images. Contrary to this, we are measuring a higher alignment signal in g and i-band. In addition, we have split the galaxy population in galaxy resolution, $R_2 > 0.9$ and $R_2 < 0.9$ for high and low resolution galaxies respectively (where R_2 was measured in the r-band, see Fig. 2.1). We see no difference in the IA difference when correlating red satellite shapes and positions, between high and low resolution galaxies. We conclude that the PSF differences in the three broad band image data do not influence our result.

2.7 Conclusions

In this work we have presented a new shape catalogue for galaxies in the GAMA spectroscopic survey (equatorial fields). Shapes were measured using deep imaging data from the KiDS survey in the three SDSS-like gri broad band filters. This allowed us to compare morphological properties of our galaxy sample between the three filters, as well as investigate whether the galaxy intrinsic alignment signal depends on the wavelength band of the observations.

The shape measurement method employed is the moment-based DEIMOS method (Melchior et al. 2011). DEIMOS corrects the measured weighted moments using a Taylor expansion of the inverse weight function, essentially using higher order weighted moments to approximate the unweighted moments. In addition, it accounts for the convolution of the galaxy and the PSF, without imposing any prior assumptions on the PSF. In order to calculate the PSF moments at the positions of our galaxies we model the PSF using shapelets (Refregier 2003), with a pipeline already tested on KiDS image data (Kuijken et al. 2015).

Dedicated image simulations were used with two goals in mind: finding the optimal setup for the shape measurement method and characterizing its bias, which can lead to false conclusions about the intrinsic alignment signal, if left uncorrected. We have shown that we can measure ellipticities of galaxies with multiplicative bias of $\sim 0.6\%, 0.4\%$ and 0.8% in the g, r and i-band images, respectively. The additive bias was found to be consistent with zero.

Ellipticity distributions of galaxies measured in the three gri filters are fairly similar, though the r-band shapes appear to peak at a lower ellipticity than the

g and i-band. The reason for this is partly the lower SNR at which galaxies are observed in g and i-band, compared to r-band images, but mostly due to galaxies having different morphology across these three bands. Galaxy sizes measured in the g-band appear to be larger than sizes measured in the r-band. The same is not as evident for sizes in r and i-band.

Tests for systematics did not reveal a source for spurious alignments. The physical size of the weight function applied when measuring shapes of galaxies is significantly smaller than the scales to which we measure the positive correlation and cannot account for the measured signal on small scales. Correlation of galaxy position with the cross ellipticity components $w_{g\times}$ is measured to be zero (as expected from symmetry). The PSF model did not seem to induce an artificial signal.

We have measured the projected correlation function w_{g+} of galaxy positions correlated with the galaxy ellipticities in the three bands and computed its difference among them. We find that the difference Δw_{g+} is significantly non-zero, positive between filters $g - r$ and negative for $r - i$. Given that g-band is bluer than r, and since galaxies generally have colour gradients and build-up hierarchically inside-out, the outer, more blue star population of galaxies will be more prominent in blue filters. Outer regions of a galaxy are also more susceptible to tidal fields and therefore we can expect a stronger alignment signal in blue filters. This can physically explain the positive signal in $g-r$ but the negative difference between the low-z $r - i$ filters is counter-intuitive. From this we conclude that this rather simple interpretation is not enough to explain the observed Δw_{g+}, and accurate modelling of the galaxy's colour gradients, between r and i-band filters, as well as of the alignment signal on these small scales is necessary to understand the observed IA differences. This, however is beyond the scope of this exploratory work. We restrict our analysis to the largest scales ($r_p > 6$ Mpc/h), which are scales where the intrinsic alignment signal is fit in Johnston et al. in prep., we find that the difference in intrinsic alignment signal between bands is consistent with zero. Comparison of the difference to the w_{g+} measured in r-band only indicates that our result cannot be neglected; on scales $\sim$ 2Mpc/h the passband dependence is significant.

We try to find the galaxies responsible for the observed difference in intrinsic alignment signal with wavelength. Splitting the galaxy sample into satellites and centrals we find large values in this difference when we correlate shapes of central or satellite galaxies with positions of satellites. Furthermore, the difference is largest when shapes and positions of red satellites are correlated. The difference is consistent with zero using centrals as the density sample. This fact suggests that the difference in alignment signal does not occur from one galaxy group to another but is a rather short-ranged phenomenon observed among the group galaxies, more accurately traced by using the satellites as density tracers.

Our analysis suggests that the intrinsic alignment signal depends on the wavelength of observations. Hence, priors of IA on a particular broad band filter should not be used in cosmic shear measurements of a different filter without accounting for this dependence. Also, the IA wavelength dependence seems to be driven by the red satellites in the galaxy sample, and disappears if only central galaxies are considered. Therefore it is important to understand the satellite fraction of a galaxy sample. Intrinsic alignments measured in low redshift samples can be different from samples at high redshift due to a change in the satellite fraction. In addition, galaxy colour gradients change as a function of redshift; in a fixed filter band galaxies at high redshift appear redder than the same galaxies at low redhshift. An apparent redshift dependence of the IA signal can be introduced, solely driven by the change of galaxy colour gradients as a function of redshift.

The dependence of the intrinsic alignment signal with wavelength could provide the ability to study cosmology as well. Similar to what has been proposed in Chisari et al. (2016), the alignment signal measured in different broad band filters can be used as a multitracer probe of intrinsic alignments and improve constraints on primordial non-Gaussianity. Building on this, future work will focus in using shape measurements with a radially varying weight function, effectively probing inner and outer regions of galaxies, and quantifying the galaxy scale dependence of the intrinsic alignment signal. Such shape measurements can also be combined to probe the intrinsic alignment contamination to galaxy-galaxy lensing more accurately, as demonstrated in Leonard & Mandelbaum (2018).

2.A Tests for systematic errors

In this section we perform tests for systematics that could contaminate the measurement of the correlation functions. We showed that the difference in the alignment signal between broad bands is dominated by satellite galaxies. We have checked that, even though satellites are generally fainter and smaller in size than the general galaxy population, this is not enough to introduce an artificial signal. We see this by splitting the sample into high/low stellar mass galaxies and finding no significant difference in the observed IA signals. Furthermore, the bias does not vary greatly with SNR, with $m \sim 3\%$ for SNR ~ 60, which is not enough to explain the observed Δw_{g+}, especially since only $\sim 1\%$ of our satellite sample have $\mathrm{SNR}_{g,i} < 60$. Also, we have checked that the bias in the shape measurement does not depend much on galaxy size either, particularly for our galaxy sample ($m < 1.5$ % in r-band simulations for any galaxy half-light radius), and satellite galaxies are, in general, not much smaller in size. In addition, the fact that splitting galaxies into centrals and satellites showcases the "appearance" and "disappearance" of an IA signal difference, together with the fact that the difference is observed at large galaxy separations (all the way to 2 Mpc/h) supports our conclusion that a physical mechanism is the cause of the signal, rather than a systematic error. In the following, we look more closely for such errors.

2.A.1 Physical scale of the weight function

The first thing to consider is the physical scale at which the galaxies are probed with the applied weight function, when measuring galaxy shapes. A large weight function may allow light from nearby galaxies to enter in the measured weighted moments and result in a systematic radial signal being present in the correlation function. The physical size of the weight function's semi-major axis ranges up to 21 kpc/h[15] but with a mean value of 8.8 kpc/h. Since this is much smaller than the lowest scales at which the correlation function is measured (100 kpc/h) and considering that most of the flux from neighbouring galaxies is masked with segmentation maps, we conclude that the weight function is not large enough to introduce a spurious signal in our data.

2.A.2 Galaxy density - cross ellipticity correlation

The correlation of galaxy positions and the *cross* ellipticity component $\xi_{g\times}$ is expected to be zero due to parity symmetry. Therefore, $w_{g\times}$ serves as a test for systematic errors in our analysis. In Fig. 2.11 we show $w_{g\times}$ measured in the three *gri* filters. Again, we test if these signals are consistent with zero by performing a χ^2 test against the null-signal hypothesis, taking into account the full shape-noise covariance matrix. It is found that the signals are consistent with zero at a 95% confidence level with p-values equal to 0.26, 0.27 and 0.32 for the g, r and i-band measurement. Therefore, $w_{g\times}$ revealed no evidence of systematic errors.

[15]Only 0.29% of our sample has a weight function larger than 21 kpc/h.

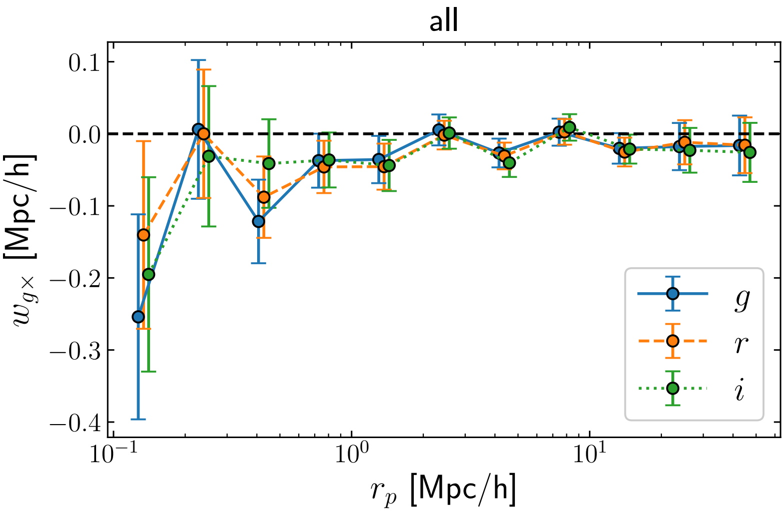

Figure 2.11: Projected correlation function between the density and cross ellipticity of all galaxies, for the three filters (gri in blue, orange and green, respectively). The x-axis shows the transverse separation of galaxy pairs. Points are horizontally displaced for clarity.

2.A.3 PSF shape contamination

The three-dimensional correlation function ξ_{g+} can be written as a sum of two terms: the first term is the correlation of the galaxy position with the galaxy's intrinsic ellipticity and the second term is proportional to the correlation of the galaxy position with the ellipticity of the PSF, as measured in the position of galaxies (Singh & Mandelbaum 2016, Eq. 24). The latter is expected to be zero since the PSF is not expected to align with galaxy position. We checked that this second term, of the correlation between PSF shapes and galaxy position, is much smaller than the correlation of galaxy shapes and positions (finding a $\sim 10^{-3}$ Mpc/h contribution to w_{g+}), and does not influence our results.

2.B IA difference for red/blue, high/low redshift galaxies

We present here the difference in intrinsic alignment signal between measurements in the *gri* broad band filters, where we split our galaxy sample into low/high redshift and intrinsically red/blue sub-samples.

In Fig. 2.12 we show the difference in alignment between galaxies at low redshift ($z < 0.26$) and galaxies at high redshift ($z > 0.26$). We notice that for galaxies at high redshift the difference in alignment signal is consistent with zero while galaxies at low redshift exhibit a clear non-zero difference. However, we note that the high redshift sample contains $\sim 15,000$ satellites, as opposed to the $\sim 33,000$ present in the low redshift sample. We also point out that a measurement in the higher redshift bin is expected to have a lower SNR due to the fact that the volume of this galaxy sample is larger than the volume of the low redshift sample.

In Fig. 2.13 the difference Δw_{g+} is shown for intrinsically red and blue galaxies. In both cases the signal is non-zero but the red galaxy population exhibits a stronger difference over larger transverse separations than the blue one. Interestingly intrinsic alignments are expected to be stronger and act on larger scales for red galaxies, compared to blue, according to the linear alignment and tidal torquing models, used commonly to describe intrinsic alignments.

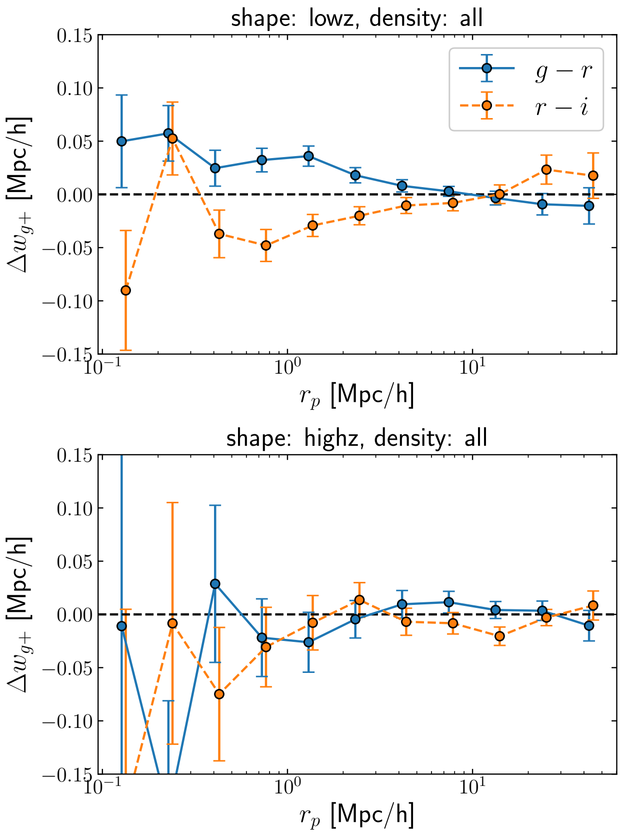

Figure 2.12: Difference in projected density-shape correlation function between the $g-r$ and $r-i$ filters (blue and orange points, respectively). The correlations were measured using low (top panel) and high (bottom panel) redshift shape samples ($z < 0.26$ and $z > 0.26$, respectively) while the density sample contained all galaxies. The x-axis shows the transverse separation of galaxy pairs. Points are horizontally displaced for clarity.

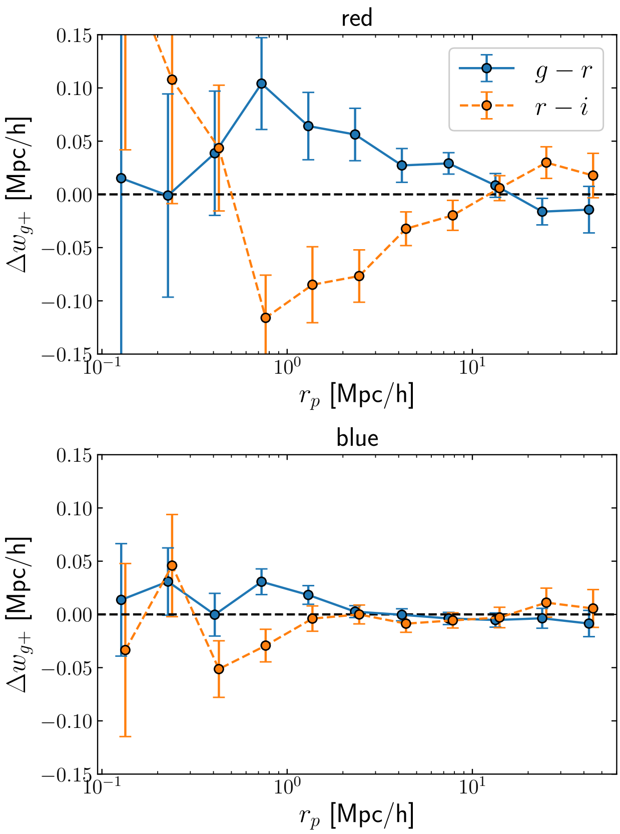

Figure 2.13: Difference in projected density-shape correlation function between the $g-r$ and $r-i$ filters (blue and orange points, respectively). The correlations were measured using intrinsically red (top panel) and blue (bottom panel) galaxy sub-samples for both the shape and density field. The x-axis shows the transverse separation of galaxy pairs. Points are horizontally displaced for clarity.

Chapter 3

KiDS+GAMA: Intrinsic alignment model constraints for current and future weak lensing cosmology

Based on
H. Johnston, C. Georgiou, B. Joachimi, H. Hoekstra,
N.E. Chisari, D.J. Farrow, M.C. Fortuna, C. Heymans,
S. Joudaki, K. Kuijken, A. Wright
A&A 624, A30 (2019)

3.1 Introduction

Light travelling towards Earth passes through the inhomogeneous universe, and consequent tidal gravitational field. In accordance with General Relativity, the light is differentially deflected, producing coherent distortions in the apparent shapes of source galaxies. This weak cosmological lensing – or cosmic shear – signal encodes information pertaining to the total matter distribution, universal geometry, and cosmic expansion and acceleration, as each evolves with redshift. Thus cosmic shear is one of the vital probes in the challenge to de-shroud the dark energy and dark matter species of the ΛCDM cosmological model.

Since its first detections around the turn of the century (Bacon et al. 2000, Kaiser et al. 2000, Wittman et al. 2000, Van Waerbeke et al. 2000), cosmic shear has matured into a powerful tool for cosmology (Heymans et al. 2013, Jee et al. 2016, Hildebrandt et al. 2018, Köhlinger et al. 2017, Troxel et al. 2017, Hikage et al. 2019), been combined with complementary probes to great effect (Abbott et al. 2018, Joudaki et al. 2018, van Uitert et al. 2018) and formed the basis of design for many next-generation wide-field sky surveys (LSST; LSST Science Collaboration et al. 2009, Euclid; Laureijs et al. 2011, WFIRST; Spergel et al. 2013).

The primary astrophysical systematic effect for cosmic shear is the *intrinsic alignment* of galaxies (Heavens, Refregier, & Heymans 2000, Croft & Metzler 2000, Catelan et al. 2001, Hirata & Seljak 2004). Cosmic shear relies upon picking up coherent, percent-level shape distortions (shears) over a statistical ensemble of galaxies. However, galaxies may interact with the gravitational field during formation, becoming aligned with their local environment. The same environment/structure also contributes to the lensing distortions observed in background galaxies. Both processes contaminate cosmic shear signals by sourcing non-random shear correlations in imaging data; between the intrinsic shapes of locally aligned galaxies (II), and between those intrinsic shapes and the gravitational shear field (GI). II correlations are restricted to physically close pairs, and are subdominant to the latter GI term, which can operate over wide separations in redshift, posing a greater threat of contamination for deep cosmic shear studies.

Tidal alignments, as they apply to galaxies, are thought to manifest through two principal mechanisms; galaxy halos are tidally (i) *stretched* (see Catelan et al. 2001), and (ii) *torqued* (see Schäfer 2009 for a review of the latter) by the interaction of the tidal shear quadrupole with the moment of inertia of the halo. Pressure-supported, red elliptical galaxies equilibrate their stellar distributions according to the ellipsoidal halo potential. Rotationally supported, blue spirals align their spin axes with the halo angular momentum (see Kiessling et al. 2015). Each type is thus imprinted with the alignments of the halo. The former effect is linear, and the latter quadratic in the matter density contrast, suggesting strong tidal alignment of blue galaxy *spin axes* at small scales, which quickly dissipate with increasing separation. These contrast with the further-reaching *shape* alignments of red galaxies. Both types of alignments should be stronger around more pronounced peaks of the matter distribution (Piras et al. 2018).

This picture is supported by observations; many studies show strong alignments out to $100\,h^{-1}$Mpc for SDSS galaxies, with luminous red galaxies (LRGs) and bright subsamples showing the largest alignment amplitudes (Mandelbaum et al. 2006b, Hirata et al. 2007, Joachimi et al. 2011, Li et al. 2013, Singh et al. 2015). Significant ($\geqslant 3\sigma$) alignments of nearby spiral galaxy spin axes, with reconstructed tidal fields, have been reported on scales $\lesssim 3\,h^{-1}$Mpc (Lee & Pen 2002, Lee & Erdogdu 2007, Lee 2011), but attempted measurements of large-scale intrinsic ellipticity correlations of spirals have thus far been consistent with zero (Hirata et al. 2007, Mandelbaum et al. 2011, Tonegawa et al. 2018). Hydrodynamical simulations corroborate these observational findings for red galaxies, but exhibit disagreements as to the form and amplitude of blue galaxy alignments (Chisari et al. 2015, Velliscig et al. 2015b, Tenneti et al. 2016, Hilbert et al. 2017).

The risk of shear contamination by intrinsic alignment (IA) of galaxies, and the associated threat posed to cosmological parameter inference, has long been known (Heavens, Refregier, & Heymans 2000, Heymans et al. 2004, Hirata & Seljak 2004). Much work has been devoted to measuring the strength of IA and forecasting its impact under various scenarios of modelling or lack thereof (Joachimi & Bridle 2010, Joachimi et al. 2011, Kirk et al. 2012, Krause, Eifler, & Blazek 2016, Blazek et al. 2017). Broadly summarised, the findings suggest (i) significant biasing of cosmological parameters if IA are not accounted for; (ii) IA mitigation schemes, involving nuisance parameters for marginalisation, which will degrade cosmological constraints but can effectively mitigate biasing of parameter inference; (iii) joint analyses of shear probes with positional information and cross-correlations, to aid with degeneracy-breaking and self-calibration of IA models; (iv) the need for increasingly detailed modelling of IA – particularly with respect to non-linearities – accompanied by simulations (for model-testing and predictions) and observational constraints upon IA parameters over a long redshift baseline.

Recent, dedicated studies of cosmic shear have allowed for the effects of intrinsic alignments with nuisance parameterisations (Heymans et al. 2013, Jee et al. 2016, Joudaki et al. 2016, Hildebrandt et al. 2018, Troxel et al. 2017, Samuroff et al. 2018). The currently preferred models, with wide prior ranges, wield great power to modulate lensing observables – this has resulted in heavy degradation of cosmological constraining power. Moreover, we cannot be certain that other systematic effects, known (e.g. photo-z errors – see Efstathiou & Lemos 2018, van Uitert et al. 2018) or otherwise, are not leaking into the IA parameterisations. Informative priors for the models are the first step to assuaging these concerns, and they must be derived from galaxy samples *representative* of cosmic shear datasets.

This work aims to motivate such a prior for current and future studies by constraining the alignment amplitudes exhibited by the flux-limited GAMA spectroscopic sample (Driver et al. 2011), with high-resolution KiDS (de Jong et al. 2013) imaging and shapes. We supplement our GAMA data with galaxies from the SDSS Main sample (York et al. 2000, Strauss et al. 2002) – the only other readily available, wide-area, flux-limited, spectroscopic dataset. This study is made unique by the lack of selection *a priori*, high completeness ($> 98\%$) and spectroscopic redshifts of GAMA and SDSS Main, and so yields a set of constraints which are uniquely instructive for future shear studies. With the aforementioned dependencies of alignments in mind, we also split our samples by colour and redshift, and fit to them with colour-specific parameters, in an effort to more comprehensively describe the contributions of the two galaxy populations.

We measure galaxy position-intrinsic shear correlations in our samples, using galaxies as a proxy to the total matter density field and measuring their tendency to align with that field over a range of scales. We simultaneously fit to clustering measurements in the same samples for self-calibration of the galaxy bias, elsewise degenerate with the intrinsic alignment amplitude. We fit to our signals with the non-linear alignment (NLA) model (Hirata & Seljak 2004, Bridle & King 2007), with and without a luminosity power-law. We forecast, via Fisher matrix analysis, the improvement in cosmological parameter constraints for a finished KiDS survey, when adopting our derived IA constraints as informative priors.

The structure of this paper is as follows; we describe our galaxy survey data in Section 3.2, along with our measurement pipeline. Section 3.3 details our models and methods of fitting, and we summarise the results of fitting in Section 3.4. Section 3.5 outlines our forecasting for a future shear analysis, and our concluding remarks are presented in Section 3.6.

Throughout our intrinsic alignment analysis, we work with rest-frame AB magnitudes, k-corrected to $z = 0$, and assume a flat ΛCDM cosmology with $\Omega_m = 0.25$, $h = 0.7$, $\Omega_b = 0.044$, $n_s = 0.95$, $\sigma_8 = 0.8$, $w_0 = -1$ and $w_a = 0$.

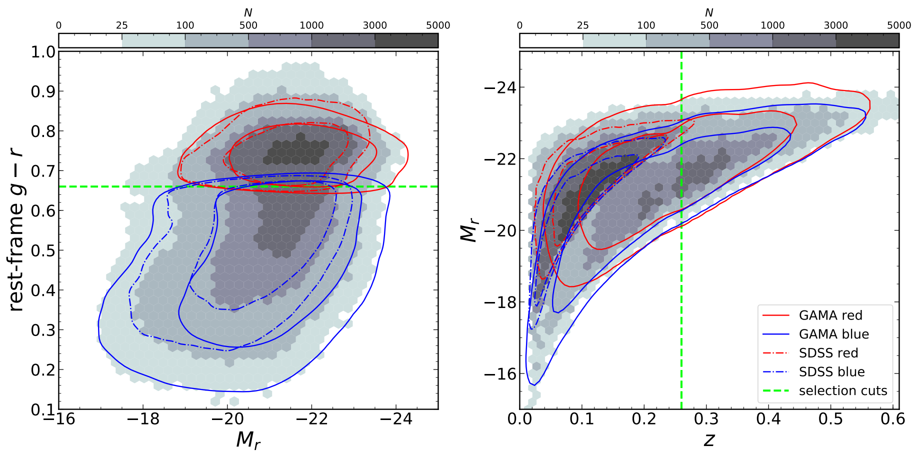

Figure 3.1: *Left:* Galaxy rest-frame colour-magnitude diagram, where we choose a cut in $g-r$ to isolate the red sequence in GAMA and SDSS. *Right:* Sample absolute r-band magnitude-redshift diagram. The total distribution of GAMA and SDSS galaxies is shown, binned in hexagonal cells with a colour scale corresponding to the counts in cells. Coloured contours indicate 75% and 95% of galaxies in a sample. Colour/redshift cuts are shown as dashed green lines, and the apparent leakage of contours is due to the grid-size used in kernel density estimation.

This is the cosmology adopted by the MICE[1] simulations, whose mocks we make use of in our analysis (see Appendix 3.A.2). It is also similar to that assumed by Joachimi et al. (2011), allowing for direct comparison of intrinsic alignment constraints.

3.2 Data

3.2.1 KiDS+GAMA

The ongoing Kilo Degree Survey (KiDS; de Jong et al. 2017) is a wide-field optical imaging survey, taking data in four passbands ($ugri$) with the OmegaCAM camera at the VLT Survey Telescope (VST). The VST-OmegaCAM system is

[1]Publicly available through CosmoHub: http://cosmohub.pic.es

optimised for producing 1 $\deg^2$ images of exceptional quality, facilitating accurate galaxy shape measurements for the primary science driver of KiDS: weak lensing studies.

KiDS aims to image 1350 $\deg^2$ of sky in 2 rougly equal-sized strips. KiDS-North, centered on the celestial equator, shares complete overlap with the Galaxy and Mass Assembly (GAMA; Driver et al. 2011) equatorial fields – a total $180\,\deg^2$, split equally between G9, G12 and G15. GAMA is a now-complete spectroscopic survey which operated on the Anglo-Australian Telescope, with the AAOmega spectrograph. GAMA galaxies possess thoroughly tested spectroscopic redshifts and are highly complete ($> 98\%$) in the r-band limit $r < 19.8$.

Our KiDS+GAMA dataset consists of the final release (Liske et al. 2015), equatorial GAMA spectroscopic sample, with shapes measured from KiDS-450[2] imaging. Galaxy shapes are measured from r-band images, for which the best dark-time seeing conditions are reserved in KiDS. Singh & Mandelbaum (2016) analysed the SDSS-III BOSS LOWZ luminous red galaxy (LRG) sample (Alam et al. 2015) with different shape measurement methods, finding variability in ellipticities, intrinsic alignment conclusions and the impacts of observational systematics. The connection between such variabilities and the radial weighting employed in shape estimation is explored in our companion paper: Georgiou et al. (2019b).

We measure shapes using the moments-based DEIMOS (DEconvolution In MOments Space) method introduced by Melchior et al. (2011). We briefly describe the DEIMOS method here, as applied to KiDS+GAMA, and refer the reader to Georgiou et al. (2019b) for details of the production of our ellipticity catalogue. The moments Q of the distribution of brightness (flux) $G(\mathbf{x})$ across an image, where $\mathbf{x} = (x\,, y)$ is a coordinate vector, are expressed in Cartesian coordinates as

$$Q_{ij} = \int G(\mathbf{x})\, x^i y^j \,\mathrm{d}x\,\mathrm{d}y \quad , \tag{3.1}$$

where $n = i + j$ gives the order of the moment. One recovers the complex ellipticity of an object from 2^{nd}-order brightness moments as

$$\epsilon \equiv \epsilon_1 + \mathrm{i}\epsilon_2 = \frac{\mathrm{Q}_{20} - \mathrm{Q}_{02} + 2\mathrm{i}\,\mathrm{Q}_{11}}{\mathrm{Q}_{20} + \mathrm{Q}_{02} + 2\,\sqrt{\mathrm{Q}_{20}\,\mathrm{Q}_{02} - \mathrm{Q}_{11}^2}} \quad , \tag{3.2}$$

which relates to the semi-major a and semi-minor b axes as $|\epsilon| = (a-b)(a+b)^{-1}$.

[2]http://kids.strw.leidenuniv.nl/DR3/

Observed galaxy flux profiles $G^*(\mathbf{x})$ are distorted by convolution with the point spread function $P(\mathbf{x})$ – determined by observing conditions, telescope optics and detector properties, the PSF describes the blurring of point-like sources in imaging. The PSF-convolved flux profile is

$$G^*(\mathbf{x}) = \int G(\mathbf{x}')\, P(\mathbf{x} - \mathbf{x}')\, \mathrm{d}\mathbf{x}' \quad . \tag{3.3}$$

Melchior et al. (2011) transform the flux profile into Fourier space and show, with the convolution theorem, that the moments of the observed flux distribution Q^*_{ij} are

$$Q^*_{ij} = \sum_k^i \sum_l^j \binom{i}{k} \binom{j}{l} Q_{kl} \{P\}_{i-k,j-l} \quad , \tag{3.4}$$

where $\{P\}_{ij}$ denotes the moments of the PSF. Thus the n^{th}-order deconvolved moments Q_{ij} of the image can be recovered from the image- and PSF-moments up to the same order. In practice, one must also account for noise in the image, from sky background, pixel noise etc. The pixel signal-to-noise ratio (SNR) is lowest at large distances from the galaxy centroid, which would tend to dominate the measurement of 2^{nd}-order brightness moments (Eq. 3.1). We suppress pixel noise using Gaussian elliptical weight functions $W(\mathbf{x})$, and recover an approximation to the unweighted brightness profile by computing a truncated Taylor expansion of $W^{-1}(\mathbf{x})$ (see Georgiou et al. 2019b).

Galaxy shapes can be obscured by overlapping objects in images. These shapes can still be measured by applying masks to the nuisance objects, but the loss of information could have an impact upon the quality of the shape measurement. We verify that excluding blended galaxies – where isophotal radii overlap – does not significantly change our measurements of alignment correlation functions, and continue to include these galaxies in our analysis. We refer the reader to Georgiou et al. (2019b) for further details on our use of weight functions and associated bias considerations, deblending, and any other details of the shape measurements.

We choose a rest-frame colour cut of $g - r > 0.66$ on inspection of the colour-r-band absolute magnitude diagram, in order to cleanly isolate the red sequence (Figure 3.1), and we define 2 redshift bins with edges $[\,0.02\,, 0.26\,, 0.5\,]$ (see Appendix 3.A for more detail on this choice). These cuts yield colour/redshift samples (Z1B, Z1R, Z2B, Z2R) of roughly equal size, and we apply the same colour cut to SDSS galaxies. For measuring position-intrinsic shear correlations in each sample, we define a 'shapes' subset of galaxies residing in unmasked[3] pixels (for details of the masking procedure, see Kuijken et al. (2015) We further exclude any galaxies flagged as having a bad shape measurement (see Georgiou et al. 2019b), and correlate the remaining ($\sim 85-87\%$) shapes against the positions of all galaxies in the same colour/redshift bin – the 'density' sample. We also measure correlations against randomly distributed points, using random catalogues specifically designed for GAMA (Farrow et al. 2015), and randomly downsampled to retain at least $10\times$ the number of galaxies in a corresponding galaxy sample. Where used in additional, demonstrative sample selections, stellar-mass estimates for GAMA galaxies are taken from `StellarMassesLambdarv20` (Wright et al. 2017).

3.2.2 SDSS Main

The Sloan Digital Sky Survey (SDSS; York et al. 2000) imaged about π steradians of the sky, drift-scanning in five bands ($ugriz$), with the purpose-built, wide-field SDSS photometric camera (Gunn et al. 1998). Of the ~ 1 million objects followed up spectroscopically, the Main galaxy sample (Strauss et al. 2002) was designed to be flux-limited and highly complete ($> 99\%$) to $r < 17.77$, thus forming a complementary dataset to GAMA, shallower and over a wider area of $\sim 3340\,\mathrm{deg}^2$. These are the same SDSS Main samples measured for IA by Mandelbaum et al. (2006b), Hirata et al. (2007) and Joachimi et al. (2011), where the latter two works also included LRG-selected samples in their analysis. We make no magnitude selections, and employ a different colour-cut in our analysis, hence we re-measure the alignment signals. We use PSF-corrected ellipticity measurements made by Mandelbaum et al. (2005) with the Reglens pipeline – Reglens measures galaxy shapes via 're-Gaussianisation' (Hirata & Seljak 2003). This is a moments-based method, which assumes Gaussianity in the PSF and galaxy profiles, treating non-Gaussianities with perturbative corrections. We refer the reader to Hirata & Seljak (2003); Mandelbaum et al. (2005) for further details.

We define red and blue SDSS samples (SR, SB) with the same rest-frame cut at $g - r = 0.66$. The SDSS density samples retain galaxies with bad shapes flags, which are excluded from the shapes samples. Figure 3.1 illustrates the colour-redshift-magnitude spaces of our selected samples, which are detailed in Table 3.1.

[3]Our mask excludes galaxies in pixels subject to readout spikes, saturation cores, diffraction spikes, primary halos of foreground objects, bad pixels and manually masked regions.

Table 3.1: Details of our density (bracketed numbers) and intrinsic shape field tracer samples, composed of GAMA and SDSS galaxies split by redshift and/or colour. $L_{\rm piv} \sim 4.6 \times 10^{10} L_{\odot}$ corresponds to an absolute r-band magnitude of -22. For purposes of clustering covariance estimation (see Appendix 3.A.2), we impose a faint limit $M_r \leq -18.9$ on our GAMA density samples – hence Z1B has fewer density galaxies than shapes.

Sample	$\langle z \rangle$	$\langle L/L_{\rm piv} \rangle$	N shapes (density)
GAMA $z > 0.26$, blue (Z2B)	0.33	1.06	31447 (36791)
GAMA $z < 0.26$, blue (Z1B)	0.15	0.21	60634 (52273)
SDSS blue (SB)	0.09	0.14	110557 (114054)
GAMA $z > 0.26$, red (Z2R)	0.33	1.47	31368 (36087)
GAMA $z < 0.26$, red (Z1R)	0.17	0.50	38011 (42078)
SDSS red (SR)	0.12	0.29	166198 (171565)

3.2.3 Estimators

We adapt the notation of Schneider et al. (2002), defining a bin filter $\Delta_{r_p,\Pi}(\mathbf{x}) = 1$ for a pair separation vector $\mathbf{x} = (x_{\parallel}\, , x_{\perp})$ where the (absolute) comoving radial component $x_{\parallel}$ is less than the maximum under consideration $\Pi_{\rm max}$, and the comoving transverse component $x_{\perp}$ satisfies $r_p/10^{\Delta \log(r_p)/2} < x_{\perp} \leqslant r_p \times 10^{\Delta \log(r_p)/2}$ for a transverse bin centred on r_p (log-space bin width $\Delta\log(r_p)$ is constant). For any other separation vector, $\Delta_{r_p,\Pi}(\mathbf{x}) = 0$. We adopt the estimator defined by Mandelbaum et al. (2006b)[4], and given as

$$\begin{aligned}\hat{\xi}_{\rm g+}(r_p, \Pi) \;=\; & \frac{1}{N_{rr_s}(r_p, \Pi)} \times \\ & \left\{ \sum_{sd} \gamma_{+,sd}\, \Delta_{r_p,\Pi}(\boldsymbol{x}_s - \boldsymbol{x}_d) \;-\; \sum_{sr} \gamma_{+,sr}\, \Delta_{r_p,\Pi}(\boldsymbol{x}_s - \boldsymbol{x}_r) \right\} \quad ,\end{aligned} \tag{3.5}$$

[4]For ease of computation, we actually normalise by the density-randoms vs. shapes paircount $N_{rs}(r_p, \Pi)$, as opposed to the density-randoms vs. shapes-randoms paircount $N_{rr_s}(r_p, \Pi)$. We verify that resulting estimates differ negligibly with respect to the noise level.

where we use subscripts to denote and index shape (s), density (d) and density-/shapes-random (r , r_s) galaxy samples, and

$$N_{ij}(r_p, \Pi) = \sum_{ij} \Delta_{r_p,\Pi}(\mathbf{x}_i - \mathbf{x}_j) \quad , \tag{3.6}$$

gives the paircount between samples i and j, which is then normalised according to the relative sample populations[5]. The tangential shear component[6] $\gamma_{+,ij}$ of a galaxy i relative to the vector connecting it to a galaxy j is given as

$$\gamma_{+,ij} = \frac{1}{\mathcal{R}} \Re\mathrm{e} \left[\epsilon_i \exp\left(-2\mathrm{i}\varphi_{ij}\right) \right] \quad , \tag{3.7}$$

where, for galaxy i, the ellipticity $\epsilon_i = \epsilon_{i1} + \mathrm{i}\epsilon_{i2}$ (see Section 3.2.1) and φ_{ij} is the polar angle of the pair separation vector. Note that the sign convention here is $\gamma_+ > 0$ for *radial* alignments, in contrast with the standard for galaxy-galaxy lensing. The shear responsivity $\mathcal{R} \approx 1 - \sigma_\epsilon^2$ in Eq. 3.7 quantifies the response of galaxy ellipticities to gravitational shearing, for a given galaxy sample. The responsivity is doubled when ellipticities are measured via polarisation (see Mandelbaum et al. 2006b), as is the case for our SDSS samples. The resulting shear corrections are then $\lesssim 8\%$ for GAMA, and $\lesssim 35\%$ for SDSS, respectively.

We consider our measurements in line-of-sight projection

$$w_{\mathrm{g}+}(r_p) = \int_{-\Pi_{\max}}^{\Pi_{\max}} \xi_{\mathrm{g}+}(r_p, \Pi)\, \mathrm{d}\Pi \quad , \tag{3.8}$$

thus compressing the measurement into fewer data points, with generally higher signal-to-noise ratios (S/N).

We test for alignment systematics by measuring (i) the position-intrinsic correlation cross-component $w_{\mathrm{g}\times}$ (replacing γ_+ with $\gamma_\times$ in Eq. 3.5, where $\gamma_\times$ is the imaginary analogue to Eq. 3.7; equivalent to γ_+ after a 45 degree rotation of the ellipticity), which must vanish on average since galaxy formation does not break parity. We also measure (ii) $w_{\mathrm{g}+}$ for galaxy pairs with large line-of-sight separations $60 \leqslant |\Pi| \leqslant 90\, h^{-1}$Mpc. Spectroscopic redshifts allow us to choose a narrower range for this test, relative to previous works (e.g. Joachimi

[5]The normalisation is by $n_i n_j$ when $iumeqj$, or else by $n_i(n_i - 1)$, i.e. the total possible number of galaxy pairs with unlimited separations.

[6]In practice, one could affix weights w_s to the shear components, to allow for down-weighting of noisier shapes – we do not apply any weights in our analysis (nor do previous direct-measurement studies of IA), as our use of elliptical weight functions in shape estimation poses problems for the estimation of ellipticity errors (see Section 2.3 of Georgiou et al. 2019b).

et al. 2011), starting at $60\,h^{-1}$Mpc given recent detections of alignments on large transverse scales (Singh et al. 2015). One expects astrophysically induced alignment signals to be dominated by short-range correlations, and consistent with zero over much larger scales, providing the second, "large-Π" systematics test.

We measure galaxy clustering with the standard Landy & Szalay (1993) estimator

$$\xi_{\rm gg}(r_p, \Pi) = \frac{N_{dd} - 2N_{dr} + N_{rr}}{N_{rr}} \quad , \tag{3.9}$$

where the $r_p\,, \Pi$ binning of paircounts is implicit. Eq. 3.9 is well known to improve the bias and covariance properties of the galaxy auto-correlation through subtraction of the random field from the density field, and this concept carries over to our alignment estimator (Eq. 3.5).

Singh et al. (2017) demonstrated that the subtraction of the galaxy-galaxy lensing signal measured around random points (i.e. a randomly distributed lens sample) also holds advantages in reducing the impact of systematics and correlated shape noise, especially on large transverse scales. This is done in the context of galaxy-galaxy lensing; long-range lens clustering introduces noise through lensed, and therefore correlated, background shapes. The GI analogy would suppose that *intrinsic* shears of the shape sample are correlated over super-sample scales – e.g. galaxies aligning with filaments/knots etc. This correlated shape noise would show in the random-intrinsic correlation, and be subtracted by our estimator (Eq. 3.5).

We compute the total projected correlation functions by summing over line-of-sight separations $-60 \leqslant \Pi \leqslant +60\,h^{-1}$Mpc, in bins of $\Delta\Pi = 4\,h^{-1}$Mpc (Eq. 3.8 & analogous for $w_{\rm gg}$) and consider the results in 11 log-spaced bins between $0.1 \leqslant r_p \leqslant 60\,h^{-1}$Mpc.

We compute all intrinsic alignment correlations using our own code, and make use of the public SWOT[7] (Coupon et al. 2012) kd-tree code for clustering correlations, which we verify against our own (brute-force) code and against external clustering measurements in GAMA (Farrow et al. 2015).

3.2.4 Covariances

We estimate signal covariances with delete-one jackknife methods, which we describe briefly here, referring the reader to Appendix 3.A for more detail.

[7]https://github.com/jcoupon/swot

Jackknife samples are defined by the consecutive exclusions and replacements of many 'patches' within the survey footprint, such that each sample constitutes most of the galaxy data. The covariance is thus estimated by considering the deviation from the mean signal upon removal of independent subsets of the data. Each subset must then correctly and independently sample the signal of interest; each patch must be larger than the largest scales under examination. Simultaneously, the number of patches must be much greater than the size of the data vector, or else estimates of the inverse covariance will suffer from excessive noise. Attempting to satisfy both requirements, we implement a 3D jackknife routine, slicing patches in redshift and multiplying the available number of independent subsets. We remain, however, unable to reliably sample large pair separations at low-redshift in GAMA (see Figure 3.11), thus we discard the largest scales ($\sim 40-60\,h^{-1}$Mpc) for GAMA samples with a significant proportion of low-redshift galaxies – see Appendix 3.A for more detail, and for assessments of the jackknife performance.

3.3 Modelling

We observe the weak lensing angular power spectrum as the sum of shear-shear (GG), intrinsic-intrinsic (II) and shear-intrinsic (GI) contributions, such that

$$C_{ij}(\ell) = C_{ij}^{\rm GG}(\ell) + C_{ij}^{\rm II}(\ell) + C_{ij}^{\rm GI}(\ell) \quad , \tag{3.10}$$

for correlations between samples i and j. The cosmic shear GG term encodes the average coherent gravitational shearing of galaxies' light by structure along the line-of-sight, and is the statistic of interest for cosmological analyses. Intrinsically correlated orientations of galaxies result in the extra intrinsic shear correlation II and interference GI terms. These angular power spectra are theoretically determined for a flat universe, by Limber projection of the matter P_{δ}, intrinsic $P_{\rm II}$ and matter-intrinsic $P_{\delta \rm I}$ power spectra, as

$$C_{ij}^{\rm GG}(\ell) = \int_0^{\chi_{\rm h}} {\rm d}\chi \, \frac{q^{(i)}(\chi) q^{(j)}(\chi)}{\chi^2} \, P_{\delta}\left(\frac{\ell}{\chi}, \chi\right) \tag{3.11}$$

$$C_{ij}^{\rm II}(\ell) = \int_0^{\chi_{\rm h}} {\rm d}\chi \, \frac{p^{(i)}(\chi) p^{(j)}(\chi)}{\chi^2} \, P_{\rm II}\left(\frac{\ell}{\chi}, \chi\right) \tag{3.12}$$

$$C_{ij}^{\rm GI}(\ell) = \int_0^{\chi_{\rm h}} {\rm d}\chi \, \frac{q^{(i)}(\chi) p^{(j)}(\chi) + p^{(i)}(\chi) q^{(j)}(\chi)}{\chi^2} \, P_{\delta \rm I}\left(\frac{\ell}{\chi}, \chi\right) \quad , \tag{3.13}$$

each weighted by an efficiency kernel describing the coincidence of sample redshift (comoving distance) distributions $p(\chi)$ and/or lensing efficiencies $q(\chi)$, where $p(\chi)\,\mathrm{d}\chi = p(z)\,\mathrm{d}z$ and

$$q(\chi) = \frac{3H_0^2\Omega_\mathrm{m}}{2c^2}\int_\chi^{\chi_\mathrm{h}} \mathrm{d}\chi'\,p(\chi')\,\frac{\chi'-\chi}{\chi'} \quad , \tag{3.14}$$

for present-day Hubble parameter H_0, matter energy-density fraction Ω_m and comoving distances χ, with χ_h denoting the horizon distance. The redshift distributions of our galaxy samples are shown in Figure 3.11 as dashed red/blue histograms.

We constrain models for $P_{\delta\mathrm{I}}$ by fitting to the real-space alignment and clustering correlation functions described in Section 3.2.3.

3.3.1 Tidal alignments

The linear alignment (LA) model assumes a linear relation between the tidal shearing of galaxies and the gravitational potential quadrupole at their epoch of formation. This form is motivated as follows: fluctuations in the large-scale potential govern the perturbation of halo ellipticites, within which galaxy ellipticities follow suit. With the large-scale fluctuations necessarily small, higher-order terms dwindle and the intrinsic shearing of galaxies by large-scale structure is thus assumed to be a localised, linear function of the potential. In the simplest case, this leads to intrinsic shear P_II and cross matter-intrinsic shear $P_{\delta\mathrm{I}}$ power spectra (Hirata & Seljak 2004)

$$P_\mathrm{II}(k,z) = \left(A_\mathrm{IA}C_1\frac{a^2\bar{\rho}(z)}{D(z)}\right)^2 P_\delta(k,z) \tag{3.15}$$

and

$$P_{\delta\mathrm{I}}(k,z) = -A_\mathrm{IA}C_1\frac{a^2\bar{\rho}(z)}{D(z)}P_\delta(k,z) \quad , \tag{3.16}$$

respectively, where A_IA is a free, dimensionless amplitude parameter, normalised to unity by the constant $C_1 = 5\times10^{-14}\,M_\odot^{-1}h^{-2}\mathrm{Mpc}^3$ – this factor is derived by comparing to the work of Brown et al. (2002) who measured II correlations in the low-redshift ($z\sim0.1$) SuperCOSMOS survey (Hambly et al. 2001), where cosmic shear is negligible. $\bar{\rho}(z)$ is the mean density of the universe and $D(z)$ is the growth factor.

In the original LA model, $P_\delta(k,z)$ is the linear matter power spectrum. Hirata et al. (2007) and Bridle & King (2007) suggested and implemented a substitution of the non-linear corrected spectrum $P_{\delta}^{\rm nl.}(k,z)$, birthing the non-linear alignment (NLA) model. Whilst without theoretical motivation, this model was seen to provide a better description of the alignments measured in LRG samples on scales approaching the non-linear. We conduct and present our analysis with both the LA and NLA models, choosing to focus on the NLA given its widespread use in the literature. Results between the N/LA models will differ only mildly for this work, since meaningful fits of these models must be restricted to quasi-linear scales – neither model provides a true consideration of non-linear evolution/dependence or of intra-halo baryonic physics (e.g. stellar/AGN feedback). However, the choice of model is expected to levy significant changes in cosmic shear analyses that extract a large fraction of their constraining power from highly non-linear scales. The development of appropriate models for IA remains an active topic of research.

We make fits of the NLA and also a luminosity-dependent analogue, henceforth NLA-β, including a power-law scaling β on the average luminosity L of samples, such that

$$A_{\rm IA} \longrightarrow A_{\beta} \left\langle \frac{L}{L_{\rm piv}} \right\rangle^{\beta} \quad , \tag{3.17}$$

where $L_{\rm piv} \sim 4.6 \times 10^{10} L_{\odot}$ is an arbitrary pivot luminosity, corresponding to an absolute r-band magnitude of -22 (see Table 3.1).

We note that fitting linear models to spiral galaxy alignments is at best an approximation to lowest order[8], and that next-stage lensing studies should consider splitting the modelling of alignments to include a quadratic alignment prescription for blue galaxies – such an analysis was recently completed by Samuroff et al. (2018); applying the mixed alignment model of Blazek et al. (2017) to DESY1 data (Abbott et al. 2018), they find the first marginal evidence for quadratic alignments of both late- and early-type galaxies.

3.3.2 Line-of-sight projection

We project matter and matter-intrinsic power spectra along the line-of-sight using Hankel transformations

$$w_{\rm g+}(r_p) = -b_{\rm g} \int {\rm d}z \, \mathcal{W}(z) \int_0^{\infty} \frac{{\rm d}k_{\perp} k_{\perp}}{2\pi} J_2(k_{\perp} r_p) P_{\delta {\rm I}}(k_{\perp}, z) \tag{3.18}$$

[8]Hui & Zhang (2008) and Blazek et al. (2017) theorise linear alignment scaling for all galaxies on sufficiently large scales, arising from non-Gaussian structure fluctuations.

$$w_{\rm gg}(r_p) = b_{\rm g}^2 \int {\rm d}z\, \mathcal{W}(z) \int_0^\infty \frac{{\rm d}k_\perp k_\perp}{2\pi} J_0(k_\perp r_p) P_\delta(k_\perp, z) \quad , \tag{3.19}$$

and jointly model position-intrinsic alignments and clustering, thereby self-calibrating for galaxy bias. J_n denotes an $n^{\rm th}$-order Bessel function of the first kind, and $b_{\rm g}$ is the linear, assumed scale-independent galaxy bias. The weight function $\mathcal{W}(z)$, as derived by Mandelbaum et al. (2011), is given by

$$\mathcal{W}(z) = \frac{p_i(z)p_j(z)}{\chi^2(z)\chi'(z)} \left[\int {\rm d}z \frac{p_i(z)p_j(z)}{\chi^2(z)\chi'(z)} \right]^{-1} \quad , \tag{3.20}$$

where $p(z)$'s are the normalised redshift probability distributions of the galaxy samples being correlated, i.e. a density and a shapes sample for alignments, or two density samples for clustering. The galaxy samples we analyse in this work are flux-limited, therefore $p(z)$ does not increase as ${\rm d}V_{\rm com}/{\rm d}z$ – the gain in comoving volume with respect to redshift. $\chi(z)\,,\chi'(z)$ are the comoving radial coordinate and its derivative with respect to z, such that $\chi^2(z)\chi'(z)$ is proportional to ${\rm d}V_{\rm com}/{\rm d}z$. Thus, $\mathcal{W}(z)$ is inversely proportional to ${\rm d}V_{\rm com}/{\rm d}z$ and acts to down-weight higher redshifts, where flux-limited samples miss faint galaxies.

3.3.3 Likelihoods

We constrain the N/LA models, fitting to $w_{\rm g+}$ and $w_{\rm gg}$ (see Section 3.2.3) by sampling multi-dimensional parameter posterior distributions, using the CosmoSIS[9] (Zuntz et al. 2015) implementation of the affine-invariant emcee (Foreman-Mackey et al. 2013) Monte Carlo Markov Chain sampler. The CosmoSIS framework supports the flexible construction of a pipeline to compute theoretical power spectra and other statistics, and to calculate likelihoods against a data vector whilst sampling over parameters. We exclude the first 30% of samples for a burn-in phase.

The non-linear processes unaccounted for by the N/LA models include non-linear density evolution and galaxy biasing, quadratic tidal torquing, and any other higher-order effects contributing to alignment signatures. The galaxy density-weighted sampling of the intrinsic alignment field is included at lowest order in the original derivation by Hirata & Seljak (2004), however Blazek, Vlah, & Seljak (2015) highlight additional, linear-scale, galaxy bias-dependent

[9]https://bitbucket.org/joezuntz/cosmosis/wiki/Home

contributions in a perturbative expansion. In light of the models' limitations, and inline with previous analyses, we limit our NLA (and LA) fits to transverse scales above $6\,h^{-1}$Mpc.

Our parameter vectors for the NLA/NLA-β (and LA/-β) models are then

$$\begin{aligned}\vec{\lambda}^{\rm NLA} &= \{\, b_{\rm g}\,, {\rm IC}\,\}_i + \{\, A_{\rm IA}\,\}_{\rm R,B} \\ \vec{\lambda}^{\rm NLA-\beta} &= \{\, b_{\rm g}\,, {\rm IC}\,\}_i + \{\, A_\beta\,, \beta\,\}_{\rm R,B} \quad ,\end{aligned} \tag{3.21}$$

where we fit a galaxy bias and 'integral constraint' (IC) to the galaxy clustering measured in each sample i. The integral constraint is a free parameter, taking the form of a small additive scalar applied to the clustering correlation function, to correct for the effects of a partial-sky survey window (Roche & Eales 1999). Subscripts R, B denote a red and blue version of each parameter, which are fit to all relevant samples. This brings the total number of parameters to 14 (16) for the NLA (NLA-β)[10]. Previous dedicated IA studies have used galaxy clustering to fit and fix galaxy bias (e.g. Joachimi et al. 2011) – we instead opt to marginalise over galaxy biases and integral constraints, thereby propagating our uncertainty in these parameters into our IA model constraints. Since our samples form independent datasets, by virtue of colour separation and disjoint areas, we can reduce the dimensionality of the problem by fitting our models to red and blue samples separately.

We choose not to include a redshift power-law scaling $\eta_{\rm other}$ in our models, as has been done in previous works (Hirata et al. 2007, Joachimi et al. 2011, Mandelbaum et al. 2011), since the redshift baseline of our measurements is short – GAMA starts to become sparse after $z \sim 0.4$. While the results of previous work do not preclude the possibility of a significant redshift evolution, we argue that there is good reason to expect it to be small. Tidal torque theories suggest angular momentum generation as the source of spiral galaxy alignments. Since the spinning-up of a proto-galaxy halo is a perturbative effect, these alignments exist in the initial conditions of the matter field. After collapse of the overdense region, the angular momentum of the galaxy dominates over tidal torquing effects, and the galaxy orientation should be 'frozen-in'. Subsequently, only merger events should change the orientation of the galaxy.

Mergers would be expected to erase the memory of previous alignments, disrupt galaxy and halo angular momenta and prompt a relaxation phase. The system should relax into a configuration with a reduced spin magnitude, diluting

[10] 6 colour and redshift samples i gives 12 clustering parameters (galaxy biases and integral constraints), plus a red and a blue amplitude for 14 in total. Another 2 luminosity scaling parameters makes 16.

the quadratic alignment signature (Cervantes-Sodi et al. 2010). However, with merger timescales much shorter than relaxation, the spiral quickly transitions to a pressure-supported elliptical. The stellar distribution will then gradually re-equilibrate according to the ellipsoidal halo potential, itself moulded by the tidal field.

Therefore we might expect to observe 'fixed' blue galaxy alignments, opposite red galaxy alignments with their evolution tied to the tidal field (and divided out of our models by the growth factor), or some diluted middling alignment for transitioning galaxies, where the change of sign takes the amplitude close to zero. Joachimi et al. (2011) constrain $\eta_{\rm other}$ to be consistent with zero for early-type galaxies over a long redshift baseline. Mandelbaum et al. (2011) analysed late-type galaxy alignments in the WiggleZ survey (Drinkwater et al. 2010), with SDSS shapes, and also found $\eta_{\rm other}$ to be consistent with zero. Furthermore, their null detection at a mean redshift $\bar{z} \sim 0.6$ was recently matched by a null detection from the FastSound galaxy redshift survey (Tonegawa et al. 2015) at $z \sim 1.4$ (Tonegawa et al. 2018), suggesting no strong evolution of spiral galaxy alignments. Considering all of the above, we suggest that a physically motivated prior on $\eta_{\rm other}$ should be narrow and centred on zero.

3.4 IA constraints for flux-limited samples

With our aim to motivate tighter, more realistic priors for intrinsic alignment parameters, we fit the standard and the luminosity-dependent N/LA models to galaxy position-intrinsic shear and clustering correlations in KiDS+GAMA and SDSS Main. We compute signal detection significances across all scales, and restrict fits of the models to transverse scales $> 6\,h^{-1}$Mpc. Our various measurements are shown in Figures 3.2, 3.3, 3.4. The results of fitting are shown in Figures 3.5 & 3.6 and Table 3.2.

3.4.1 Clustering

Relating the matter-intrinsic power spectrum $P_{\delta \rm I}$ to $w_{\rm g+}$ requires estimations of the galaxy bias $b_{\rm g}$ of our density tracers. Hence we measure galaxy clustering in our density samples and perform fits of a linear, scale-independent bias with the full matter power spectrum (Eq. 3.19). We verify that our clustering pipeline reproduces the GAMA measurements of Farrow et al. (2015) for their sample selection.

Table 3.2: NLA model parameter and galaxy bias 1D marginalised constraints for our samples, with 68% confidence intervals and the reduced χ^2 ($\chi^2_\nu = \chi^2$ per degree of freedom) statistics for the global fit. A_β denotes the alignment amplitude parameter of the NLA-β model (Eq. 3.17). The mean galaxy biases shift slightly with the NLA-β – these changes are insignificant within statistical errors on these parameters, and are not shown in the table. Bracketed numbers indicate properties of density samples, as opposed to shapes samples. 'G' and 'S' denote GAMA and SDSS samples, respectively.

Sample	$\langle z \rangle$	$\langle L/L_{\rm piv} \rangle$	$b_{\rm g}$	$A_{\rm IA}$	χ^2_ν	$p(>\chi^2)$	A_β	β	χ^2_ν	$p(>\chi^2)$
GAMA full	0.23 (0.24)	0.51 (0.70)	$1.57^{+0.08}_{-0.09}$	$1.06^{+0.47}_{-0.46}$	1.32	0.21	$0.87^{+4.00}_{-1.43}$	$2.06^{+2.20}_{-2.82}$	1.12	0.34
SDSS Main full	0.11 (0.11)	0.22 (0.22)	$0.94^{+0.10}_{-0.11}$							
G: $z > 0.26$, blue	0.33 (0.33)	1.06 (1.09)	$1.10^{+0.07}_{-0.07}$	$0.21^{+0.37}_{-0.36}$	1.37	0.14	$0.65^{+0.50}_{-0.51}$	$2.47^{+1.68}_{-1.59}$	1.34	0.17
G: $z < 0.26$, blue	0.15 (0.17)	0.21 (0.36)	$1.55^{+0.09}_{-0.08}$							
S: blue	0.09 (0.09)	0.14 (0.14)	$0.88^{+0.12}_{-0.14}$							
G: $z > 0.26$, red	0.33 (0.33)	1.47 (1.48)	$1.52^{+0.11}_{-0.11}$	$3.18^{+0.46}_{-0.45}$	1.28	0.20	$3.40^{+0.59}_{-0.56}$	$0.18^{+0.20}_{-0.22}$	1.34	0.17
G: $z < 0.26$, red	0.17 (0.18)	0.50 (0.56)	$1.84^{+0.12}_{-0.12}$							
S: red	0.12 (0.12)	0.29 (0.29)	$1.19^{+0.11}_{-0.11}$							

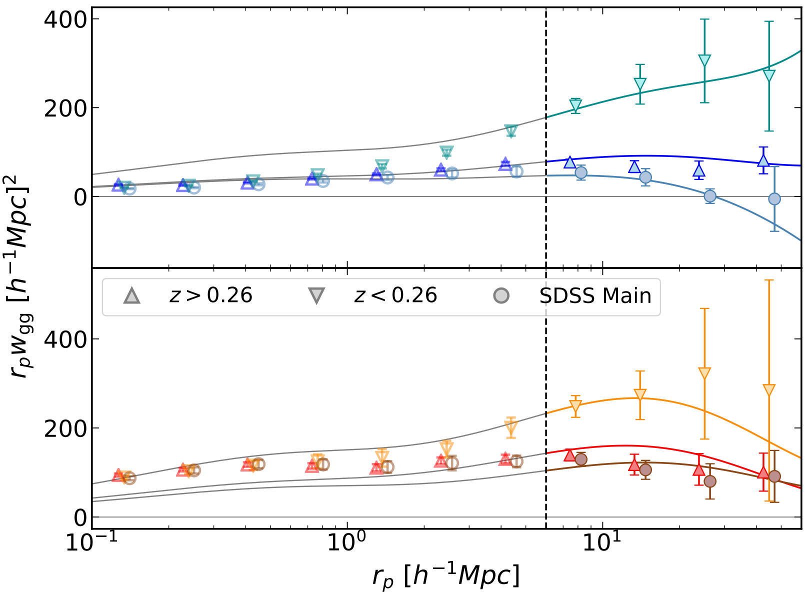

Figure 3.2: Measured galaxy clustering for our blue (*top*) and red (*bottom*) galaxy samples. Solid curves illustrate the best-fit linear clustering per sample (Eq. 3.19). The vertical dashed line indicates $r_p = 6\,h^{-1}$Mpc, below which scales are excluded from fitting (Section 3.3.3).

Figure 3.2 shows our measurements of $w_{\rm gg}$ in GAMA and SDSS, with best-fit linear clustering overlaid. Our fits include the integral constraint correction (Section 3.3.3), which is small ($|\mathrm{IC}| \lesssim 3\,h^{-1}$Mpc) and therefore negligible on small scales. Fits of the linear clustering model are restricted to scales $> 6\,h^{-1}$Mpc, indicated by vertical dashed lines. Our sample galaxy bias fits are summarised in Table 3.2. The biases form a consistent and expected picture – more luminous samples are more biased at the same redshifts.

3.4.2 Alignments

Figure 3.3 shows our colour-split measurements of $w_{\rm g+}$, overlaid with the best-fitting NLA (solid lines). We also perform fits to our data with the LA model, shown as dot-dashed lines in Figure 3.3 (to SR only) and Figure 3.4. Table

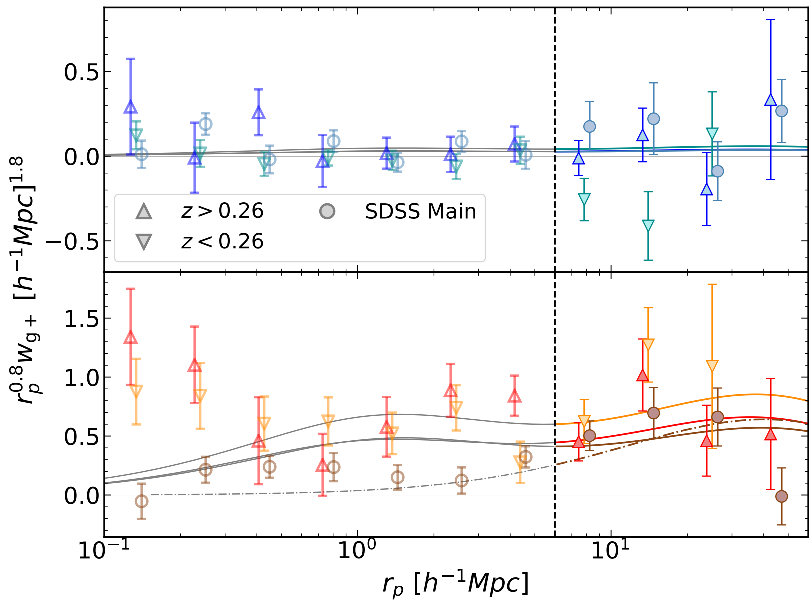

Figure 3.3: Measured galaxy position-intrinsic shear correlations for our blue (*top*) and red (*bottom*) galaxy samples. Best-fit NLA models are shown as solid curves, and the vertical dashed line indicates $r_p = 6\,h^{-1}$Mpc, below which scales are excluded from fitting (Section 3.3.3). The best-fit LA model to SR is shown as a dot-dashed line.

3.3 lists signal detection significances for the alignment signals and systematics tests (described in Section 3.2.3).

Signals & NLA results

We find blue galaxy alignments to be consistent with zero, in agreement with previous studies of this population (Mandelbaum et al. 2011, Tonegawa et al. 2018). The NLA-β amplitude A_β and power-law β are also consistent with zero, at 95% confidence. For blue galaxies on the whole, or for individual blue samples, we make no significant detections of w_{g+}, whether restricting to linear scales, or considering the full range in r_p (Table 3.3). Fits to GAMA-only: $A_{IA} = 0.04^{+0.44}_{-0.42}$, and SDSS-only: $A_{IA} = 1.03^{+0.90}_{-0.85}$, are consistent with each

Table 3.3: Reduced χ^2 statistics to assess the significance of signal detections against the null hypothesis (i.e. a zero-signal), for w_{g+} and for systematics tests; $w_{g\times}$ and w_{g+} limited to large line-of-sight separations ($60 \leqslant |\Pi| \leqslant 90\,h^{-1}$Mpc), denoted $\Pi+$. Bracketed numbers indicate the statistics when restricting to the r_p-scales $> 6\,h^{-1}$Mpc which are fitted in the analysis.

Sample	Signal	$\chi^2_{\nu,\mathrm{null}}$	$p(>\chi^2)$	σ
Blue total	w_{g+}	0.85 (1.24)	0.71 (0.25)	0.37 (1.14)
GAMA,	w_{g+}	0.31 (0.38)	0.98 (0.82)	0.02 (0.22)
$z > 0.26$,	$w_{g+}(\Pi+)$	0.20 (0.00)	0.98 (1.00)	0.03 (0.00)
blue	$w_{g\times}$	0.93 (1.66)	0.51 (0.16)	0.66 (1.42)
GAMA,	w_{g+}	0.85 (2.55)	0.58 (0.05)	0.56 (1.93)
$z < 0.26$,	$w_{g+}(\Pi+)$	0.41 (1.27)	0.87 (0.28)	0.16 (1.08)
blue	$w_{g\times}$	0.44 (0.22)	0.94 (0.93)	0.08 (0.09)
SDSS Main,	w_{g+}	1.38 (1.12)	0.17 (0.34)	1.36 (0.95)
blue	$w_{g+}(\Pi+)$	0.44 (0.78)	0.85 (0.46)	0.19 (0.74)
	$w_{g\times}$	1.14 (1.30)	0.33 (0.27)	0.98 (1.11)
Red total	w_{g+}	5.03 (6.86)	0.00 (0.00)	8.93 (6.79)
GAMA,	w_{g+}	4.03 (4.37)	0.00 (0.00)	4.51 (3.17)
$z > 0.26$,	$w_{g+}(\Pi+)$	0.74 (2.97)	0.62 (0.05)	0.50 (1.95)
red	$w_{g\times}$	0.31 (0.42)	0.98 (0.79)	0.02 (0.26)
GAMA,	w_{g+}	6.27 (8.85)	0.00 (0.00)	6.09 (4.48)
$z < 0.26$,	$w_{g+}(\Pi+)$	0.32 (0.30)	0.93 (0.74)	0.09 (0.33)
red	$w_{g\times}$	0.75 (1.20)	0.69 (0.31)	0.40 (1.02)
SDSS Main,	w_{g+}	4.90 (7.86)	0.00 (0.00)	5.29 (4.71)
red	$w_{g+}(\Pi+)$	0.84 (0.87)	0.54 (0.42)	0.61 (0.81)
	$w_{g\times}$	0.28 (0.20)	0.99 (0.94)	0.01 (0.08)

other, and the total-fit, at 68% confidence.

In agreement with previous work (Hirata et al. 2007, Joachimi et al. 2011), we measure a significantly positive amplitude of alignments for red galaxies, in both modes of fitting and at $> 95\%$ confidence. The total significance of detection we find for red galaxy alignments is close to 9σ over the full range in r_p, and 6.79σ when limited to linear scales ($\geqslant 6\,h^{-1}$Mpc). The β luminosity-scaling is found to be comfortably consistent with zero, and thus results in a poorer fit (owing to a lost degree of freedom) than for the 1-parameter NLA. This is in contrast with previous observations of near-linear scalings of red galaxy/LRG alignments with luminosity (e.g. Hirata et al. 2007, Joachimi et al. 2011, Singh et al. 2015). The perturbative IA model of Blazek, Vlah, & Seljak (2015) uncovered additional contributions to the observed large-scale intrinsic shape correlation, arising from source density weighting (Hirata & Seljak 2004) – as galaxies preferentially exist in overdense space, our sampling of the intrinsic ellipticity field is necessarily biased, as briefly discussed in Section 3.3.3. This contribution was found to be galaxy bias-dependent, and mooted as responsible for such observed luminosity-scalings – indeed we measure SDSS red to have the weakest alignment signature (see Section 3.4.2) of our red samples, although the significance of this is questionable. A GAMA-only fit results in a slightly higher red galaxy alignment amplitude of $A_{\rm IA} = 3.52^{+0.60}_{-0.56}$, whilst SDSS-only returns $A_{\rm IA} = 2.50^{+0.77}_{-0.73}$, again comfortably consistent with each other and the total fit.

For the 'full' (all-galaxy) samples, we measure a positive NLA amplitude at just over 95% confidence, whilst the NLA-β is poorly constrained, owing to a sparse luminosity baseline. A point of interest is the apparently larger amplitude of $w_{\rm g+}$ measured for SDSS, compared with GAMA, for which the N/LA models are unable to account – the green and purple curves in Figure 3.4 differ only by their dependence on the (subdominant) weight function $\mathcal{W}(z)$ and the fitted galaxy bias per sample. Individual fits to these samples yield $A_{\rm IA} = 0.26^{+0.63}_{-0.62}$, and $A_{\rm IA} = 2.01^{+0.79}_{-0.71}$, for GAMA and SDSS, respectively – mildly discrepant at $\sim 1.8\sigma$. GAMA is brighter, and constrained to be more biased, than SDSS, seemingly ruling-out luminosity/bias-dependences as explanations. It must, however, be noted that these all-galaxy signals constitute muddy combinations of clearly dichotomous alignment signatures, and that GAMA and SDSS sample different environments – something we explore in the next section.

A primary motive for this work was to take advantage of highly complete, flux-limited data in order to constrain IA as it pertains to cosmic shear contamination. The only comparable analyses to date are the SDSS Main studies of Mandelbaum et al. (2006b) – M06, and Hirata et al. (2007)[11] – H07, each of which was conducted slightly differently to this work. For example, neither study made use of the N/LA models as they are typically formulated today, allowing for no easy comparison of fitted alignment amplitudes $A_{\rm IA}$. In any case, our sample selections are also quite different – both M06 & H07 made use of the long luminosity baseline in SDSS to create subsamples, and whilst H07 also split their samples into red/blue galaxies, their cut was performed using observer-frame magnitudes. Nevertheless, we make some broadly similar find-

[11] Hirata et al. (2007) also studied LRGs - we only discuss their work on the flux-limited SDSS Main sample.

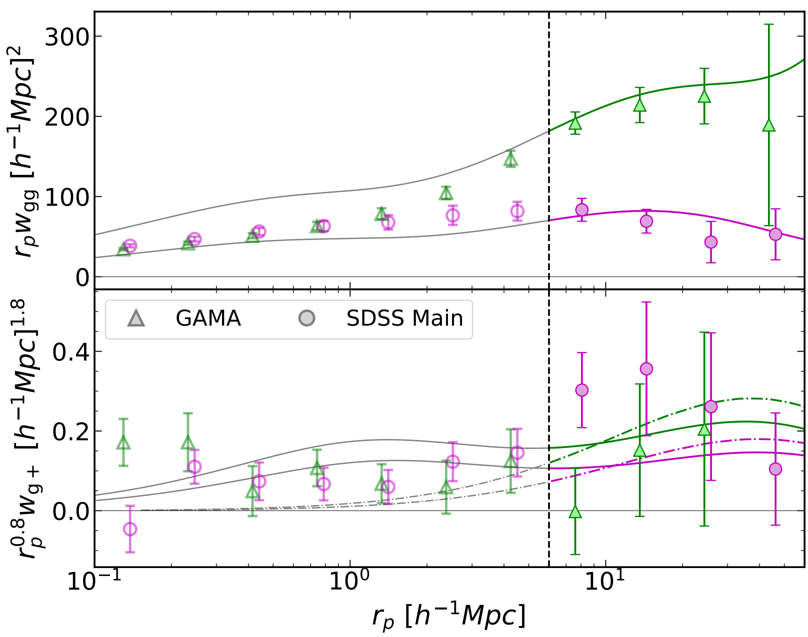

Figure 3.4: Galaxy clustering (*top*) and position-intrinsic shear correlations (*bottom*) measured in the full KiDS+GAMA and SDSS Main datasets. Solid lines illustrate the best-fit NLA model, and dot-dashed lines the LA. The vertical dashed line indicates $r_p = 6\,h^{-1}$Mpc, below which scales are excluded from fitting (Section 3.3.3).

ings; H07 made robust detections of IA in red galaxies, as did M06 for their brightest sample, itself dominated by red galaxies. Additionally, H07 also failed to make a significant detection for blue galaxies.

We do however seem to find some indirect disagreement in the alignment amplitude vs. sample luminosity trend inferred from the data. Each of M06 & H07 saw trends of increasing signal amplitudes with sample luminosity, whilst we find no evidence for luminosity evolution in our model fits. Furthermore, the far brighter Z2R sample exhibits an amplitude of alignment entirely consistent with the Z1R fit, and as mentioned above, we measure a larger amplitude of alignment for the fainter (uncut) SDSS sample than for GAMA. We explore these individual fits, and how they correlate with sample properties, in the next

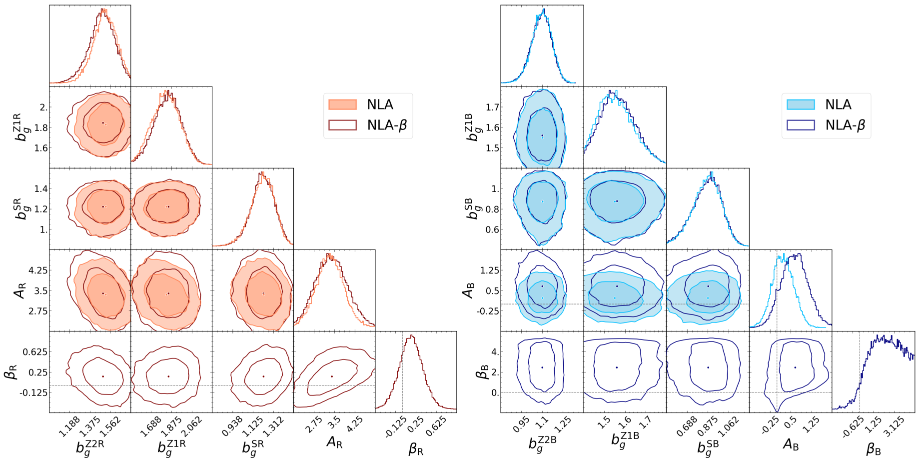

Figure 3.5: Posterior probability contours of our fitted galaxy bias $b_{\rm g}$, NLA amplitude A and luminosity power-law β parameters, for red (*left*) and blue (*right*) galaxies. The filled (unfilled) contours are for the NLA (NLA-β) models. Dashed grey lines mark values of zero for IA parameters.

Section.

Individual sample fits

We make additional, individual fits of $A_{\rm IA}$ to each of our galaxy samples, to gain further insight into trends with colour, luminosity and redshift. Figure 3.6 illustrates the results of fitting individual amplitudes to (i, squares in top left panel) red and blue signals, (ii, filled points in right panels) signals from each of our colour/redshift-split samples in GAMA and SDSS, (iii, unfilled triangles/circles) individual signals from uncut GAMA and SDSS, (iv, pentagon in top left panel) all signals from the uncut samples, and (v, stars in right panels) signals from GAMA galaxies with stellar-mass $M_* \geqslant 10^{11} M_\odot$. Only the filled data points are independent of each other, as the unfilled points are each fitted to some collection/subset of the independent samples – Table 3.6 details the constraints from each sample, with independent samples denoted by †.

In each panel of the figure, there is a clear dichotomy in the fitted amplitudes for red and blue galaxies, highlighted in the right-hand panels by dashed lines and shading. The top right panel shows $A_{\rm IA}$ vs. sample luminosity, and reveals a

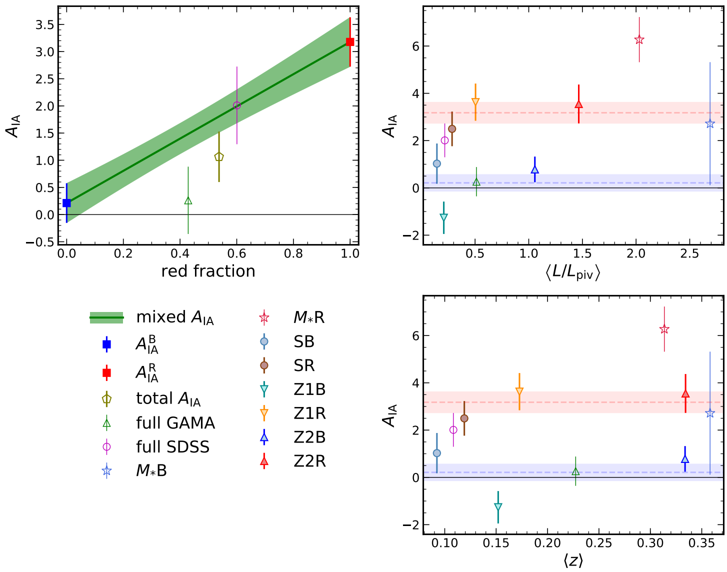

Figure 3.6: Constraints on the NLA model alignment amplitude $A_{\rm IA}$, from various subsamples of GAMA and SDSS (Table 3.1), plotted against sample properties. The constraints illustrated here are also given in Table 3.6. *Top left:* $A_{\rm IA}$ vs. shape sample red galaxy fraction. We interpolate (green line/shading) between our fits to blue (blue square) and red (red square) galaxy samples, according to $A_{\rm IA} = A_{\rm IA}^{\rm R} f_{\rm red} + A_{\rm IA}^{\rm B}(1 - f_{\rm red})$, where $f_{\rm red}$ is the red fraction and we assume linearity in the contributions of galaxy populations to the total alignment signal/amplitude. The inconsistency of mixed-sample signals (open points) with this interpolation is due to variable contributions of satellite galaxies – this is discussed in Section 3.4.2. *Top right:* $A_{\rm IA}$ vs. shape sample luminosity (as a ratio to the pivot $L_{\rm piv} \sim 4.6 \times 10^{10} L_{\odot}$, corresponding to absolute r-band magnitude $M_r = -22$). *Bottom right:* $A_{\rm IA}$ vs. shape sample mean redshift. All plotted data points illustrate the mean and 68% confidence interval of 1D marginalised posterior distributions on $A_{\rm IA}$, after fitting to relevant alignment/clustering signals. Only the filled points are independent of each other; each of the open points is in some way correlated with the others. Dashed lines and shading indicate the mean and 68% CI of the total-colour fits, highlighting the type-dependence of alignments.

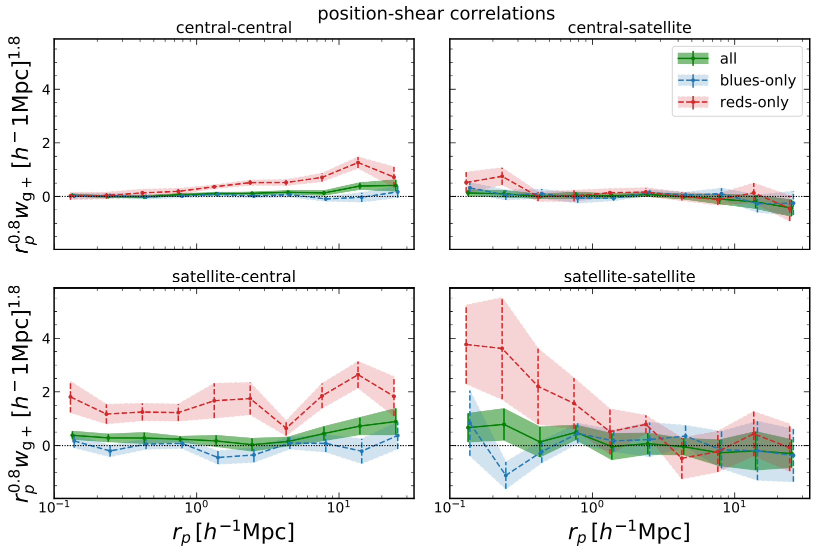

Figure 3.7: Various position-intrinsic shear correlations measured between GAMA samples of exclusively central or satellite galaxies, with errors estimated via jackknife. The title of each panel indicates the central/satellite composition of the position-shear (i.e. density-shape) samples, and we measure correlations in the mixed samples, and for red- (red dashed) and blue-only (blue dashed) subsets.

vaguely positive correlation in the filled data points, but at very low significance, especially if one (i) considers blue and red separately, and (ii) notes that the Z1B fitted amplitude is anomalously low with respect to the other blue sample amplitudes[12].

[12]We note that the Z1B amplitude is consistent with zero at 95% confidence, and that this signal (downward cyan triangles in the top panel of Fig. 3.3) is not found to be a particularly significant detection, at $< 2\sigma$ (Table 3.3). Additionally, the signal becomes comfortably consistent with zero upon removal of the faint-limit we apply to our GAMA density samples (explained in Appendix 3.A.2), which affects the Z1B sample far more significantly than each of the others combined. This could be interpreted as follows; the Z1B sample shows a net tangential alignment at $\sim 1.7\sigma$, but *only* when excluding the faintest ($\sim 27\%$ here) galaxies from the density sample. However, the faint-limit is part of our clustering covariance estimation (see Appendix 3.A.2) – removing it may invalidate the clustering fits which anchor the galaxy bias, so this interpretation must be taken with moderation. A linear-scale tangential

The bottom right panel shows $A_{\rm IA}$ vs. sample mean-redshifts, with any correlation even less pronounced. To date, no direct IA analyses have found evidence for redshift evolution of intrinsic alignments (Joachimi et al. 2011, Mandelbaum et al. 2011, Tonegawa et al. 2018), and our results seem to agree – although it should be noted that our baseline is short, and limited to the relatively near universe. Some works have reported evidence for scaling of IA with sample luminosity (Hirata et al. 2007, Joachimi et al. 2011, Singh et al. 2015), findings unsupported by our measurements – we do make a clean detection for massive, red GAMA galaxies (red stars), at 9.1σ and with a large fitted amplitude of alignment, but these galaxies are effectively a subset of (primarily) the Z2R sample. Thus the large-M_* points are highly correlated with their high-redshift counterparts; these points (upward triangles) disagree with the notion of luminosity dependence. As discussed above, it may be that such an observed dependence is due to environmental properties which correlate with luminosity. Our data points might weakly support this assertion for red galaxies, given that we constrain SDSS red to be less biased than the red GAMA samples (see Table 3.2), however the significance is extremely low; more work is needed for a concrete answer to this question.

In the top left panel, we interpolate between the fitted red and blue alignment amplitudes according to

$$A_{\rm IA} = A_{\rm IA}^{\rm R} f_{\rm red} + A_{\rm IA}^{\rm B}(1 - f_{\rm red}) \tag{3.22}$$

where $f_{\rm red} \in [\,0\,,1\,]$ is the sample red fraction, and we assume that the red and blue galaxy populations contribute linearly to the measurable alignment of the full sample. Thus we provide predictions[13] for the $A_{\rm IA}$ one might measure in a flux-limited sample of mixed galaxy-type, given the red galaxy fraction, and *provided* that the red/blue dichotomy is the dominant driver of the alignment profile.

Shown also in the top-left panel are the two $A_{\rm IA}$ fitted to the total GAMA (green triangle) and total SDSS (pink circle) signals (shown in the bottom panel of Figure 3.4), and the single amplitude fitted to both signals (gold pentagon). One clearly sees that GAMA galaxies are less radially aligned than is predicted

alignment of blue galaxies, dependent on the bias of the density tracer, is an interesting result which would call for further work. However, it should be noted that (i) tidal torquing mechanisms ought to be weak on these scales, so this signal is not expected, (ii) the significance of the negative amplitude is low, and (iii) the signal itself lacks a clear detection.

[13]Inserting our IA model constraints from Tables 3.2 or 3.7 into the functional form of Eq. 3.22, one can derive an expected confidence interval on $A_{\rm IA}$, for the NLA or LA, given a sample red-fraction.

by the interpolation. We find this discrepancy to be driven by a significant fraction of satellite galaxies in GAMA, with differing alignment behaviour – previous work has found satellite galaxy alignments to be weaker than those of central galaxies, or altogether non-existent (Sifón et al. 2015, Singh et al. 2015, Huang et al. 2018), in particular when considering larger pair-separations as we do when fitting our models.

Figure 3.7 breaks down the central[14] and satellite, red and blue contributions to the total GAMA alignment signature. The low amplitude fitted to GAMA is simply understood in this context – the left-hand panels demonstrate linear-scale ($\gtrsim$ a few h^{-1}Mpc) alignments to be sourced entirely by red central galaxy *shapes*. All other galaxy shapes – red satellites, blue centrals and blue satellites – are unaligned on these scales (seen in all panels), and thus dampen the overall alignment signature with zero-mean white noise. Thus the linear-scale alignment correlation can be thought of as 'set' by the red central galaxies, and then repeatedly damped upon the inclusion of other species; blue galaxies have zero-signal, and so force an effective rescaling of $w_{\mathrm{g}+}$ by a factor $\sim f_{\mathrm{red}}$; red satellites do source a strong signal (bottom-left panel) through the inclusion of their positions (which are highly correlated with centrals on these scales), but this is slashed by their own lack of alignment (right-panels), making the overall dampening a more complicated function of red central/satellite fractions.

Being ~ 2 magnitudes shallower than GAMA, and at less than a tenth of the on-sky density, SDSS is comparatively deficient in fainter satellite galaxies at low redshift (see right-panel of Figure 3.1). Thus the linear-scale alignment dampening described above is more severe for GAMA than for SDSS, explaining the behaviour seen in Figures 3.4 & 3.6. Indeed, we find an alignment amplitude fit to the mixed central galaxy signal in GAMA (Figure 3.7, top-left panel, green curve) to sit comfortably atop the interpolation of Figure 3.6, with an almost unchanged red fraction.

Inspecting the signals themselves, we note first that blue galaxies exhibit null signals under every division of the data. We also see that red central galaxies align radially with each other at large-r_p (top-left), and with satellites at small-r_p (bottom-left) – we re-measure this signal with $|\Pi_{\mathrm{max}}| = 12\,h^{-1}$Mpc to confirm that these centrals are aligning with *their own* satellite distribution. In comparison, red satellites align strongly, but more noisily, with each other on smaller scales (bottom-right), and are elsewise unaligned. With these measurements we can make the following statements about red galaxies: satellite

[14] We count field galaxies as centrals, assuming that their satellites are simply too faint to be detected.

galaxies exist preferentially along the semi-major axis direction of the central galaxy, and the satellite galaxies are, on average, aligned with this direction. These are interesting considerations for future work, given that the satellite distribution is thought to trace that of the underlying dark matter.

Satellite considerations thus explain the discordance between the blue-to-red amplitude interpolation in Figure 3.6 and the amplitudes fitted to GAMA signals, and call for additional work; a motivated prior for the amplitude of intrinsic alignments in a cosmic shear study may need to consider not only the red fraction of the galaxy sample, but also the satellite fraction. Such population fractions will correlate with each other to an extent, with redshift as the universal galaxy population evolves, and with spatially variable limiting magnitudes for any given survey. To complicate matters further, Georgiou et al. (2019b) find these influential red satellite galaxies to drive variation in measurable alignment signatures as a function of the passband of observation; cosmic shear studies in different bands can expect different contributions of alignments to shear signals. Thus predicting the IA contamination of shear in a galaxy survey is highly non-trivial.

LA results

Linear alignment model fits to the data (fully detailed in Table 3.7) result in consistency with analogous parameters from the NLA/NLA-β at 68% in all cases. The slightly larger amplitudes seen for red galaxies reflect the smaller amplitude of fluctuations in the linear matter power spectrum (see Section 3.3.1). This can be seen most clearly in the bottom panel of Figure 3.3, where the LA fit to SR (brown dot-dashed line) happens to closely match the NLA-Z1R fit (orange solid line) in amplitude. The linear model shows a clear deficit in power at scales $\lesssim 20\,h^{-1}$Mpc, relative to the NLA. Consistency between the blue LA and NLA models is even stronger, as expected for null-signals.

The χ^2 statistics in Tables 3.2 & 3.7 purport the LA model to describe these data almost as well as the NLA on scales $\geqslant 6\,h^{-1}$Mpc, though it is clear from the N/LA illustrations in Figures 3.3 & 3.4 that (i) neither model is sufficient to capture the complex variation of alignments as a function of galaxy sample properties and (ii) only the red GAMA signals would seem to explicitly prefer the enhancement offered by the NLA on scales of a few h^{-1}Mpc. The inclusion of blue galaxies efficiently washes out the $w_{\rm g+}$ signal on those scales (green points in Figure 3.4), such that something in-between the N/LA models would appear closer to the truth. This result reaffirms the need for more complex modelling of IA in cosmic shear, highlighting the non-trivial contributions of various (i.e.

Table 3.4: Gaussian priors on cosmological and IA/photo-z nuisance parameters adopted for our Fisher forecasts. Centres are those of the fiducial cosmology, which includes the maximum likelihood points (not the 1D marginals) of our IA analysis. The 'Informative' set of priors for photo-z bias parameters are approximations of constraints on equivalent parameters from the KiDS joint-probe analysis by van Uitert et al. (2018), with an extension for a fifth redshift bin.

Parameter	centre	width
h	0.7	0.15
n_s	0.95	0.01
A_{β}^{B}	0.58	20
β_{B}	3.15	5
Modest:		
a_{z_1}	0	0.05
a_{z_2}	0	0.055
a_{z_3}	0	0.06
a_{z_4}	0	0.065
a_{z_5}	0	0.07
Informative:		
a_{z_1}	0	0.036
a_{z_2}	0	0.042
a_{z_3}	0	0.048
a_{z_4}	0	0.054
a_{z_5}	0	0.062

colour, environment) sub-samples to overall alignment signatures.

3.4.3 Systematics tests

Table 3.3 lists the detection significances of our measured signals – $w_{\mathrm{g+}}$, $w_{\mathrm{g+}}\{60 < |\Pi| < 90\,h^{-1}\mathrm{Mpc}\}$ and $w_{\mathrm{g\times}}$ – across all r_p-scales, and when limited to the scales of fitting ($> 6\,h^{-1}$Mpc; bracketed numbers). We make no significant ($> 2\sigma$) detections of any systematic signals (see Section 3.2.3) in our samples.

3.5 Impact on cosmology

Here we forecast the impact of our informative IA priors upon a colour-split cosmic shear analysis over a completed KiDS survey. We assume that the alignments in the data are perfectly described by the N/LA models – something we will investigate in future work. This assumption is questionable for the NLA, but given its widespread use in current surveys, and since we are not concerned with biasing of parameters here, but rather the pure impact of priors, we continue as such. The model survey is described by an area of $1,350\,\mathrm{deg}^2$ with a total galaxy number density of 9 arcmin^{-2} (Hildebrandt et al. 2017), and a total shape dispersion of 0.41. We model the $n(z)$, over $z \in [\,0.1\,,1.2\,]$, according to (Smail et al. 1995)

$$n_{\mathrm{total}}(z) \propto z^{\alpha} \exp\left\{ -\left(\frac{z}{z_0}\right)^{\gamma} \right\} \quad , \tag{3.23}$$

where $\alpha = 2$, $\gamma = 1.5$ and $z_0 = 0.375$. We define 5 tomographic bins in redshift, with edges (KiDS+VIKING-450; Hildebrandt et al. 2018): $[\,0.1\,,0.3\,,0.5\,,0.7\,,0.9\,,1.2\,]$, each scattered about the bin centre with $\sigma_z = 0.05(1+z)$ and with no catastrophic outliers. Using KV450 galaxies, we estimate $\langle L/L_{\mathrm{piv}}\rangle$ for each colour/redshift bin, with the unchanged pivot $L_{\mathrm{piv}} \sim 4.6\times 10^{10} L_{\odot}$. We also assume the KV450 red galaxy fraction per redshift bin for our toy survey; approx. $[\,0.13\,,0.23\,,0.27\,,0.26\,,0.26\,]$ (Wright et al. 2018). Splitting the model survey by colour more than doubles the available information when computing auto- and cross-correlations – our data vector $\vec{d}$ consists of shear angular power spectra $C(\ell)$ with intrinsic contributions (Eqs. 3.10-3.13), for all colour/redshift bin combinations, in 10 logarithmic bins $\ell \in [\,50\,,2000\,]$

$$\begin{aligned} \vec{d} = \{\, & C_{i_\mathrm{B} j_\mathrm{B}}(\ell) \quad \forall \quad i\,,j \in [1\,,5] \cap i \leqslant j \quad , \\ & C_{i_\mathrm{B} j_\mathrm{R}}(\ell) \quad \forall \quad i\,,j \in [1\,,5] \quad , \\ & C_{i_\mathrm{R} j_\mathrm{R}}(\ell) \quad \forall \quad i\,,j \in [1\,,5] \cap i \leqslant j \,\} \quad , \end{aligned} \tag{3.24}$$

for a total of 550 data points. We compute a full analytical covariance matrix (see Hildebrandt et al. 2017, Section 5), with non-Gaussian and super-sample contributions, for computation of the Fisher information (see Tegmark, Taylor, & Heavens 1997, and references therein). Our cosmological parameter vector is

$$\vec{\lambda}^{\mathrm{Fisher}} = \{\, \Omega_m\,, \Omega_b\,, h\,, \sigma_8\,, n_s\,, w_0 \,\} \quad , \tag{3.25}$$

and we fix $\Omega_k = 0$. We append the parameter vector with nuisance parameters for the NLA/NLA-β, and for characterising the impact of additive photometric redshift biases – modern shear surveys rely upon photo-z, and as such are prone to systematic bias in redshift distributions and resultant constraints. We parameterise the additive photo-z bias per colour/redshift bin, such that $n_{\rm x}(z) \rightarrow n_{\rm x}(z - a_{z_{\rm x}})$, where $n_{\rm x}(z)$ is the redshift distribution of bin $\rm x \in [\,1\,,5\,]_{R,B}$. Our nuisance parameters are then

$$\{A_{\rm IA}\,,\beta\,,a_{z_1}\,,a_{z_2}\,,a_{z_3}\,,a_{z_4}\,,a_{z_5}\,\}_{\rm R,B} \quad , \tag{3.26}$$

giving a total of 18 (20) parameters with NLA (NLA-β) alignments in the data. We take the MICE cosmology from our IA analysis as the fiducial cosmology about which Fisher derivatives are computed, and apply Gaussian priors as listed in Table 3.4. Adding a Gaussian prior to the Fisher information is necessary in the case of $A_\beta^{\rm B}$ and $\beta_{\rm B}$, as small-amplitude signals result in a total degeneracy between these parameters. We limit their variability – in the NLA-β forecast, only – in order to demonstrate a meaningful application of our derived IA priors. The results of our forecasts are shown in Figures 3.8 & 3.9, and condensed in Figure 3.10 to show the IA prior impacts on the $S_8 \equiv \sigma_8\sqrt{\Omega_{\rm m}/0.3}$ parameter, and dark energy equation of state w_0. We note that the Fisher approximation – the mean curvature of the likelihood function about the fiducial cosmology – is inexact in the case of non-Gaussian posterior probability distributions, such that the banana-like $\Omega_{\rm m} - \sigma_8$ degeneracy observed in cosmic shear analyses (Hildebrandt et al. 2017, Abbott et al. 2018) is not exactly captured. Thus our forecasts are demonstrative in purpose, and may differ from analogous full, simulated likelihood forecasts (e.g. Krause, Eifler, & Blazek 2016).

Figures 3.8 & 3.9 depict forecasted constraints for final KiDS-like colour-split cosmic shear, with NLA and NLA-β alignments in the modelled data, respectively. Clear improvements are seen in $\Omega_m\,,\sigma_8\,,w_0$ constraining power when applying our 68% confidence intervals as informative priors on the IA parameters (grey vs. cyan contours). This demonstrates the degrading influence of free-to-roam IA nuisance parameters in cosmic shear analyses – the application of our priors results in up to $\sim$ 50% reductions in the size of errorbars on S_8 and w_0 for the NLA forecast, and 20% for the LA whose weaker contribution levies smaller gains when constrained. The gains in constraints upon crucial parameters are illustrated in Figure 3.10 (circles vs. stars) and fully detailed in Table 3.5, for each of the photo-z bias prior setups detailed in Table 3.4. The 'Modest' case features a rough estimate for a monotonically increasing uncertainty in the real positions of tomographic bin-centres, and serves as a yard-stick

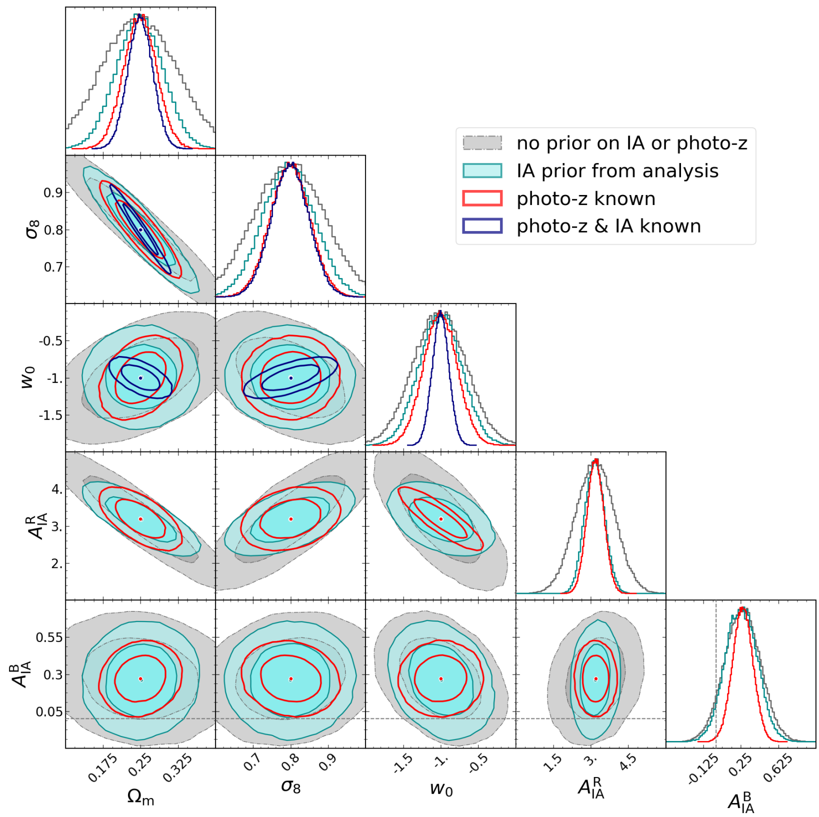

Figure 3.8: Fisher forecasted cosmological constraints for a KiDS-like survey, with (cyan) and without (grey) the application of our derived IA priors, assuming intrinsic alignments obey the non-linear alignment (NLA) model. Filled contours correspond to forecasts without any priors upon photo-z bias parameters (c.f. the 'Modest' and 'Informative' prior cases in Table 3.4). Forecasts with photo-z bias fixed to zero are represented by navy and red unfilled contours, where navy also assumes perfect knowledge of IA model parameters. Dashed grey lines mark values of zero for nuisance parameters.

between the case without any priors and the 'Informative' case, where we adapt the constraints of van Uitert et al. (2018) for use as priors.

Table 3.5: Forecasted improvements in constraining power for key cosmological parameters when employing IA model constraints as informative prior ranges on IA nuisance parameters. The variable parameters for each mode of an N/LA forecast are indicated by curly brackets {} in the left-most column. Improvements are given as the percentage reductions in the sizes of 1σ confidence intervals on respective parameters, for the no-prior, modest-prior and informative-prior photo-z bias prior setups (see Table 3.4), hence we only display a single reduction for the cases without any photo-z bias.

{Nuisance} Parameters	$\Omega_{\rm m}$	σ_8	$S_8 \equiv \sigma_8\sqrt{\Omega_{\rm m}/0.3}$	w_0
Linear alignments (LA)				
$\{A_{\rm IA}^{\rm R}, A_{\rm IA}^{\rm B}\}$, photo-$z$ known	2%	1%	1%	1%
$\{A_{\rm IA}^{\rm R}, A_{\rm IA}^{\rm B}, \beta_{\rm R}, \beta_{\rm B}\}$, photo-$z$ known	6%	2%	4%	7%
$\{A_{\rm IA}^{\rm R}, A_{\rm IA}^{\rm B}, a_{z_{1-5},{\rm R,B}}\}$	3%, 4%, 3%	2%, 1%, 1%	2%, 2%, 2%	2%, 1%, 1%
$\{A_{\rm IA}^{\rm R}, A_{\rm IA}^{\rm B}, \beta_{\rm R}, \beta_{\rm B}, a_{z_{1-5},{\rm R,B}}\}$	27%, 24%, 20%	22%, 17%, 14%	25%, 21%, 17%	17%, 22%, 20%
Non-linear alignments (NLA)				
$\{A_{\rm IA}^{\rm R}, A_{\rm IA}^{\rm B}\}$, photo-$z$ known	7%	1%	4%	14%
$\{A_{\rm IA}^{\rm R}, A_{\rm IA}^{\rm B}, \beta_{\rm R}, \beta_{\rm B}\}$, photo-$z$ known	2%	0%	1%	15%
$\{A_{\rm IA}^{\rm R}, A_{\rm IA}^{\rm B}, a_{z_{1-5},{\rm R,B}}\}$	38%, 28%, 25%	27%, 18%, 14%	36%, 25%, 21%	20%, 27%, 26%
$\{A_{\rm IA}^{\rm R}, A_{\rm IA}^{\rm B}, \beta_{\rm R}, \beta_{\rm B}, a_{z_{1-5},{\rm R,B}}\}$	64%, 38%, 32%	56%, 23%, 17%	62%, 36%, 27%	51%, 43%, 39%

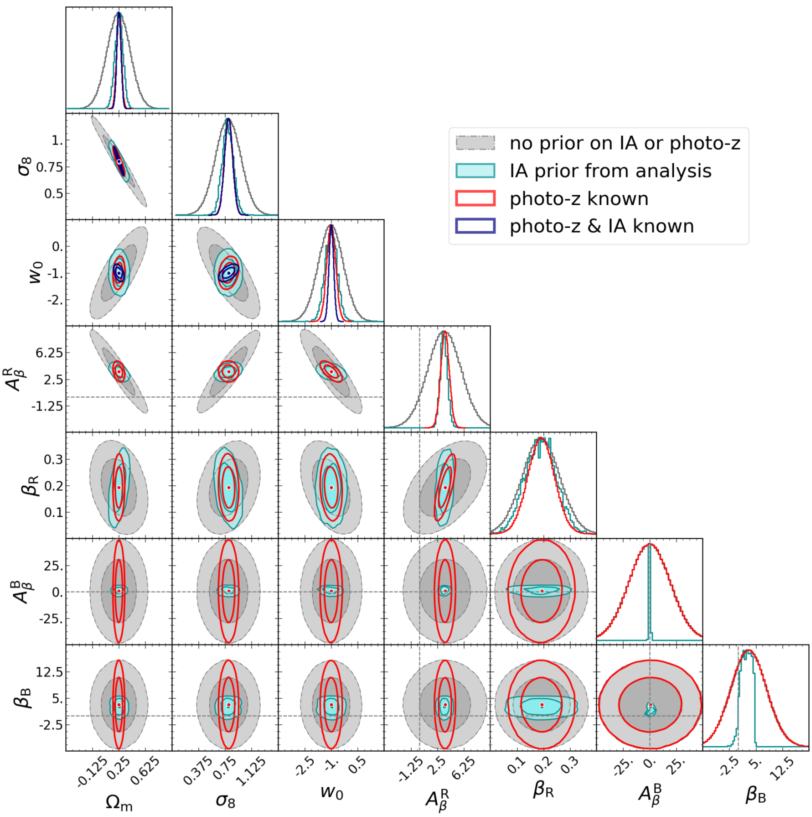

Figure 3.9: The same as Figure 3.8, but assuming luminosity-dependent non-linear alignments (NLA-β) in the data.

Figures 3.8, 3.9 & 3.10 also plot some idealised cases – assuming perfect knowledge of both intrinsic alignments and photometric redshift distributions we plot navy, unfilled contours in Figures 3.8 & 3.9, and cyan/grey diamonds in Figure 3.10. For perfect photo-z alone, we include red, unfilled contours (Figures 3.8 & 3.9) and mauve/red diamonds (Figure 3.10). In the latter case, our analysis priors are not applied, as they have a negligible effect upon the constraining power of the model survey – i.e. with perfect knowledge of source redshifts, such a survey could self-calibrate for intrinsic alignments beyond the

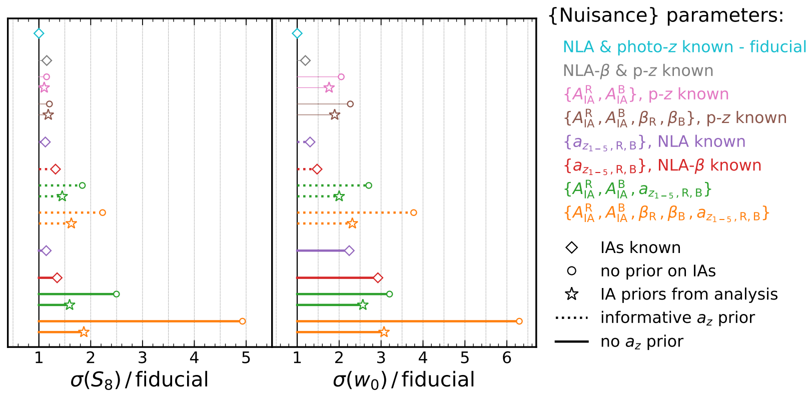

Figure 3.10: Comparison of marginalised 68% confidence intervals on $S_8 \equiv \sigma_8\sqrt{\Omega_{\rm m}/0.3}$ and w_0, forecasted for varied sets of nuisance parameters, with (stars) and without (circles) the application of our intrinsic alignment parameter priors. Diamonds illustrate cases with perfect knowledge of the alignments in the simulated data. The intervals are plotted as ratios to the fiducial case (cyan), where NLA parameters and photo-z distributions are perfectly known. Dotted lines denote cases with the 'Informative' photo-z bias priors (Table 3.4), and solid lines those without any prior. Nuisance (free) parameters are denoted for each case by curly brackets {} in the legend.

precision of our direct analysis. The difference between the red/blue unfilled contours in Figures 3.8 & 3.9 is then the potential gain in precision from even tighter IA model constraints, which is seen to be particularly large for the dark energy equation of state w_0.

The advantages of informative priors on intrinsic alignment model parameters are clearly demonstrated here, especially when considering that the current modes of modelling are too simple – our colour-split analysis is already more complex than most. Alignment models with additional freedoms must be used, in order to characterise the variable contributions of galaxies of different types and in different environments – e.g. the mixed alignment perturbative model of Blazek et al. (2017), recently applied to DES Y1 data (Troxel et al. 2017) and accompanied by losses in constraining power. The mitigation of such losses demands dedicated IA studies, producing reliable priors for model parameters.

3.6 Conclusions

We have measured the galaxy position-intrinsic shear and position-position correlations in the GAMA and SDSS Main galaxy samples, selecting subsamples by colour and redshift. We undertook a detailed consideration of reliable subsample covariance estimation, implementing a 3-dimensional jackknife routine for the relatively small-area GAMA samples. We jointly fit to our intrinsic alignment and clustering measurements with several models; the non-linear and linear alignment models (N/LA), and luminosity-dependent analogues (N/LA-β).

Our NLA fits yield constraints (quoted to 1σ) upon the intrinsic alignment amplitude $A_{\rm IA}$ for 3 cases; unselected, early-type and late-type galaxies, each representing a step forward in precision for constraints of their type from dedicated, spectroscopic studies of intrinsic alignments. Our findings agree with the literature, wherein red galaxies exhibit significant, positive (radial) alignments, and blue galaxy alignments are thus far undetectable. We also fit the LA model to our data, finding comfortable consistency with each of our results for the NLA. As noted in the text, this is largely due to our restriction to linear scales $> 6\,h^{-1}$Mpc where the N/LA difference is minimal.

Our red galaxy alignment constraint $A_{\rm IA} = 3.18^{+0.46}_{-0.45}$ appears to demonstrate that fainter, non-LRG galaxies are still privy to a radial alignment mechanism on large scales (up to $60\,h^{-1}$Mpc in this analysis), although not as strongly as LRGs (e.g. Joachimi et al. 2011, Singh et al. 2015). We are able to improve constraints upon the blue galaxy alignment amplitude to $A_{\rm IA} = 0.21^{+0.37}_{-0.36}$, consistent with the work of Mandelbaum et al. (2011), and still consistent with a null signal. This result, from scales $> 6\,h^{-1}$Mpc[15], supports the quadratic alignment picture of weak spiral galaxy alignments on linear scales. Fitting jointly to the $w_{\rm g+}$ (and $w_{\rm gg}$) signals measured in GAMA and SDSS, without any colour or redshift selections, yields $A_{\rm IA} = 1.06^{+0.47}_{-0.46}$, signifying a net radial alignment of galaxies in the combined dataset.

In the context of contaminations to weak lensing, the result for blue galaxies may be the most pertinent – whilst our flux-limited samples offer the most representative dataset we can muster, the difficulties of spectroscopy limit them to relatively bright galaxies at low redshifts. Thus our model constraints for the unselected case are likely to over-predict red galaxy contributions – photometric cosmic shear datasets extend to greater depths and hence higher redshifts, where faint, blue galaxies dominate samples. While the results of our fitting to

[15] The small scales neglected in fitting are similarly discarded in most 3×2pt analyses, due to uncertainties in the modelling of non-linearities and baryonic contributions.

individual galaxy samples reveal weak/non-existent correlations between IA and galaxy luminosity/redshift, we also find significant, scale-dependent variability of IA when separating central/satellite contributions. In GAMA, red central and satellite galaxies align with their local galaxy distribution, i.e. that of the group halo, whilst red central shapes are solely responsible for the linear-scale correlation. Any blue central/satellite galaxy alignments remain undetectable. A full consideration is beyond the scope of this work, however our derived IA constraints remain the most representative for shear-like samples, and should be instructive for future studies.

We recommend the use of our colour-specific alignment constraints, and our interpolation between them (Eq. 3.22), in formulating a prior range on $A_{\rm IA}$ for future cosmic shear signal fitting. An average of our constraints, weighted by the relative red/blue galaxy populations, is likely to provide a more realistic description of the alignments present in a dataset – noting the GAMA satellite fraction of $\sim 27\%$, one can consider the $A_{\rm IA}$ interpolation to serve as a conservative upper-limit for similarly satellite-heavy samples.

Our fits of the luminosity-dependent NLA resulted in null detections for the β power-law, at 95% confidence. The blue galaxy β parameter is poorly constrained by the data, as the luminosity baseline of the samples is sparse and ineffectual, and the signals are close to zero. The red galaxy result is interesting, as it seems to contradict previous works which have found a roughly linear scaling of alignments with sample luminosity (Joachimi et al. 2011, Singh et al. 2015). The reason for this is that the red galaxy alignments show little/no evolution over a luminosity baseline of (rescaled to start at unity) $\sim [\,1\,, 1.67\,, 5\,]$. This observation might be partly explained by the density weighting and consequent bias-dependent signal enhancement described by Blazek, Vlah, & Seljak (2015), and certainly lends support to the notion that the current methods of modelling for IA are insufficient to grasp the complexity of contributions from galaxies in different environments.

We forecasted the cosmological parameter constraining capabilities of red/blue-split cosmic shear in a completed KiDS survey, assuming that alignments in the simulated data were described by the NLA or LA models. Applying our IA nuisance parameter constraints as informative priors, we find reductions of up to $\sim 50\%$ (or $\sim 20\%$ for the LA) in the size of confidence intervals for the S_8 parameter and w_0, dependent on the freedoms of photometric redshift bias parameters. Our forecasts demonstrate the potential utility of independent intrinsic alignment model constraints as informative priors in cosmic shear analyses, particularly as IA parameterisations become more complex and impactful.

In the era of LSST, Euclid and WFIRST, our current prescriptions for the intrinsic alignment contamination of cosmic shear would lag behind greatly increased statistical power – one fears that the limit of cosmological inference could be determined by the uncertainty in models for IA (and other systematics), and open to strong biases as a result. Our work has attempted to characterise the alignment signatures of a purely flux-limited sample, finding complexity beyond the divergent behaviour of elliptical and spiral galaxies, extending to the non-trivial contributions of red centrals and satellites. These findings motivate us to explore IA models with galaxy red- and satellite-fraction considerations, and to constrain such models with representative spectroscopic data – such work will aid in the maximisation of potential for the next generation of lensing surveys.

Looking forward, we hope to perform this analysis with a halo model for intrinsic alignments, adapted from the formalism of Schneider & Bridle (2010), fitting to all scales, including a satellite-alignment prescription, and taking full advantage of the high completeness of these data (Fortuna et al., in prep.). In the meantime, our derived NLA model constraints will provide useful priors for current and future shear surveys, improving cosmological constraints and blocking the influence of unknown systematics on IA parameterisations. New, narrow-band photometric datasets are currently being amassed (PAUS; Benítez et al. 2009, J-PAS; Benítez et al. 2014), with the potential for the production of unprecedented IA model constraints, for use in future weak lensing analyses. Furthermore, the statistical power and associated precision of these datasets will enable the use of intrinsic-intrinsic shear (II) correlations in studying the type- and environment-dependence of galaxy alignment mechanisms. Powerful and additional statistics, cross-correlations between galaxy types, and increased depths in these analyses will shed new light on the intrinsic alignment contamination of cosmic shear, and on the physics of galaxy formation and evolution.

3.A Covariances

To quantify sample variance, one would ideally prefer to use many realisations of simulated data in estimating errors on a statistic. Unfortunately, there remain qualitative disagreements between the latest hydrodynamical simulations with respect to the form of late-type galaxy intrinsic alignments (Tenneti et al. 2016). More fundamental road-blocks are small volumes and a lack of multiple realisations of these simulations, making them unsuitable for covariance purposes, as yet. We prefer our IA measurement errors to come from the data.

With an eye to include the largest possible transverse scales in our analysis, we implement a 3-dimensional delete-one jackknife. The jackknife covariance is estimated as

$$\hat{\mathsf{C}}_{\rm jack} = \frac{N-1}{N} \sum_{\alpha=1}^{N} (\vec{w}^{\alpha} - \bar{\vec{w}})(\vec{w}^{\alpha} - \bar{\vec{w}})^{\rm T} \quad , \tag{3.27}$$

where $\vec{w}^{\alpha}$ is the signal of interest, as measured from jackknife sample α, and $\bar{\vec{w}}$ is the average over N samples. T denotes the conjugate transpose of the mean-subtracted signal vector. N jackknife samples are defined by dividing the survey into N subvolumes and excluding one at a time, measuring $\vec{w}^{\alpha}$ in the rest of the survey. The performance of jackknife covariance estimation relies on a balance between (i) the number of jackknife subvolumes N, and (ii) the angular scale of their corresponding 'patches' in the RA-DEC plane, where one always compromises the other. N should be $\gg$ the size of the data vector, or else the covariance becomes noisy and eventually singular. And yet, the scale of the subvolumes must be greater than the largest scales of interest, or the variance over those scales will not be captured and errors will be underestimated.

Figure 3.11 illustrates the mapping from an angular scale on the sky to a comoving transverse scale at a given redshift, with our log-spaced r_p-bin edges shown as horizontal black lines. This plot is interpreted as follows: coloured lines give the maximum comoving separations captured by an angular scale, thus anything below each line is correctly sampled by a sky-patch of that size, at that redshift. Normalised redshift distributions of GAMA and SDSS Main are overlaid, along with the redshift boundary defining our high- and low-z GAMA samples (vertical red line). At high redshift, the GAMA jackknife demands patches of scale $\gtrsim 4.5$ degrees for all r_p scales to be captured, whilst the lower redshifts, which include all of the SDSS sample, are significantly hamstrung by the jackknife requirement. Contiguous regions of equatorial GAMA are $12\,\rm deg \times 5\,deg$ in size, rendering ideal patches too few in number. SDSS Main covers a much larger area, but requires even larger patches at lower redshift. Thus we define a series of redshift slices, each with comparable numbers of galaxies, and subdivide jackknife patches into 'cubes'. We take care to ensure that the resulting cubes are of more than sufficient depth to be considered statistically independent, and to accomodate the largest line-of-sight separations under consideration – $|\Pi_{\rm max}| = 60\,h^{-1}$Mpc, so we ensure that all cubes are deeper than $150\,h^{-1}$Mpc. This requirement, along with the need for many jackknife regions of roughly equal galaxy numbers, is what informs our GAMA samples' shared redshift boundary at $z = 0.26$. The large-Π systematics test extends to $|\Pi_{\rm max}| = 90\,h^{-1}$Mpc, and we opt for a standard 2D jackknife in this case, reducing the binning of the measured signal in order to stabilise the covariance matrix.

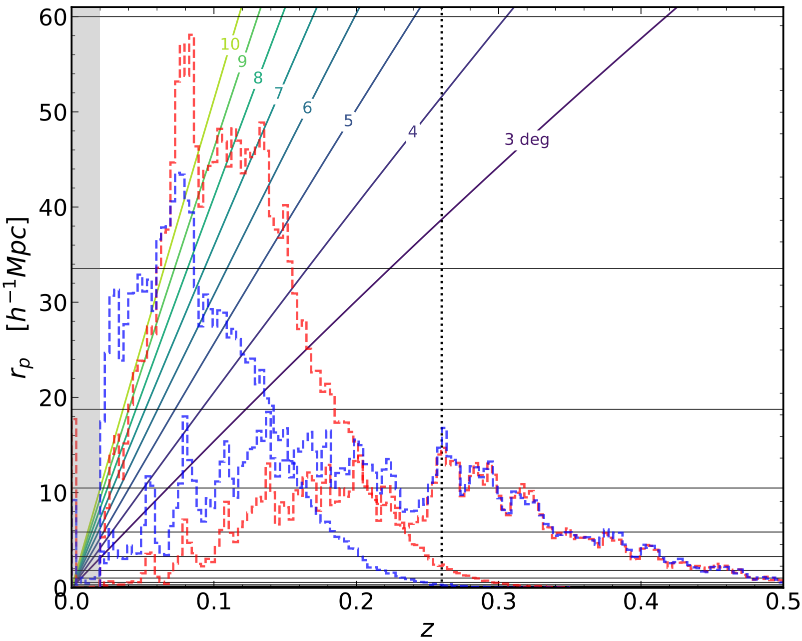

Figure 3.11: As a function of redshift, the comoving transverse vs. on-sky angular scale relation, for a range of scales in degrees. The r_p bin edges we employ are plotted as horizontal black lines, highlighting the limitations of too-small patches to sample larger r_p pairs, esp. at lower redshifts. The vertical dotted line indicates the $z = 0.26$ redshift division for our GAMA samples, and redshift distributions of red and blue galaxies in SDSS ($z \sim [0.02, 0.3]$) and GAMA ($z \sim [0.02, 0.5]$) are overlaid as coloured, dashed histograms. Grey shading indicates $z < 0.02$, which we exclude from our analysis.

We note that by slicing subvolumes in redshift, we are assuming that we can approximate the variance over a redshift bin by the combined variance of its sub-bins, and thus that any redshift evolution is subdominant to the variance over different pointings. Since previous studies (Joachimi et al. 2011, Mandelbaum et al. 2011, Tonegawa et al. 2018) support weakly- or non-evolving alignments – albeit for differently selected samples – and our redshift baseline is short, we believe this assumption is reasonable.

Figure 3.12 compares the performance of various 2D and 3D jackknife con-

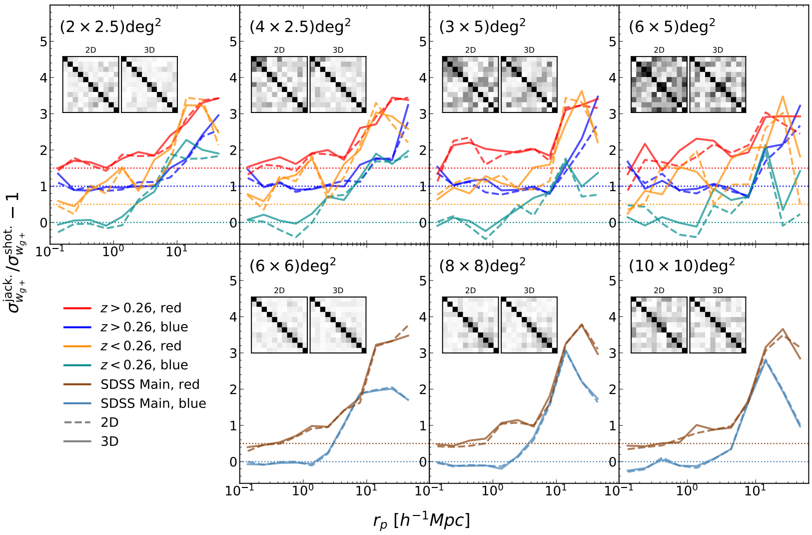

Figure 3.12: Performance of the 3D (solid lines) and 2D (dashed lines) jackknife in various configurations, plotted as ratios to analytical (shot-noise) errors estimated for the w_{g+} statistic. GAMA configurations are plotted on the top row, with SDSS on the bottom. Colour/redshift sample error ratios are vertically offset by increments of 0.5 (equivalent to a 50% difference in the error on w_{g+}) for clarity, and $\sigma^{\rm jack.}/\sigma^{\rm shot.} = 1$ is indicated for each sample by a dotted horizontal line. Also shown are the Z2R and SR samples' 2D (*left-in-panel*) and 3D (*right-in-panel*) jackknife estimates of absolute correlation matrices $|R_{ij}| = |C_{ij}| / \sqrt{C_{ii}C_{jj}}$, for covariance C_{ij}, with $i, j \in [1, 11]$ for 11 bins in r_p. The angular dimensions (RA × DEC) of jackknife patches, in degrees, are indicated. Clearly visible trends are increasingly noisy covariances from larger/fewer patches, and the tendency of the 3D jackknife to smooth this noise. The jackknife configurations we employ in our likelihood analysis are $(3 \times 5)\,\mathrm{deg}^2$ and $(10 \times 10)\,\mathrm{deg}^2$ for GAMA and SDSS, respectively.

figurations. For our GAMA intrinsic alignment measurements we choose to work with $(3 \times 5)\,\mathrm{deg}^2$ patches, sliced into cubes – the performance of this configuration is indicated by solid lines in the top-middle-right panel of Figure 3.12. Subvolumes of this size combat the noise evident for $(6 \times 5)\,\mathrm{deg}^2$ patches (top-right panel), and remain large enough to sample all but the largest transverse scales at low redshifts – we opt to drop only the largest-r_p data point for low-redshift measurements. We describe our method for estimating clustering covariances in GAMA in Appendix 3.A.2. For SDSS, we estimate both IA and clustering covariances with a $(10 \times 10)\,\mathrm{deg}^2$ jackknife cube configuration (Figure 3.12, bottom-right, solid lines) – the largest scales allowing for acceptable numbers of patches in the irregular SDSS footprint. We choose to retain all data points for SDSS measurements.

Our chosen configurations yield 36 , 24 and 74 jackknife cubes per low-redshift GAMA, high-redshift GAMA and SDSS sample, respectively. Large-Π test jackknife errors are derived from 12 and 37 patches (2D) for GAMA and SDSS, respectively.

3.A.1 Masking

While patches are chosen to be roughly equal in area, this is not always achieved due to masking and irregular survey edges. A patch covering less area translates into a less variant jackknife sample upon deletion. Thus when estimating the covariance from jackknife measurements, the noise at large scales is spuriously lowered, and inter-bin correlations are biased.

We quantify this effect using data from the MICE Simulation. The Marenostrum Institut de Ciéncies de l'Espai (MICE) Grand Challenge galaxy catalogue (Carretero et al. 2015, Hoffmann et al. 2015) was assembled from a 7×10^{10} dark matter particle, $\sim (3\,h^{-1}\mathrm{Gpc})^3$ comoving volume simulation (Fosalba et al. 2015), with halo occupation and abundance matching techniques (Crocce et al. 2015). The resulting catalogue spans a $5000\,\mathrm{deg}^2$ octant, complete down to an absolute r-band magnitude of $M_r < -18.9$.

For a GAMA-sized patch of MICE, we generate a random ellipticity distribution and mask-out chunks of area in a similar fashion to the real masking in our KiDS images, estimating the jackknife alignment covariance before and after masking. We find that, whilst off-diagonal covariance elements can be severely mis-estimated, on-diagonal elements are recovered at $\sim 23\%$ or better. We can lower this margin of error – with a particular impact on the larger scales we use in fitting – to $\sim 18\%$ or better by applying weights to jackknife samples, equal to the relative areas of their respective deleted subvolumes (we apply an approximate re-normalisation incorporating the weights).

To test whether the more serious mis-estimation of off-diagonal covariance elements biases our results significantly, we set them all to zero and repeat our likelihood analysis. In comparison with our results quoted in Table 3.2, we find consistency at 68% confidence in all cases, with our fitted LA parameter values shifting as follows; $\{A_{\rm IA}^{\rm B} : -1.2\sigma\ , \quad A_{\rm IA}^{\rm R} : +0.33\sigma\ , \quad A_{\rm IA}^{\rm full} : +0.30\sigma\}$. Whilst red- and all-galaxy amplitude shifts are small at just $\sim 0.3\sigma$, the larger, negative shift of $\sim 1.2\sigma$ in the blue-galaxy amplitude fit acts to strengthen consistency with zero. For the LA-β, the red- and all-galaxy β parameters shift to centre on zero, with small shifts taking the amplitudes toward the 1-parameter LA centres. The blue-galaxy β parameter is relatively unchanged, with the amplitude centre shifting close to zero. Since none of these shifts contradict our original findings, the omission of inter-bin correlations can be said not to affect the conclusions of this work. We know that the worst biases of the off-diagonal covariance in our MICE test were equivalent to shifts in correlation coefficients of $\lesssim 0.2$, thus we further conclude that biases of the signal covariance due to survey masking are subdominant to statistical errors for these data.

3.A.2 GAMA clustering covariance

We make further use of MICE in estimating clustering covariances for GAMA – for consistency, we impose the MICE faint-limit ($M_r \leqslant -18.9$) on our GAMA density samples, for losses of { Z1B : 27.3% , Z1R : 5.6% , Z2B : 0.1% , Z2R : 0.1% } – see Table 3.1 for sample details.

We apply the GAMA flux-limit $r < 19.8$ to MICE and make a flat cut in absolute rest-frame $g - r$ to isolate the red sequence. Dividing the MICE area (with declination $\leqslant 40\,\mathrm{deg}$) into 18 rectangular patches, each $\sim 180\,\mathrm{deg}^2$, we measure the clustering signals in each patch and find the spread to be slightly disagreeable with the clustering of analogous samples in GAMA (Figure 3.13). Thus we choose to validate the SWOT clustering jackknife routine (SWOT-jk), and its sensitivity to the jackknife subvolume numbers-vs.-size trade-off, using MICE.

We first obtain SWOT-jk estimates of the MICE sample clustering signals and covariances, per patch. We then estimate total MICE sample clustering covariances by constructing 2D jackknifes with all 18 patches. The variance[16] over SWOT-jk estimates then approximates the sample variance of a $180\,\mathrm{deg}^2$ – i.e. GAMA-like – survey. If this is greater than any systematic offset between the mean covariance over the patches and the (area-scaled) total jackknife covariance, then the bias of the SWOT-jk is subdominant to the statistical error of a GAMA-like survey. This is indeed the case for smaller transverse pair separations, which are well-sampled even by small angular scales. Samples at high

[16] We are now discussing the variance over independent estimates of the clustering covariance.

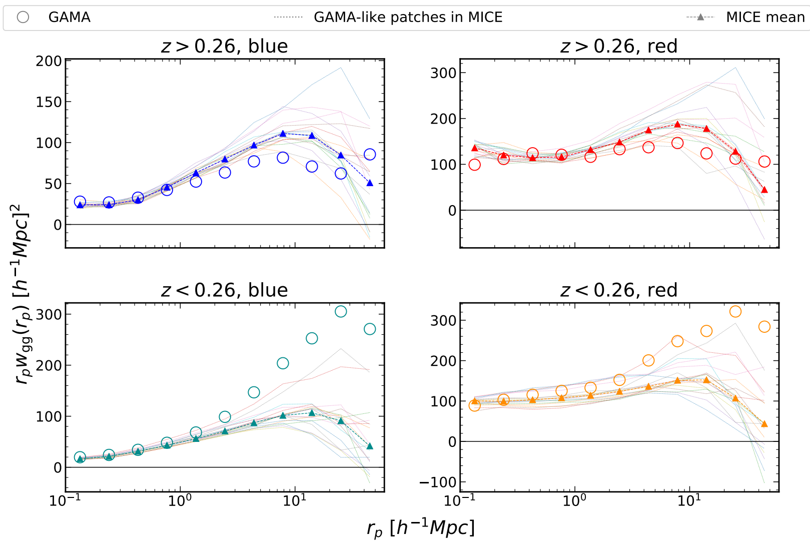

Figure 3.13: Clustering measurements from our defined GAMA galaxy samples (open circles) overlaid with corresponding measurements from individual, $\sim 180\,\mathrm{deg}^2$ MICE subvolumes (dotted lines). Filled triangles show the means of the MICE clustering signals. We see significant differences between MICE and GAMA, particularly at low redshift and large scales, and so choose not to estimate covariances directly from MICE – see Appendix 3.A.2 for details.

redshift also do well in this regard, as smaller angular scales trace large spatial volumes. As Figure 3.14 illustrates, however, the SWOT-jk significantly underestimates large-scale covariance elements for low-redshift samples (bottom panels; green lines & shading vs. solid coloured lines). As discussed in Appendix 3.A above, this is due to poor sampling of these pairs, and thus diminished variation across jackknife samples.

Since the jackknife performance differential is dominated by sample redshift, rather than colour, we attempt to quantify the lost variance by fitting 1 scaling variable to each of the 3 largest transverse separation bins i under consideration. Boosting each covariance element with the product a_{ij} of the 2 relevant scaling variables, we are able to bring the mean-over-patches (pink lines & hatching in Fig. 3.14) into closer agreement with the total MICE jackknife. We take these scaling factors to be approximately representative of the large-scale performance

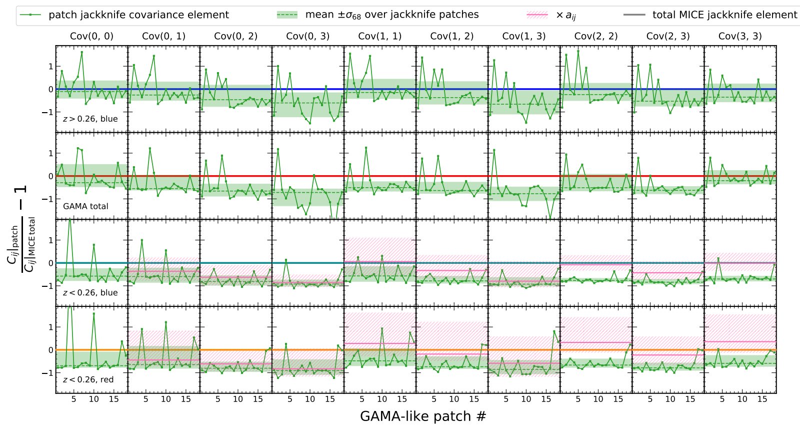

Figure 3.14: A comparison of clustering covariance elements (*columns*), estimated for each redshift/colour galaxy sample (*rows*) with the SWOT internal jackknife per MICE patch (X, green) and the total jackknife over all patches (Y, solid coloured lines), plotted as $X/Y - 1$. The $0.16\,, 0.5\,, 0.84$ percentiles over the patch estimates are indicated by dashed lines and shading. Pink solid lines and hatching indicate covariance elements scaled by the fitted variables a_{ij} described in Appendix 3.A.2.

drop-off inherent to the SWOT-jk at low redshift, and apply them to our low-z GAMA clustering covariances.

3.B Individual sample fits

Table 3.6 details the individual fits of the 1-parameter NLA model to galaxy samples, as described in Section 3.4.2, along with the relevant sample properties displayed in Figure 3.6, and constraints upon the galaxy biases of corresponding density samples.

Table 3.6: 1D marginalised constraints (to 1σ) upon the 1-parameter NLA amplitude A_{IA} for each sample under consideration – each of the points shown in Figure 3.6 corresponds to a row here. 'G' and 'S' denote GAMA and SDSS samples, respectively. The independent galaxy samples whose signals constrain the 'All blue' or 'All red' amplitudes are denoted with †. Samples denoted 'high-M_*' are selected from GAMA to have stellar masses $> 10^{11} M_\odot$. Also shown are red galaxy fractions f_{red}, mean redshifts and mean luminosities (relative to the pivot $L_{\mathrm{piv}} = 4.6 \times 10^{10} L_\odot$) per shapes sample, and marginalised galaxy bias fits to corresponding density samples. Rows without these numbers correspond to amplitudes which were fit to multiple $w_{\mathrm{g+}}$ signals from samples with different properties.

Sample	f_{red}	$\langle z \rangle$	$\langle L/L_{\mathrm{piv}} \rangle$	b_{g}	A_{IA}
G+S: full	0.54	–	–	–	$1.06^{+0.47}_{-0.46}$
G: full	0.43	0.23	0.51	$1.57^{+0.08}_{-0.08}$	$0.26^{+0.63}_{-0.62}$
S: full	0.60	0.11	0.22	$0.91^{+0.11}_{-0.12}$	$2.01^{+0.79}_{-0.71}$
All blue	0	–	–	–	$0.21^{+0.37}_{-0.36}$
G: high-M_*, blue	0	0.36	2.69	$1.62^{+0.11}_{-0.11}$	$2.72^{+2.54}_{-2.60}$
†G: $z > 0.26$, blue	0	0.33	1.06	$1.10^{+0.07}_{-0.07}$	$0.78^{+0.55}_{-0.54}$
†G: $z < 0.26$, blue	0	0.15	0.21	$1.55^{+0.09}_{-0.08}$	$-1.26^{+0.75}_{-0.69}$
†S: blue	0	0.09	0.14	$0.88^{+0.12}_{-0.14}$	$1.03^{+0.90}_{-0.85}$
All red	1	–	–	–	$3.18^{+0.46}_{-0.45}$
G: high-M_*, red	1	0.31	2.03	$1.93^{+0.09}_{-0.10}$	$6.27^{+0.98}_{-0.96}$
†G: $z > 0.26$, red	1	0.33	1.47	$1.52^{+0.11}_{-0.11}$	$3.55^{+0.90}_{-0.82}$
†G: $z < 0.26$, red	1	0.17	0.50	$1.84^{+0.12}_{-0.12}$	$3.63^{+0.79}_{-0.79}$
†S: red	1	0.12	0.29	$1.19^{+0.11}_{-0.11}$	$2.50^{+0.77}_{-0.73}$

3.C Linear alignment model fits

Here we present fits of the linear alignment model to our IA data. Table 3.7 shows the results of our LA fitting, which are discussed in Section 3.4.2.

Table 3.7: The same as Table 3.2, here for the parameters of the linear alignment (LA) model (Section 3.3.1) and its luminosity-dependent analogue (LA-β).

Sample	$\langle z \rangle$	$\langle L/L_* \rangle$	$b_{\rm g}$	$A_{\rm IA}$	χ^2_ν	$p(>\chi^2)$	A_β	β	χ^2_ν	$p(>\chi^2)$
GAMA full	0.23 (0.24)	0.51 (0.70)	$1.56^{+0.09}_{-0.08}$	$1.23^{+0.57}_{-0.52}$	1.48	0.14	$1.37^{+4.09}_{-2.45}$	$2.25^{+1.95}_{-2.53}$	1.54	0.13
SDSS Main full	0.11 (0.11)	0.22 (0.22)	$0.94^{+0.10}_{-0.11}$							
G: $z > 0.26$, blue	0.33 (0.33)	1.06 (1.09)	$1.10^{+0.07}_{-0.07}$	$0.35^{+0.45}_{-0.43}$	1.35	0.15	$0.80^{+0.55}_{-0.60}$	$2.57^{+1.59}_{-1.69}$	1.34	0.17
G: $z < 0.26$, blue	0.15 (0.17)	0.21 (0.36)	$1.55^{+0.09}_{-0.08}$							
S: blue	0.09 (0.09)	0.14 (0.14)	$0.88^{+0.13}_{-0.15}$							
G: $z > 0.26$, red	0.33 (0.33)	1.47 (1.48)	$1.52^{+0.10}_{-0.12}$	$3.70^{+0.52}_{-0.53}$	1.34	0.16	$3.93^{+0.66}_{-0.63}$	$0.17^{+0.20}_{-0.20}$	1.40	0.14
G: $z < 0.26$, red	0.17 (0.18)	0.50 (0.56)	$1.85^{+0.13}_{-0.13}$							
S: red	0.12 (0.12)	0.29 (0.29)	$1.19^{+0.11}_{-0.12}$							

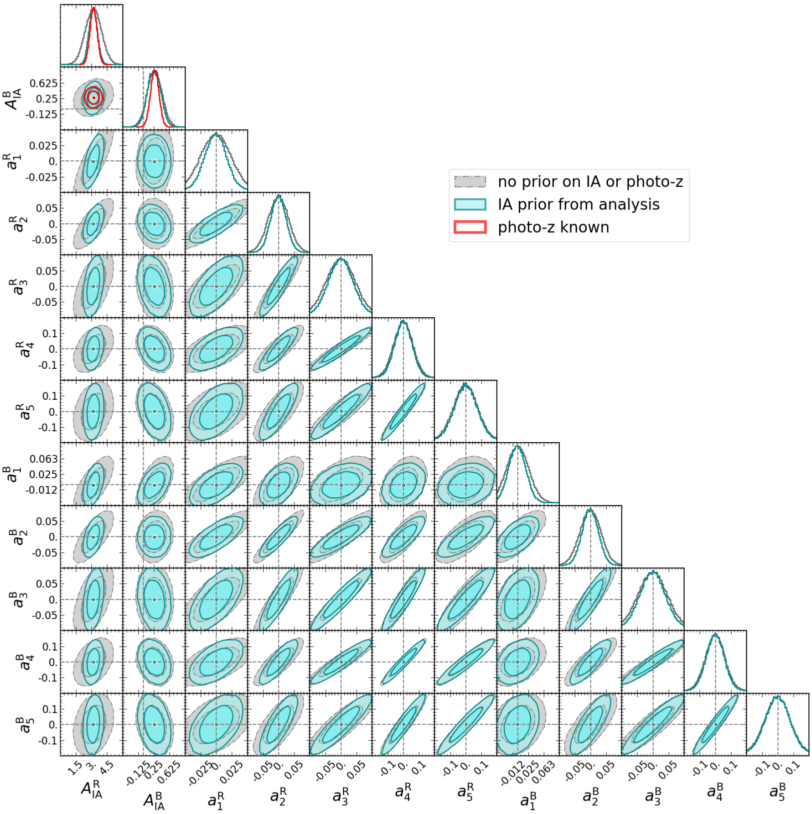

Figure 3.15: The same as Figure 3.8, for nuisance parameters only.

3.D Photo-z bias parameter contours

Here we include our Fisher forecasted constraints for all IA and photo-z nuisance parameters considered (Section 3.5), before and after application of our derived IA model priors (Section 3.4). Figures 3.15 & 3.16 accompany the LA/LA-β model forecasts of Figures 3.8 & 3.9, respectively.

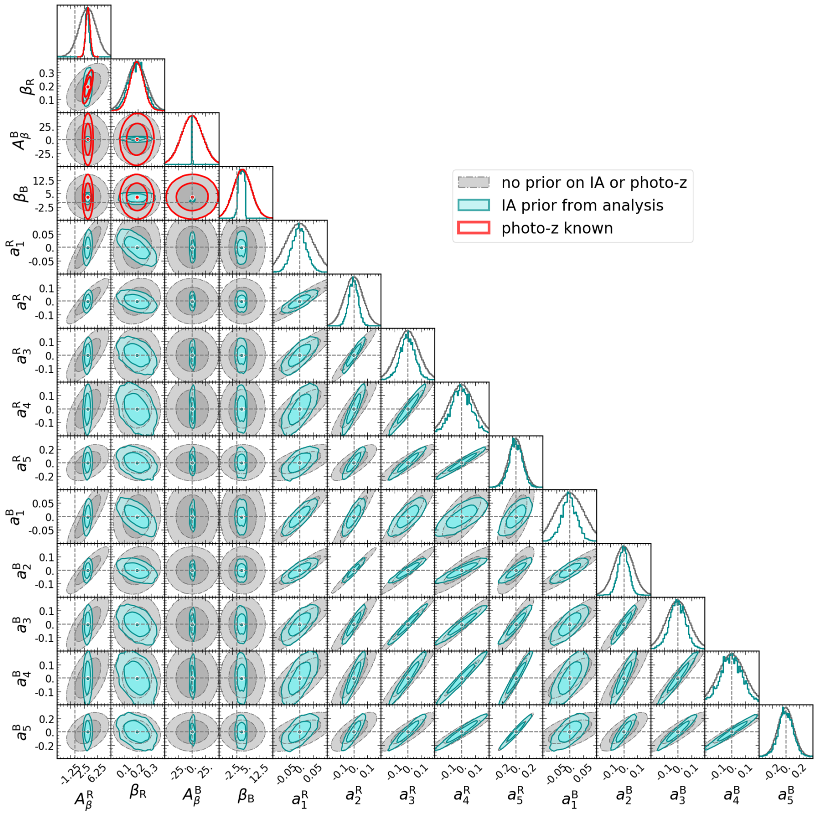

Figure 3.16: The same as Figure 3.9, for nuisance parameters only.

Chapter 4

GAMA+KiDS: Alignment of galaxies in galaxy groups and its dependence on galaxy scale

Based on
C. Georgiou, N.E. Chisari, M.C. Fortuna, H. Hoekstra,
K. Kuijken, B. Joachimi, M. Vakili, M. Bilicki,
A. Dvornik, T. Erben, B. Giblin, C. Heymans,
N.R. Napolitano, H. Shan
A&A 628, A31 (2019)

4.1 Introduction

One of the major unsolved problems of modern cosmology, and the established concordance model, dubbed ΛCDM, entails the mystery around dark matter and dark energy. These components account for approximately 95% of the energy density of the universe today, with their presence established through several observations (e.g. Betoule et al. 2014; Alam et al. 2017; Planck Collaboration et al. 2018) but their nature remaining elusive. This is mostly due to the exceptionally low, if not null, cross-section for interactions involving the non-baryonic particles of dark matter (see e.g. Bertone et al. 2005, for a review) as well as the difficulty in observationally obtaining enlightening information about dark energy (for a review, see Huterer & Shafer 2018).

In order to shed light onto the nature of these "dark" components of the universe we need to use robust and complementary observations that are sensitive to their effects. One observational technique of particular interest is weak gravitational lensing, the coherent distortion of light bundles that travel through a matter-bent spacetime (see e.g. Bartelmann & Schneider 2001; Bartelmann 2010). Lensing is sensitive to the intervening matter (baryonic and non-baryonic) between the light source and the observer as well as the geometry of the universe, thus serves as a great tool for constraining both dark matter and dark energy.

Weak gravitational lensing measurements use shape correlations of galaxies in order to extract the lensing signal and infer cosmological parameters (for a review see Kilbinger 2015; Bartelmann & Maturi 2017). However, lensing measurements are sensitive to certain physical and observational systematic uncertainties that need to be taken into account. One major astrophysical contaminant is the alignment of galaxies with other galaxies and the matter density field, known as intrinsic galaxy alignment (see e.g. Joachimi et al. 2015, for a review). Intrinsic alignments produce shape correlations between physically associated galaxies (named intrinsic-intrinsic or II), as well as the more complicated correlation between background and foreground galaxy shapes (named gravitational-intrinsic or GI correlation). These correlations, if ignored, can significantly bias lensing measurements (e.g. Kirk et al. 2015; Troxel & Ishak 2015).

Intrinsic alignments are commonly mitigated by marginalising over modelled parameters describing them, when extracting lensing information. The most common approach is to use the linear alignment model (Hirata & Seljak 2004), which assumes that galaxy alignments are linearly related to the gravitational field, while often replacing the linear matter power spectrum with its non-linear counterpart, dubbed non-linear linear alignment model (NLA, Bridle & King 2007). This model has been successful in describing direct measurements of intrinsic alignments on scales down to a few Mpc/h (e.g. Singh et al. 2015), and has been used in many studies measuring lensing from large-scale structure (cosmic shear, e.g. Hildebrandt et al. 2018; Abbott et al. 2018; Hikage et al. 2019) or combining it with weak lensing from individual lens galaxies (galaxy-galaxy lensing, e.g. van Uitert et al. 2018; Joudaki et al. 2018; DES Collaboration et al. 2017).

For smaller scales, the linear alignment model fails to reproduce observations since the physical mechanism that aligns galaxies at such scales is fundamentally different (Pereira et al. 2008). Consequently, devising a descriptive model for intrinsic alignments at these scales is challenging, yet crucial to using these information-rich scales in lensing measurements. One approach is the halo model, which describes how galaxies (central and satellites) populate a dark matter halo given its mass, as well as how they are oriented (Schneider & Bridle 2010). This model is the only description of the alignment signal at small scales so far, and can in principle be extended to describe extra dependencies of the signal. While a general consensus for the intrinsic alignment signal on small scales has not yet been reached, it is important to study the phenomenon directly on intra-halo scales and provide insight for building an accurate halo model.

Intrinsic alignments have been studied in many cosmological and numerical simulations, both on large and intra-halo scales (e.g. Knebe et al. 2008, 2010; Tenneti et al. 2014; Velliscig et al. 2015b; Chisari et al. 2015; Hilbert et al. 2017). A strong alignment signal on small scales is seen in these simulations, with satellite galaxies being radially aligned with their host halo centres. However, the picture is not very clear in observations, with many studies finding satellite orientations consistent with random (e.g. Schneider et al. 2013; Chisari et al. 2014; Sifón et al. 2015) while others see a positive radial alignment signal (e.g. Agustsson & Brainerd 2006; Huang et al. 2018).

This discrepancy can be attributed to a difference in galaxy populations, but also to a scale dependence of the alignment signal, i.e. outer galaxy regions exhibiting a stronger alignment than inner ones. Such a dependence is expected due to the tidal nature of the phenomenon and has been seen in hydrodynamical simulations, where the alignment signal was stronger when the method used to define galaxy shapes up-weighted outer regions of galaxies (Velliscig et al. 2015b; Chisari et al. 2015; Hilbert et al. 2017). Observations have also hinted towards this, with Singh & Mandelbaum (2016); Huang et al. (2018) looking into alignments as measured by different shape measurement methods and finding stronger alignments for methods more sensitive to the outer shape of a galaxy. In addition, Georgiou et al. (2019b) found that the alignment signal changes on small scales when shapes were measured from different broad band filters, with the change mostly sourced by satellite galaxies. Since galaxies exhibit colour gradients, certain regions of galaxies can be more prominent in one broad band filter observation than another, hinting towards a scale dependence of the alignment signal.

In this work we measure the alignment of shapes of satellite galaxies with respect to their group's centre (traced by the brightest group galaxy, or BGG), as well as the alignment of shapes of BGGs with the positions of satellites. We use galaxy groups from the Galaxy And Mass Assembly survey[1] (GAMA; Driver et al. 2009, 2011; Liske et al. 2015; Baldry et al. 2018) and apply the DEIMOS shape measurement method (Melchior et al. 2011) on imaging data from the Kilo Degree Survey[2] (KiDS; de Jong et al. 2015, 2017; Kuijken et al. 2019). Possible trends with observed wavelength, magnitude, group mass and galaxy colour are examined. We also look into the galaxy scale dependence of these alignments by varying the radial weight function employed when measuring galaxy shapes and comparing the resulting alignment signal. This will shed light onto the discrepancy of alignments between observations and simulations, as well as allow for better calibration of the halo model for intrinsic alignments in the future. Lastly, we look at the global intrinsic alignment signal and its dependence on galaxy scale.

This paper is organised as follows: in Sect. 4.2 we describe the data used, and the methodology for obtaining a robust alignment signal is outlined in Sect. 4.3. Satellite galaxy alignments are presented in Sect. 4.4, BGG alignments with its satellites in Sect. 4.5, and the scale dependence of central galaxies is shown in Sect. 4.6. Conclusions follow in Sect. 4.7. Throughout this paper we use flat ΛCDM cosmology with $h = 0.7$ and $\Omega_{\mathrm{m}} = 0.315$.

4.2 Data

Measuring the alignment of galaxies in galaxy groups requires a robust group catalogue and good imaging data. The former is obtainable from a galaxy sample with accurate redshifts (usually obtained spectroscopically) as well as a highly complete and deep sample, with which we can identify as many group

[1] http://www.gama-survey.org
[2] http://kids.strw.leidenuniv.nl/

members as possible. The latter can be acquired from several deep imaging surveys that cover large parts of the sky. In this work, we use data from the GAMA survey, combined with the deep and high quality imaging data of the KiDS survey for highly accurate shape measurements.

4.2.1 Galaxy group sample

Our galaxy group sample is drawn from the final release of the GAMA survey (Liske et al. 2015; Baldry et al. 2018). The survey acquired spectroscopy for $\sim$300,000 galaxies across a total $\sim$286 deg^2 of sky. The survey is split into 5 patches of roughly equal area, three of them in the equatorial regions (named G09, G12 and G15) and two in the southern celestial hemisphere (G02 and G23). Region G02 does not overlap with our imaging data while region G23 has a slightly different target selection and, to avoid complications that may arise due to this difference, we restrict our analysis to the three equatorial regions. That leaves us with $\sim$180 deg^2 of area and $\sim$180,000 galaxies. The limiting magnitude for the equatorial regions is $r < 19.8$ mag.

The unique characteristic of the survey is its high completeness; in the equatorial regions, redshift information is obtained for 98.5% of the target galaxies. This allows for a robust estimation of galaxy alignments on small scales, where complications such as fiber collisions are not present. In addition, the completeness enables the construction of a high fidelity group catalogue (Robotham et al. 2011).

The group catalogue was created using a friends-of-friends grouping algorithm of variable linking length, and contains $\sim$23,600 galaxy groups (with at least two member galaxies) in the equatorial regions, for a total of $\sim$75,000 group galaxies. The redshifts of these groups extend to $z \simeq 0.6$ with a median group redshift of $z_{\rm med} = 0.213$, which is practically the same as the parent sample. The grouping algorithm has been tested and calibrated using mock catalogues from semi-analytic galaxy models applied to N-body simulations, specifically designed to capture the properties of galaxies in the GAMA survey (see Robotham et al. 2011, for details). These mocks also enable the calculation of unbiased group luminosities, which we make use of in Sec. 4.4.

We calculate the alignment of satellite galaxies with respect to the brightest group galaxies, which may not always coincide with the group's dark matter halo. This mis-centring was examined in Viola et al. (2015) for GAMA groups where different group centre definitions were considered. It was found that consistent results were produced using the BGG and using the centre as defined iteratively by removing the galaxy further away from the group's centre of light.

In this work, for simplicity, we use the BGG as a proxy for the group's centre.

4.2.2 Galaxy shape measurements

A robust shape measurement requires high quality, deep imaging data as well as an accurate shape measurement method. We use imaging data from KiDS (de Jong et al. 2015, 2017; Kuijken et al. 2019), a survey specifically designed and optimised for weak gravitational lensing science. The survey aims to cover 1,350 deg^2 in the four optical SDSS-like broad bands u, g, r and i, down to limiting magnitude of 24.3, 25.1, 24.9 and 23.8 (5σ in a 2 arcsec aperture), respectively. This results in deep, high quality images, with a small, nearly uniform Point-Spread function (PSF) (Kuijken et al. 2015).

The shape measurement method we choose is DEIMOS (Melchior et al. 2011). This is a moment-based method, extracting shape information using moments as measured directly from the image. It is an improvement over other similar techniques (e.g. Kaiser et al. 1995; Hirata & Seljak 2003) because it allows usage of high-order moments in correcting for the employed radial weight function, necessary when dealing with noisy imaging data. In addition, the PSF is treated in a fully analytical way, without any prior assumptions on its properties; the limiting factor is how well one can model the PSF on the positions of galaxies. Finally, unlike model-dependent shape measurement techniques (e.g. Miller et al. 2013), we can directly vary the radial weight function, which translates to measuring galaxy shapes sensitive to different galaxy regions. A larger weight function will be more sensitive to outer galaxy regions, and using this we can probe the galaxy scale dependence of the alignment signal.

The PSF used in this work is modelled using orthogonal shapelets (Refregier 2003), which are Hermite polynomials multiplied by Gaussian functions. Shapelets can be linearly combined (to arbitrary extent) to describe image shapes. This model has been shown to adequately describe the PSF variations in KiDS images (Kuijken et al. 2015). The weight function is a 2D Gaussian, initially circular, with the scale of the Gaussian being a free parameter called r_{wf}. The weight function is then matched iteratively to the ellipticity and centroid of each galaxy while preserving its area to the initial circular function. In order to mask neighbouring galaxies, segmentation maps from SExtractor are used that identify pixels associated with other sources. These pixels are then replaced with random Gaussian noise of the same level as the image. The process followed for the shape measurement is described in detail in Georgiou et al. (2019b), where characteristics such as the galaxy ellipticity distribution and signal-to-noise can also be seen.

In this work, we measure shapes of galaxies from r-band imaging data of KiDS Data Release 4 (DR4), using five different radial weight function sizes (see Sec. 4.3.2). In order to probe differences of the alignment with the observed wavelength, we use shapes measured in g, r and i-band with a single weight function from Georgiou et al. (2019b), which were based on KiDS Data Release 3 (DR3) and covers fully the GAMA equatorial fields as well. Images based on DR4 are slightly different than those of DR3, because of improvements made in the photometry pipeline. The r-band shapes of DR4 and DR3 images are not exactly the same, however, the alignment measurements from the two releases are quantitatively the same.

4.3 Methodology

4.3.1 Radial alignment measurement

Measurements of alignments are often obtained by a statistical averaging of galaxy ellipticities. The ellipticity is defined in a Cartesian coordinate system as a non-linear manipulation of the galaxy surface brightness moments. The moments are given by

$$Q_{ij} = \int G(\mathbf{x})\, x_1^i\, x_2^j\, \mathrm{d}\mathbf{x}\,, \tag{4.1}$$

with x_1, x_2 the Cartesian coordinates where the galaxy is position at the coordinate system's origin and G being the galaxy's surface brightness. The ellipticity is then computed from

$$\epsilon = \frac{Q_{20} - Q_{02} + \mathrm{i}2Q_{11}}{Q_{20} + Q_{02} + 2\sqrt{Q_{20}Q_{02} - Q_{11}^2}}\,, \tag{4.2}$$

where $\epsilon = \epsilon_1 + \mathrm{i}\epsilon_2$, and the ellipticity modulus is $|\epsilon| = (1-q)/(1+q)$, with q being the semi-minor to semi-major axis ratio of the ellipse. This ellipticity measure is also often called the third flattening.

To quantify satellite alignments, it is useful to rotate the Cartesian coordinate system so that the x-axis coincides with the vector pointing from the centre of the galaxy group to the centre of the satellite galaxy. In this frame, $\epsilon_1 \mapsto \epsilon_+$ and $\epsilon_2 \mapsto \epsilon_\times$, which are called tangential and cross ellipticity components, respectively. These are computed by

$$\epsilon_+ = \epsilon_1 \cos 2\theta_s + \epsilon_2 \sin 2\theta_s \tag{4.3}$$

$$\epsilon_\times = \epsilon_1 \sin 2\theta_s - \epsilon_2 \cos 2\theta_s\,, \tag{4.4}$$

where θ_s is the azimuthal angle of the satellite galaxy with respect to the group's centre (Figure 4.1).

When the tangential ellipticity is positive the satellite's semi-major axis points towards the centre of the group and the satellite is radially aligned with the group's centre. On the other hand, a negative value of ϵ_+ means the satellite is tangentially aligned. Computing the average tangential ellipticity of a population of satellites will therefore reveal whether they preferentially align radially to the group's centre (in the case of a positive average ϵ_+), tangentially (when negative) or their orientation is random (when the mean tangential ellipticity is zero). Note that the sign convention used in this work is opposite from the tangential ellipticity used in weak lensing analysis.

4.3.2 Varying weight function

Measuring un-weighted moments, such as in Eq. (4.1), from real astronomical images is not possible in practice. The most important reason for this is the presence of noise in the imaging data, whose contribution to the moments diverges as we go away from the galaxy's centre. One way to deal with this is to radially weight the galaxy's surface brightness, suppressing the noise at large separations. However, since the calculated moments are now weighted by this function, the resulting shapes will be biased. To minimise this, in the context of DEIMOS, a Taylor expansion is used to approximate the un-weighted moments by calculating higher order weighted moments (see Melchior et al. 2011, for details). We truncate the Taylor series at $n_w = 4$, which has been shown to be a good approximation and results in a smooth behaviour of biases associated with the overall shape measurement (Melchior et al. 2011; Georgiou et al. 2019b).

The weight function ideally needs to match the galaxy's profile, and a common choice is a 2D Gaussian function, which is an adequate approximation. Here, we use an elliptical 2D Gaussian function, whose ellipticity and centroid are matched iteratively per galaxy. The size of the Gaussian is preserved at each matching iteration. At first, the ellipticity of the Gaussian function is 0 and its initial scale r_{wf} is a free parameter, determined separately for each galaxy. This parameter will determine the galaxy scale taken into account during the shape measurement. A small initial r_{wf} will generally measure the shape of the inner regions of the galaxy (e.g. the bulge) while a large r_{wf} will reveal the shape of the outer galaxy regions (e.g. the disk).

We choose to relate the initial weight function scale r_{wf} to the galaxy's isophote radius r_{iso} at 3σ above the background noise RMS, which is calculated using SExtractor (Bertin & Arnouts 1996). We aim to probe the galaxy

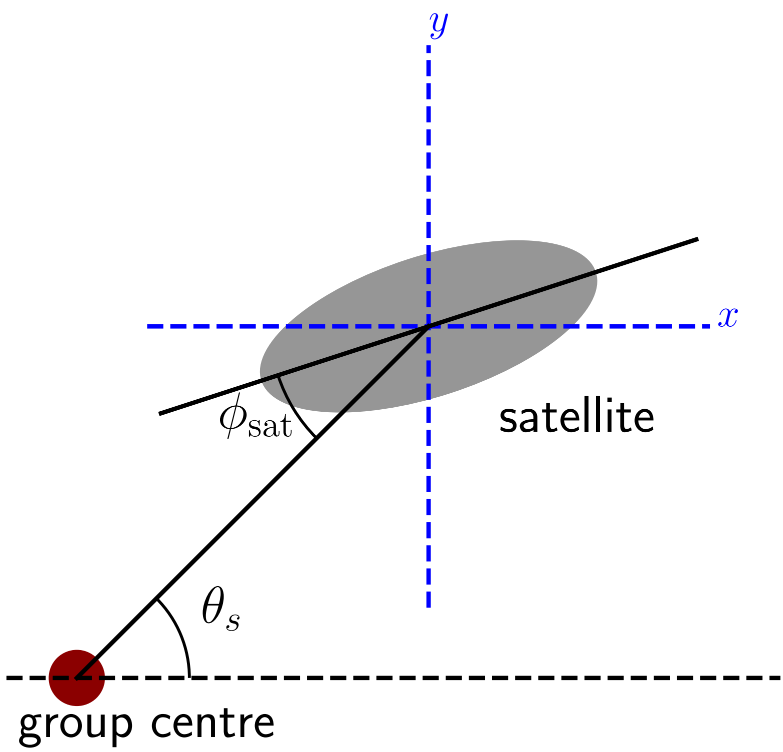

Figure 4.1: Definition of the azimuthal angle of a satellite galaxy $\theta_{\rm s}$, as well as the angle between the line connecting the BGG and the satellite and the semi-major axis of the satellite $\phi_{\rm sat}$. The dashed black line coincides with the x-axis of the coordinate system, which is the same for every measured galaxy.

scale dependence of the intrinsic alignments by measuring the signal using shape measurements obtained for several values of $r_{\rm wf}$. We use a total of 5 different weight functions, namely $r_{\rm wf}/r_{\rm iso} = \{0.5, 1, 1.25, 1.5, 2\}$, and restrict this to r-band images, which are higher quality, taken under better observing conditions compared to g and i. On shapes from g and i-band observations, the weight function size is fixed $r_{\rm wf} = r_{\rm iso}$, where the isophote is measured in the deepest

r-band images.

The physical regions probed by a certain weight function vary for each galaxy, depending on the physical size probed by the isophote of the galaxy. The mean isophote size in our galaxy sample is around 10 kpc with a standard deviation of 3.7 kpc. Therefore, even for the largest weight function we considered, the physical regions probed for each galaxy do not extend beyond the galaxy itself.

4.3.3 Tests for systematic errors

Here we discuss a few sources of potential contamination to our satellite alignment signal measurement and several ways to quantify and control this contamination, in order to robustly measure the alignment of satellite galaxies.

Shape measurement bias

There are several effects that can produce a systematic error when measuring galaxy shapes. This is often characterized with the multiplicative m and additive c bias, through the equation (Heymans et al. 2006),

$$\epsilon_i^{\mathrm{obs}} = (1 + m_i)\epsilon_i^{\mathrm{true}} + c_i \,, \tag{4.5}$$

where the observed galaxy ellipticity is related to the true ellipticity and the index runs through the two ellipticity components. An additive bias in the shape measurement method (often a product of incorrect treatment of the PSF) can bias the alignment measurement. However, as we compute the average tangential ellipticity component, such additive biases will average to zero. Indeed we show in Section 4.3.3 that we do not measure an additive bias caused by the shape measurement procedure alone in our image simulations. However, an additive c_+ term caused by the light of the BGG can offset our alignment signal (see e.g. Sifón et al. 2018, for a similar analysis), and we quantify this in Sect. 4.3.3.

Another bias that affects the alignment signal is multiplicative bias (or m-bias). This is unavoidable when measuring shapes from noisy images, due to the non-linear manipulation of pixel data, required to obtain shape information (see e.g. Viola et al. 2014). Fortunately, the m-bias can be determined through image simulations of galaxies that represent the overall galaxy sample. It is important to construct realistic and representative simulations (Hoekstra et al. 2017) as well as to use a shape measurement method that is robust, with shape measurement accuracy that depends weakly on galaxy properties. In Georgiou et al. (2019b) it was shown that DEIMOS applied on simulations of GAMA galaxies, which have generally high signal-to-noise ratio (SNR) in KiDS images, does not depend strongly on input ellipticity, size or SNR.

Following the work in Georgiou et al. (2019b), we simulate galaxy images using the GalSim python package (Rowe et al. 2015). We obtain galaxy morphological parameters from the GAMA Sersic Photometry Data Management Unit (DMU) which includes single component Sérsic profile fits to reprocessed r-band Sloan Digital Sky Survey images (Kelvin et al. 2012). We perform certain quality control cuts that are present in the catalogue (`GAL_QFLAG`, `GAL_GHFLAG` and `GAL_CHFLAG` equal to zero, which ensures there were no problems during the parametric fit). We also avoid simulating galaxies with Sérsic indices $n_{\rm s} < 0.3$ and $n_{\rm s} > 6.2$ due to limitations of the GalSim (Rowe et al. 2015). In these cases we set $n_{\rm s} = 0.3$ or 6.2, respectively, which, as discussed in Georgiou et al. (2019b), does not affect the bias calibration significantly. Galaxy profiles are truncated at 4.5 times their half-light radius. The input flux and ellipticity of the galaxy image simulations are measured from the real KiDS images. Galaxies are simulated on a grid, with a 300×300 pixels postage stamp. The simulated PSF is an elliptical Gaussian with ellipticity and full width at half maximum matching the median value of real KiDS images. Finally, we take into account the effect of masking neighbouring galaxies by using the segmentation map of each simulated galaxy as measured in the KiDS images from SExtractor. The masked pixels are replaced with Gaussian noise of the same RMS as the image, to create an individual postage stamp for each galaxy from which the shape is measured.

Using these image simulations we calculate the bias for the five different weight functions considered in this work, with simulations of KiDS r-band images. We confirm that values of m_1 and m_2 agree within the statistical error bars of their measurement and, for simplicity, we use the average value $\langle m \rangle = (m_1 + m_2)/2$. The m-bias was found to be relatively small and is corrected for when computing the average ellipticity components. The values are presented in Table 4.1.

We also look into the radial satellite alignment at different broad band filters and for these we obtain bias values from Georgiou et al. (2019b) (note that when comparing the different filters we use the same weight function $r_{\rm wf} = r_{\rm iso}$). While the galaxy population considered in this work is not the same as in our previous study (i.e. here we only consider shapes of group galaxies and not of the full GAMA galaxy sample) and the m-bias for it could be different, it has been shown in Georgiou et al. (2019b) that the bias does not depend on galaxy properties very strongly for the GAMA galaxy sample. Therefore we choose to use this previously determined g, r and i-band shape m-bias estimation for our

Table 4.1: Mean multiplicative and bias obtained from image simulations for the various weight functions used in the r-band shape measurement.

$r_{\rm wf}/r_{\rm iso}$	$\langle m \rangle$
0.5	0.02145 ± 0.00089
1.0	-0.00373 ± 0.00084
1.25	-0.00652 ± 0.00121
1.5	-0.01120 ± 0.00181
2.0	-0.04945 ± 0.00397

calibration.

Our sample of galaxies has a high SNR (mean value of 300 for r-band images) and the shape measurements are robust against galaxy properties. For example, shapes depend very weakly on galaxy ellipticity (Georgiou et al. 2019b). This guarantees that any trend observed of the alignment signal for different galaxy sub-samples is robust against ellipticity measurements.

“Stray” BGG light

An important systematic effect that could bias the satellite alignment signal is the contamination from light of the group’s brightest galaxy, the BGG. The light measured in images of satellite galaxies includes the light profile of the satellite as well as the faint “tail” from the light profile of the BGG. Ultimately, this will lead to the background light of the satellite being slightly “tilted” towards the direction of the group’s centre, meaning the side of the satellite closer to the group’s centre will have a slightly higher background compared to the side further away from it (see also Sifón et al. 2018). Since to extract the alignment signal we average the tangential ellipticities of all satellite galaxies, this effect gets amplified and can increase the radial alignment signal or even produce a completely artificial one. The BGG contamination will be more severe for satellites closer (in projection) to the group’s centre, as well as for shapes measured using a higher weight function, which will allow more of the BGG’s light to impact the shape measurement.

In order to quantify and correct for the contamination from the BGG’s “stray” light we again use image simulations, very similarly to 4.3.3. We emulate the GAMA galaxy groups by simulating galaxies for each group in their relative positions. The satellite galaxy profiles are truncated at a distance of 4.5 times their half-light radius while for the BGGs, simulated in the centre of the image, the light extends throughout the whole image. The input ellipticity of each satellite is such that the ellipticity modulus, $|\epsilon|$, is obtained using DEIMOS on KiDS r-band images with a weight function $r_{\rm wf} = r_{\rm iso}$ and ϵ_1, ϵ_2 are constructed using a random position angle. This ensures that the input average ellipticity is zero, i.e. the satellites are randomly oriented in our image simulations. The input ellipticity of the BGG is the same as the one observed in the real images. Even though the input ellipticity is based on one weight function, the output ellipticity is corrected for m-bias, which is anyway negligibly small, and our results are not affected by this.

We measure the shapes of the satellite galaxies in the simulated r-band images, which are affected by the light from the BGG. We then subtract the input ellipticity from the output and compute the average tangential ellipticity difference $\langle \Delta\epsilon_+ \rangle$. The results are presented if Figure 4.2 with the y-axis showing the contamination from the BGG in the alignment signal and the x-axis the projected physical distance of the satellite from the BGG, normalized by the group's r_{200} (see Sect. 4.4). As expected, satellites closer to the BGG and shapes with a larger weight function are more heavily contaminated by the BGG's light.

We note that, when comparing the alignment signal between different filters, we use the same correction for the BGG's light. We check that quantitatively similar results are obtained with g and i-band image simulations, with larger error bars, hence we use r-band simulations also for calibrating the alignment measured in the other two bands.

The correction of the BGG's light to the alignment signal is heavily influenced by the fidelity of our image simulations. While simulating galaxies that are representative of the galaxy sample is essential, it is also important to understand the actual light profiles of these galaxies. In our image simulations we assume galaxies can be represented by a single Sérsic profile, but this is a simplification since in reality galaxies have complicated morphologies, such as bulges, bars and star-forming regions. In addition, the isophotes of the BGGs twist their position angles the further away they are, which is not included in our simulations. Also, we choose to truncate the satellite's profile and leave the BGG Sérsic profile to extend indefinitely. Finally, we do not capture the effect of background subtraction applied in the reduction of the KiDS imaging data, which can affect the faint tail of the BGG light. Doing so would require a full reduction of image simulations in a similar manner to KiDS images but would not eliminate all the uncertainties mentioned, and we choose not to do so. Hence, we cannot guarantee that the correction applied is accurate enough. However, as long as the correction is small, compared to a non-zero intrinsic

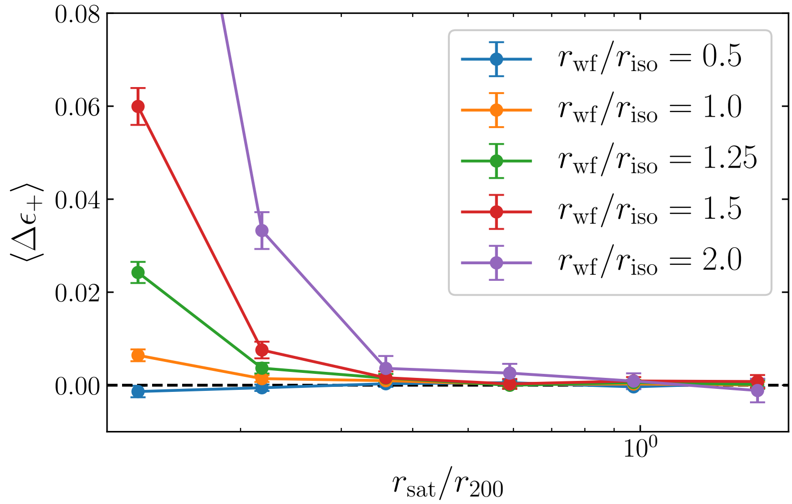

Figure 4.2: Mean tangential ellipticity as a function of distance from the group's center, calculated using $\epsilon^{\rm out} - \epsilon^{\rm in}$ from simulated KiDS r-band images of GAMA groups. The input ellipticity is constructed using the measured $|\epsilon|$ for each satellite galaxy and assigning a random position angle. The output ellipticity is measured from the images, which all contain the corresponding BGG in the centre. Therefore the mean tangential ellipticity difference shows the contribution of the BGG's stray light to the satellite's radial alignment signal measurement.

alignment signal measurement, we can be confident that the measurement is robust against the contamination from the BGG's light.

Lastly, we produced a set of image simulations with the satellite galaxies but without including the BGG. The input alignment signal of these simulated satellites is also zero. Therefore, any bias caused solely by the shape measurement method would be detected in these simulations. Such bias is not found, as the alignment signal measured from the output ellipticities was also measured to be zero.

4.4 Satellite galaxy alignments

We present the satellite radial alignment signal as obtained through measurements of the average tangential ellipticity of our satellite galaxy sample, with respect to the position of the group's BGG. In all of our measurements we correct for multiplicative bias (Table 4.1) as well as subtracting the artificial signal from the BGG's light (Figure 4.2). The shape measurement method is capable of flagging measurements of ellipticity that were problematic (e.g. when the centroid determination failed or the image moments are nonsensical, see also Georgiou et al. 2019b). We reject such galaxies and only consider objects with well defined ellipticity. We calculate the virial mass and radius for each group using the group's luminosity (column `LumB` in the galaxy group DMU). This is an unbiased measure of the group's luminosity, calibrated against specialized mock galaxy catalogues (see Robotham et al. 2011, for details). Using the scaling relation computed specifically for GAMA galaxy groups in Viola et al. (2015), we get the virial mass from

$$\left(\frac{M_{200}}{10^{14}M_{\odot}h^{-1}}\right) = (0.95 \pm 0.14)\left(\frac{L_{\rm grp}}{10^{11.5}L_{\odot}h^{-2}}\right)^{1.16\pm0.13}, \tag{4.6}$$

where $L_{\rm grp}$ is the group luminosity, and the virial radius from

$$M_{200} = \frac{4\pi}{3}\rho_{\rm c}r_{200}^3\,, \tag{4.7}$$

with $\rho_{\rm c}$ the critical density of the universe. We look into the dependence of the signal on the projected distance of the satellites from the group's centre $r_{\rm sat}$, normalized by the group's r_{200}. Trends of the alignment signal with satellite absolute magnitude (but not with the BGG's magnitude) have been observed in clusters (Huang et al. 2018), and we examine this in groups. Groups are also binned in mass, since groups with different gravitational potential could exhibit differences in their alignments. To identify possible trends, we fit the satellite alignment measurements with a power-law function of the form $\langle\epsilon_+\rangle = A(r_{\rm sat}/r_{200})^g$, where A and g are the amplitude and index of the power-law. Fitting for both these parameters yields very weak constraints, and we choose to fix one, specifically the power-law index, to the value of $g = -2$, which seems to describe the data adequately. This arbitrary choice of fitting function is justified by the fact that we are not trying to find a physical model for the alignment signal but rather quantify trends and significance, hence a fully empirical description is enough. We fit our data using the non-linear least

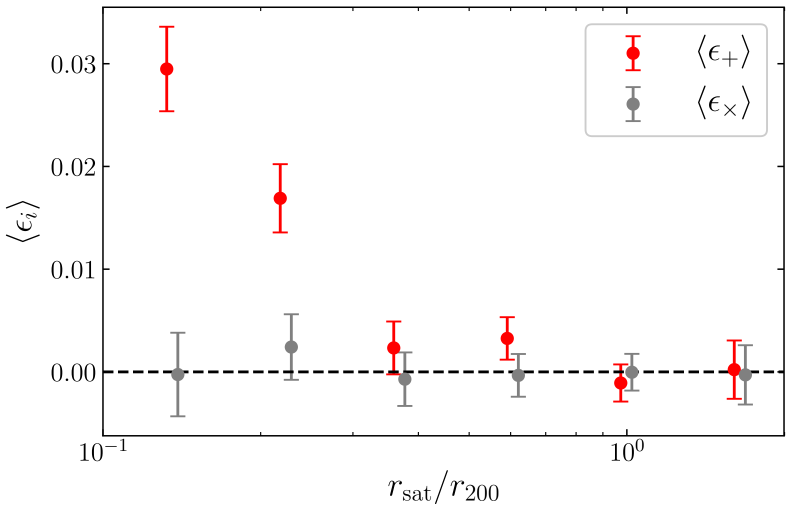

Figure 4.3: Mean tangential/cross ellipticity (red/gray points) versus projected satellite distance from the group's BGG, obtained using satellite shape - BGG position pairs. Positive values of $\langle\epsilon_+\rangle$ indicate radial alignment while randomly oriented galaxies exhibit $\langle\epsilon_+\rangle = 0$. Results shown for shape measurements obtained from r-band images, with $r_{\rm wf} = r_{\rm iso}$.

squares fitting method from the SCIPY python package. The error bars in our measurements are standard errors. We have checked that the mean tangential ellipticity distribution is Gaussian and the standard error should accurately reflect the significance of a detection. We use groups with 3 or more members (including the BGG). Our results do not change within our error bars when using groups with 5 or more members.

4.4.1 Full sample and wavelength dependence

We measure the satellite radial alignment signal for our galaxy group sample. We reject failed shape measurements as well as galaxies residing in masked regions (except for secondary and tertiary stellar halos, which are expected to be too dim to affect the shape measurements). This leaves us with 29953 satellite-BGG pairs. We first present results for shapes measured in r-band images, since these are the deepest observations with the smallest shape noise in our sample. The weight function used is $r_{\rm wf} = r_{\rm iso}$, and we use this weight function for all subsequent measurements, unless otherwise stated. The results are shown in Figure 4.3. Significant radial alignments are observed for satellites close to the BGG. The alignment signal decreases for satellites further away, eventually reaching zero at scales $r_{\rm sat} \sim r_{200}$. We also note that the cross ellipticity component is consistent with zero, which holds true for all subsequent measurements.

We then compute the alignment signal using shapes from Georgiou et al. (2019b) (which are based on KiDS DR3, see Sect. 4.2.2), for g, r and i-band observations. We consider only galaxies that are not masked or flagged in any of the three filters, and compare the alignment signals in Figure 4.4. It is clear that in the smallest radial bin $r_{\rm sat} \sim 0.13 r_{200}$ the alignments in g and i are much larger than the r-band. Even though the BGG's "stray light" correction for this radial bin is large (~20% of the r-band signal in Fig. 4.3) and robust quantitative conclusions are hard to draw, there is a significant excess alignment signal in the first bin, observed in g and i-band in comparison to the r-band. A possible concern is that bright sources (such as the brightest group galaxy) have a higher flux in r-band compared to g- or i-band, and therefore the background subtraction of the area around this bright source can be more aggressive in r-band images compared to g- and i-band. However, we do not look into this further in this work.

4.4.2 Absolute magnitude dependence

We study the dependence of satellite alignments on the r-band absolute magnitude of satellites and centrals. Magnitudes are obtained from stellar population fits to galaxy SEDs in multiple bands using LAMBDAR, made available through the GAMA `StellarMassLambdarv20` DMU (Taylor et al. 2011; Wright et al. 2016). Histograms can be seen in the top panel of Fig. 4.5. We first look at the dependence on the satellite magnitude, in Figure 4.6, top panel. In order to quantify any dependence on satellite magnitude, we fit a power-law with a fixed slope of -2 to all radial bins except the first (due to the BGG light correction being too large to make robust quantitative statements about this bin). The fit is also shown in Figure 4.6, with the 1-σ confidence intervals. No clear trend is observed for the three magnitude bins within the 1-σ limit.

Similar results are obtained when considering the central galaxy's absolute magnitude. This is shown in Figure 4.6, bottom panel, where again the 1-σ limits are not strong enough to identify any trends in the alignment signal.

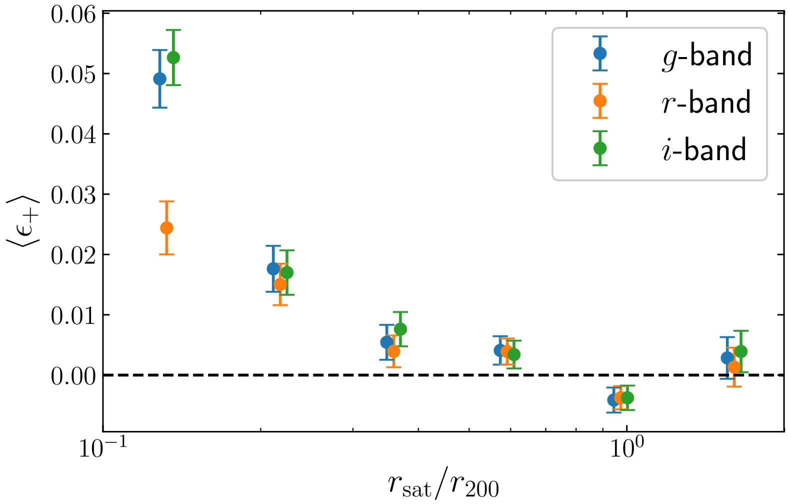

Figure 4.4: Mean tangential ellipticity versus satellite distance from the group's BGG, obtained using satellite shape - BGG position pairs. Positive values indicate radial alignment, randomly oriented galaxies give $\epsilon_+ = 0$. Results shown for shape measurements obtained from g, r and i-band images.

When looking at galaxy clusters, Huang et al. (2018) found a dependence of the alignment with satellite absolute magnitude, which we do not detect. This could mean that this dependence is stronger in clusters than groups. However, the galaxy shapes in Huang et al. (2018) were not corrected for shape measurement biases. Multiplicative bias scales with the galaxy SNR, which can be correlated with its absolute magnitude, and can drive part or all of this dependency, so a robust conclusion is unclear.

4.4.3 Group mass dependence

Here we look into the dependence of the satellite alignment signal for groups of different mass. We calculate virial masses of groups according to equation (4.6). A histogram of the resulting group masses is shown in the bottom panel of Fig. 4.5. We present the average tangential ellipticity versus distance of satellite to the group's BGG, binned in M_{200}, in Figure 4.7. We fit a power-law with fixed

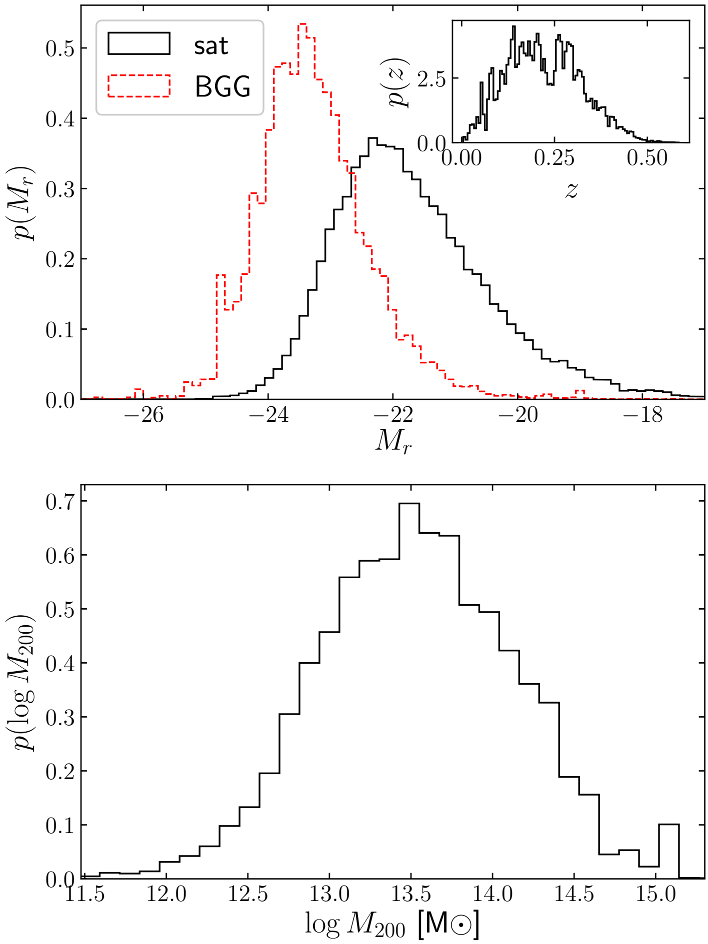

Figure 4.5: *Top*: Histograms of the absolute r-band magnitude of the BGG (solid black) and satellite (dashed red) galaxy samples. The inset figure shows the distribution of the galaxy group redshifts. *Bottom*: Histogram of the group virial mass, computed with Eq. (4.6).

amplitude as previously, but do not see any significant trend within the 1-σ

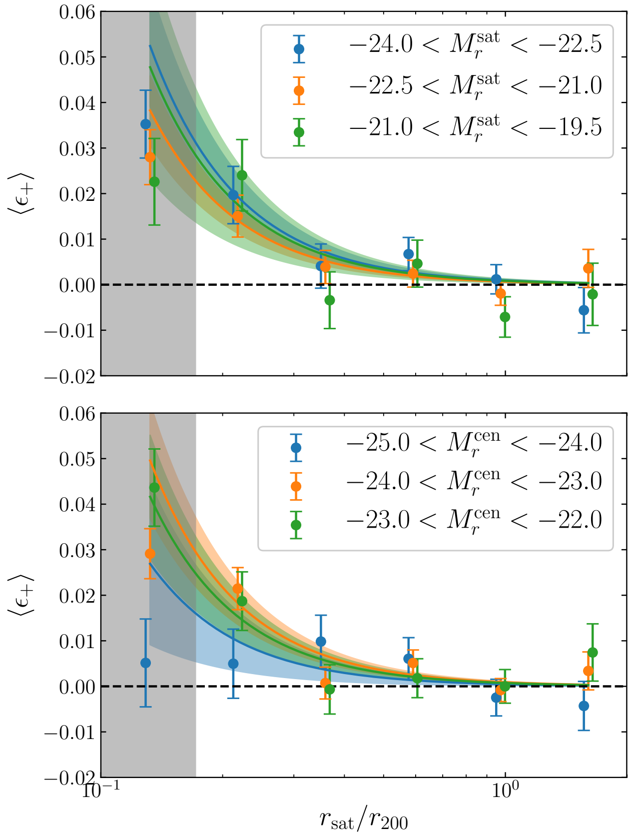

Figure 4.6: Mean tangential/cross ellipticity components versus satellite distance from the BGG, obtained using satellite shape - BGG position pairs. *Top:* binned in satellite's r-band absolute magnitude. *Bottom:* binned in BGG's r-band absolute magnitude. Power-law fits with fixed index are over-plotted, with the 1-σ uncertainty on the fit, for the three bins. The grey area covers the radial bins over which we regard the BGG light correction to be too significant, and these scales are not used for our model fitting. Shapes were measured in r-band for $r_{\rm wf} = r_{\rm iso}$.

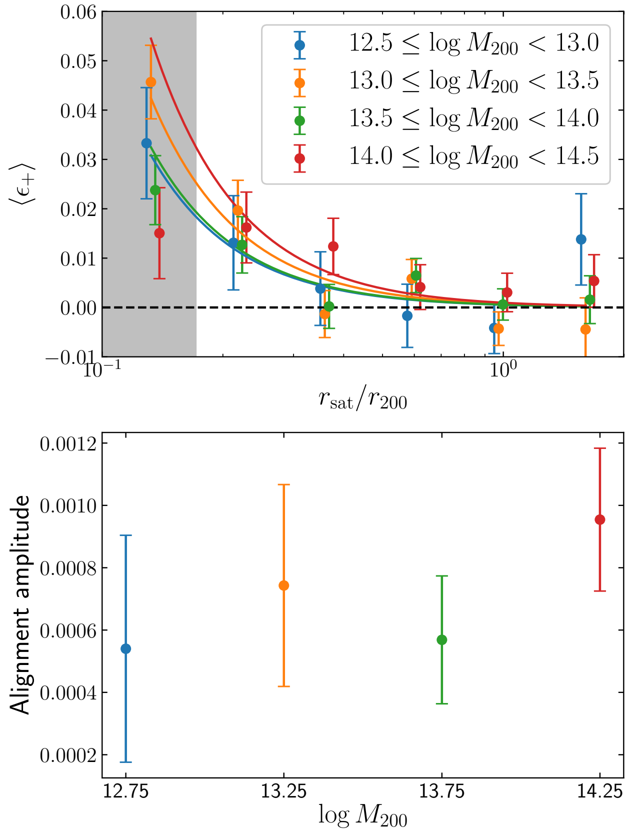

Figure 4.7: *Top:* mean tangential/cross ellipticity as a function of satellite distance from the group's BGG, obtained using satellite shape - BGG position pairs, binned in the group's M_{200}. The best fit power-law with a fixed slope is overplotted for each mass bin. The grey area covers the radial bins over which we regard the BGG light correction to be too significant, and these scales are not used for our model fitting. Shapes were measured in r-band for $r_{\rm wf} = r_{\rm iso}$. *Bottom:* Amplitude of the power-law fit to the alignment signal for each individual group mass bin.

limit.

4.4.4 Dependence on star formation rate

We now distinguish our satellite galaxy sample to satellites that may have arrived in the group recently or have been orbiting for a longer period. Galaxies entering a group will experience star formation quenching through several processes, such as tidal stripping. Therefore, these members will have mostly old stellar populations and appear red in colour. Galaxies that have recently fallen into the group will generally have a higher star formation rate with new stars constantly generated, and hence will appear bluer (except for galaxies that are already red). Thus, a proxy for distinguishing between "old" and "new" group members would be using colour and specific star formation rate information.

We use the GAMA `StellarMassesLambdarv20` catalogue to obtain dust-corrected, rest-frame $g-i$ colour information for our satellite galaxy sample, and the `MagPhysv06` GAMA DMU (Baldry et al. 2018; Driver et al. 2018) which contains specific star formation rate (sSFR) measurements acquired from running the SED-fitting code MagPhys (da Cunha et al. 2008). We show the $g-i$ colour of satellites against the sSFR in Figure 4.8. It is clear that the galaxies are divided into two distinct populations: blue galaxies with high star formation rate (in the bottom right of the Figure) and red galaxies with low star formation rate (in the top left of the Figure). By visual inspection, we divide our galaxy sample into blue and red galaxies, using the red line in Figure 4.8,

$$g-i = 0.21\log(\mathrm{sSFR}\,\mathrm{yr}^{-1}) + 3.03\,. \tag{4.8}$$

We compute the alignment signals of red and blue galaxies and show the results in Figure 4.9. It is clear that red satellites have a much stronger alignment signal than blue ones. This behaviour can be explained considering that red galaxies have likely spent more time in the group environment and have had more time to interact gravitationally with the group and become aligned with it compared to blue satellites that have likely been in the galaxy group for less time. Blue satellites are also generally rotationally supported and have a different alignment mechanism than red, pressure supported galaxies. We note that the difference in the alignment signal observed here cannot be attributed to differences in the ellipticity distributions of the two sub-samples, as the ellipticity estimation for our sample does not depend strongly on the galaxy ellipticity (Georgiou et al. 2019b).

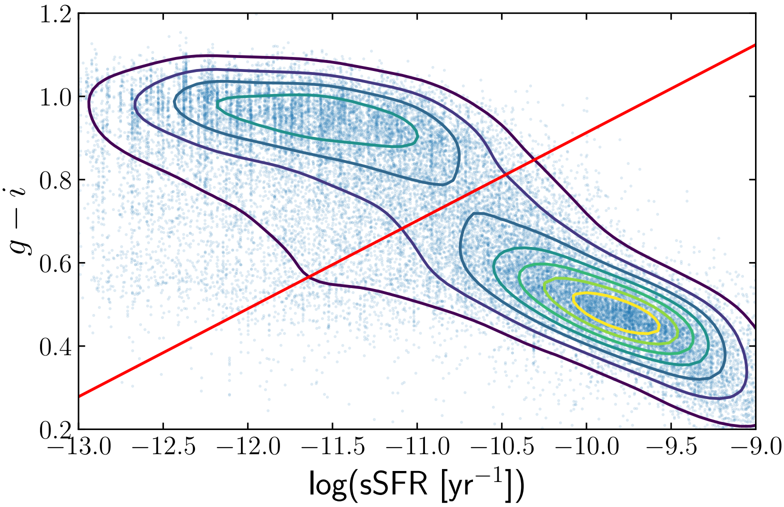

Figure 4.8: Rest-frame, dust-corrected $g-i$ colour of our satellite galaxy sample against their specific star formation rate. Smoothed density contours are shown, with dense regions appearing more yellow. The red line indicates the cut performed to divide our galaxy sample into blue star forming, and red galaxies with lower star formation rate.

4.4.5 Galaxy scale dependence

Lastly, we perform the satellite radial alignment measurement with shape measurements obtained using weight functions of different sizes. This results in shape measurements being more sensitive to the different parts of the galaxies. For example, a smaller weight function will mostly probe the shape of the inner part of a galaxy (e.g. the bulge) while a larger weight function will be more sensitive to the shape of the outer part (e.g. the disk). We measure shapes of galaxies using five different weight function sizes r_{wf}, which corresponds to the scale of the initial (circular) Gaussian weight function applied when measuring galaxy shapes. This weight function eventually matches the ellipticity of the galaxy after several matching iterations, while retaining its original size (see Sect. 4.3.2).

In Figure 4.10, we show the alignment signal for the full satellite sample,

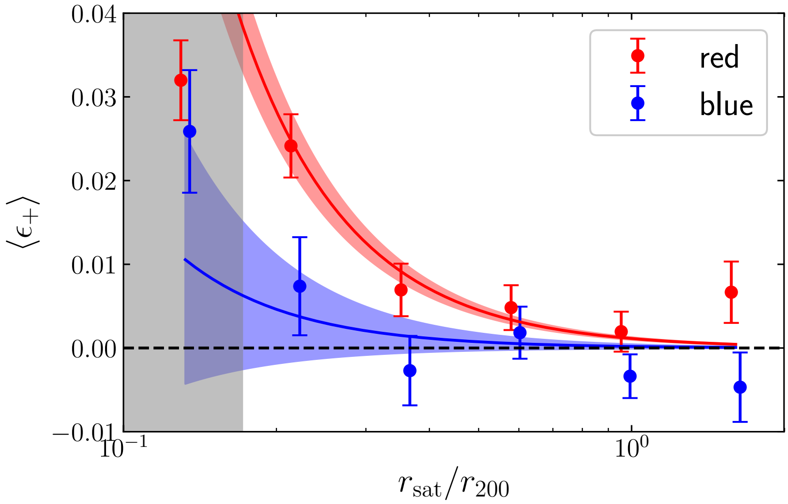

Figure 4.9: Average tangential ellipticity against projected satellite distance from the group BGG, obtained using satellite shape - BGG position pairs. Results shown for red, low sSFR and blue, high sSFR galaxies. Power-law fits of fixed index are overplotted, with the shaded region indicating the 1-σ confidence limit. The grey area covers the radial bins over which we regard the BGG light correction to be too significant, and these scales are not used for our model fitting.

as computed for the five different weight function sizes that are related to the isophote at 3σ above the background noise. Note that the x-axis of this plot has different limits than similar figures in the section. We use only 4 instead of 5 bins for the largest weight function, which suffers more severely from contamination from the BGG's light. Fitting a power-law model with a fixed index of -2 we can see that the alignment signal increases for larger weight functions (bottom panel of Figure 4.10). In the bottom panel of the figure we also show the alignment amplitude for red and blue galaxies. We see that blue galaxies exhibit an increase in alignment for larger weight functions, but are always smaller than red galaxies. For the larger weight function sizes, the blue alignment signal is significantly non-zero.

We note here that the ellipticity distribution of galaxies obtained from the 5

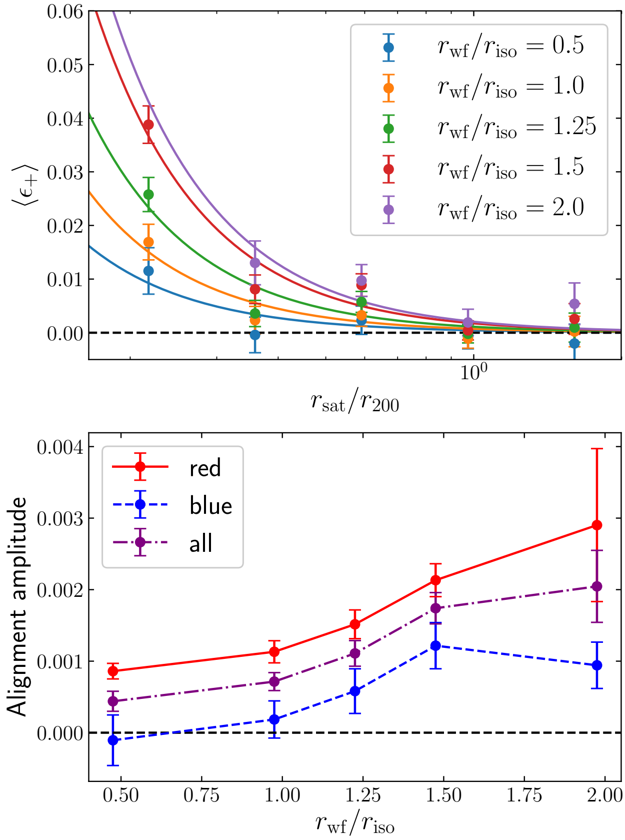

Figure 4.10: *Top:* Average tangential ellipticity of the *full* satellite galaxy sample versus projected satellite distance from the group BGG, obtained using satellite shape - BGG position pairs. Results shown for different weight function sizes used in the shape measurement process. The $r_{\rm wf}$ indicates the size of the initial weight function and $r_{\rm iso}$ is the isophote of the galaxy. *Bottom:* Amplitude of power-law fits with fixed exponent, to the average ellipticities for all, red and blue galaxies, for the different weight function sizes involved. Lines connecting the data points added for clarity.

different weight functions are not identical, as is expected since galaxy isophotes twist in the outer regions (first observed by Evans 1951). Since the mean tangential ellipticity (shown in Fig. 4.10) depends on the ellipticity distribution, the observed alignment signal dependence could be caused by these differences. However, we have checked, using a different alignment estimator, the mean satellite alignment angle $\langle\phi_{\rm sat}\rangle$ (Fig. 4.1), that the behaviour is present. Therefore, the behaviour of Fig. 4.10 cannot be explained by the differences of ellipticity measurements between the different weight functions.

Recent measurements of alignments in groups and clusters have yielded conflicting results (Schneider et al. 2013; Chisari et al. 2014; Sifón et al. 2015; Huang et al. 2018). Cluster studies have been performed using shape measurement methods that optimize the size of the weight function with SNR (such as the KSB or re-Gaussianization methods) and find no significant alignment (e.g. Chisari et al. 2014; Sifón et al. 2015). We have tested this approach with DEIMOS and found that the highest SNR is obtained when the weight function is as small as possible, where the bulge dominates the light profile. Given that the satellite alignment signal drops for smaller weight functions (Figure 4.10), studies using this approach are not expected to detect a strong alignment signal. In addition, the shape noise and statistics of these studies drive up the error bars (in comparison to our work) and make the detection even less likely. Model-fitting shape measurement methods have also been used in some of the studies above, but since the bulge of the galaxy carries most of the light profile it is also possible that the derived shape from such methods is greatly influenced by the inner galaxy regions, and the alignment signal is again hard to detect. In GAMA groups, Schneider et al. (2013) looked into satellite alignments with shapes from similar shape measurement methods applied to SDSS images and found no significant alignment, which can be accounted for in the same way as for the cluster studies.

In contrast to the studies described above, Huang et al. (2018) looked at satellite alignments in clusters using three different shape estimators: moment-based, model-fitting and isophote fitting. They found a significant alignment that decreases for galaxies further away from the BGG, in agreement with out results. A difference in alignment was also observed for the three different estimators, which are sensitive to different galaxy scales. However, these estimators have different multiplicative biases, which were not corrected for, and understanding how much of the bias drives these differences is non-trivial.

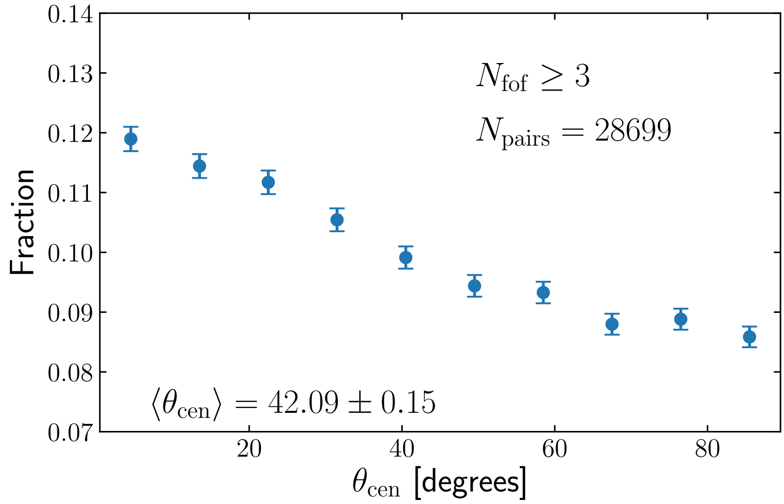

Figure 4.11: Distribution of the angle $\theta_{\rm cen}$ between the BGG's semi-major axis and the line connecting the BGG-satellite pair. The mean value of the angle is shown in the bottom left of the plot.

4.5 BGG shape - satellite position alignment

Intra-halo alignments can have multiple components, as one can correlate the shape or position of satellites with the shape or position of the central galaxy. In the previous section we have focused on the alignment of satellite shapes with the position of the central galaxy. Another interesting component, useful when constructing the halo model for intrinsic alignments, is the alignment of the central galaxy shape with the position of satellites. This is computed through Eq. 4.3 by substituting the ellipticity components with the ones of the BGG.

We compute the angle $\theta_{\rm cen}$ between the BGG's semi-major axis and the line connecting a pair of BGG-satellite galaxies. When this angle is $0°$ (or $90°$) the BGG is pointing radially (or tangentially) to the direction of the satellite. When $\langle\theta_{\rm cen}\rangle = 45°$ the satellites are randomly (circularly) positioned around the BGG but when this average angle is smaller than $45°$, they are mostly distributed along the BGG's semi-major axis. In Figure 4.11 we plot the fraction of BGG-satellite pairs against the value of $\theta_{\rm cen}$. We see that the distribution

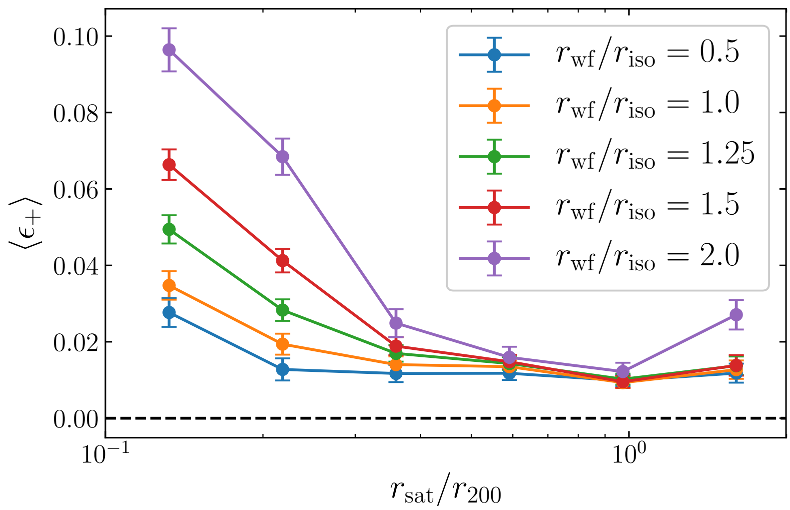

Figure 4.12: Average tangential ellipticity of the BGG shape with respect to the satellites position, as a function of the projected distance of the satellite to the BGG. Results are obtained using 5 different weight function sizes, and are shown with a different colour.

is not uniform, with more satellites positioned close to the BGG's semi-major axis rather than perpendicular to it. The average angle is computed to be $\langle \theta_{\rm cen} \rangle = 42.09 \pm 0.15$, which is significantly lower from 45°.

We also compute the average tangential ellipticity of the BGG's shape with respect to the satellite's position. This statistic is more easily related to the halo model formalism, and the mean ϵ_+ is shown in Figure 4.12 as a function of galaxy pair separation, for shapes obtained with the 5 different weight functions. The average tangential ellipticity is non-zero and higher for galaxy pairs closer together, dropping to a plateau at larger separations. In addition, the alignment is stronger for shapes obtained with a larger weight function.

From this we conclude that satellites are preferentially distributed along the BGG's semi-major axis. Satellites closer to the BGG are more tightly aligned with this axis. Furthermore, the outer regions of the BGG are more aligned with the overall satellite distribution, as can be seen from the dependence of the alignment signal on the weight function size, particularly on smaller scales.

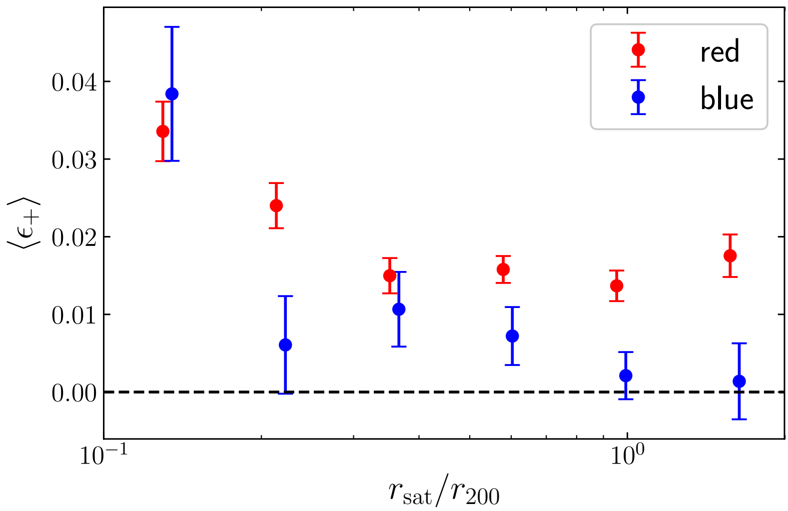

Figure 4.13: Average tangential ellipticity of the BGG shape with respect to the satellites position, for red and blue BGGs. Results are obtained using $r_{\rm wf} = r_{\rm iso}$.

Assuming that the satellite distribution traces the shape of the dark matter halo of the galaxy group, we conclude that the outer regions of the BGG are aligned more strongly with the group halo shape than the inner regions. This could be the result of the gravitational interaction of the BGG with the dark matter halo, or a reflection of the fact that streams of infalling matter in a galaxy group follow the ellipticity of the group's halo.

We now split the BGGs into two populations: blue, high sSFR and red, low sSFR galaxies, using Eq. (4.8). This essentially splits the group samples into groups with a red or a blue central galaxy. We note here that 37% of groups in our sample contain a blue BGG; these are likely groups that were formed recently, and are very different from galaxy clusters, where the brightest cluster galaxy will almost always be red. The alignment of the BGG shape with the satellite positions for these two sub-samples is shown in Figure 4.13. We see that the alignment is driven mostly by red BGGs, with blue BGGs being strongly aligned with their innermost satellites, weakly aligned in intermediate scales and unaligned with the positions of their outermost satellites. These results are in agreement with what has been found in recent literature (e.g. Yang et al. 2006;

van Uitert et al. 2017; Wang et al. 2018).

4.6 Global intrinsic alignments

In the previous sections we saw that satellite-BGG and BGG-satellite alignments exhibit a galaxy scale dependence, with the outer galaxy regions aligned more strongly than the inner ones. This naturally leads to the question whether halo-halo alignments (among central galaxies) also exhibit this dependence. We therefore calculate the projected shape - position correlation function from a shape and density sample consisting of the non-satellite galaxies of the GAMA group catalogue, which we call central galaxies sample. The correlation function is computed from

$$w_{g+}(\mathbf{r}_p) = \int_{-\Pi_{\max}}^{+\Pi_{\max}} \xi_{g+}(\mathbf{r}_p, \Pi) \mathrm{d}\Pi \,, \tag{4.9}$$

where r_p and Π is the transverse and line of sight separation between a galaxy pair, respectively, and ξ_{g+} is the three dimensional position-shape correlation function, measured using the modified Landy-Szalay estimator (Landy & Szalay 1993; van Uitert & Joachimi 2017)

$$\xi_{g+}(\mathbf{r}_p, \Pi) = \frac{S_+D}{D_\mathrm{S}D} - \frac{S_+R}{D_\mathrm{S}R} \,. \tag{4.10}$$

In the above equation we define three galaxy samples, density (D), shape (S) and random points (R) with the density of the shape sample being D_S. The quantities D_SD and D_SR are normalized galaxy pairs (see e.g. Kirk et al. 2015, for more details) and

$$S_+D = \sum_{i \neq j} \epsilon_+(i|j) \,. \tag{4.11}$$

Galaxy i is selected from the shape sample and j from the density sample. Similarly we compute S_+R, using the random catalogues specifically produced for GAMA galaxies (Farrow et al. 2015).

Following Georgiou et al. (2019b), we compute the difference in alignment

$$\Delta w_{g+} = w_{g+}(r_\mathrm{wf} = 2r_\mathrm{iso}) - w_{g+}(r_\mathrm{wf} = r_\mathrm{iso}) \,, \tag{4.12}$$

where the first term of the right hand side is computed with shapes obtained in the r-band, using a weight function $2r_\mathrm{iso}$ and the second term using $1r_\mathrm{iso}$, both from shape and density samples of GAMA central galaxies. If Δw_{g+} is

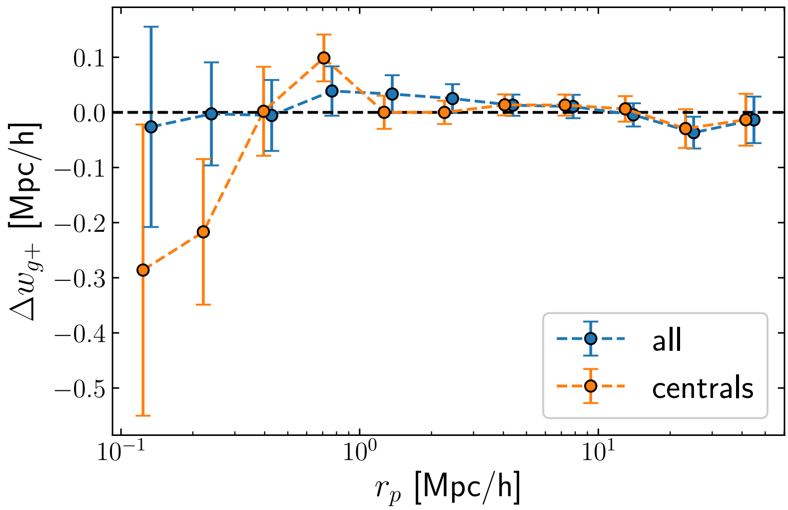

Figure 4.14: Intrinsic alignment signal difference, as measured from shape measurements of two different weight functions, $r_{\rm wf} = \{r_{\rm iso}, 2r_{\rm iso}\}$, as a function of projected galaxy pair separation. Results obtained from shape and density samples consisting of central galaxies are shown with an orange dashed line, while the same results using all GAMA galaxies are shown with the blue solid line. Points are horizontally displaced for clarity.

significantly positive then central galaxies also exhibit a similar scale dependence to the one seen from satellite galaxies in Section 4.4.5.

To compute error bars for our measurements we run 100 realisations of the Δw_{g+} measurement but adding a random position angle to galaxies each time. Georgiou et al. (2019b) showed that error bars obtained this way agree with bootstrap estimated errors, while other techniques such as jackknife might not be optimal. We ensure that the same galaxies are used when computing the two w_{g+} terms of (4.12) which ensures that the sample variance contribution to the error bar can be neglected, since we are subtracting signals affected by the same sample variance (see Georgiou et al. 2019b, for a discussion).

Figure 4.14 shows the results for the alignment signal difference of central galaxies using two weight functions in the shape measurement. The alignment difference Δw_{g+} is consistent with zero. It is clear that, for central galaxies, no galaxy scale dependence is evident, and the two alignment measurements agree well within the errorbars. In addition, we repeat the same exercise using the full GAMA galaxy sample and find differences consistent with zero, except for intermediate scales, $\sim 1-2$ Mpc$/h$, where the alignment signal difference is consistently positive. However the error bars of our measurements do not allow for a robust detection.

Studies of cosmological simulations have measured a dependence of the global intrinsic alignment signal on the way galaxy shapes were determined (e.g. Velliscig et al. 2015b; Chisari et al. 2015; Hilbert et al. 2017). Shapes derived with a radial weighting scheme (therefore suppressing outer galaxy regions) revealed a lower amplitude of IA than shapes without a weight, which is not in agreement with our results. However, shapes that have been obtained with a weighting scheme must also suffer from shape bias, as well as bias due to the finite number of particles used to define galaxies. The effect of such bias is unclear. Furthermore, the intrinsic alignment amplitude measured in these simulations was found to be higher than the amplitude measured in GAMA (Johnston et al. 2019), and the galaxy population in these simulations does not necessarily resemble the sample we used in this work, therefore a direct robust comparison is difficult.

Comparing to other observations, Singh & Mandelbaum (2016) found, using low redshift luminous red galaxies, that alignment measurements with different shape estimators resulted in different inferred intrinsic alignment amplitudes. One of the possible reasons for this is that these shape estimators are sensitive to different galaxy scales. However, we do not find such a dependence in this work when we consider centrals or the full galaxy sample. This can be due to the fact that the sample of galaxies in the two studies are different, with the GAMA sample containing also fainter, blue galaxies with a wider redshift range. Indeed, the alignment signal of GAMA galaxies is measured to have a much smaller amplitude (Johnston et al. 2019) than the galaxies in Singh & Mandelbaum (2016). Multiplicative bias can also cause such a difference, as the observed alignment signal scales linearly with bias (Eq. 24 Singh & Mandelbaum 2016), and the shape measurements in Singh & Mandelbaum (2016) were not corrected for it.

4.7 Conclusion

We quantified the alignment of satellite galaxies with respect to the BGG in galaxy groups. Using galaxies from the GAMA survey and KiDS imaging data in g, r and i-band filters we ensured a high fidelity galaxy group catalogue and accurate shape measurements from the DEIMOS shape measurement method. We controlled systematic effects due to the shape measurement process as well as contamination to the alignment signal from the extended light profile of the BGG with dedicated image simulations.

The satellite alignment signal was obtained by calculating the average tangential ellipticity of satellite galaxies relative to the BGG position. Our measurements for shapes in the r-band revealed a significant radial satellite alignment signal that is stronger for satellites closer to the BGG and vanishes at large projected separations. Measurements in the g and i-band images implied an apparent stronger alignment in these filters compared to r-band observations, but the data did not allow for a robust conclusion. We did not detect any significant trend of the amplitude of the satellite alignment signal as a function of satellite/BGG absolute magnitude or of group mass.

We also split the satellite sample into red galaxies with low sSFR and blue galaxies with high sSFR. We found that red satellites have a higher alignment signal than blue satellites. This behaviour could arise from the fact that blue satellites have spent less time in the environment of the group, therefore having weaker alignment with it, as well as the difference in alignment mechanism between the two galaxy populations.

Furthermore we probed the galaxy scale dependence of satellite alignments. We varied the radial weight function employed during the shape measurement process, which results in shape measurements that reveal different parts of the galaxy. A small weight function gives more emphasis to the central region of a galaxy while shapes with a large weight function are also affected by the galaxy outer regions. Fitting a power-law function with a fixed slope of -2, we found a dependence of the satellite radial alignment on the weight function size for both red and blue satellite galaxies. The alignment signal is stronger for outer satellite galaxy regions. Notably, we detected a strong alignment signal for blue satellites around their BGG when using the two largest weight functions. These results are in line with the expectation that intrinsic alignments are mainly generated by tidal forces and outer, less bound, regions of a galaxy are more affected by these forces.

We found that satellites are preferentially distributed along the semi-major axis of the BGG, with the innermost satellites being more strongly aligned than the outermost. In addition, when the BGG's shape is determined with a larger weight funciton, the alignment at small scales is stronger, meaning that outer isophotes of the BGG are more strongly aligned with their satellites. Splitting the sample into groups with a red or a blue BGG, we found that red BGGs are more strongly aligned than blue ones, the latter being aligned mostly with their close satellites. It is not clear whether the BGG-satellite alignment scale dependence is caused by the tidal nature of the intrinsic alignments or from the direction of the in-falling matter into the galaxy group.

We also examined whether the global intrinsic alignment signal (correlating all galaxy shapes with all galaxy positions) depends on the galaxy scale. We computed the projected position-shape correlation function using shapes from two different weight functions and then subtracted the two alignment measurements. We found that the intrinsic alignment signal difference, when using only central galaxies, is consistent with zero; no galaxy scale dependence is detected for central galaxies. When we consider the whole GAMA galaxy sample there seems to be a positive difference of alignment signal in intermediate scales, which however is small compared to our error bars. From this result we conclude that the global intrinsic alignment signal does not depend strongly on the galaxy scale, within the errors of our measurements.

The GAMA sample is flux limited and the galaxy population resembles samples commonly used in cosmic shear studies (see e.g. Johnston et al. 2019). Since the galaxy scale dependence on the alignment signal is measured to be consistent with zero, we conclude that weak gravitational lensing studies that use informative priors of intrinsic alignments, where the alignment signal is measured with a different shape estimator than the shear signal, will not be biased because of the difference in shape measurements.

Chapter 5

Halo ellipticity constrained from a pure sample of central galaxies in KiDS-1000

Based on
C. Georgiou, H. Hoekstra, K. Kuijken, M. Bilicki,
A. Dvornik, T. Schrabback, A. Wright
to be submitted to A&A

5.1 Introduction

The current standard model of cosmology, dubbed ΛCDM, has been very successful in describing a large number of independent cosmological probes, such as CMB observations (e.g. Planck Collaboration et al. 2018), galaxy clustering signal (e.g. Alam et al. 2017) and Baryon Acoustic Oscillations (e.g. Anderson et al. 2014; Bautista et al. 2018), among many others. According to this model, dark matter makes up for the majority of the matter density content of the Universe and provides the seeds upon which galaxies and larger structures can form and evolve.

From numerical simulations, it is understood that dark matter forms halos that are roughly triaxial, which appear elliptical in projection (Dubinski & Carlberg 1991; Jing & Suto 2002). Observations on the shape of these halos can, therefore, be used as a test for the current cosmological model, as well as extensions to it, such as modifications to the gravity theory or the dark matter component (e.g. Hellwing et al. 2013; L'Huillier et al. 2017; Peter et al. 2013; Elahi et al. 2014).

Observationally, many attempts have been made towards measuring halo ellipticities. Techniques include satellite dynamics (e.g. Brainerd 2005; Azzaro et al. 2007; Bailin et al. 2008; Nierenberg et al. 2011), tidal streams in the Milky Way (e.g. Helmi 2004; Law & Majewski 2010; Vera-Ciro & Helmi 2013), HI gas observations (e.g. Olling 1995; Banerjee & Jog 2008; O'Brien et al. 2010), planetary nebulae (e.g. Hui et al. 1995; Napolitano et al. 2011), X-ray observations (e.g. Donahue et al. 2016) as well as strong lensing (e.g. Caminha et al. 2016), also accompanied by stellar dynamics (e.g. van de Ven et al. 2010). These techniques rely on luminous tracers of the dark matter shape, which can lead to biases, complicate the interpretation of the measurements and cannot provide information on the larger scales of the dark matter halo, where visible light is absent.

One observational technique that does not suffer from this drawback is weak gravitational lensing, the coherent distortion of light rays from background sources from the intervening matter distribution (for a review, see Bartelmann & Schneider 2001). Since gravitational lensing is sensitive to all matter (also non-baryonic), it serves as a great tool to study the dark matter halos. The distortion of the galaxy shapes due to weak lensing is very small, and in order to extract a measurable signal one needs to statistically average over large ensembles of galaxies. If the stacking is done around other galaxies, a technique called galaxy-galaxy lensing, only the matter at the lens galaxy redshift contributes coherently to the lensing signal, and the structures along the line of sight simply add noise to the measurement.

Triaxial dark matter halos will cause an azimuthal variation in the weak lensing signal, enhancing it along the direction of the semi-major axis of the projected halo and reducing it along the semi-minor axis. For very massive structures, such as large galaxy clusters, this variation is strong enough to be measured for individual (e.g. Corless et al. 2009; Umetsu et al. 2018) or stacked weak lensing maps of cluster samples (Evans & Bridle 2009; Oguri et al. 2012). For galaxy-scale halos, this variation can be measured by weighting the lensing measurements according to the halo's semi-major axis.

In most applications of weak lensing based measurements of dark matter halo ellipticity, the lens galaxy semi-major axis is used as a proxy for the dark matter halo axis (Hoekstra et al. 2004; Mandelbaum et al. 2006a; Parker et al. 2007; van Uitert et al. 2012; Schrabback et al. 2015; van Uitert et al. 2017). The measured quantity is, then, the ratio of the halo ellipticity to the galaxy ellipticity, weighted by the average mis-alignment angle between the two, i.e. $f_{\rm h} = \langle \cos(2\Delta\phi_{\rm h,g})|\epsilon_{\rm h}|/|\epsilon_{\rm g}|\rangle$. This makes the measurement of $f_{\rm h}$ a useful step in determining the alignment between the dark matter halo and its host galaxy. The mis-alignment angle has been measured in numerical simulations, with results from the most recent hydrodynamical simulations suggesting a value of $\langle\Delta\phi_{\rm h,g}\rangle \sim 30^\circ$ (Tenneti et al. 2014; Velliscig et al. 2015a; Chisari et al. 2017). The mis-alignment is decreasing with decreasing redshift and increasing halo mass, which suggests that massive central galaxies are expected to carry most of the signal. Indeed van Uitert et al. (2017) detected a non-zero halo ellipticity with $\gtrsim 3\sigma$ significance using only ~ 2500 galaxies by using an friends-of-friends-based group catalogue to remove satellites from the lens sample.

Motivated by this, we aim to define a sample of central galaxies with very high purity from a photometric galaxy sample, and use these as lenses to measure the anisotropic weak lensing signal around them. We use the fourth data release of the Kilo-Degree-Survey (KiDS, Kuijken et al. 2019) and construct an algorithm that preferentially selects central galaxies using apparent magnitudes and photometric redshifts. These redshifts are obtained from a machine learning technique, focusing on the bright-end sample of galaxies in KiDS, and achieve very high precision (Bilicki et al. 2018). We validate our central galaxy selection by quantifying the sample's purity using the group catalogue from the Galaxy And Mass Assembly survey (GAMA, Driver et al. 2011; Robotham et al. 2011), as well as mock galaxy catalogues from the MICE Grand Challenge run (Crocce et al. 2015).

In Sec. 5.2 we present the data used for constructing and validating our lens sample, consisting of highly pure central galaxies, which we describe in detail in Sec. 5.3. The methodology used to measure the lensing signal is described in Sec. 5.4. The results obtained are shown in Sec. 5.5 and we discuss the measurements and conclude with Sec. 5.6. To calculate angular diameter distances we use a flat ΛCDM cosmology with parameters obtained from the latest CMB constraints (Planck Collaboration et al. 2018), i.e. $H_0 = 67.4$ km/s/Mpc and $\Omega_{m,0} = 0.313$.

5.2 Data

Measuring the anisotropic lensing signal requires a wide survey of deep imaging data, so that accurate unbiased galaxy shapes can be measured and the lensing signal can be statistically extracted. For this reason, we use data from KiDS. Moreover, massive central galaxies are expected to yield the highest signal-to-noise ratio (SNR) for anisotropic lensing; we thus need a way of selecting a pure sample of central galaxies as well as a means to validate our selection. To this end, we make use of the GAMA survey, as well as mock catalogues from the Marenostrum Institut de Ciéncies de l'Espai (MICE) Grand Challenge galaxy catalogue.

5.2.1 KiDS-1000

KiDS[1] (de Jong et al. 2015, 2017; Kuijken et al. 2019) is a deep imaging ESO public survey carried out using the VLT Survey Telescope and the OmegaCam camera. The survey has covered 1,350 deg^2 of the sky in three patches in the north and south equatorial hemispheres, in four broad band filters (u, g, r and i). The mean limiting magnitudes are 24.23, 25.12, 25.02 and 23.68, for the four filters respectively (5σ in a $2''$ aperture). The survey was specifically build for weak lensing science and the image quality is high, with small nearly round point-spread function (PSF), especially in the r-band observations, which were taken during dark time with the best seeing conditions. We use the fourth data release of the survey, with 1006 1×1 deg^2 image tiles (KiDS-1000).

KiDS is complemented by the VISTA Kilo-Degree Infrared Galaxy Survey (VIKING, Edge et al. 2013), which has imaged the same footprint as KiDS in the near-infrared (NIR) Z, Y, J, H and K_s bands. This addition allows for the determination of more accurate photometric redshifts from 9 broad band filters. For our source galaxy sample, redshifts are retrieved with the template fitting

[1] http://kids.strw.leidenuniv.nl

Bayesian Photometric Redshift (BPZ) code (Benítez 2000; Coe et al. 2006), applied on the 9 band photometry. To estimate source redshift distributions, we use the direct calibration scheme to weight the spectroscopic sample according to our photometric one. The process is described in detail in Hildebrandt et al. (2018).

For our lens sample, we choose to use the bright end ($m_r \lesssim 20$) sample with photometric redshifts estimated with the artificial neural network machine learning code ANNz2 (Sadeh et al. 2016), presented in Bilicki et al. (2018), but extended to the full KiDS-1000 sample. This sample was trained on the highly complete GAMA spectroscopic redshift catalogue. The two samples are very similar in galaxy properties which results in very precise photometric redshift estimates for our lens sample. In this work, we use redshifts obtained from the optical *ugri* band photometry alone, as, since the lens sample is bright and relatively high redshift, NIR photometry does not significantly improve the photometric redshift estimation. Using the NIR photometry would introduce additional masking to our data, which would reduce our lens galaxy sample. As we will show in Sec. 5.3, the redshift accuracy is not very crucial in obtaining a pure sample of central galaxies. We restrict the lens redshifts to $0.1 < z_{\rm l} < 0.5$, according to Bilicki et al. (2018).

Galaxy shapes for our source galaxy sample are measured using the THELI-reduced r-band images with the *lens*fit shape measurement method (Miller et al. 2007, 2013). This method is a likelihood-based algorithm that fits surface brightness profiles to observed galaxy images, and takes into account the convolution with the PSF. Using a self-calibrating scheme, it has been shown to measure shear of galaxies to percent level accuracy, in simulated KiDS r-band images (Fenech Conti et al. 2017; Kannawadi et al. 2019).

Shears are obtained using *lens*fit for galaxies with an r-band magnitude larger than 20, which does not allow us to use these for shapes of our lens sample. In addition, *lens*fit is optimised for small SNR galaxies and a set-up for measuring bright galaxies is not readily available. To acquire shape information for our lens sample we apply the DEIMOS shape measurement method (Melchior et al. 2011) on the AstroWise reduced r-band KiDS images.

DEIMOS is based on measuring weighted surface brightness moments from galaxy images and using these to infer the galaxy's ellipticity. Unlike other moment-based techniques, it allows for a mathematically accurate correction of the PSF convolution with the galaxy's light profile avoiding any assumptions on the profile or behaviour of the PSF. The accuracy of this correction is only limited by the accuracy of the PSF modelling. Moreover, a correction for the necessary radial weighting, employed during moment measurement, is used;

higher order moments are calculated in order to approximate the unweighted galaxy moments from measured weighted moments.

To model the PSF we use shapelets (Refregier 2003); orthogonal Hermite polynomials multiplied with Gaussian functions that can be linearly combined to describe image shapes. The process is described in Kuijken et al. (2015), where the model has been shown to perform very well in KiDS imaging data, showing very small residual correlation between the modelled ellipticities and the ones measured by the stars in the image. To measure galaxy moments, we use an elliptical Gaussian weight function, following a per-galaxy matching procedure. The size of the weight function is tied to the scale of this Gaussian, and we use two different scales in this work, equal to the isophote of the galaxies $r_{\rm iso}$ and $1.5r_{\rm iso}$. We use these two values to probe potential differences in the measured ellipticity ratio with the galaxy scale probed; a larger weight function will reveal more of the shape of the outer galaxy regions. Neighbouring sources in the image are masked using segmentation maps from SExtractor (Bertin & Arnouts 1996). A detailed description of the shape measurement process can be found in Georgiou et al. (2019b).

For the GAMA galaxy sample, which is very similar in properties to the lens sample used here, Georgiou et al. (2019b) showed that the multiplicative bias on the ellipticity (not shear) is lower than 1%, and does not depend strongly on the galaxy properties. This is attributed to the great flexibility of the DEIMOS method, as well as the fact that these galaxies have a very high SNR in the KiDS imaging data (with a mean SNR around 300 in r-band images) and are generally very resolved compared to the PSF size.

In our analysis, we do not probe the lensing signal on very large scales and, therefore, we do not subtract the signal around random points, which in any case has been shown to be consistent with zero in other KiDS weak lensing measurements (Dvornik et al. 2017). Additive bias in the shape measurements is not expected to bias the spherically averaged gravitational shear measurements. The anisotropic lensing measurements are not expected to be affected either, since sources and lenses were measured using different shape measurement methods, and any additive biases (which are anyway measured to be negligibly small) are not expected to be correlated. Multiplicative biases are also not expected to play a significant role, since they affect the isotropic and anisotropic lensing signal in the same way, which would leave the measurement of halo ellipticity unaffected. Furthermore, multiplicative bias for the lens shapes have been shown to be on the sub-percent level (Georgiou et al. 2019b), and do not affect the calculation of the position angle of the lens.

5.2.2 GAMA

The Galaxy And Mass Assembly[2] (GAMA, Driver et al. 2009, 2011; Liske et al. 2015) survey is a spectroscopic survey carried out with the Anglo-Australian Telescope, using the AAOmega multi-object spectrograph. It provides spectroscopic information for $\sim 300,000$ galaxies over five sky patches of equal area for a total coverage of ~ 286 deg^2. The three equatorial patches (G09, G12, G15) have a completeness of 98.5% and are flux limited to $r_{\mathrm{petrosian}} < 19.8$ mag; out of the two south patches, only G23 overlaps with the KiDS footprint and has a completeness of 94.5% with a flux limit $i < 19.2$ mag. These samples, together with an unpublished deep spectroscopic sample in the G15 patch, are used during the training of the machine learning-based photo-z estimation for our lens galaxy sample (Bilicki et al. 2018).

The unique aspect of the GAMA sample is the high completeness, together with the fact that no pre-selection is made on the target galaxies besides imposing a flux limit. This nullifies any selection effects and provides the means to produce a highly pure and accurate group catalogue (Robotham et al. 2011). We use this group catalogue to validate our central galaxy sample selection from our lens galaxy sample, and quantify its purity. We use the 10th version of this group catalogue, which does not contain the G23 region. After masking the lens sample according to the KiDS mask, we are left with $\sim 120,000$ galaxies matched with the group galaxy catalogue. In Fig. 5.1, we show the satellite fraction of the sample in bins of redshift; at higher redshift, satellites fall below the detection limit and the satellite fraction of the sample is decreased.

5.2.3 MICE

The GAMA group catalogue used in this work is susceptible to imperfections, especially for the more massive groups. Robotham et al. (2011) showed that the number of high richness groups was lower than what was expected from mock group catalogue specifically designed for validation of the group finding algorithm. In addition, Jakobs et al. (2018) found, using hydrodynamical simulations, that the group algorithm tends to fragment larger groups into smaller ones. Because of this, we choose to also validate our central sample selection using mock galaxy catalogues from a cosmological simulation, the MICE Grand Challenge run (Crocce et al. 2015).

MICE is an N-body simulation containing $\sim 70 \times 10^{10}$ dark-matter particles in a $(3h^{-1}\mathrm{Gpc})^3$ comoving volume, from which a mock galaxy catalogue has been

[2] http://www.gama-survey.org/

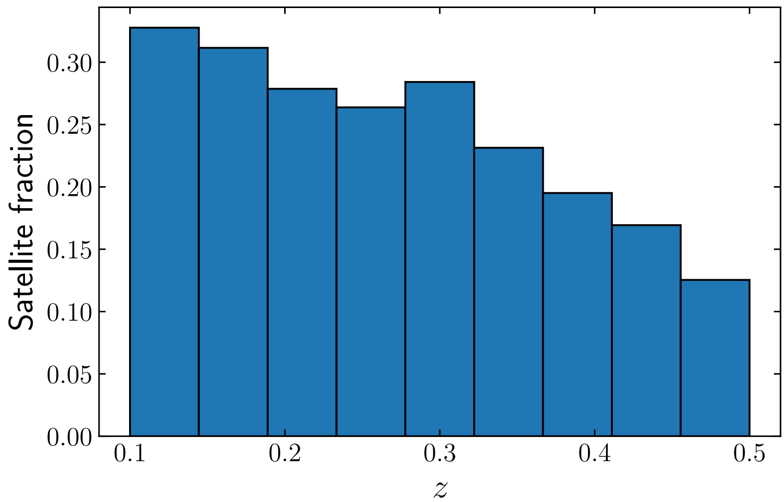

Figure 5.1: The satellite fraction ($N_{\rm sat}/N_{\rm all}$) in the GAMA galaxy sample, in bins of redshift.

built, using Halo Occupation Distribution and Abundance Matching techniques (Carretero et al. 2015). The catalogue contains information for a large number of galaxy properties, such as apparent magnitude, stellar mass, as well as a distinction of the galaxies into centrals and satellites, which we use in this work. Other applications of the catalogue include galaxy clustering, weak lensing and higher order statistics (Fosalba et al. 2015; Fosalba et al. 2015; Hoffmann et al. 2015). We download the publicly available version 2 of the catalogue from cosmohub[3] (Carretero et al. 2017). From the 5000 deg^2 that the whole mock catalogue covers, we cut out 200 deg^2 and select galaxies with apparent SDSS-like r-band magnitude of < 20.3 mag, to match the cut performed in Bilicki et al. (2018).

[3]https://cosmohub.pic.es

5.3 Central galaxy sample

5.3.1 The algorithm

In order to optimally extract the anisotropic weak lensing signal of elliptical dark matter halos, it is important to exclude galaxies in our sample that reside in sub-halos, i.e. satellite galaxies (see e.g. van Uitert et al. 2017). Because of the hierarchical way of structure formation, central galaxies are commonly found in overdense regions of the Universe, where other neighbouring galaxies are also likely to be found. Based on this, we developed an algorithm to search for galaxies in our sample that have a high chance of being a central halo galaxy.

The algorithm is as follows: For every galaxy in our sample, we search for neighbouring galaxies inside a cylinder in sky and redshift space. The cylinder radius has a fixed physical length while the depth of the cylinder is determined by the accuracy of our redshift estimation. If neighbouring galaxies are indeed found, we ask the question whether the galaxy we selected, that lies in the middle of the cylinder, is the brightest galaxy (in the r-band) inside that cylinder. If this is true, we identify this galaxy as a central. We tested two different cylinder depths, $\pm \mathrm{d}z$ and $\pm 2\mathrm{d}z$ (where $\mathrm{d}z$ is the redshift uncertainty, equal to $\sim 0.02(1+z)$ for our lens galaxy sample) and chose the latter which was found to perform better.

5.3.2 Sample purity

We test the performance of this algorithm on the GAMA galaxy survey sample as well as the mock galaxy catalogues from the MICE simulation. The spectroscopic information together with the high completeness of the GAMA sample allows the construction of a highly accurate group galaxy catalogue, which we use here to identify central and satellite galaxies. We select central galaxies by removing any galaxy that is a satellite (we keep both brightest group galaxies as well as field galaxies, the latter are expected to live in their own isolated dark matter halo or have satellites around them too faint to detect).

However, imperfections are present in this group catalogue (see Sec. 5.2.3). Therefore, we also use the MICE mock galaxy catalogues to validate our algorithm, where we know a priori the central and satellite galaxies. We mimic the photometric redshift uncertainty in the mock catalogue redshifts by adding a random number to them, drawn from a Gaussian distribution with scale equal to the redshift uncertainty, i.e. $\sim 0.02(1+z)$.

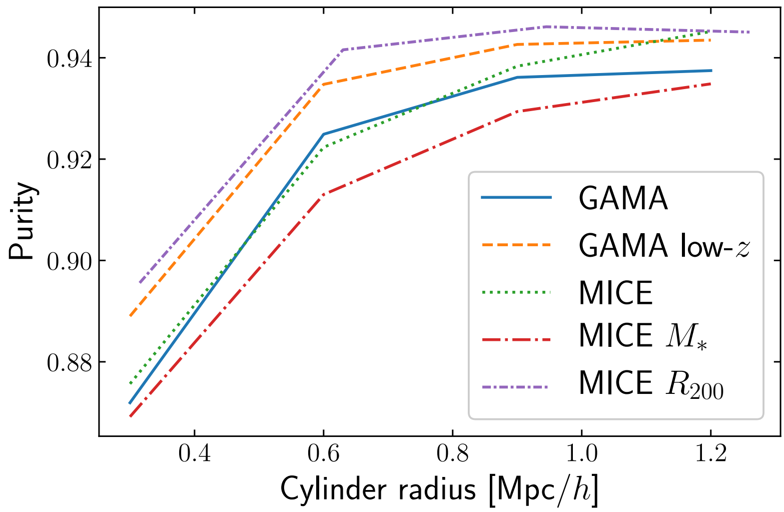

Figure 5.2: Purity of our central galaxy sample, as a function of fixed cylinder radius used to identify centrals in overdense regions. Lines connect the individual points. In solid blue we show results from the GAMA+KiDS-1000 overlap, over the photometric redshift space of $0.1 < z < 0.5$. We also show the results for redshifts between $0.1 < z < 0.3$ with a dashed orange line. The dotted green line shows the purity of the sample obtained using the MICE2 mock catalogues, for $0.1 < z < 0.5$. The red dash-dotted line are results obtain when we look for the most massive (in terms of stellar mass) galaxy in the cylinder centre, instead of the brightest one. Finally, the purple dense dash-dotted line represents results obtain when, instead of a fixed cylinder radius we use multiples k of the galaxy's R_{200} to define the radius size, with $k = \{1, 2, 3, 4\}$. In this case, we plot the median value of the cylinder radius in the x-axis.

We show the performance of our algorithm in Fig. 5.2, where we plot the purity (number of true centrals we identify over the total number of centrals we identify) of our central galaxy sample, as a function of the fixed cylinder radius used. When using the GAMA survey as a reference, we see that we can achieve purity of up to ~ 94 % for the largest cylinder radius. We can also see that the purity of the sample increases when a larger cylinder is used, which is expected as it is less likely to mis-identify a very bright nearby satellite as a central when using a larger cylinder, that is more likely to also contain the central galaxy.

We also check the purity of our sample in low redshift galaxies ($0.1 < z < 0.3$) of the GAMA sample, where the satellite fraction remains high, around ~ 27 % (Fig. 5.1), since the algorithm could under-perform in this satellite-rich redshift space. We find, however, that the purity of the central sample is higher in this regime, building confidence in the validity of our central sample selection.

Results from applying the algorithm to the MICE2 mock galaxy catalogue are also shown in Fig. 5.2. We see that the values for purity that we achieve are very similar to the values we get using GAMA, except for when using the largest cylinder radius. This means that, for the largest radius, the actual purity of our central sample is higher than the one we measure using GAMA.

In addition, we try to optimise our central selection by using the stellar masses in the mock galaxy catalogues. First, we modify the algorithm so as to select the most massive galaxy in the cylinder's centre, instead of the brightest one. For this, we use the stellar mass, and plot the purity in Fig. 5.2. The performance is worse compared to using apparent brightness, suggesting that the central galaxy is more often the brightest one in the halo, but not the most massive, in terms of stellar mass.

Lastly, instead of using a fixed cylinder radius to search for overdense regions, we use a per-galaxy cylinder radius, tied to the R_{200} of the galaxy. To compute this, we use the stellar-to-halo mass relation computed for GAMA central galaxies (van Uitert et al. 2016),

$$M_*^{\mathrm{c}}(M_{\mathrm{h}}) = M_{*,0} \frac{(M_{\mathrm{h}}/M_{\mathrm{h},1})^{\,\beta_1}}{[1 + (M_{\mathrm{h}}/M_{\mathrm{h},1})]^{\,\beta_1 - \beta_2}}\,, \tag{5.1}$$

where M_*^{c} is the stellar mass of the central galaxy and M_{h} the halo mass. We use the best fit values from van Uitert et al. (2016) for the rest of the parameters in this model and solve numerically for M_{h}. We then compute the R_{200} from $M_{\mathrm{h}} \equiv 4\pi(200\bar{\rho}_{\mathrm{m}})R_{200}^3/3$, where $\bar{\rho}_{\mathrm{m}} = 8.74 \times 10^{10} h^2 M_\odot/\mathrm{Mpc}^3$ is the comoving matter density. As can be seen from Fig. 5.2, the purity of the sample generally increases when using a more per-galaxy optimised cylinder.

It is clear that increasing the cylinder radius increases the purity of our central galaxy sample, but this comes at a cost. Specifically, the completeness of the sample drops as the radius increases, and we end up with fewer galaxies for our analysis. This is expected, as larger cylinders will encompass more and more central galaxies, making the sample less complete. Even the gain using the galaxy R_{200} as a cylinder radius causes the completeness to drop by ~ 3 %. It is, therefore, important to find a good compromise between the sample's purity and the total number of central galaxies that will be used.

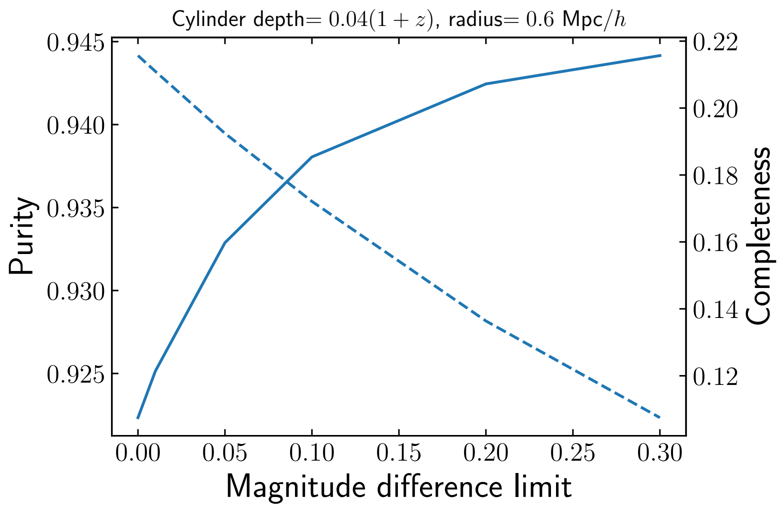

Figure 5.3: Purity (solid, left y-axis) and completeness (dashed, right y-axis) of our central galaxy sample after rejecting centrals with a galaxy brighter than a magnitude difference from the central's brightness, shown in the x-axis. The cylinder used was fixed at 0.6 Mpc/h. Lines connect the individual points.

As a last step in this direction, we look at the second brightest galaxy in the cylinder, and the difference in magnitude from the brightest one. If two galaxies are in the same overdensity but are too close in magnitude, it is possible that the centre of the halo does not correspond to the brightest galaxy. Therefore, we reject centrals that have a galaxy inside the same cylinder up to a magnitude difference limit. We plot the purity of the central sample following this procedure, as a function of the magnitude difference limit for a fixed cylinder of 0.6 Mpc/h radius in Fig. 5.3. We see that the purity increases as the magnitude difference limit increases, but the completeness drops.

Based on this, we choose to use a magnitude difference limit of 0.1 in our final sample. To increase the sample size while not compromising much on its purity, we opt for using a fixed cylinder radius of 0.6 Mpc/h. With this setup, we achieve a purity of 93.36%, as quantified from the overlap with the GAMA group catalogue. The total number of central galaxies for the whole KiDS-1000 area, after masking, is 138,607. Shape measurements are successfully obtained

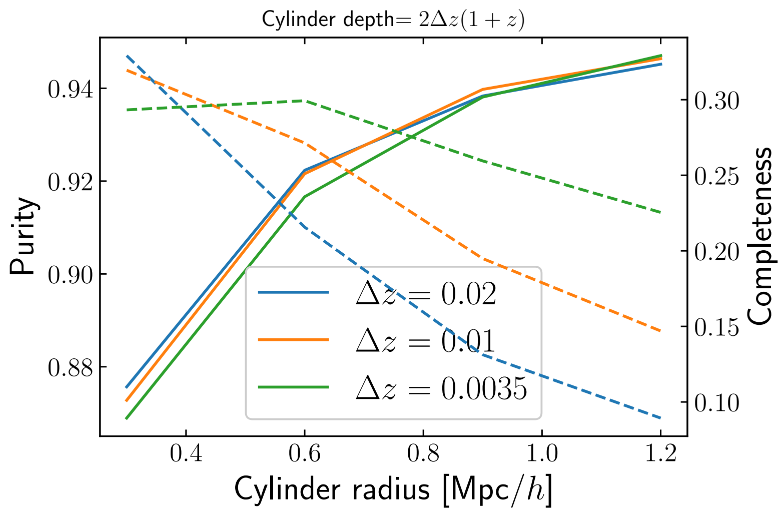

Figure 5.4: Purity (solid lines) of our central galaxy sample selection as a function of the fixed cylinder radius. Lines connect the individual points. Results shown for three different simulated photometric redshift accuracies. The depth of the cylinder is equal to ± 2 times the redshift uncertainty. The completeness of the central galaxy sample is also shown, on the right y-axis, overplotted with dashed lines.

for 128,680 galaxies using a weight function with scale equal to $r_{\rm iso}$ and 126,201 galaxies using $1.5 r_{\rm iso}$.

5.3.3 Scaling with photo-z accuracy

Interestingly, the purity of the sample seems to plateau for large cylinders. To understand this better, we repeated the analysis using the mock galaxy catalogues and sampling photometric redshifts with three different values of accuracy, $\mathrm{d}z = \{0.02, 0.01, 0.0035\}(1+z)$. The first choice represents our lens galaxy sample, the second corresponds to the photometric redshifts achievable for Luminous Red Galaxies (LRGs, Vakili et al. 2019), and the last one is the expected redshift accuracy from a narrow-band based survey, such as the PAUS (Eriksen et al. 2019).

Results are shown in Fig. 5.4, where we plot the purity and completeness for the different redshift accuracies. We also change the size of the cylinder in redshift space according to the redshift accuracy. Interestingly, the purity of the sample remains the same in all three cases. As the redshift accuracy and cylinder depth reduces, we see that the completeness of the sample increases as well. From this we conclude that improvements to the purity cannot be made by reducing the redshift uncertainty.

The lack of improvement in purity can be understood by the fact that in generally lower mass groups, the central halo galaxy does not always correspond to the brightest galaxy (see e.g. Lange et al. 2018). Increasing the redshift accuracy allows for better determination of centrals in less massive halos, which, however, are expected to carry a weaker signal of halo ellipticity. Therefore, it is more optimal to increase the area of the survey, if possible, instead of the redshift accuracy. This justifies our choice to use the much larger in area KiDS-1000 data, compared to the spectroscopic redshifts of the GAMA survey, for our analysis.

5.3.4 Sample characteristics

We present here the characteristics of the final sample of central galaxies we compiled. The sample's properties are obtained for the overlap with the GAMA survey, where an extensive photometry and stellar mass catalogue is used (`StellarMassesLambdarv20`, Taylor et al. 2011; Wright et al. 2016). This catalogue provides estimates of the stellar mass, absolute magnitudes and rest-frame colours of galaxies using fits to galaxy SEDs from photometry in the optical+NIR broad bands.

In addition, we split the central sample into intrinsically red and blue galaxies. To do so, we isolate the red sequence galaxies by inspecting the distribution of apparent $g-i$ colour versus m_r in 10 linear redshift bins in the redshift range of the lens sample. With this division, we obtain 62426 red and 53504 blue lens galaxy sub-samples. Their average ellipticity is the same as for the full sample, but their distributions show that slightly more blue galaxies have ellipticities < 0.1 and > 0.3 than red galaxies.

In the top panel of Fig. 5.5 we show the distribution of stellar mass for the full galaxy population in the bright KiDS-1000 sample, as well as for our central galaxy sample, divided also into red and blue centrals. The central galaxies are generally more massive than galaxies in the whole population, as we would expect. The mean stellar mass of the red and blue central sample is $\sim 10^{11}$ M$_{\odot}$ and $10^{10.6}$ M$_{\odot}$, respectively.

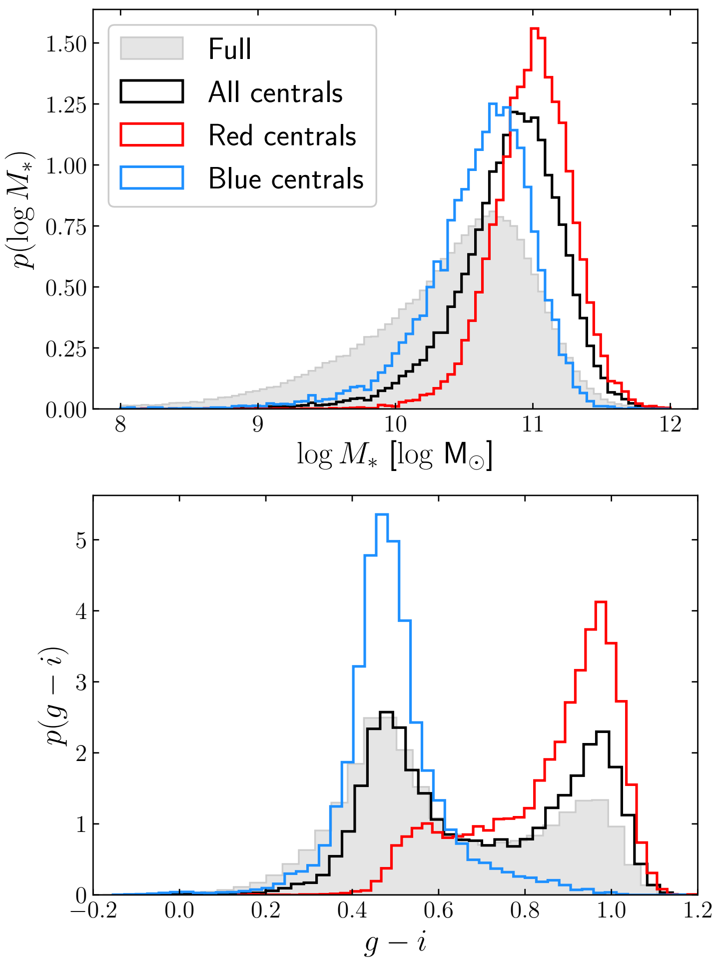

Figure 5.5: *Top:* normalised distribution of stellar mass of the full sample (in filled grey) and our central galaxy sample (in black, red and blue for all, red and blue centrals, respectively) in the GAMA overlap. *Bottom:* normalised distribution of restframe, dust corrected $g-i$ colour for the same galaxy samples.

In addition to this, we show the distribution of restframe $g-i$ colours, corrected for dust extinction, in the bottom panel of Fig. 5.5, again for the full KiDS-1000 and central (all, blue and red) galaxy sample. We see that the central galaxy sample consists of generally more red galaxies than the full sample. We also see that the colour distributions of our selection of red and blue centrals generally follows the expected restframe $g-i$ distribution, building confidence in our colour selection.

5.4 Methodology

Gravitational lensing has the effect of coherently distorting light rays of background galaxies (sources) from the intervening matter along the line of sight. Since galaxies are biased tracers of the matter density in the Universe, one expects to find a correlation between the position of foreground galaxies (lenses) and source galaxy shapes. In its weak regime, the effect is very small, and the intrinsic ellipticities of source galaxies are only affected on the order of 1%. Large statistical ensembles of lens-source galaxy pairs are therefore required to extract the weak lensing signal.

In this work, both for lens and source galaxies, we use the third flattening, $\epsilon = \epsilon_1 + \mathrm{i}\epsilon_2$, as an ellipticity measure, which is related to the semi-minor to semi-major axis ratio, q, by $|\epsilon| = (1-q)/(1+q)$. We can then express the tangential and cross ellipticity of source galaxies with respect to the lens position as

$$\epsilon_+ = -\epsilon_1 \cos(2\theta) - \epsilon_2 \sin(2\theta)\,, \tag{5.2}$$

$$\epsilon_\times = \epsilon_1 \sin(2\theta) - \epsilon_2 \cos(2\theta)\,, \tag{5.3}$$

where θ is the position angle of the line connecting the lens-source galaxy pair. When averaged, ϵ_+ provides an unbiased but noisy estimate of the gravitational shear γ, i.e. $\langle\epsilon_+\rangle \approx \gamma$, which can then be related to the excess surface mass density through

$$\Delta\Sigma(R) = \bar{\Sigma}(<R) - \Sigma(R) = \gamma(R)\Sigma_{\mathrm{crit}}\,, \tag{5.4}$$

with Σ_{crit} the critical surface density, defined by

$$\Sigma_{\mathrm{crit}} = \frac{c^2}{4\pi G}\frac{D_{\mathrm{s}}}{D_{\mathrm{l}}D_{\mathrm{ls}}}\,. \tag{5.5}$$

In the above equation, c and G are the speed of light and gravitational constant, respectively, D_{s} is the angular diameter distance to the source galaxy, D_{l} to the lens galaxy and D_{ls} between the lens and source galaxy.

The isotropic (azimuthally averaged) part of the lensing signal can be calculated from the data using the estimator

$$\widehat{\Delta\Sigma}(R) = \left(\frac{\sum_{\rm ls} w_{\rm ls} \epsilon_t \Sigma_{\rm crit}}{\sum_{\rm ls} w_{\rm ls}} \right) , \tag{5.6}$$

where the sum runs over all lens-source galaxy pairs, that fall in a given projected radius bin R. We weight each pair with ellipticity weights, $w_{\rm s}$, computed by *lens*fit, which accounts for uncertainty in the shear estimate, and define

$$w_{\rm ls} = w_{\rm s} \Sigma_{\rm crit}^{-2} . \tag{5.7}$$

Since galaxy redshifts are computed through photometry, it is important to account for the full posterior redshift distribution of source galaxies, $p(z_{\rm s})$ (see Sec. 5.2.1), when computing $\Sigma_{\rm crit}$. This is done with equation

$$\Sigma_{\rm crit}^{-1} = \frac{4\pi G}{c^2} \int_{z_{\rm l}}^{\infty} \frac{D_{\rm l}(z_{\rm l}) D_{\rm ls}(z_{\rm l}, z_{\rm s})}{D_{\rm s}(z_{\rm s})} p(z_{\rm z}) {\rm d}z_{\rm s} . \tag{5.8}$$

5.4.1 Anisotropic lensing model

We model the anisotropic part of the lensing signal following the formalism presented in Schrabback et al. (2015) which is based on work by Natarajan & Refregier (2000) and Mandelbaum et al. (2006a). The excess surface mass density of a lens is modelled as

$$\Delta\Sigma_{\rm model}(r, \Delta\theta) = \Delta\Sigma_{\rm iso}(r)[1 + 4 f_{\rm rel}(r)|\epsilon_l| \cos(2\Delta\theta)] . \tag{5.9}$$

In the above, $\Delta\Sigma_{\rm iso}$ is the excess surface mass density for a spherical halo (estimated from data using Eq. (5.6)), ϵ_l is the lens ellipticity and $\Delta\theta$ is the position angle coordinate in the lens plane, measured from the halo's semi-major axis. The anisotropy of the elliptical halo's lensing is described by $f_{\rm rel}(r)$, which depends on the assumed halo density profile and is generally a function of the projected separation r. For elliptical halos not described by a single power-law, $f_{\rm rel}(r)$ needs to be computed numerically, and we interpolate this quantity (using a cubic interpolation) from tabulated values. In order to avoid systematic biases in our anisotropic lensing signal measurement, it is also necessary to define the excess surface mass with lens and source ellipticities rotated by $\pi/4$, where we have

$$\Delta\Sigma_{45,\rm model}(r, \Delta\theta) = \Delta\Sigma_{\rm iso}(r)[4 f_{\rm rel,45}(r)|\epsilon_l| \cos(2\Delta\theta + \pi/2)] , \tag{5.10}$$

where $f_{\mathrm{rel},45}(r)$ is obtained in the same manner as $f_{\mathrm{rel}}(r)$.

The quantity of interest is the ellipticity ratio, $\tilde{f}_{\mathrm{h}} = |\epsilon_h|/|\epsilon_g|$. However, we can only measure this quantity weighted by the average mis-alignment angle between the halo and host galaxy's semi-major axis, $\Delta\phi_{\mathrm{h,g}}$. Consequently, the measured quantity $f_{\mathrm{h}} = \tilde{f}_{\mathrm{h}}\langle\cos(2\Delta\phi_{\mathrm{h,g}})\rangle$ (where we also assume that the mis-alignment angle does not depend on $|\epsilon_{\mathrm{h}}|$). In order to extract f_{h} from data, we use the following estimators,

$$\widehat{f\Delta\Sigma} = \frac{\sum_{\mathrm{ls}} w_{\mathrm{ls}}\epsilon_t \Sigma_{\mathrm{crit}}|\epsilon_l|\cos(2\phi_{\mathrm{ls}})}{\sum_{\mathrm{ls}} w_{\mathrm{ls}}|\epsilon_l|^2\cos^2(2\phi_{\mathrm{ls}})}\,, \tag{5.11}$$

and

$$\widehat{f_{45}\Delta\Sigma} = -\frac{\sum_{\mathrm{ls}} w_{\mathrm{ls}}\epsilon_\times \Sigma_{\mathrm{crit}}|\epsilon_l|\sin(2\phi_{\mathrm{ls}})}{\sum_{\mathrm{ls}} w_{\mathrm{ls}}|\epsilon_l|^2\sin^2(2\phi_{\mathrm{ls}})}\,, \tag{5.12}$$

where ϕ_{ls} is the angle between the lens semi-major axis and the position vector connecting the lens-source galaxy pair. These two estimators can be predicted from $f_{\mathrm{h}} f_{\mathrm{rel}}\Delta\Sigma_{\mathrm{iso}}$ and $f_{\mathrm{h}} f_{\mathrm{rel},45}\Delta\Sigma_{\mathrm{iso}}$, respectively. However, the estimators are easily contaminated by systematic errors in the lensing signal measurements, such as imperfections due to incorrect PSF modelling or cosmic shear from structures between the lens and the observer (Mandelbaum et al. 2006a; Schrabback et al. 2015). An estimator insensitive to these systematic effects can be constructed by subtracting the two,

$$\widehat{(f - f_{45})\Delta\Sigma} = \widehat{f\Delta\Sigma} - \widehat{f_{45}\Delta\Sigma}\,. \tag{5.13}$$

For measuring the ellipticity ratio, we use this estimator, and the analysis we follow is described below.

5.4.2 Extracting f_h

To measure f_{h} from data, we consider the two estimators $x_i = \widehat{\Delta\Sigma}_i$ and $y_i = \widehat{(f - f_{45})\Delta\Sigma}_i/(f_{\mathrm{rel}}(r_i) - f_{\mathrm{ref},45}(r_i))$, where the index i runs over the radial bins over which we calculate the lensing signal and r_i is the central value of that bin. These are two random Gaussian variables, which prohibits us from simply computing their fraction $m = y_i/x_i$, which would lead to a biased estimate of f_{h}. To overcome this, we consider, for a given m, the quantity $y_i - mx_i$. This is a random Gaussian variable drawn from $N(0, w_i^{-1})$, with $w_i^{-1} = \sigma_y^2 + m^2\sigma_x^2$ and σ_x, σ_y are the error on the measured estimators x_i and y_i, respectively (Mandelbaum et al. 2006a).

The following sum ratio

$$\frac{\sum_i w_i(y_i - mx_i)}{\sum_i w_i} \sim N\left(0, \frac{1}{\sum_i w_i}\right) \tag{5.14}$$

is also a random Gaussian variable. Based on this, we determine confidence intervals of $\pm 1\sigma$ in measuring m, by considering the inequality

$$\frac{-Z}{\sqrt{\sum_i w_i}} < \frac{\sum_i w_i(y_i - mx_i)}{\sum_i w_i} < \frac{+Z}{\sqrt{\sum_i w_i}} \,. \tag{5.15}$$

We use m drawn from a grid and calculate $f_{\rm h}$ by requiring $f_{\rm h} = m(Z=0)$. We also determine the $\pm 1\sigma$ intervals by setting $Z = \pm 1$. In addition, we compute the reduced χ^2 from n radial bins using

$$\chi^2_{\rm red} = \frac{\sum_i w_i(y_i - m(Z=0)x_i)^2}{n-1} \,. \tag{5.16}$$

This method does not take into account the off-diagonal elements of the covariance matrix of our measurements. These, however, where estimated to be very small (see Sec. 5.5), with the standard deviation of the correlation matrix off-diagonal elements being 4×10^{-2}.

5.5 Halo Ellipticity

We measure the weak lensing signal around our central galaxy sample using 25 radial bins, logarithmically spaced between 20 kpc/h and 1.2 Mpc/h. We restrict the sample to lens galaxies with well defined ellipticities, $0.05 < \epsilon_{\rm l} < 0.95$. The median redshift of the lenses is 0.26 and their average ellipticity is 0.188 for shapes obtained using weight function of $r_{\rm iso}$ and 0.183 when using $1.5 r_{\rm iso}$. We fit the isotropic weak lensing signal with an NFW profile (Navarro et al. 1996; Wright & Brainerd 2000), while fixing the concentration-mass relation to Duffy et al. (2008),

$$c = 5.71 \left(\frac{M_{200}}{2 \times 10^{12} {\rm M}_\odot/{\rm h}}\right)^{-0.084} (1+z)^{-0.47} \,, \tag{5.17}$$

to finally obtaining an estimate for the scale radius r_s. This is then used to calculate $f_{\rm rel}(r)$ and $f_{\rm rel,45}(r)$. In NFW profile fits, we use the mean redshift of the full lens sample. We also restrict the fit to the range from 40 kpc/h up

Table 5.1: Results from fits to the weak lensing signal, for the full sample, as well as the red and blue central galaxy sub-samples. The mean stellar mass is shown, obtained in GAMA overlap. We also show the best fit M_{200} values from the NFW profile fits to the isotropic weak lensing and the resulting ellipticity ratio f_{h} fit, with its reduced χ^2.

Sample	M_* [10^{10} $\mathrm{M}_\odot$]	M_{200} [10^{12} $\mathrm{M}_\odot$]	f_{h}	χ^2_{red}
Full	9.28	3.678	$0.20^{+0.19}_{-0.19}$	1.25
Red	12.14	6.442	$0.35^{+0.18}_{-0.17}$	0.82
Blue	5.63	1.402	$0.00^{+0.53}_{-0.54}$	0.77

to 200 kpc/h. The first limit ensures that signal from baryons in the centre of the halo is not included in the fit; it also minimizes contamination of the source galaxy's shear by the extended light of each lens (Schrabback et al. 2015; Sifón et al. 2018). The second limit ensures that we do not include contributions from the 2-halo term when fitting the lensing signal. This is a conservative limit since we do not expect a strong 2-halo term in our lensing signal given that our galaxy sample has very small satellite galaxy contamination.

To calculate the covariance of our measurements we use a bootstrap technique. We sample 10^5 random bootstrap samples from the lens catalogue (with replacement) and use this data vector to calculate the covariance matrix, obtaining error bars for our measurements from its diagonal elements. This technique ignores errors due to sample variance from large scale structure. However, these are expected to be negligible given the scales we probe. We test this by computing the covariance and errors from a per-area bootstrap technique, dividing the survey into 1 deg^2 patches and computing the lensing signal in each patch. We then select 10^5 random bootstrap patches, weighting them by the number of lenses (since patches with significantly fewer than average lenses will have a more uncertain signal measurement) and arrive at fully consistent error bars. We also find the off-diagonal elements of the covariance matrix to be negligible on all scales, justifying the analysis outlined in Sec. 5.4.2.

We present our measurements in Fig. 5.6 for the case when the shape of the lens galaxy is measured using a weight function with scale equal to r_{iso}. Results around the full, red and blue lens galaxy sample are shown in the left, right and middle column, respectively. The first row shows the isotropic lensing signal measurement, spherically averaged, as well as the best fit NFW profile, with the ranges used in the fit indicated with dashed vertical lines. We also overplot the isotropic lensing signal obtained from the full KiDS-1000 bright-end catalogue in the same redshift range in the top left panel, for comparison. We see that our central galaxy sample is generally more massive and is not affected by a strong 2-halo term, contrary to the full sample. The resulting average halo mass for the three sub-samples can be seen in Table 5.1. We have also checked that $\Delta\Sigma_{45}$, which is calculated by substituting the tangential with the cross ellipticity component in Eq. (5.6), is consistent with zero across all measured scales. This is expected, since a spherically averaged cross component is not generated by gravitational lensing, and serves as a useful sanity check for a potential systematic offset.

In the next three rows of Fig. 5.6, we present the measurement of the anisotropic lensing signal for the three sub-samples. We use these measurements to calculate the ellipticity ratio, $f_{\rm h}$, following Sec. 5.4.2, as well as the 1-σ confidence intervals. For the $f_{\rm h}$ measurement, we use scales from 40 kpc/h up to the estimated r_{200} for the corresponding galaxy sample, which can be seen as dashed lines in the figure. For visualisation, we overplot the best fit NFW profile of the corresponding galaxy sample, multiplied by $f_{\rm rel}$, $f_{\rm rel,45}$ or their difference, accordingly, as well as the best fit value of $f_{\rm h}$.

The resulting values of $f_{\rm h}$, as well as the reduced χ^2 of the fit are presented in Table 5.1. We see that the ellipticity ratio is fit reasonably well, as expressed by the χ^2 values. For the full sample we measure an ellipticity ratio of 0.2 with a 1-σ statistical significance. For the red galaxies, the measured ratio is higher, 0.35, and the significance also increases to 2-σ. Finally, we do not measure a significant ellipticity ratio for blue galaxies.

5.5.1 Mis-alignment dependence on galaxy scale

Following the results presented in the previous section, we re-measure the ellipticity ratio, $f_{\rm h}$, using lens galaxy shapes with a weight function of scale equal to $1.5r_{\rm iso}$. By using a larger weight function, the measured shapes will be more sensitive to the morphology of outer galaxy regions. The mean ellipticity of the lens sample is measured to be very similar when using the two weight functions (with a difference of 0.005) and their distributions were inspected to be nearly the same. Therefore, any difference measured in $f_{\rm h}$ will be directly related to differences in the mean mis-alignment angle, $\langle\cos(2\Delta\phi_{\rm h,g})\rangle$.

The results obtained with the larger weight function look very similar to what is shown in Figure 5.6, hence we do not show them. However, the measured signal for $(f - f_45)\Delta\Sigma$ is significantly higher. When analysing the full sample, we measure an $f_{\rm h} = 0.50{\pm}0.20$, which is ~ 1.5 times higher than the value obtained using the smaller weight function. Looking at the red and blue galaxy subsamples, we find $f_{\rm h} = 0.55{\pm}0.19$ and $f_{\rm h} = 0.29{\pm}0.56$, respectively, both of which are higher than the values obtained by using a smaller weight function. For red galaxies the detection of a non-zero ellipticity ratio is increased to $\sim 2.9\sigma$, while blue galaxies are still found to have a value $f_{\rm h}$ fully consistent with zero.

From this analysis we conclude that outer galaxy regions are more aligned with the shape of the dark matter halo. This result is in agreement with other observations, where central galaxies where found to be more aligned with their satellite galaxy distributions if the shape measurement used was more sensitive to their outer regions (Huang et al. 2016; Georgiou et al. 2019a). The physical processes causing this behaviour can be explained either by tidal interactions between the central galaxy and the dark matter halo affecting the outer, less bound galaxy regions more strongly, or by the fact that infalling material to the central galaxy generally follows the ellipticity of the dark matter halo.

5.5.2 Comparison with the literature

Our analysis closely follows work done in previous studies. Mandelbaum et al. (2006a) used a very similar estimator on a much larger lens sample, split in colour and luminosity. For their L6 luminosity bin, which is closer to the mean luminosity of our sample, they found $f_{\rm h} = 0.29{\pm}0.12$ for red and $f_{\rm h} = 1.0^{+1.3}_{-0.9}$ for blue galaxies. van Uitert et al. (2012) also studied a large lens sample consisting of less massive galaxies than ours, and found $f_{\rm h} = 0.19 \pm 0.10, 0.13 \pm 0.15$ and $-0.16^{+0.18}_{-0.19}$ for all, red and blue lens samples, respectively. Following the same methodology, Schrabback et al. (2015) studied a sample of lenses split in colour and stellar mass, and found $f_{\rm h} = -0.04 \pm 0.25$ for all red lenses and $f_{\rm h} = 0.69^{+0.37}_{-0.36}$ for all blue ones. They also provided predictions of $f_{\rm h}$ from the Millennium Simulation, which agree with the values we obtain here. The studies above used almost identical methodology as in this work and lens samples much larger than ours, but which were contaminated by satellite galaxies. Our study indicates the importance of selecting central galaxies for an anisotropic lensing signal measurement.

The pioneering work, Hoekstra et al. (2004) and Parker et al. (2007), conducted similar measurements of $f_{\rm h}$ for single band photometric data and found $f_{\rm h} = 0.77^{+0.18}_{-0.21}$ and $f_{\rm h} = 0.76 \pm 0.10$, respectively. However, these results do not correct for systematic effects (such as PSF residuals or cosmic shear), which is likely to bias the resulting $f_{\rm h}$ measurement to high values (Schrabback et al. 2015).

Focusing on the brightest group galaxies (BGG) of the GAMA group catalogue specifically (using groups with more than 5 members), van Uitert et al. (2017) detected an halo ellipticity of $\epsilon_{\rm h} = 0.38 \pm 0.12$, using the BGG semi-major axis as a proxy for the halo's orientation and focusing on scales below 250 kpc. Similar ellipticity has also been detected for dark matter halos of galaxy clusters (Evans & Bridle 2009; Clampitt & Jain 2016; Shin et al. 2018; Umetsu et al. 2018). For comparison, we find $\epsilon_{\rm h} = 0.038 \pm 0.036$ for the full sample and $\epsilon_{\rm h} = 0.066^{+0.034}_{-0.032}$ for red galaxies, using the average lens galaxy ellipticity of our sample and assuming zero mis-alignment angle.

Note that galaxies in these groups and clusters are generally more massive than our central galaxy sample (see Table 5.1), with the GAMA BGG sample having a mean stellar mass of 2.25×10^{11} M$_\odot$, and cluster central galaxies being typically more massive than that. In order to check whether more massive galaxies in our sample have higher ellipticity ratio, we select galaxies based on stellar mass, obtained by running Le Phare (Ilbert et al. 2006) on the KiDS-1000 9-band photometry (Wright et al. in prep.). Using all galaxies with $M_* > 1.58 \times 10^{11}$ M$_\odot$ we find $f_{\rm h} = 0.24 \pm 0.20$, which is slightly higher than the value for the whole sample.

The ellipticty we obtain is significantly lower than what is measured in galaxy groups. This suggests that either halos of galaxy groups and clusters are more elliptical than those of relatively isolated galaxies[4] or that the mean misalignment between halos and galaxies is smaller for group and cluster central galaxies. In cosmological simulations, higher mass halos where found to be more elliptical and less misaligned with their host galaxy than lower mass ones, which agrees with the trend observed here (e.g. Chisari et al. 2017). However, we do not measure a significant increase in $f_{\rm h}$ when we restrict our sample to high stellar mass galaxies, which leaves the interpretation unclear.

Another possible reason for the discrepancy may be differences in the shape measurement of the lenses. Shapes of lens galaxies were derived using a generally large weight function in van Uitert et al. (2017) (private communication). We measure a significantly larger $f_{\rm h}$ when using a larger weight function for measuring shapes of lens galaxies in our sample, which might explain at least part of the low halo ellipticity value we find in comparison to galaxy groups.

[4]Our sample consists of both BGG and field galaxies, the latter expected to be either isolated galaxies or BGGs of groups whose satellites are too faint to be detected within the imposed magnitude limit.

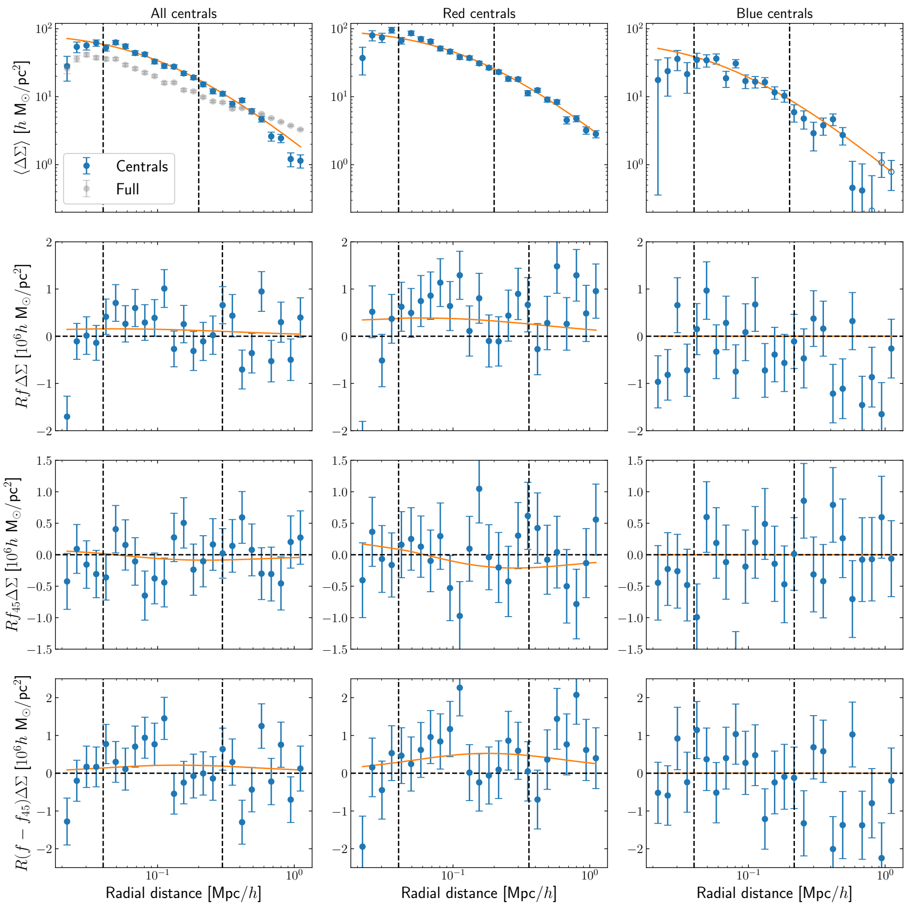

Figure 5.6: Measurements of the weak lensing signal around our central galaxy sample. The first column shows results obtained for the all centrals (with open circles placed for negative measurements), while the second and third columns show results for the red and blue subsamples, respectively. The first row shows the isotropic lensing signal, the second and third row show the anisotropic lensing signal obtained with the estimators of Eqs. (5.11)-(5.12), while the last row shows the difference, Eq. (5.13). The best fit NFW profile is overplotted on the first row, with dashed vertical lines depicting the ranges that were used during the fit. We also show the isotropic lensing signal of the full KiDS-1000 sample in grey points, as a comparison to the signal obtain using only the central galaxies. For the next rows we show the best fit NFW profile multiplied by the best fit $f_{\rm h}$ and $f_{\rm rel}, f_{\rm rel,45}$ and their difference, respectively, as well as the ranges used during the fit with dashed lines.

5.6 Conclusions

In this work we measure the anisotropic lensing signal and halo-to-galaxy ellipticity ratio of galaxies for a bright sample ($m_r \lesssim 20$) with accurate redshifts acquired through a machine learning technique, trained on a similar spectroscopic sample (GAMA, $m_{r,\mathrm{petro}} < 19.8$). We minimize satellite contamination, as it would complicate the interpretation and modelling of the measured signal. To construct the sample, we identify galaxies in regions of high galaxy number density and select the brightest one (in r-band) in a cylindrical area. We test the purity of our central galaxy sample in the overlap with GAMA, as well as in the MICE mock galaxy catalogues (built from N-body cosmological simulations) and find the purity to be $\sim 93.5\%$ in both cases.

We use the central galaxy sample as lens galaxies and background sources from the KiDS-1000 shear catalogues. We also split the lens sample in intrinsically red and blue galaxies. Using the measured lensing signal, we extract the ellipticity ratio f_h (weighted by the misalignment angle between the galaxy and the halo semi-major axis) using an estimator unaffected by systematic errors, such as incorrect PSF modelling and cosmic shear. We measure a non-zero ratio for the full and red central galaxy sample with 1 and 2-σ confidence, respectively, while for blue galaxies the ratio is fully consistent with zero. Our measurements are in agreement with predictions based on cosmological simulations and we demonstrate the importance of using a highly pure sample of central galaxies for the halo ellipticity measurement.

Our results are generally in agreement with studies of similar galaxy samples. However, we find a significantly lower halo ellipticity when we compare to central galaxies of galaxy groups and clusters. Cosmological simulations predict that lower mass halos are rounder and/or more misaligned with their host halo than more massive ones, which may explain part of this difference. Using shape estimates that are more sensitive to outer galaxy regions, we find a higher value for f_h, which suggests there is a galaxy scale dependence of the mis-alignment angle $\Delta\phi_{\mathrm{h,g}}$, with outer regions of the host galaxy being more aligned with its dark matter halo.

Our results can also be connected with the difference found between the predicted galaxy intrinsic alignment signal of dark matter halos and the observationally measured alignment of galaxies which are found to have a much lower signal (e.g. Faltenbacher et al. 2009; Okumura et al. 2009). In addition, galaxy intrinsic alignments have been observed to depend on the galaxy properties, with more luminous (and therefore massive) galaxies indicating a stronger alignment amplitude than less luminous ones (Singh & Mandelbaum 2016; Johnston et al. 2019). This trend of the alignment signal is in the same direction with the decreasing misalignment of halos and galaxies with increasing halo mass seen here and in cosmological simulations.

Bibliography

Abazajian, K. N., Adelman-McCarthy, J. K., Agüeros, M. A., et al. 2009, ApJS, 182, 543

Abbott, T. M. C., Abdalla, F. B., Alarcon, A., et al. 2018, Phys. Rev. D, 98, 043526

Agustsson, I. & Brainerd, T. G. 2006, ApJ, 644, L25

Alam, S., Albareti, F. D., Prieto, C. A., et al. 2015, Astrophysical Journal, Supplement Series, 219 [arXiv:1501.00963]

Alam, S., Ata, M., Bailey, S., et al. 2017, MNRAS, 470, 2617

Anderson, L., Aubourg, É., Bailey, S., et al. 2014, MNRAS, 441, 24

Azzaro, M., Patiri, S. G., Prada, F., & Zentner, A. R. 2007, MNRAS, 376, L43

Bacon, D. J., Refregier, A. R., & Ellis, R. S. 2000, Monthly Notices of the Royal Astronomical Society, 318, 625

Bailin, J., Power, C., Norberg, P., Zaritsky, D., & Gibson, B. K. 2008, MNRAS, 390, 1133

Baldry, I. K., Liske, J., Brown, M. J. I., et al. 2018, MNRAS, 474, 3875

Banerjee, A. & Jog, C. J. 2008, ApJ, 685, 254

Bartelmann, M. 2010, Classical and Quantum Gravity, 27, 233001

Bartelmann, M. & Maturi, M. 2017, Scholarpedia, 12, 32440

Bartelmann, M. & Schneider, P. 2001, Physics Reports, 340, 291

Bautista, J. E., Vargas-Magaña, M., Dawson, K. S., et al. 2018, ApJ, 863, 110

Begeman, K., Belikov, A. N., Boxhoorn, D. R., & Valentijn, E. A. 2013, Experimental Astronomy, 35, 1

Benítez, N. 2000, ApJ, 536, 571

Benítez, N., Dupke, R., Moles, M., et al. 2014, eprint arXiv:1403.5237, 215

Benítez, N., Gaztañaga, E., Miquel, R., et al. 2009, The Astrophysical Journal, 691, 241

Bernstein, G. M. & Jarvis, M. 2002, AJ, 123, 583

Bertin, E. & Arnouts, S. 1996, A&AS, 117, 393

Bertone, G., Hooper, D., & Silk, J. 2005, Phys. Rep., 405, 279

Betoule, M., Kessler, R., Guy, J., et al. 2014, A&A, 568, A22

Bilicki, M., Hoekstra, H., Brown, M. J. I., et al. 2018, A&A, 616, A69

Blazek, J., MacCrann, N., Troxel, M. A., & Fang, X. 2017, eprint arXiv:1708.09247, 1

Blazek, J., Vlah, Z., & Seljak, U. 2015, Journal of Cosmology and Astroparticle Physics, 2015, 015

Brainerd, T. G. 2005, ApJ, 628, L101

Bridle, S., Balan, S. T., Bethge, M., et al. 2010, MNRAS, 405, 2044

Bridle, S. & King, L. 2007, New Journal of Physics, 9, 444

Brown, M. L., Taylor, A. N., Hambly, N. C., & Dye, S. 2002, Monthly Notices of the Royal Astronomical Society, 333, 501

Caminha, G. B., Grillo, C., Rosati, P., et al. 2016, A&A, 587, A80

Capaccioli, M. 1989, in World of Galaxies (Le Monde des Galaxies), ed. H. G. Corwin, Jr. & L. Bottinelli, 208–227

Carretero, J., Castander, F. J., Gaztañaga, E., Crocce, M., & Fosalba, P. 2015, MNRAS, 447, 646

Carretero, J. et al. 2017, PoS, EPS-HEP2017, 488

Catelan, P., Kamionkowski, M., & Blandford, R. D. 2001, Monthly Notices of the Royal Astronomical Society, 320, L7

Cervantes-Sodi, B., Hernandez, X., & Park, C. 2010, Monthly Notices of the Royal Astronomical Society, 402, 1807

Chisari, N., Codis, S., Laigle, C., et al. 2015, MNRAS, 454, 2736

Chisari, N. E., Dvorkin, C., Schmidt, F., & Spergel, D. N. 2016, Phys. Rev. D, 94, 123507

Chisari, N. E., Koukoufilippas, N., Jindal, A., et al. 2017, MNRAS, 472, 1163

Chisari, N. E., Mandelbaum, R., Strauss, M. A., Huff, E. M., & Bahcall, N. A. 2014, MNRAS, 445, 726

Clampitt, J. & Jain, B. 2016, MNRAS, 457, 4135

Clowe, D., Gonzalez, A., & Markevitch, M. 2004, ApJ, 604, 596

Coe, D., Benítez, N., Sánchez, S. F., et al. 2006, AJ, 132, 926

Corless, V. L., King, L. J., & Clowe, D. 2009, MNRAS, 393, 1235

Coupon, J., Kilbinger, M., McCracken, H. J., et al. 2012, Astronomy & Astrophysics, 542, A5

Crocce, M., Castander, F. J., Gaztañaga, E., Fosalba, P., & Carretero, J. 2015, MNRAS, 453, 1513

Croft, R. A. C. & Metzler, C. A. 2000, The Astrophysical Journal, 545, 561

da Cunha, E., Charlot, S., & Elbaz, D. 2008, MNRAS, 388, 1595

de Jong, J. T. A., Verdoes Kleijn, G. A., Boxhoorn, D. R., et al. 2015, A&A, 582, A62

de Jong, J. T. A., Verdoes Kleijn, G. A., Erben, T., et al. 2017, A&A, 604, A134 de Jong, J. T. A., Verdoes Kleijn, G. A., Kuijken, K. H., & Valentijn, E. A. 2013, Experimental Astronomy, 35, 25

de Jong, R. S. 1996, A&A, 313, 377

DES Collaboration, Abbott, T. M. C., Abdalla, F. B., et al. 2017, arXiv e-prints, arXiv:1708.01530

Donahue, M., Ettori, S., Rasia, E., et al. 2016, ApJ, 819, 36

Drinkwater, M. J., Jurek, R. J., Blake, C., et al. 2010, Monthly Notices of the Royal Astronomical Society, 401, 1429

Driver, S. P., Andrews, S. K., da Cunha, E., et al. 2018, MNRAS, 475, 2891

Driver, S. P., Hill, D. T., Kelvin, L. S., et al. 2011, MNRAS, 413, 971

Driver, S. P., Norberg, P., Baldry, I. K., et al. 2009, Astronomy and Geophysics, 50, 5.12

Dubinski, J. & Carlberg, R. G. 1991, ApJ, 378, 496

Duffy, A. R., Schaye, J., Kay, S. T., & Dalla Vecchia, C. 2008, MNRAS, 390, L64

Dvornik, A., Cacciato, M., Kuijken, K., et al. 2017, MNRAS, 468, 3251

Edge, A., Sutherland, W., Kuijken, K., et al. 2013, The Messenger, 154, 32

Efstathiou, G. & Lemos, P. 2018, Monthly Notices of the Royal Astronomical Society, 476, 151

Elahi, P. J., Mahdi, H. S., Power, C., & Lewis, G. F. 2014, MNRAS, 444, 2333

Eriksen, M., Alarcon, A., Gaztanaga, E., et al. 2019, MNRAS, 484, 4200

Evans, A. K. D. & Bridle, S. 2009, ApJ, 695, 1446

Evans, D. S. 1951, MNRAS, 111, 526

Faltenbacher, A., Li, C., White, S. D. M., et al. 2009, Research in Astronomy and Astrophysics, 9, 41

Farrow, D. J., Cole, S., Norberg, P., et al. 2015, MNRAS, 454, 2120

Fenech Conti, I., Herbonnet, R., Hoekstra, H., et al. 2017, MNRAS, 467, 1627

Foreman-Mackey, D., Hogg, D. W., Lang, D., & Goodman, J. 2013, Publications of the Astronomical Society of the Pacific, 125, 306

Fosalba, P., Crocce, M., Gaztañaga, E., & Castander, F. J. 2015, MNRAS, 448, 2987

Fosalba, P., Gaztañaga, E., Castander, F. J., & Crocce, M. 2015, Monthly Notices of the Royal Astronomical Society, 447, 1319

Franx, M., Illingworth, G., & Heckman, T. 1989, AJ, 98, 538

Freese, K. 2017, International Journal of Modern Physics D, 26, 1730012

Georgiou, C., Chisari, N. E., Fortuna, M. C., et al. 2019a, A&A, 628, A31

Georgiou, C., Johnston, H., Hoekstra, H., et al. 2019b, A&A, 622, A90

Gunn, J. E., Carr, M., Rockosi, C., et al. 1998, The Astronomical Journal, 116, 3040

Hambly, N., MacGillivray, H., Read, M., et al. 2001, Monthly Notices of the Royal Astronomical Society, 326, 18

Heavens, A., Refregier, A., & Heymans, C. 2000, Monthly Notices of the Royal Astronomical Society, 319, 649

Hellwing, W. A., Cautun, M., Knebe, A., Juszkiewicz, R., & Knollmann, S. 2013, J. Cosmology Astropart. Phys., 2013, 012

Helmi, A. 2004, MNRAS, 351, 643

Hewitt, J. N., Turner, E. L., Schneider, D. P., Burke, B. F., & Langston, G. I. 1988, Nature, 333, 537

Heymans, C., Brown, M., Heavens, A., et al. 2004, Monthly Notices of the Royal Astronomical Society, 347, 895

Heymans, C., Grocutt, E., Heavens, A., et al. 2013, MNRAS, 432, 2433

Heymans, C., Van Waerbeke, L., Bacon, D., et al. 2006, MNRAS, 368, 1323

Hikage, C., Oguri, M., Hamana, T., et al. 2019, Publications of the Astronomical Society of Japan, 22

Hilbert, S., Xu, D., Schneider, P., et al. 2017, MNRAS, 468, 790

Hildebrandt, H., Köhlinger, F., van den Busch, J. L., et al. 2018, arXiv e-prints, arXiv:1812.06076

Hildebrandt, H., Viola, M., Heymans, C., et al. 2017, MNRAS, 465, 1454

Hinshaw, G., Larson, D., Komatsu, E., et al. 2013, ApJS, 208, 19

Hirata, C. & Seljak, U. 2003, MNRAS, 343, 459

Hirata, C. M., Mandelbaum, R., Ishak, M., et al. 2007, MNRAS, 381, 1197

Hirata, C. M. & Seljak, U. 2004, Phys. Rev. D, 70, 063526

Hivon, E., Górski, K. M., Netterfield, C. B., et al. 2002, ApJ, 567, 2

Hoekstra, H. 2004, MNRAS, 347, 1337

Hoekstra, H. & Jain, B. 2008, Annual Review of Nuclear and Particle Science, 58, 99

Hoekstra, H., Viola, M., & Herbonnet, R. 2017, MNRAS, 468, 3295

Hoekstra, H., Yee, H. K. C., & Gladders, M. D. 2004, in IAU Symposium, Vol. 220, Dark Matter in Galaxies, ed. S. Ryder, D. Pisano, M. Walker, & K. Freeman, 439

Hoffmann, K., Bel, J., Gaztañaga, E., et al. 2015, MNRAS, 447, 1724

Hu, W. & White, M. 2001, ApJ, 554, 67

Huang, H.-J., Mandelbaum, R., Freeman, P. E., et al. 2018, MNRAS, 474, 4772

Huang, H.-J., Mandelbaum, R., Freeman, P. E., et al. 2016, MNRAS, 463, 222

Hui, L. & Zhang, J. 2008, The Astrophysical Journal, 688, 742

Hui, X., Ford, H. C., Freeman, K. C., & Dopita, M. A. 1995, ApJ, 449, 592

Huterer, D. & Shafer, D. L. 2018, Reports on Progress in Physics, 81, 016901

Ilbert, O., Arnouts, S., McCracken, H. J., et al. 2006, A&A, 457, 841

Jakobs, A., Viola, M., McCarthy, I., et al. 2018, MNRAS, 480, 3338

Jee, M. J., Tyson, J. A., Hilbert, S., et al. 2016, The Astrophysical Journal, 824, 77

Jing, Y. P. & Suto, Y. 2002, ApJ, 574, 538

Joachimi, B. & Bridle, S. L. 2010, Astronomy & Astrophysics, 523, A1

Joachimi, B., Cacciato, M., Kitching, T. D., et al. 2015, Space Sci. Rev., 193, 1

Joachimi, B., Mandelbaum, R., Abdalla, F. B., & Bridle, S. L. 2011, A&A, 527, A26

Johnston, H., Georgiou, C., Joachimi, B., et al. 2019, Astronomy and Astrophysics, 624, A30

Joudaki, S., Blake, C., Heymans, C., et al. 2016, Monthly Notices of the Royal Astronomical Society, 000, stw2665

Joudaki, S., Blake, C., Johnson, A., et al. 2018, MNRAS, 474, 4894

Kaiser, N., Squires, G., & Broadhurst, T. 1995, ApJ, 449, 460

Kaiser, N., Wilson, G., & Luppino, G. a. 2000, eprint arXiv:astro-ph/0003338, 2

Kannawadi, A., Hoekstra, H., Miller, L., et al. 2019, A&A, 624, A92

Kelvin, L. S., Driver, S. P., Robotham, A. S. G., et al. 2012, MNRAS, 421, 1007

Kiessling, A., Cacciato, M., Joachimi, B., et al. 2015, Space Sci. Rev., 193, 67

Kilbinger, M. 2015, Reports on Progress in Physics, 78, 086901

Kirk, D., Brown, M. L., Hoekstra, H., et al. 2015, Space Sci. Rev., 193, 139

Kirk, D., Rassat, A., Host, O., & Bridle, S. 2012, Monthly Notices of the Royal Astronomical Society, 424, 1647

Kitching, T. D., Heavens, A. F., Alsing, J., et al. 2014, MNRAS, 442, 1326

Knebe, A., Libeskind, N. I., Knollmann, S. R., et al. 2010, MNRAS, 405, 1119

Knebe, A., Yahagi, H., Kase, H., Lewis, G., & Gibson, B. K. 2008, MNRAS, 388, L34

Köhlinger, F., Viola, M., Joachimi, B., et al. 2017, Monthly Notices of the Royal Astronomical Society, 471, 4412

Kormendy, J. 1982, Morphology and dynamics of galaxies; Proceedings of the Twelfth Advanced Course, Saas-Fee, Switzerland, March 29-April 3, 1982 (A84-15502 04-90). Sauverny, Switzerland, Observatoire de Geneve, 1983, p. 113-288., 12, 113

Koyama, K. 2016, Reports on Progress in Physics, 79, 046902

Krause, E., Eifler, T., & Blazek, J. 2016, MNRAS, 456, 207

Kuijken, K., Heymans, C., Dvornik, A., et al. 2019, A&A, 625, A2

Kuijken, K., Heymans, C., Hildebrandt, H., et al. 2015, MNRAS, 454, 3500

Kunz, M. 2012, Comptes Rendus Physique, 13, 539

Landy, S. D. & Szalay, A. S. 1993, Astrophys. J., 412, 64

Lange, J. U., van den Bosch, F. C., Hearin, A., et al. 2018, MNRAS, 473, 2830

Laureijs, R., Amiaux, J., Arduini, S., et al. 2011, eprint arXiv:1110.3193 [arXiv:1110.3193]

Law, D. R. & Majewski, S. R. 2010, ApJ, 714, 229

Lawrence, A., Warren, S. J., Almaini, O., et al. 2007, MNRAS, 379, 1599

Lee, J. 2011, The Astrophysical Journal, 732, 99

Lee, J. & Erdogdu, P. 2007, The Astrophysical Journal, 671, 1248

Lee, J. & Pen, U.-L. 2002, The Astrophysical Journal, 567, L111

Leonard, C. D. & Mandelbaum, R. 2018, MNRAS[arXiv:1802.08263]

L'Huillier, B., Winther, H. A., Mota, D. F., Park, C., & Kim, J. 2017, MNRAS, 468, 3174

Li, C., Jing, Y. P., Faltenbacher, A., & Wang, J. 2013, ApJ, 770, L12

Liske, J., Baldry, I. K., Driver, S. P., et al. 2015, MNRAS, 452, 2087

LSST Science Collaboration, Abell, P. A., Allison, J., et al. 2009, eprint arXiv:0912.0201 [arXiv:0912.0201]

MacArthur, L. A., Courteau, S., & Holtzman, J. A. 2003, ApJ, 582, 689

Mandelbaum, R., Blake, C., Bridle, S., et al. 2011, MNRAS, 410, 844

Mandelbaum, R., Hirata, C. M., Broderick, T., Seljak, U., & Brinkmann, J. 2006a, MNRAS, 370, 1008

Mandelbaum, R., Hirata, C. M., Ishak, M., Seljak, U., & Brinkmann, J. 2006b, MNRAS, 367, 611

Mandelbaum, R., Hirata, C. M., Leauthaud, A., Massey, R. J., & Rhodes, J. 2012, MNRAS, 420, 1518

Mandelbaum, R., Hirata, C. M., Seljak, U., et al. 2005, Monthly Notices of the Royal Astronomical Society, 361, 1287

Mandelbaum, R., Rowe, B., Armstrong, R., et al. 2015, MNRAS, 450, 2963

Massey, R., Hoekstra, H., Kitching, T., et al. 2013, MNRAS, 429, 661

Massey, R., Kitching, T., & Richard, J. 2010, Reports on Progress in Physics, 73, 086901

Melchior, P. & Viola, M. 2012, MNRAS, 424, 2757

Melchior, P., Viola, M., Schäfer, B. M., & Bartelmann, M. 2011, MNRAS, 412, 1552

Miller, L., Heymans, C., Kitching, T. D., et al. 2013, MNRAS, 429, 2858

Miller, L., Kitching, T. D., Heymans, C., Heavens, A. F., & van Waerbeke, L. 2007, MNRAS, 382, 315

Mo, H., van den Bosch, F. C., & White, S. 2010, Galaxy Formation and Evolution

Napolitano, N. R., Romanowsky, A. J., Capaccioli, M., et al. 2011, MNRAS, 411, 2035

Natarajan, P. & Refregier, A. 2000, ApJ, 538, L113

Navarro, J. F., Frenk, C. S., & White, S. D. M. 1996, ApJ, 462, 563

Nierenberg, A. M., Auger, M. W., Treu, T., Marshall, P. J., & Fassnacht, C. D. 2011, ApJ, 731, 44

O'Brien, J. C., Freeman, K. C., van der Kruit, P. C., & Bosma, A. 2010, A&A, 515, A60

Oguri, M., Bayliss, M. B., Dahle, H., et al. 2012, MNRAS, 420, 3213

Okumura, T., Jing, Y. P., & Li, C. 2009, ApJ, 694, 214

Olling, R. P. 1995, AJ, 110, 591

Parker, L. C., Hoekstra, H., Hudson, M. J., van Waerbeke, L., & Mellier, Y. 2007, ApJ, 669, 21

Peletier, R. F., Valentijn, E. A., & Jameson, R. F. 1990, A&A, 233, 62

Peng, C. Y., Ho, L. C., Impey, C. D., & Rix, H.-W. 2002, AJ, 124, 266

Pereira, M. J., Bryan, G. L., & Gill, S. P. D. 2008, ApJ, 672, 825

Peter, A. H. G., Rocha, M., Bullock, J. S., & Kaplinghat, M. 2013, MNRAS, 430, 105

Piras, D., Joachimi, B., Schäfer, B. M., et al. 2018, Monthly Notices of the Royal Astronomical Society, 474, 1165

Planck Collaboration, Ade, P. A. R., Aghanim, N., et al. 2016, A&A, 594, A13

Planck Collaboration, Aghanim, N., Akrami, Y., et al. 2018, arXiv e-prints, arXiv:1807.06209

Pujol, A., Sureau, F., Bobin, J., et al. 2017, ArXiv e-prints [arXiv:1707.01285]

Refregier, A. 2003, MNRAS, 338, 35

Riess, A. G., Filippenko, A. V., Challis, P., et al. 1998, The Astronomical Journal, 116, 1009

Robotham, A. S. G., Norberg, P., Driver, S. P., et al. 2011, MNRAS, 416, 2640

Roche, N. & Eales, S. A. 1999, Monthly Notices of the Royal Astronomical Society, 307, 703

Rowe, B. T. P., Jarvis, M., Mandelbaum, R., et al. 2015, Astronomy and Computing, 10, 121

Sadeh, I., Abdalla, F. B., & Lahav, O. 2016, PASP, 128, 104502

Samuroff, S., Blazek, J., Troxel, M. A., et al. 2018, eprint arXiv:1811.06989 [`arXiv:1811.06989v1`]

Schäfer, B. M. 2009, International Journal of Modern Physics D, 18, 173

Schneider, M. D. & Bridle, S. 2010, Monthly Notices of the Royal Astronomical Society, 402, 2127

Schneider, M. D. & Bridle, S. 2010, MNRAS, 402, 2127

Schneider, M. D., Cole, S., Frenk, C. S., et al. 2013, MNRAS, 433, 2727

Schneider, P., van Waerbeke, L., Kilbinger, M., & Mellier, Y. 2002, Astronomy & Astrophysics, 396, 1

Schrabback, T., Hilbert, S., Hoekstra, H., et al. 2015, MNRAS, 454, 1432

Scolnic, D. M., Jones, D. O., Rest, A., et al. 2017, ArXiv e-prints [`arXiv:1710.00845`]

Shin, T.-h., Clampitt, J., Jain, B., et al. 2018, MNRAS, 475, 2421

Sifón, C., Herbonnet, R., Hoekstra, H., van der Burg, R. F. J., & Viola, M. 2018, MNRAS, 478, 1244

Sifón, C., Hoekstra, H., Cacciato, M., et al. 2015, A&A, 575, A48

Singh, S. & Mandelbaum, R. 2016, MNRAS, 457, 2301

Singh, S., Mandelbaum, R., & More, S. 2015, MNRAS, 450, 2195

Singh, S., Mandelbaum, R., Seljak, U., Slosar, A., & Vazquez Gonzalez, J. 2017, Monthly Notices of the Royal Astronomical Society, 471, 3827

Smail, I., Hogg, D. W., Yan, L., & Cohen, J. G. 1995, The Astrophysical Journal, 449 [`arXiv:9506095`]

Spergel, D., Gehrels, N., Breckinridge, J., et al. 2013, eprint arXiv:1503.03757 [`arXiv:1305.5422`]

Strauss, M. A., Weinberg, D. H., Lupton, R. H., et al. 2002, The Astronomical Journal, 124, 1810

Taylor, E. N., Hopkins, A. M., Baldry, I. K., et al. 2011, MNRAS, 418, 1587

Tegmark, M., Taylor, A. N., & Heavens, A. F. 1997, The Astrophysical Journal, 480, 22

Tenneti, A., Mandelbaum, R., & Di Matteo, T. 2016, Monthly Notices of the Royal Astronomical Society, 462, 2668

Tenneti, A., Mandelbaum, R., Di Matteo, T., Feng, Y., & Khandai, N. 2014, MNRAS, 441, 470

Tonegawa, M., Okumura, T., Totani, T., et al. 2018, Publications of the Astronomical Society of Japan, 70, 1

Tonegawa, M., Totani, T., Okada, H., et al. 2015, Publications of the Astronomical Society of Japan, 67, 81

Tortora, C., Napolitano, N. R., Cardone, V. F., et al. 2010, MNRAS, 407, 144

Troxel, M. A. & Ishak, M. 2015, Phys. Rep., 558, 1

Troxel, M. A., MacCrann, N., Zuntz, J., et al. 2017, ArXiv e-prints [arXiv:1708.01538]

Umetsu, K., Sereno, M., Tam, S.-I., et al. 2018, ApJ, 860, 104

Vakili, M., Bilicki, M., Hoekstra, H., et al. 2019, MNRAS, 487, 3715

Valentijn, E. A., McFarland, J. P., Snigula, J., et al. 2007, in Astronomical Society of the Pacific Conference Series, Vol. 376, Astronomical Data Analysis Software and Systems XVI, ed. R. A. Shaw, F. Hill, & D. J. Bell, 491

van de Ven, G., Falcón-Barroso, J., McDermid, R. M., et al. 2010, ApJ, 719, 1481

van Uitert, E., Cacciato, M., Hoekstra, H., et al. 2016, MNRAS, 459, 3251

van Uitert, E., Hoekstra, H., Joachimi, B., et al. 2017, MNRAS, 467, 4131

van Uitert, E., Hoekstra, H., Schrabback, T., et al. 2012, A&A, 545, A71

van Uitert, E. & Joachimi, B. 2017, MNRAS, 468, 4502

van Uitert, E., Joachimi, B., Joudaki, S., et al. 2018, MNRAS, 476, 4662

Van Waerbeke, L., Mellier, Y., Erben, T., et al. 2000, Astronomy & Astrophysics, 594, A13

Velliscig, M., Cacciato, M., Schaye, J., et al. 2015a, MNRAS, 453, 721

Velliscig, M., Cacciato, M., Schaye, J., et al. 2015b, MNRAS, 454, 3328

Vera-Ciro, C. & Helmi, A. 2013, ApJ, 773, L4

Viola, M., Cacciato, M., Brouwer, M., et al. 2015, MNRAS, 452, 3529

Viola, M., Kitching, T. D., & Joachimi, B. 2014, MNRAS, 439, 1909

Walsh, D., Carswell, R. F., & Weymann, R. J. 1979, Nature, 279, 381

Wang, P., Luo, Y., Kang, X., et al. 2018, ApJ, 859, 115

Wittman, D. M., Tyson, J. A., Kirkman, D., Dell'Antonio, I., & Bernstein, G. 2000, Nature, 405, 143

Wright, A. H., Hildebrandt, H., Kuijken, K., et al. 2018, eprint arXiv:1812.06077, 1

Wright, A. H., Robotham, A. S. G., Bourne, N., et al. 2016, MNRAS, 460, 765

Wright, A. H., Robotham, A. S. G., Driver, S. P., et al. 2017, Monthly Notices of the Royal Astronomical Society, 470, 283

Wright, C. O. & Brainerd, T. G. 2000, ApJ, 534, 34

Yang, X., van den Bosch, F. C., Mo, H. J., et al. 2006, MNRAS, 369, 1293

York, D. G., Adelman, J., Anderson, John E., J., et al. 2000, AJ, 120, 1579

Zuntz, J., Paterno, M., Jennings, E., et al. 2015, Astronomy and Computing, 12, 45

Summary

The subject of cosmology has gained a lot of interest in the last few decades, as astronomical data improve and the precision with which we can measure statistical observable quantities in the Universe is increasing. A broad picture of the physical processes that dictate the evolution of the Universe has been developed, summarized in the standard cosmological model, which has been successful in describing increasingly more precise and independent astronomical observations.

The biggest questions yet to be answered within the standard cosmological model concern dark matter and dark energy, components that make up $\sim 95\%$ of the energy density of the Universe today. The former has the effect of speeding up the formation of structures and the latter the opposite. Some of the key questions surrounding these mysterious contents of the Universe are: how much dark matter is there, and how strongly does it cluster (encoded in the cosmological parameter S_8)? Is there a tension of the S_8 parameter in high- and low-redshift astronomical observations? What is the equation of state of dark energy (parametrised by w)? Is it a cosmological constant, or does it vary with time?

Observational techniques that are sensitive to dark matter and dark energy are required to shed light onto these questions. One such technique is weak gravitational lensing: the distortion of light sources (e.g. background galaxies) from the matter density between the source and the observer. The distortion caused by gravitational lensing depends on the intervening mass and geometry of the Universe, which makes it suitable to study dark matter and dark energy.

Future weak lensing surveys aim to greatly increase the statistical precision of lensing measurements. However, this means that the systematic uncertainty in the measurement needs to be controlled to very high accuracy. The most important astrophysical systematic contamination are intrinsic alignments, the alignment of the orientation of galaxies with the matter density field. Intrinsic alignments add in the data a distortion pattern that is not caused by weak lensing and can significantly bias the measurement of cosmological parameters, if left unaccounted for. In this thesis, the intrinsic alignment signal is measured from ground-based survey data with unprecedented image quality and data fidelity, and the dependence of the signal with various galaxy properties is examined. This knowledge will allow the development of more precise models for the intrinsic alignment signal, as well as help better mitigate its effect on weak lensing measurements and allow the full usage of the statistical power of the future weak lensing surveys.

In order to measure the intrinsic alignment signal from galaxies, we need galaxy distance information (i.e. redshift), to identify physical galaxy pairs that interact gravitationally, as well as deep, high-quality imaging data to determine the shapes of galaxies and quantify their alignment. Throughout the thesis, highly accurate redshifts are obtained from the Galaxy And Mass Assembly (GAMA) spectroscopic survey. The survey's high completeness ensures that redshift information is available for the vast majority of our galaxy sample, even for galaxies that are close together on the sky, and allows the robust determination of the alignment signal from large to small scales. Galaxy shapes are measured with imaging data from the Kilo Degree Survey, a survey specifically designed for weak lensing science. Because of this, the imaging data are deep, with minimal artifacts from the telescope's optics and the Earth's atmosphere (quantified by the point-spread function, PSF). The measurement of shapes is carried out using the DEIMOS method, which relies on measuring weighted galaxy surface brightness moments and uses a scheme to approximate the un-weighted moments while it also analytically treats the effects of the PSF.

Using this dataset, we begin in **chapter 2** by measuring shapes of galaxies in images obtained using three different broad band filters, g, r and i-band. The intrinsic alignment signal of our galaxy sample is found to appear stronger when observations are made in the g and i-band filters, compared to r-band. This difference is primarily sourced by red satellite galaxies, and is only evident in small scales, below a few Mpc$/h$. One possible mechanism that can explain this difference is the tidal nature of the intrinsic alignments, together with the colour gradients of galaxies: outer regions of galaxies are more susceptible to tidal fields, and intrinsic alignments are expected to more strongly affect these outer galaxy scales compared to inner regions. In addition, galaxies build up hierarchically, and the inner regions are generally more red, populated with older stars than the outer ones. Hence, observations at different wavelength can potentially reveal different regions of the galaxies. However, this picture is further complicated by the redshifting of galaxy spectral energy distributions and the 4000 Å break, with respect to the observed broad-band filters. While a prediction for the expected difference in alignment with wavelength is complicated, it is clear that there are interesting discoveries to be made about the alignment of galaxies at small scales.

We continue this thesis with **chapter 3**, where we look at the intrinsic alignment signal observed in the r-band, at large scales. The aim is to provide a direct measurement of the signal to be used as an informative prior for weak lensing studies, which will improve the constraints on the cosmological parameters. To do this, it was important that we use a representative sample of galaxies, as similar as possible to what would be used by a weak lensing survey. We find that intrinsically red galaxies exhibit a strong alignment signal while blue galaxies have a signal consistent with zero, in agreement with previous literature. Using these direct measurements of intrinsic alignments, we forecast that current weak lensing surveys can achieve significantly more accurate constraints on the measurement of the S_8 parameter.

We then focus on the alignment of galaxies in smaller scales, looking specifically at galaxy groups in **chapter 4**. We measure a significant radial alignment of satellite galaxies with respect to the group's centre, which reduces to zero at large separations. In addition, we find that the outer regions of satellite galaxies (probed by increasing the radial weighting of the shape measurement method) are more strongly aligned than the inner ones. Intrinsically red satellites exhibit a generally stronger alignment than blue ones. Moreover, central galaxies of these groups are also aligned with the distribution of the satellite galaxies, with outer regions of centrals being more strongly aligned than inner ones and red centrals showing a stronger alignment than blue ones. These measurements suggest that intrinsic alignments at small scales are generally complicated, and the dependencies studied here can be used to tailor and improve existing models of the alignment signal at these small scales.

In **chapter 5** we zoom in further and study the alignment of central galaxies with their host dark matter halo. To do this, we measure the anisotropic weak lensing signal around a sample of galaxies that is optimised to have small contamination of satellite galaxies. We constraint $f_{\rm h}$, a parameter sensitive to the relative ellipticity of the dark matter halo and the galaxy, as well as their average mis-alignment angle. We find that red central galaxies have a non-zero

f_{h} at a 2σ significance. The measured value of f_{h} significantly increases if we repeat the lensing measurement using galaxy shapes that are more sensitive to the outer parts of the galaxy. Since the average ellipticity of the shapes of inner and outer galaxy regions do not vary significantly, we conclude that outer galaxy regions are more aligned with their dark matter halo than inner ones.

Nederlandse samenvattig

De interesse in het onderwerp kosmologie is de afgelopen decennia sterk toegenomen, dankzij een toename in de kwaliteit van sterrenkundige data en in de precisie waarmee we statistische, waarneembare grootheden in het universum kunnen meten. Er is een uitgebreid model ontwikkeld van de fysieke processen die de evolutie van het universum bepalen, samengevat in het standaardmodel van de kosmologie, dat met succes steeds preciezere, onafhankelijke sterrenkundige waarnemingen heeft kunnen beschrijven.

De grootste nog onbeantwoorde vragen binnen het standaardmodel van de kosmologie hebben betrekking tot donkere materie en donkere energie, componenten die $\sim 95\%$ van de energiedichtheid in het huidige universum voorstellen. De eerste versnelt de vorming van structuren terwijl de tweede dat juist vertraagt. Enkele van de kernvragen rond deze mysterieuze onderdelen van het universum zijn: hoeveel donkere materie is er, en hoe sterk clustert het (vastgelegd in de kosmologische parameter S_8)? Zit er spanning in de S_8-parameter in sterrenkundige waarnemingen op hoge en lage roodverschuiving? Wat is de toestandsvergelijking van donkere energie (geparametriseerd door w)? Is het een kosmologische constante, of verandert het mettertijd?

Om een licht te werpen op deze vragen, zijn waarneemtechnieken nodig die gevoelig zijn voor donkere materie en donkere energie. Eén zo'n techniek is zwakke lenswerking door zwaartekracht: de vervorming van lichtbronnen (bijv. sterrenstelsels in de achtergrond) door de dichtheid van materie tussen bron en waarnemer. De vervorming door zwaartekrachtslenzen hangt af van de tussenliggende massa en de geometrie van het universum, waardoor het geschikt is om donkere materie en donkere energie mee te bestuderen. Toekomstige onderzoeken naar zwakke lenswerking hebben als doel om de statistische precisie van lensmetingen sterk te vergroten. Dit betekent echter dat de systematische onzekerheid in de meting met zeer hoge nauwkeurigheid beheerst moet worden. De belangrijkste astrofysische systematische contaminatie komt door intrinsieke uitlijning, de uitlijning van de oriëntatie van sterrenstelsels naar het dichtheidsveld van materie. Intrinsieke uitlijningen voegen aan de data een vervormingspatroon toe dat niet wordt veroorzaakt door zwakke lenswerking en kunnen een significante verschuiving in metingen van kosmologische parameters veroorzaken, als er geen rekening mee wordt gehouden. In deze proefschrift wordt het signaal van intrinsieke uitlijning gemeten uit data vanaf de grond met ongekende beeldkwaliteit en getrouwheid van data, en wordt de afhankelijkheid van dit signaal van verschillende eigenschappen van sterrenstelsels bestudeerd. Deze kennis zal zowel bijdragen aan de ontwikkeling van preciezere modellen van het signaal door intrinsieke uitlijning als helpen het effect ervan op metingen van zwakke lenswerking beter te beperken, en zal zorgen dat de statistische kracht van toekomstige onderzoeken naar zwakke lenswerking volledig gebruikt kan worden.

Om het intrinsieke uitlijningssignaal van sterrenstelsels te meten, hebben we zowel informatie nodig over de afstanden van sterrenstelsels (d.w.z. roodverschuiving), om fysieke paren sterrenstelsels te identificeren die een interactie door zwaartekracht hebben, als diepe beeldgegevens van hoge kwaliteit, om de vorm van sterrenstelsels te bepalen en hun uitlijning te kwantificeren. In heel deze proefschrift zijn zeer nauwkeurige roodverschuivingen verkregen van het spectroscopische onderzoek *Galaxy And Mass Assembly* (GAMA). De grote volledigheid van dit onderzoek zorgt ervoor dat informatie over roodverschuiving beschikbaar is voor de overgrote meerderheid van ons monster sterrenstelsels, zelfs voor sterrenstelsels die dicht bij elkaar staan aan de hemel, en zorgt dat het uitlijningssignaal robuust kan worden gemeten van grote tot kleine schalen. De vorm van sterrenstelsels wordt gemeten met beelddata van de *Kilo Degree Survey*, een onderzoek specifiek ontworpen voor analyse van zwakke lenswerking. Hierdoor zijn de beelddata diep, met geringe artefacten door de optiek van de telescoop en de atmosfeer van de aarde (gekwantificeerd door de *point-spread function* of PSF). De vormmeting wordt gedaan met behulp van de *DEIMOS*-methode, die afhankelijk is van het meten van gewogen oppervlaktedichtheidsmomenten van sterrenstelsels en de ongewogen momenten benadert, en tegelijkertijd de PSF-effecten analytisch behandelt.

In **hoofdstuk 2** beginnen we door, aan de hand van deze dataset, de vorm van sterrenstelsels te meten in afbeeldingen die in drie verschillende breedbandfilters (g, r en i) zijn genomen. Het intrinsieke uitlijningssignaal van ons monster sterrenstelsels blijkt sterker in metingen in de g- en i-banden dan in de r-band. Dit verschil komt voornamelijk voor uit rode satellietstelsels en is alleen zichtbaar op kleine schalen, minder dan een paar Mpc/h. Een mechanisme dat dit verschil mogelijk kan verklaren is de oorsprong van intrinsieke uitlijningen in de getijdewerking, samen met de kleurgradiënten van sterrenstelsels: de uiterste regionen van sterrenstelsels zijn gevoeliger voor getijdevelden en men zou verwachten dat intrinsieke uitlijningen een sterker effect hebben op deze uiterste schalen van sterrenstelsels dan op de binnenste regionen. Bovendien bouwen sterrenstelsels zich hiërarchisch op en zijn de binnenste regionen over het algemeen roder, met meer oude sterren dan in de buitengebieden. Waarnemingen op verschillende golflengtes kunnen dus mogelijk verschillende regionen van sterrenstelsels onthullen. Dit beeld wordt echter verder gecompliceerd ten opzichte van de gemeten breedbandfilters door de roodverschuiving van de spectrale energieverdeling van sterrenstelsels en de breuk op 4000 Å. Hoewel het ingewikkeld is om het verwachte verschil in uitlijning op verschillende golflengtes te voorspellen, is het duidelijk dat er interessante ontdekkingen gemaakt kunnen worden over de uitlijning van sterrenstelsels op kleine schalen.

We vervolgen de proefschrift in **hoofdstuk 3**, waarin we kijken naar het intrinsieke uitlijningssignaal waargenomen in de r-band, op grote schalen. Het doel is om een directe meting van het signaal te gebruiken, die gebruikt kan worden als a-priori informatie voor onderzoeken naar zwakke lenswerking, waardoor de limieten op kosmologische parameters verbeterd zullen kunnen worden. Hiervoor was het belangrijk dat we een representatief monster sterrenstelsels gebruikten, zo gelijk mogelijk aan het monster dat een onderzoek naar zwakke lenswerking zou gebruiken. We zagen dat intrinsiek rode sterrenstelsels een sterk uitlijningssignaal vertonen, terwijl blauwe sterrenstelsels een signaal consistent met nul vertonen; dit komt overeen met de bestaande literatuur. Met behulp van deze directe metingen van intrinsieke uitlijning voorspellen we dat onderzoeken naar zwakke lenswerking significant nauwkeurigere limieten op de S_8-parameter kunnen stellen.

Daarna richten we ons op de uitlijning van sterrenstelsels op kleine schalen, waarbij we in **hoofdstuk 4** specifiek kijken naar groepen sterrenstelsels. We meten een significante radiale uitlijning van satellietstelsels ten opzichte van het centrum van de group, dat op grote afstanden afvalt naar nul. Bovendien zien we dat de buitenste regionen van satellietstelsels (gepeild door de radiale gewichten te vergroten van de methode om vormen te meten) sterker uitgelijnd zijn dan de binnenste. Intrinsiek rode satellieten laten over het algemeen een sterkere uitlijning zien dan blauwe. Verder zijn de centrale sterrenstelsels in deze groepen ook uitgelijnd met de verdeling van satellietstelsels, waarbij de buitendelen van de centrale stelsels sterker uitgelijnd zijn dan de binnendelen en rode centrale stelsels sterker dan blauwe. Deze metingen suggereren dat intrinsieke uitlijningen op kleine schalen over het algemeen complex zijn; de afhankelijkheden die hier zijn bestudeerd, kunnen worden gebruikt om de bestaande modellen van het uitlijningssignaal op deze kleine schalen af te stemmen en te verbeteren.

In **hoofdstuk 5** zoomen we verder in en bestuderen we de uitlijning van centrale sterrenstelsels met de donkere materiehalo waarin ze leven. Daartoe meten we het anisotropische zwakke lenswerkingssignaal rond een monster sterrenstelsels dat is geoptimaliseerd om weinig contaminatie van satellietstelsels te hebben. We stellen een limiet aan $f_{\rm h}$, een parameter die gevoelig is voor zowel de relatieve ellipticiteit van de donkere materiehalo en het sterrenstelsel als hun gemiddelde afwijkingshoek. We zien dat rode centrale stelsels een niet-nul $f_{\rm h}$ hebben met een significantie van 2σ. De gemeten waarde van $f_{\rm h}$ neemt significant toe als we de lenswerkingsmeting herhalen met vormen van sterrenstelsels die gevoeliger zijn voor de buitendelen van het stelsel. Aangezien de gemiddelde ellipticiteit van de vormen van de binnen- en buitendelen van sterrenstelsels niet significant verschilt, concluderen we dat de buitenregionen van sterrenstelsels meer uitgelijnd zijn met hun donkere materiehalo dan de binnenste.

Σύνοψη

Η κοσμολογία έχει τραβήξει μεγάλο ενδιαφέρον τις τελευταίες δεκαετίες, με τη βελτίωση αστρονομικών δεδομένων και την αύξηση στην ακρίβεια με την οποία μπορούμε να μετρήσουμε στατιστικές παρατηρήσιμες ποσότητες στο Σύμπαν. Η γενική εικόνα των φυσικών διεργασιών που διαπρέπουν την εξέλιξη του Σύμπαντος συνοψίζεται στο καθιερωμένο κοσμολογικό μοντέλο, το οποίο επιτυγχάνει στο να περιγράφει ολοένα και πιο ακριβείς μετρήσεις από ανεξάρτητες αστρονομικές παρατηρήσεις.

Τα μεγαλύτερα ερωτήματα που δεν έχουν ακόμη απαντηθεί εντός του καθιερωμένου κοσμολογικού μοντέλου αφορούν τη σκοτεινή ύλη και σκοτεινή ενέργεια, στοιχεία που ευθύνονται για το $\sim 95\%$ της ενεργειακής πυκνότητας του Σύμπαντος σήμερα. Η σκοτεινή ύλη αυξάνει το ρυθμό της δημιουργίας δομών ενώ η σκοτεινή ενέργεια κάνει το αντίθετο. Μερικά από τα βασικά ερωτήματα περί αυτών των μυστήριων στοιχείων του Σύμπαντος είναι: πόση σκοτεινή ύλη υπάρχει και πόσο έντονα σμηνεύει (που κωδικοποιούνται στην κοσμολογική παράμετρο S_8); Υπάρχει ασυμφωνία στην παράμετρο S_8 μεταξύ αστρονομικών παρατηρήσεων του πρώιμου και τωρινού σύμπαντος; Ποια είναι η καταστατική εξίσωση της σκοτεινής ενέργειας (παραμετροποιημένη από την w); Είναι κοσμολογική σταθερά ή μεταβάλλεται με το χρόνο;

Παρατηρησιακές τεχνικές ευαίσθητες στη σκοτεινή ύλη και σκοτεινή ενέργεια απαιτούνται για να ρίξουμε φως σε αυτές τις ερωτήσεις. Μία τέτοια τεχνική είναι μέσω ασθενείς βαρυτικών φακών, οι οποίοι διαστρεβλώνουν το φως (π.χ. από μακρινούς γαλαξίες) λόγω της ύλης μεταξύ της πηγής φωτός και του παρατηρητή. Η διαστρέβλωση που προκαλούν οι βαρυτικοί φακοί εξαρτάται από την μάζα και γεωμετρία του σύμπαντος, πράγμα το οποίο τους καθιστά κατάλληλους για μελέτες της σκοτεινής ύλης και σκοτεινής ενέργειας. Μελλοντικές έρευνες με ασθενείς βαρυτικούς φακούς έχουν στόχο να αυξήσουν δραματικά τη στατιστική ακρίβεια με την οποία μετράμε αυτή τη διαστρέβλωση. Ωστόσο, αυτό σημαίνει πως το συστηματικό σφάλμα αυτών των μετρήσεων θα πρέπει να προσδιοριστεί με πολύ μεγάλη ακρίβεια. Το πιο σημαντικό συστηματικό σφάλμα που πηγάζει από αστροφυσικά φαινόμενα είναι λόγω ευθυγράμμισης των γαλαξιών, οι οποίοι τείνουν να ευθυγραμμίζουν το σχήμα τους με την κατανομή μάζας στο σύμπαν. Η ευθυγράμμιση αυτή προσθέτει ένα μοτίβο διαστρέβλωσης στα παρατηρησιακά δεδομένα το οποίο δεν οφείλεται στους βαρυτικούς φακούς και μπορεί να οδηγήσει σε σημαντικά εσφαλμένες μετρήσεις κοσμολογικών παραμέτρων, αν δεν ληφθεί υπ΄ όψην. Σε αυτή την εργασία, μετράμε το σήμα της διαστρέβλωσης λόγω ευθυγραμμίσεων των γαλαξιών με αστρονομικές παρατηρήσεις πρωτοφανής ποιότητας εικόνων και δεδομένων, και εξετάζουμε την εξάρτηση του σήματος με διάφορες ιδιότητες των γαλαξιών. Η γνώση αυτή καθιστά εφικτή την ανάπτυξη ακριβή μοντέλων του σήματος λόγω ευθυγράμμισης γαλαξιών, που με τη σειρά τους βοηθούν στο να απαλλάξουμε τη μέτρηση βαρυτικών φακών από αυτό το σήμα και να χρησιμοποιήσουμε καθολικά τη στατιστική δύναμη των μελλοντικών ερευνών.

Για να μετρήσουμε το σήμα από την ευθυγράμμιση γαλαξιών, χρειάζεται να γνωρίζουμε την απόσταση των γαλαξιών από εμάς (ή αλλιώς την ερυθρομετάθεσή τους), ώστε να αναγνωρίσουμε τα φυσικώς συνδεδεμένα ζεύγη γαλαξιών που αλληλεπιδρούν βαρυτικά, καθώς επίσης και βαθιές αστρονομικές εικόνες υψηλής ποιότητας για να προσδιορίσουμε σχήματα γαλαξιών και να ποσοτικοποιήσουμε την ευθυγράμμισή τους. Σε αυτή την εργασία, μετρήσεις ερυθρομετάθεσης υψηλής ακρίβειας παρέχονται από την φασματοσκοπική έρευνα Galaxy And Mass Assembly (GAMA). Τα δεδομένα της έρευνας παρέχουν μετρήσεις για τους περισσότερους γαλαξίες στο δείγμα μας, ακόμη και για γαλαξίες πολύ κοντά ο ένας με τον άλλο στον ουρανό, και κάνουν εφικτή τη μέτρηση του σήματος ευθυγραμμίσεων σε μεγάλες και μικρές κλίμακες. Μετράμε σχήματα γαλαξιών με εικόνες από την Kilo Degree Survey, έρευνα ειδικά σχεδιασμένη για μετρήσεις βαρυτικών φακών. Λόγω αυτού, οι εικόνες είναι βαθέως ουρανού, με ελάχιστες επιρροές από τα οπτικά του τηλεσκοπίου και την ατμόσφαιρα της Γης (μετρούμενες μέσω της point-spread function, PSF). Η μέτρηση των σχημάτων γίνεται με τη μέθοδο DEIMOS, που μετράει σχήματα μέσω ολοκληρωμάτων των εικόνων των γαλαξιών και εφαρμόζει διορθώσεις για τη συνάρτηση βαρύτητας στη μέτρηση ολοκληρωμάτων και την PSF.

Με τα δεδομένα αυτά, ξεκινάμε στο **κεφάλαιο 2** μετρώντας σχήματα γαλαξιών σε τρία διαφορετικού μήκους κύματος φίλτρα, g, r και i. Η ευθυγράμμιση των γαλαξιών φαίνεται να είναι πιο ισχυρή όταν οι παρατηρήσεις γίνονται στο g

και i φίλτρο, σε σύγκριση με το r. Η διαφορά αυτή οφείλεται κατά κύριο λόγο στους κόκκινους γαλαξίες δορυφόρους, και εμφανίζεται μόνο σε μικρές κλίμακες, μικρότερες από μερικά Mpc$/h$. Ένας πιθανός φυσικός μηχανισμός που εξηγεί αυτές τις διαφορές είναι η παλιρροιακή φύση του φαινομένου ευθυγράμμισης, μαζί με την χρωματική βαθμίδα των γαλαξιών: οι εξωτερικές περιοχές των γαλαξιών επηρεάζονται περισσότερο από παλιρροιακές δυνάμεις, και το φαινόμενο ευθυγράμμισης προβλέπεται να επηρεάζει περισσότερο τις εξωτερικές από τις εσωτερικές περιοχές των γαλαξιών. Επιπλέον, οι γαλαξίες μεγαλώνουν ιεραρχικά, και οι εσωτερικές περιοχές τους είναι γενικά πιο κόκκινες από τις εξωτερικές, αφού έχουν περισσότερο κόκκινα, παλαιά αστέρια. Έτσι, παρατηρήσεις σε διαφορετικά φίλτρα μπορούν να δίνουν έμφαση σε διαφορετικές περιοχές των γαλαξιών. Η εικόνα αυτή περιπλέκεται αν λάβουμε υπόψη την ερυθρομετάθεση των γαλαξιών και το 4000 Å break, σε σύγκριση με τα φίλτρα παρατήρησης. Ενώ η ακριβής πρόβλεψη του αναμενόμενου σήματος ευθυγράμμισης σε διαφορετικά φίλτρα είναι περίπλοκη, είναι εμφανής ότι ενδιαφέρουσες ανακαλύψεις κρύβονται στην ευθυγράμμιση γαλαξιών σε μικρές κλίμακες.

Συνεχίζουμε την εργασία με το **κεφάλαιο 3**, όπου κοιτάμε την ευθυγράμμιση γαλαξιών στο φίλτρο r, σε μεγάλες κλίμακες. Στόχος είναι να παρέχουμε μια απευθείας μέτρηση του σήματος, για να το χρησιμοποιήσουμε ως α-πριόρι γνώση. Για να το επιτύχουμε, είναι πολύ σημαντικό να χρησιμοποιήσουμε δείγμα γαλαξιών όσο το δυνατό πιο αντιπροσωπευτικό μιας έρευνας βαρυτικών φακών. Βρίσκουμε πως οι κόκκινοι γαλαξίες έχουν δυνατό σήμα ευθυγράμμισης ενώ οι μπλε γαλαξίες έχουν σήμα συμβατό με μηδέν, σε συμφωνία με προηγούμενες μελέτες. Χρησιμοποιώντας αυτές τις μετρήσεις ευθυγράμμισης, υπολογίζουμε πως οι σημερινές έρευνες βαρυτικών φακών μπορούν να επιτύχουν σημαντικά πιο ακριβή μετρήσεις της S_8 παραμέτρου.

Στη συνέχεια, εστιάζουμε στην ευθυγράμμιση γαλαξιών σε μικρότερες κλίμακες, κοιτώντας ιδιαίτερα στα γκρουπ γαλαξιών στο **κεφάλαιο 4**. Μετράμε σημαντική αξονική ευθυγράμμιση των γαλαξιακών δορυφόρων σε σχέση με το κέντρο του γαλαξιακού γκρουπ, η οποία μειώνεται στο μηδέν σε μεγάλες αποστάσεις. Επιπλέον, βρίσκουμε πως οι εξωτερικές περιοχές των δορυφόρων (οι οποίες στοχεύονται καθώς αυξάνουμε τη συνάρτηση βαρύτητας κατά τη μέτρηση του σχήματός τους) είναι περισσότερο ευθυγραμμισμένες από τις εσωτερικές περιοχές τους. Κόκκινοι δορυφόροι δείχνουν γενικά πιο ισχυρή ευθυγράμμιση από τους μπλε. Επίσης, οι κεντρικοί γαλαξίες των γκρουπ είναι ευθυγραμμισμένοι με την κατανομή των γαλαξιακών δορυφόρων, με τις εξωτερικές περιοχές των κεντρικών γαλαξιών να είναι πιο ισχυρά ευθυγραμμισμένες από τις εσωτερικές, και τους κόκκινους κεντρικούς γαλαξίες να δείχνουν πιο ισχυρή ευθυγράμμιση από τους μπλε. Οι μετρήσεις αυτές υποδεικνύουν ότι η ευθυγράμμιση γαλαξιών σε μικρές κλίμακες είναι γενικά περίπλοκο φαινόμενο, και τα ευρήματά μας μπορούν να χρησιμοποιηθούν για να βελτιώσουμε υπάρχοντα μοντέλα του σήματος ευθυγράμμισης στις μικρές αυτές κλίμακες.

Στο **κεφάλαιο 5** εμβαθύνουμε περαιτέρω και μελετάμε την ευθυγράμμιση των κεντρικών γαλαξιών με την δική τους άλω σκοτεινής ύλης. Για το σκοπό αυτό, μετράμε το ανισοτροπικό σήμα βαρυτικών φακών γύρω από δείγμα γαλαξιών ειδικά διαλεγμένο με μικρή ποσότητα γαλαξιακών δορυφόρων. Ποσοτικοποιούμε την f_{h}, μια παράμετρο ευαίσθητη στη σχετική ελλειπτικότητα της άλως σκοτεινής ύλης και του γαλαξία, καθώς επίσης και στην μέση σχετική τους γωνία. Βρίσκουμε πως οι κόκκινοι κεντρικοί γαλαξίες έχουν μη-μηδενική f_{h} με 2σ στατιστική βεβαιότητα. Η μετρούμενη τιμή της f_{h} αυξάνεται σημαντικά αν επαναλάβουμε τη μέτρηση χρησιμοποιώντας σχήματα γαλαξιών που είναι πιο ευαίσθητα στις εξωτερικές περιοχές των γαλαξιών. Εφ΄ όσον η μέση ελλειπτικότητα του σχήματος των γαλαξιών στις εσωτερικές και εξωτερικές περιοχές δεν αλλάζει σημαντικά, συμπεραίνουμε πως οι εξωτερικές περιοχές των γαλαξιών είναι περισσότερο ευθυγραμμισμένες με την άλω σκοτεινής ύλης τους από τις εσωτερικές περιοχές.

List of publications

First Author

Halo shapes constrained from a pure sample of central galaxies in KiDS-1000
C. Georgiou, H. Hoekstra, K. Kuijken, M. Bilicki, A. Dvornik, T. Schrabback, A&A, in prep.

GAMA+KiDS: Alignment of galaxies in galaxy groups and its dependence on galaxy scale
C. Georgiou, N.E. Chisari, M.C. Fortuna, H. Hoekstra, K. Kuijken, B. Joachimi, M. Vakili, M. Bilicki, A. Dvornik, T. Erben, B. Giblin, C. Heymans, N.R. Napolitano, H. Shan, A&A 628, A31 (2019)

The dependence of intrinsic alignment of galaxies on wavelength using KiDS and GAMA
C. Georgiou, H. Johnston, H. Hoekstra, M. Viola, K. Kuijken, B. Joachimi, N.E. Chisari, D.J. Farrow, H. Hildebrandt, B.W. Holwerda, A. Kannawadi, A&A 622, A90 (2019)

Contributing Author

Luminous red galaxies in the Kilo-Degree Survey: selection with broad-band photometry and weak lensing measurements
M., Vakili, M. Bilicki, H. Hoekstra, N.E. Chisari, M.J.I. Brown, **C. Georgiou**, A. Kannawadi, K. Kuijken, A.H. Wright, MNRAS 487, 3 (2019)

Consistent cosmic shear in the face of systematics: a B-mode analysis of KiDS-450, DES-SV and CFHTLenS
M. Asgari, C. Heymans, H. Hildebrandt, L. Miller, P. Schneider, A. Amon, A. Choi, T. Erben, **C. Georgiou**, J. Harnois-Deraps, K. Kuijken, A&A 624, A134 (2019)

KiDS+GAMA: Intrinsic alignment model constraints for current and future weak lensing cosmology
H. Johnston, **C. Georgiou**, B. Joachimi, H. Hoekstra, N.E. Chisari, D.J. Farrow, M.C. Fortuna, C. Heymans, S. Joudaki, K. Kuijken, A.H. Wright, A&A 624, A30 (2019)

Photometric redshifts for the Kilo-Degree Survey. Machine-learning analysis with artificial neural networks
M. Bilicki, H. Hoekstra, M.J.I. Brown, V. Amaro, C. Blake, S. Cavuoti, J.T.A de Jong, **C. Georgiou**, H. Hildebrandt, C. Wolf, A. Amon, M. Brescia, S. Brough, M.V. Costa-Duarte, T. Erben, K. Glazebrook, A. Grado, C. Heymans, T. Jarrett, S. Joudaki, K. Kuijken, G. Longo, N.R Napolitano, D. Parkinson, C, Vellucci, G.A. Verdoes Kleijn, L. Wang, A&A 616, A69, (2018)

Curriculum Vitae

I was born in Ioannina on 1992 and grew up in a small, seaside town called Igoumenitsa in the north-west of Greece. I developed an inquisitive and curious nature since I was little, which made it natural to be drawn to the sciences of physics and mathematics. I was fascinated by the fact that we can predict the travel time of a falling object or the deflection of light rays using simple mathematics and hypotheses, and I wondered how many more secrets of physical phenomena could be unravelled. Motivated by this, I joined national competitions in physics and astronomy during high school receiving honourable mentions for my performance, and I participated in a summer school in astronomy in Corinth, Greece.

After high school, I joined the BSc programme in physics, in the Aristotle university of Thessaloniki, Greece in September of 2010. During my studies, I was drawn to the biggest mysteries and questions about nature on a grand scheme, and chose the specialization of astronomy. On top of that, I attended two more summer schools on astronomy in Volos, Greece and an international conference on X-ray astronomy, to cultivate my research interest. I was also selected as a teaching assistant (problem sheet marker) on the undergraduate courses of Calculus I and Introduction to Astronomy. During my final year, I focused on cosmology and general relativity which led to my thesis, titled "Covariant and Gauge-Invariant perturbations in Tilted FLRW models", under the supervision of Prof. dr. Christos Tsagkas. In this work, I studied linear perturbations, using general relativity, for observers that have a peculiar velocity with respect to the Hubble flow. My performance in the overall BSc programme allowed me to receive a scholarship from the bequest of "Afon Zosima" as well as graduate cum laude. In the summer of 2014, I attended the summer school on cosmology in Trieste, Italy, where I presented my undergraduate thesis.

I proceeded to enroll in the MSc of theoretical physics, in the university of Edinburgh, in September of 2014. I was able to secure funding for my masters through the "Highly skilled workforce scholarship" together with a scholarship from the "Lilian Voudouri" foundation. I chose many elective courses focused on astronomy, and ultimately carried out my master thesis on "Enzo AMR simulations of cooling gas in galaxy haloes", supervised by Prof. dr. Avery Meiksin and Dr. Eric Tittley, where we investigated the performance of different AMR simulation setups with regards to dark matter and gas profiles. I graduated with a distinction in August of 2015.

Following my graduate studies, I joined the Leiden Observatory as a PhD Candidate in October of 2015. Under the supervision of Prof. dr. Koen Kuijken and the now Prof. dr. Henk Hoekstra, I joined the Kilo Degree Survey (KiDS) collaboration to work on gravitational lensing. Together with Dr. Massimo Viola, I used a sophisticated method to measure galaxy shapes from the high quality KiDS imaging data and quantify the intrinsic galaxy alignment signal, the coherent orientation patterns of physically associated galaxies due to their interaction with the tidal gravitational field. The measurement of intrinsic alignments will ultimately help better understand and model the phenomenon, which will bias cosmological parameters inferred through weak gravitational lensing measurements, if left unaccounted for. Moreover, I was involved in the Physics of the Accelerating Universe Survey (PAUS), and worked on developing a part of the photometry pipeline. I attended the winter school in cosmology in Tonale, Italy and presented my research during the PhD in several conferences in Netherlands, Australia, China and Japan. I also served as a teaching assistant for the astronomy bachelor course "astronomy lab & observing project" in Leiden University, organised the weekly group meetings of the weak gravitational lensing group during 2018-2019 and gave a public science talk on gravitational lensing, organised by "Astronomy on Tap" in 2018.

Looking ahead, I wish to employ my skills and knowledge to help us better understand the world and how best to use it.

Acknowledgements

A great many number of people have made their contribution, in many ways, to my endeavour to obtain my PhD. I would not be in this position today without the massive, selfless support of my parents, in their many ways, since the very beginning of my undergraduate studies. Σας ευχαριστώ από τα βάθη της καρδιάς μου.

The work I have conducted during my research is the product of a large team of scientists, namely the KiDS and GAMA collaborations, and this thesis would not have been possible without their hard work. In particular, I thank my close collaborators, Harry Johnston and Elisa Chisari for always being willing to help and making work fun. In addition, I would like to thank Massimo Viola for his support in the early days of my PhD and for having his way of making me feel excited to work after each and every one of our meetings. I am also grateful to the weak gravitational lensing group in Leiden, for all our meetings and discussions; thank you Andrej, Stijn, Lammim, Maria Cristina, Patricia, Yannick, Matthieu, Mohammadjavad, Arun, David, Alessandro, Omar, Riccardo, Cristobal, Margot, Fabian and Marcello.

In my experience, the quality of work during the PhD is somewhat intertwined with one's private life, and vice versa. I was fortunate enough to be surrounded by wonderful people during these four years, that made a direct or indirect contribution to the finishing of this thesis. Tommaso, I was certain we would be good friends since the first day of work that I met you. Jit, I admired your kindness and selflessness and I was happy and honoured to be your close friend. A big thanks to both of you, for all the beers, trips, talks and late nights, and always being helpful and supportive to me no matter what; I could not go on without you. A big thank you also goes to Eleonora and Maria Cristina, for the many trips, dinners, talks and for being there for me and willing to help even when I did not know I needed it. My thanks extend to the rest of my friends who made my everyday life more interesting and fun: Andrej, Valeriya, Fraser, Dilovan, Gabriela, Aayush, Alberto, Emanuele, Clément, Vincenzo, Kim, Pedro, Francesco and Kirsty. Andrea, thank you for your valuable support in these last months of my PhD.

It is not a coincidence that many astronomers and physicists enjoy the sport of climbing, since it requires an analytic mind's approach. During my PhD, climbing was a safe haven where my mind would stop being occupied with anything except for how to top the climb in question. I made many friends during this activity which made climbing and life a lot better for me and led to many nice trips and experiences. For this, I would like to thank Andrea, Jit, Christiane, Pablo, Marta, Lieslore, Liuba, Filippo, Vincenzo, Lise, Chloe and Arthur.

Lastly, I thank my brother and sister, for their support in their many ways, during the years of my PhD, as well as my grandfather and grandmother, for their unconditional love and support.